UNIVERSIDAD COMPLUTENSE DE MADRID

FACULTAD DE CIENCIAS FÍSICAS

Departamento de Física de Materiales

TESIS DOCTORAL

Caracterización de superficies y películas de óxidos: crecimiento en tiempo real, efectos de intercara y magnetismo

Characterization of oxide surfaces and films : real-time growth, interface effects and magnetism

MEMORIA PARA OPTAR AL GRADO DE DOCTOR

PRESENTADA POR

Laura Martín García

Directores

Juan de la Figuera Bayón
José Francisco Marco Sanz

Madrid, 2018

UNIVERSIDAD COMPLUTENSE DE MADRID

FACULTAD DE CIENCIAS FÍSICAS

Departamento de Física de Materiales

Caracterización de superficies y películas de óxidos: crecimiento en tiempo real, efectos de intercara y magnetismo

Characterization of oxide surfaces and films: real-time growth, interface effects and magnetism

Memoria presentada por

Laura Martín García

para obtener el título de Doctor en Física

Directores:

Dr. Juan de la Figuera Bayón

Dr. José Francisco Marco Sanz

Madrid, 2017

Resumen

Objetivos y metodología

Los óxidos son los compuestos más abundantes que existen en nuestro entorno y la humanidad lleva haciendo uso de sus propiedades desde hace miles de años. En concreto, la invetigación basada en óxidos de metales de transición ha sido fundamental en el desarrollo de campos tan importantes como la catálisis o el almacenamiento de energía. Su potencial reside en la gran variedad de propiedades que pueden exhibir. Dependiendo de los elementos que los componen y de su estructura, los óxidos de metales de transición pueden ser conductores, superconductores, ferromagnéticos, ferroeléctricos, antiferromagnéticos, etc. Entre ellos, la magnetita (Fe_3O_4) es un material ampliamente estudiado tanto desde un enfoque fundamental como aplicado para su uso en campos como la biofísica, la catálisis o la espintrónica. Una parte de la presente tesis está enfocada en el estudio de sus propiedades estructurales y magnéticas en superficie haciendo uso de técnicas de microscopía de electrones de baja energía polarizados en spin y de fotoemisión.

Desde la segunda mitad del siglo XX, la miniaturización de los dispositivos ha dado lugar a una revolución en el campo de la microelectrónica. Por ello, uno de los principales objetivos en los que se investiga es en adquirir la habilidad para sintetizar materiales a escala nanométrica manteniendo el control de sus propiedades en volumen. Sin embargo, estas propiedades pueden verse deterioradas por la presencia de defectos, provocando

una pérdida de funcionalidad del dispositivo en el que están integrados. Una parte del presente trabajo se centra en la síntesis de películas de monóxidos de hierro (FeO) y de cobalto (CoO) y composiciones mixtas de ambos estudiando el proceso de crecimiento por medio de microscopía de electrones de baja energía. La caracterización se lleva a cabo por medio de técnicas de difracción y de fotoemisión. Finalmente, la observación del proceso de crecimiento en tiempo real se utiliza como herramienta para la síntesis de películas de ferrita de cobalto ($CoFe_2O_4$), material muy relacionado con la magnetita y de gran interés en el campo de la espintrónica, con una alta calidad cristalina.

Resultados y conclusiones

Fe_3O_4

La primera parte del trabajo se centra en el estudio de la superficie (001) de un cristal de magnetita. Se ha realizado una caracterización estructural y magnética en superficie por medio de microscopía de electrones de baja energía polarizados en spin. Se ha estudiado la configuración de dominios magnéticos siguiendo su evolución con la temperatura. De este modo, hemos observado que los dominios magnéticos se ven alterados a medida que la temperatura de la muestra aumenta hasta desaparecer al llegar a la temperatura de Curie. Hemos detectado que la configuración de dominios se recupera una vez se retorna a la temperatura ambiente y que los cambios observados en los dominios magnéticos son equivalentes a los obtenidos al enfriar la muestra por debajo de temperatura ambiente hasta la temperatura de reorientación de spin. Además hemos observado que la transición de reorientación de spin ocurre en dos etapas: primero tiene lugar la nucleación de nuevos dominios con los ejes fáciles de imanación correspondientes a los de la fase de baja temperatura seguido de una reorientación del resto de dominios. Lo observado se ha explicado basándose en la dependencia de la anisotropía magnetocristalina de la magnetita con la temperatura.

La caracterización magnética se ha completado mediante la determinación de los momentos magnéticos orbital y de spin de la muestra por medio de dicroismo magnético circular de rayos X. Los valores obtenidos son diferentes del esperado para magnetita estequiométrica en volumen lo que se ha explicado en base a la reconstrucción $\sqrt{2} \times \sqrt{2}$R45° exhibida por la superficie (001) de la magnetita.

Monóxidos de Fe-Co en Ru(0001)

La segunda parte del trabajo se centra en el estudio del crecimiento de películas de monóxidos de hierro y de cobalto sobre Ru(0001). Empleando la técnica de deposición por láser pulsado se han sintetizado películas de monóxido de hierro de varios nanómetros de espesor. Estas películas exhiben unas propiedades que se han explicado proponiendo una terminación en superficie con estructura de wurzita distinta de la estructura de "sal común" exhibida en volumen. Por otra parte, se ha estudiado el crecimiento de FeO y CoO por epitaxia de haces moleculares siguiendo el crecimiento en tiempo-real por microscopía de electrones de baja energía. Se ha observado que el CoO crece en islas pequeñas, de manera tridimensional mientras que el FeO crece cubriendo la superficie del substrato de manera bidimensional. Finalmente, se han hallado las condiciones para sintetizar películas de monóxidos de composiciones mixtas de hierro y cobalto.

$CoFe_2O_4$ en Ru(0001)

La tercera parte del trabajo consiste en el estudio del crecimiento de películas de ferrita de cobalto en Ru(0001) por epitaxia de haces moleculares. El crecimiento se ha seguido en tiempo-real por microscopía de electrones de baja energía. Se han conseguido sintetizar islas monocristalinas, atómicamente planas, con dominios magnéticos varios órdenes de magnitud mayores que los reportados previamente en la literatura. Las muestras se han caracterizado *in situ* por técnicas de difracción y fotoemisión y *ex situ*

por AFM/MFM. El método de crecimiento se propone como método que permita evitar la formacion de defectos como fronteras de antifase que resultan en el deterioro de las propiedades exhibidas por el material.

Abstract

Objective and methodology

Oxides are the most abundant compounds around us and their properties have been exploited by people for thousands of years. Particularly, transition metal oxide research contributed to the development of important fields like catalysis and energy storage. Depending on their composition and structure, transition metal oxides exhibit a wide range of physical properties: they can exhibit conductivity, semiconductivity, ferromagnetism, ferrolectricity, antiferromagnetism, etc. Among them, magnetite (Fe_3O_4) is a widely studied material, both in fundamental and in applied research for applications in biophysics, catalysis or spintronics. A part of this thesis is focused on the study of the surface structure and the surface magnetic properties of magnetite by means of spin-polarized low-energy electron and photoemission microscopy.

Nowadays, advances in microelectronics come with the miniaturization of devices. This requires the ability to synthesize nanosized materials while keeping the control of their properties. However, the presence of defects can deteriorate these properties and thus, the functionality of the device in which they are integrated. Part of this work is focused on studying the synthesis of iron monoxide (FeO) and cobalt monoxide (CoO) films and monoxides with mixed compositions of both elements following the growth process by means of low-energy electron microscopy. The samples will be characterized

by diffraction and photoemission techniques. Finally, the observation in real-time of the growth process will be used to explore a route to synthesize high quality cobalt ferrite ($CoFe_2O_4$) films, a promising material for spintronic applications and closely related to magnetite.

Results and conclusions

Fe_3O_4

The first part of this thesis is focused on the study of the (001) surface of a magnetite single crystal. The surface structure and the surface magnetic properties have been characterized by means of spin-polarized low-energy electron microscopy. The evolution of the magnetic domains has been followed as a function of the sample's temperature. The domains change with increasing temperature until they disappear when the Curie temperature is reached. It has been observed that the magnetic domain configuration is recovered after decreasing the temperature back to room temperature and that the observed changes are equivalent to those observed when decreasing the temperature of the sample from room temperature to the spin reorientation transition temperature. The spin reorientation transition is observed to take place in two stages: first, there is a nucleation of new domains oriented along the easy axes of the low temperature phase of magnetite followed by a reorientation of the magnetization of the rest of domains. The observed changes have been explained based on the dependence of the magnetocrystalline anisotropy of magnetite with the temperature.

In order to complete the magnetic characterization of the sample, the spin and orbital magnetic moments have been determined by means of X-ray magnetic circular dichroism. The measured values are different to those expected for stoichiometric bulk magnetite. These results have been related to the $\sqrt{2} \times \sqrt{2}R45^\circ$ reconstruction exhibited by the (001) surface of magnetite.

Fe-Co monoxides on Ru(0001)

The second part of this thesis is focused on the study of the iron and cobalt monoxide thin film growth on Ru(0001). Iron monoxide films with thicknesses up to few nanometers have been synthesized by pulsed laser deposition. The films exhibit some properties that are explained by theoretical calculations suggesting a wurtzite surface termination in contrast with the expected rock salt bulk structure. On the other hand, FeO and CoO films have been synthesized by molecular beam epitaxy on Ru(0001) following the growth in real-time by low-energy electron microscopy. The CoO growth proceeds in a tridimensional way with the nucleation of small islands while the FeO grows wetting the substrate. Finally, films of mixed compositions of iron-cobalt monoxides were synthesized.

$CoFe_2O_4$ on Ru(0001)

The third part of this thesis is focused on the study of the cobalt ferrite thin film growth on Ru(0001) by molecular beam epitaxy. The growth was investigated by means of low-energy electron microscopy. The obtained islands are single crystal, atomically flat and present magnetic domains several orders of magnitude wider than those reported in the literature. The islands were characterized *in situ* by diffraction and photoemission techniques and *ex situ* by AFM/MFM. The growth method is proposed as a mechanism to avoid the formation of defects, like antiphase boundaries (APBs), that deteriorates the exhibited properties of the material.

Contents

CHAPTER 1

Preface

Transition metal oxides are important materials that cover a wide range of applications in catalysis, spintronics, energy storage and other fields [1–3]. They can present different structures. Among them, spinels comprise an oxide family with the general formula XY_2O_4. The structure consists in a face centred-cubic (fcc) lattice of oxygen anions where the cations occupy octahedral (B) and tetrahedral (A) interstitial sites. The unit cell contains 32 O^{2-}, 16 Y^{3+} and 8 X^{2+} where X and Y stand for metal cations. The structure can accommodate various cations that can appear with multiple oxidations states, for example Fe^{2+} and Fe^{3+} coexist in Fe_3O_4. Spinels are divided into normal, with divalent/trivalent cations in tetrahedral/octahedral sites respectively and inverse spinels, with divalent cations in octahedral sites and trivalent cations occupying both tetrahedral and octahedral sites. However, partially inverse spinels exhibiting a structure between this two ideal cases are also possible. This chemical flexibility is the reason for the wide variety of properties that they exhibit such as ferri- (Fe_3O_4, $CoFe_2O_4$, $NiFe_2O_4$) or antiferromagnetism (Co_3O_4), ferroelectricity ($CoCr_2O_4$), superconductivity ($LiTi_2O_4$), conductivity ($CuCo_2O_4$) or half-metallicity (Fe_3O_4). The control over the cations and their distribution allows to tune their physical properties. This is specially relevant in

the case of surfaces and thin films, the main subject of this thesis.

Part of this thesis is focused on the study of the (001) surface of a Fe_3O_4 single crystal. Fe_3O_4 is the oldest magnetic material known and has been used for many purposes since the antiquity, as source of iron, as a pigment, or as a catalyst among other uses [3, 4]. The lowest energy surface of magnetite is the (111) [4]. However, compared to Fe_3O_4(111) and Fe_3O_4(110), Fe_3O_4(001) is the most studied surface [3]. The main reason for that is because the Fe_{oct}-O termination can be prepared in a reproducible way by annealing the crystal at $\sim$ 900 K in 10^{-7} - 10^{-5} mbar O_2 in the final stage of the surface preparation. Being able to reproduce the same surface termination facilitates the study and the interpretation of the results obtained. In comparison, the preparation of the Fe_3O_4(111) and the Fe_3O_4(110) surfaces is more difficult. Two different surface terminations can be obtained in Fe_3O_4(111) under similar preparation conditions [3]. There are also difficulties to prepare Fe_3O_4(110) surfaces as it has been recently reported that the surface is unstable towards the formation of (111) nanofacets [5]. Additionally Fe_3O_4(001) presents a $\sqrt{2} \times \sqrt{2}$R45° surface reconstruction, recently explained, and with important implications for the properties exhibited by the surface [6].

The cobalt ferrite spinel, $CoFe_2O_4$, is another material that has been intensively studied in the last years as it presents very interesting properties to be exploited in nanotechnology [1]: it is a ferrimagnetic insulator with a high magnetocrystalline anisotropy and a large magnetostriction. However, the synthesis of high quality $CoFe_2O_4$ thin films remains a challenge due to the increased presence of defects at the nanoscale that deteriorates the properties exhibited in bulk. This motivated us to study a via to synthesize $CoFe_2O_4$ thin films free from defects as a necessary step previous to the successful integration of this material into devices. Furthermore, the magnetic and structural properties of the $CoFe_2O_4$ films are studied in detail.

FeO and CoO [4, 7, 8] present a rocksalt structure that can be considered as based on the spinel one where the tetrahedral positions are empty and the divalent cations

occupy all the available octahedral sites. FeO and CoO present similarities in terms of the lattice spacings, conductivity and magnetic properties. They both present cation defects although the concentration of vacancies in FeO is larger than in CoO [4, 8]. Actually the presence of vacancies in FeO has been related to the appearance of Fe_3O_4 [9]. When using molecular beam epitaxy, the maximum FeO thickness that can be grown depends on the substrate, with up to four FeO layers on Ru(0001) [10]. Further deposition of material leads to the nucleation of Fe_3O_4 islands. In this thesis we demonstrate that the pulsed laser deposition technique, which enables a large energy per atom to be deposited on the surface, is well-suited to obtain large thin film thicknesses of FeO on Ru(0001) without the appearance of other oxide phases. The growth of FeO on Ru(0001) by pulsed laser deposition is also compared with the growth of FeO and CoO on Ru(0001) by molecular beam epitaxy.

Outline

Here we introduce a brief description of the chapters in which this thesis is divided:

Chapter 2. In this chapter the deposition and the characterization techniques employed to grow and study the samples are presented, with a description of the systems where these techniques were employed. The chapter finishes with a description of the samples and the preparation methods used in this thesis.

Chapter 3. In this chapter the reconstructed (001) surface of a magnetite single crystal is studied. It begins with an introduction of the crystal structure and the magnetic properties of both the bulk and the surface of the material. Next, the study of the evolution of the magnetic domain configuration with the temperature with special attention devoted to the spin reorientation transition is presented. The results are discussed in terms of the magnetic anisotropies present in the material. Finally, the spin and orbital magnetic moments of the reconstructed surface are determined by means of X-ray magnetic circular dichroism.

Chapter 4. This chapter is dedicated to the growth of FeO and CoO thin films on Ru(0001). It begins with an introduction of the main properties of both materials followed by a review of the thin film growth studies found in the literature. Next, the growth of FeO by pulsed laser deposition is investigated. The properties of the obtained thin films are explained by theoretical calculations based on a surface structure which is different from that of the bulk. The FeO and CoO thin film growth on Ru(0001) by molecular beam epitaxy is studied next by low-energy electron microscopy observing significant differences in the growth of both materials. The chapter finishes with the investigation of the growth of mixed Fe and Co monoxides on Ru(0001).

Chapter 5. Here the growth of cobalt ferrite thin films on Ru(0001) is studied. The chapter begins with the introduction of the crystal structure and the magnetic properties of cobalt ferrite with special emphasis on the observed deterioration of the thin film properties due to the presence of antiphase boundaries. Next, the study of the growth of cobalt ferrite on Ru(0001) by molecular beam epitaxy is presented with a detailed characterization of the structural and the magnetic properties. Based on the obtained result, this growth approach is presented as a method to obtain high quality nanostructures of materials free of antiphase boundaries.

Chapter 6. This chapter summarizes the main results obtained in this thesis.

Bibliography

[1] J.-B. Moussy. From epitaxial growth of ferrite thin films to spin-polarized tunnelling. *Journal of Physics D: Applied Physics*, 46(14):143001, 2013.

[2] M. Opel. Spintronic oxides grown by laser-MBE. *Journal of Physics D: Applied Physics*, 45(3):033001, 2012.

[3] G. S. Parkinson. Iron Oxide Surfaces. *Surface Science Reports*, 2016.

[4] R. M. Cornell and U. Schwertmann. *The Iron Oxides: Structure, Properties, Reactions, Occurrences and Uses*. VCH, Weinheim, 1997.

[5] G. S. Parkinson, P. Lackner, O. Gamba, S. Maaß, S. Gerhold, M. Riva, R. Bliem, U. Diebold, and M. Schmid. $Fe_3O_4(110)$-(1×3) revisited: Periodic (111) nanofacets. *Surface Science*, 649:L120 – L123, 2016.

[6] R. Bliem, E. McDermott, P. Ferstl, M. Setvin, O. Gamba, J. Pavelec, M. A. Schneider, M. Schmid, U. Diebold, P. Blaha, L. Hammer, and G. S. Parkinson. Subsurface cation vacancy stabilization of the magnetite (001) surface. *Science*, 346(6214):1215–1218, 2014.

[7] R. M. Hazen and R. Jeanloz. Wüstite ($Fe_{1-x}O$): a review of its defect structure and physical properties. *Reviews of Geophysics and Space Physics*, 22:37, 1984.

[8] M. Chen, B. Hallstedt, and L. J. Gauckler. Thermodynamic assessment of the Co-O system. *Journal of Phase Equilibria*, 24(3):212–227, 2003.

Bibliography

[9] I. Bernal-Villamil and S. Gallego. Electronic structure and polaronic charge distributions of fe vacancy clusters in $Fe_{(1-x)}O$. *Physical Review B*, 90(19):192126, 2014.

[10] G. Ketteler and W. Ranke. Heteroepitaxial growth and nucleation of iron oxide films on Ru(0001). *Journal of Physical Chemistry B*, 107(18):4320–4333, 2003.

CHAPTER 2

Experimental Details

This chapter presents the deposition techniques employed to grow the samples and the characterization techniques used during this thesis. Next, there is a description of the systems and places where these techniques were employed, the "Surfmoss" system at the Instituto de Química Física "Rocasolano"(CSIC), located in Madrid (Spain), the SPLEEM system at the National Center for Electron Microscopy at Lawrence Berkeley National Laboratory located in Berkeley (California) and the SPELEEM system at the CIRCE beamline of the ALBA Synchrotron Light Facility located in Barcelona (Spain). Finally, there is a brief description of the samples employed in this work and their preparation details.

2.1 Thin film deposition techniques

2.1.1 Molecular Beam Epitaxy

Molecular beam epitaxy (MBE) [1, 2] is a technique to grow thin films that consists on a beam of atoms of an element that arrives to a heated substrate. The beam of atoms comes from a doser, in our case a metal rod heated by electron bombardment. The electron source is a W filament that is heated to produce electrons. The electrons are accelerated towards the metal rod by an

applied high voltage (HV) heating the metal rod and causing the evaporation of the atoms. If oxygen is supplied during the MBE process, the technique is known as oxygen assisted molecular beam epitaxy (O-MBE) [3]. During this thesis O-MBE was employed to grow Fe-Co oxide films by dosing Co and Fe onto a heated Ru(0001) substrate in an oxygen background.

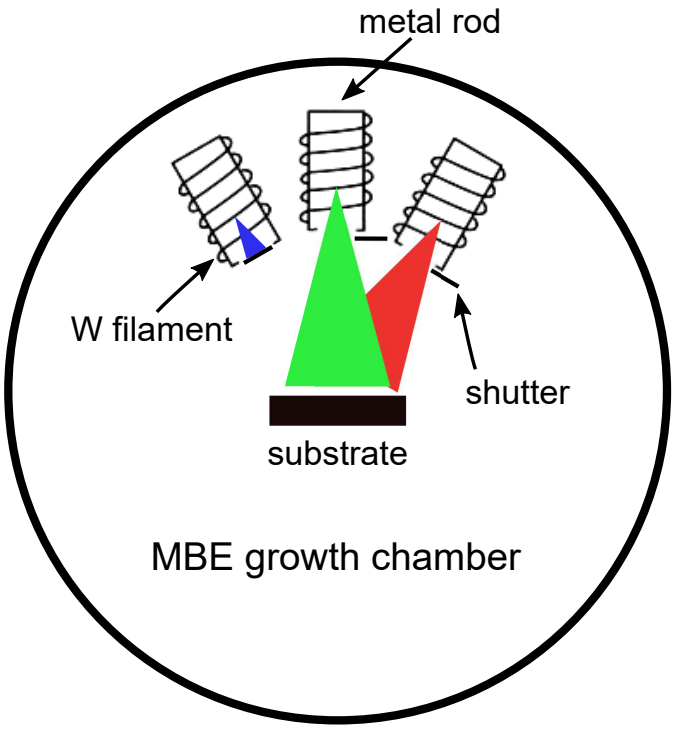

Figure 2.1: Schematics of an MBE growth chamber.

In MBE, the deposition rates are lower than for other methods. In our work, they were typically of the order of 1 monolayer (ML) per few minutes. On one hand, this implies the use of ultra-high vacuum (UHV) to maintain the surface clean during the growth, otherwise the film would be contaminated by the residual gas in the growth chamber. On the other hand, the slow deposition rate allows for a precise control of the growth process. Films of high crystalline quality with dimensions and interfaces controlled to the atomic level can be obtained by this technique.

Controlling the evaporation rate is crucial, specially when the film is composed by more than one element. In this case, the evaporation rate of each element has to be controlled in order to obtain the desired ratio of the elements constituting the film. In this thesis, the dosers

were tested separately by evaporating 1 monolayer of Fe or Co on Ru(0001) and adjusting the emission flux to obtain the desired evaporation rate. For Fe, typical evaporation conditions were a HV = 2 kV, a filament current (I_{Fil}) = 2.5 A and an emission current (I_{emiss}) = 12 mA while for Co, HV = 2 kV, I_{Fil} = 3.3 A and I_{emiss} = 13 mA were employed. A typical oxygen pressure was 10^{-6} mbar.

2.1.2 Pulsed Laser Deposition

Pulsed laser deposition (PLD) is another common technique to grow thin films [4–6]. An schematic diagram of a PLD system is shown in Figure 2.2. Laser pulses are focused onto a rotating target[1], which in our case is a pellet of hematite (α-Fe_2O_3), at an angle of 45°[2]. As a consequence of the laser irradiation, the target is strongly heated ensuring that all target components, independent of their binding energies, evaporate at the same time causing the stoichiometric removal of the material. The material ejected forms a plasma of neutral and ionized species that moves away from the target and towards the substrate located opposite to the target where the film is deposited.

It should be noted that the stoichiometric removal of material from the target does not imply a deposition of a film with stoichiometric composition. Under UHV conditions, volatile elements like oxygen can be lost during the ablation process or be re-sputtered from the substrate [6–8]. This can be compensated by supplying oxygen into the growth chamber or for other cases, employing a target enriched with the volatile element.

The deposition rate in PLD is high compared to MBE. It is related to different factors like the laser energy, the laser repetition rate or the target-substrate distance. In our case, the deposition rate is in the order of 2 nm/min calculated for a target-substrate distance of 2 cm, i.e. about 100 times faster than the MBE deposition rate.

The characteristics of the deposited films like the microstructure or the composition can vary upon changing experimental conditions such as the background gas pressure [9], the laser

[1] The rotation of the target is needed to provide a fresh area under irradiation.

[2] A 45° has been found to be the optimum to keep the energy density constant over the illuminated target area.

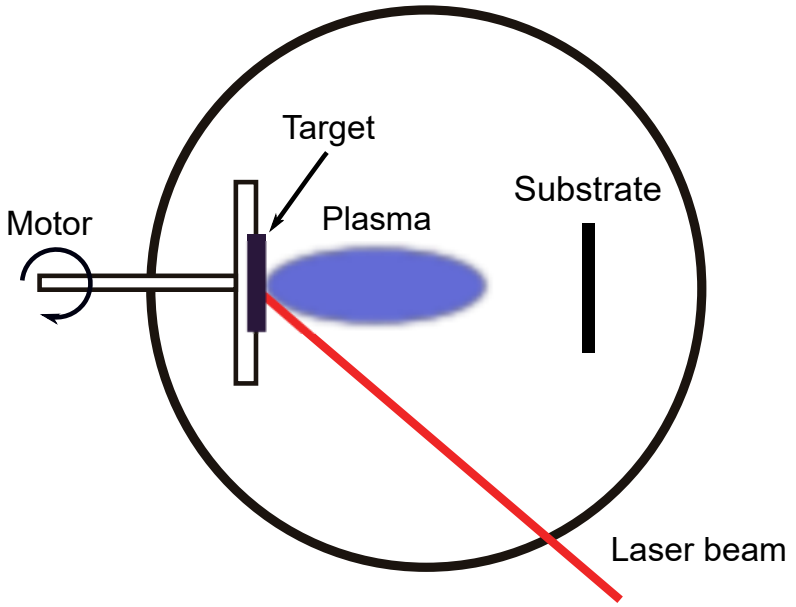

Figure 2.2: Schematics of a PLD system.

wavelength [10], the laser repetition rate [11] or the substrate temperature [7, 10]. In this work, on one hand the modification of some of the preparation conditions, like the target-to-substrate distance and the substrate temperature was investigated. On the other hand, the laser parameters were the same for all the experiments: a Q-switched Nd:YAG laser with a pulse duration of 5 ns and a repetition rate of 10 Hz was employed. The laser wavelength was 1064 nm, the laser spot area on the target was 0.15 mm^2 and the fluence (laser energy per unit area) was fixed to a value of 4.4 Jcm^{-2} which corresponds to 8 times the ablation threshold fluence of the target. This threshold value was determined by measuring the minimum single pulse energy necessary to yield a luminous plume detected by eye on the target.

2.2 Characterization techniques

2.2.1 Low-Energy Electron Diffraction

Low-energy electron diffraction (LEED) [12–14] is an essential tool in the study of cystal surfaces. A LEED diffractometer consists in an electron gun that generates a monoenergetic beam that

impinges on the sample surface. The electrons are then diffracted in different directions. The inelastically scattered electrons are suppressed by a set of hemispherical grids and the elastically diffracted electrons are imaged after being accelerated and impinge on a phosphor screen. The diffraction process is explained on the basis of the wave-particle duality. The electron beam may be regarded as a set of electron waves incident on the sample with an associated wavelength given by the de Broglie relation [12]:

$$\lambda = \frac{h}{\sqrt{2meV}} \tag{2.1}$$

where h is the Planck's constant, m is the electron mass, e is the electron charge and V is the beam voltage. The range of energies employed in LEED (typically in the range 20-500 eV) corresponds to electron wavelengths comparable with inter-atomic distances, a necessary condition to observe diffraction effects associated with an atomic structure [12].

At the electron energies used in LEED, the mean free path of the electrons is very low, of the order of 1–3 ML (see Figure 2.4 and its discussion). Thus, only the electrons scattered by the near surface of the crystal contribute to the diffraction, giving the technique a high surface sensitivity. Not only the bare surface structure may be determined but any situation that gives rise to a new arrangement of the atoms on the surface with a long range order, i.e. adsorbate atoms at the surface or a reconstruction, may be investigated by LEED.

In order to understand a diffraction pattern it is useful to introduce the concepts of direct and reciprocal lattice. The surface of a crystal can be considered as a two-dimensional lattice, named direct lattice, described by the real space unit vectors, $\mathbf{a}$ and $\mathbf{b}$. The reciprocal of a two-dimensional lattice is described by two unit vectors, $\mathbf{a}^*$ and $\mathbf{b}^*$, related with the real space unit vectors, $\mathbf{a}$ and $\mathbf{b}$, of the direct lattice. To describe the relationship between the reciprocal and direct vectors it is necessary to introduce a third vector, $\mathbf{c}$, perpendicular to the ($\mathbf{a}$, $\mathbf{b}$) plane:

$$\mathbf{a}^* = 2\pi \frac{\mathbf{b} \times \mathbf{c}}{\mathbf{a} \cdot (\mathbf{b} \times \mathbf{c})} \qquad \mathbf{b}^* = 2\pi \frac{\mathbf{c} \times \mathbf{a}}{\mathbf{a} \cdot (\mathbf{b} \times \mathbf{c})} \tag{2.2}$$

that implies:

$$\mathbf{a}^* \cdot \mathbf{b} = 0 \qquad \mathbf{a} \cdot \mathbf{a}^* = 2\pi \tag{2.3}$$

$$\mathbf{a} \cdot \mathbf{b}^* = 0 \qquad \mathbf{b} \cdot \mathbf{b}^* = 2\pi \tag{2.4}$$

Any reciprocal lattice vector can be expressed as a sum of these reciprocal unit vectors: $\mathbf{G}$ = h·$\mathbf{a}^*$ + k·$\mathbf{b}^*$ where h and k are integers. The direct and reciprocal spaces can be related to the diffraction pattern in the following way. Lets consider an electron wave with wave vector $\mathbf{k}_0$ = $2\pi/\lambda_0$ and scattered wave vector $\mathbf{k}$ = $2\pi/\lambda$. In the two dimensional case, the conditions for diffraction by a periodic structure are defined by the Laue condition:

$$\Delta\mathbf{k} = \mathbf{k}_0 - \mathbf{k} = \mathbf{G} = h \cdot \mathbf{a}^* + k \cdot \mathbf{b}^* \tag{2.5}$$

In other words, the diffracted electrons beams will contribute to constructive interference if the change in the electron wave vector corresponds to a reciprocal lattice vector. Thus, the LEED pattern is just an image of the reciprocal lattice. And given the relations between direct and reciprocal spaces, the real space surface lattice can be reconstructed based on the information obtained on the reciprocal lattice.

2.2.2 X-Ray Photoelectron Spectroscopy

X-ray photoelectron spectroscopy (XPS) [15, 16] is a widely used method to determine the composition of the near surface region of a sample. In an XPS experiment, the sample surface is irradiated by X-rays. The absorption of the X-rays results in the ionization of the surface atoms and on the ejection of electrons that can be detected as photoelectrons if their kinetic energy is sufficiently large to escape from the surface by overcoming the sample work function. The photoelectron kinetic energy (E_k) is given by the Einstein relation:

$$E_k = h\nu - E_b - \phi_s \tag{2.6}$$

where $h\nu$ is the X-ray energy, E_b is the photoelectron binding energy and ϕ_s is the spectrometer work function. As the binding energy of a core electron is characteristic of the individual atom to which it is bound, XPS allows us to determine the surface chemical composition of the sample under investigation.

The kinetic energy distribution of the photoelectrons, i.e. the number of emitted photoelectrons as a function of their kinetic energy, is composed by different features that will be briefly discussed. In an XPS spectrum, core level peaks are representative of the electronic configuration of the sample and are the result of the photoionisation process discussed before. The observed binding energies of a particular element may experience changes due to variations in the oxidation state or ligand type ("chemical shift"). In addition, all core levels with angular momentum l≠0 will produce two peaks in the XPS spectrum. This is due to the spin orbit coupling that splits the l≠0 degenerate energy levels into two levels characterized by the number j=l±s, where s is the electron spin.

Multiplet splitting can occur when the system has unpaired electrons in the valence levels. After the emission of a photoelectron from a core level, the remaining unpaired electron in the core can interact with the unpaired electrons in the valence band. This interaction can create different final states that will be reflected in the XPS spectrum as a multi core level peak structure. The outgoing photoelectron can also excite an electron from a core level into a higher state. The energy lost by the photoelectron will be reflected in the XPS spectrum by a "shake-up" satellite at higher binding energies than the corresponding photoelectron peak.

The Fe 2p core level spectra will be used during the thesis to determine the oxidation state of Fe in the samples. The Fe 2p XPS spectra for Fe metal, FeO (Fe^{2+}), Fe_3O_4 (Fe^{2+} and Fe^{3+}) and Fe_2O_3 (Fe^{3+}) are shown in Figure 2.3. Due to the spin orbit coupling, the Fe 2p core level is splitted into two peaks: Fe $2p_{1/2}$ and Fe $2p_{3/2}$. Both peaks are located at different energies depending on the oxidation state of Fe. In addition, Fe_2O_3 and FeO present characteristic satellite peaks located at particular energies: for Fe_2O_3 (FeO) the satellite peak of Fe $2p_{3/2}$ is located approximately 8 eV (6 eV) higher in binding energy than the main Fe $2p_{3/2}$ peak. The positions of the Fe 2p peaks are summarized in table 2.1.

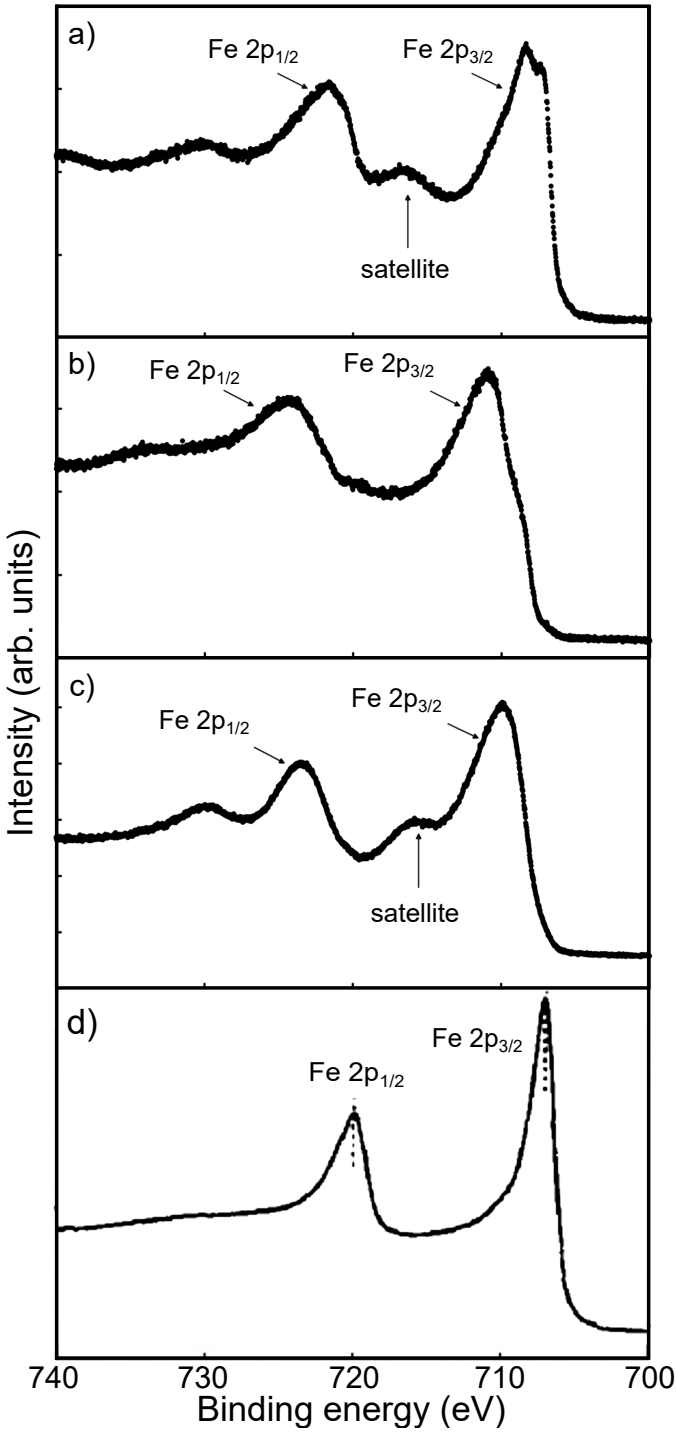

Figure 2.3: XPS spectrum of the Fe 2p core level for a) Fe_2O_3, b) Fe_3O_4 c) FeO and d) Fe metal. Reprinted from [17, 18].

Compound	**Fe 2p$_{3/2}$**	**Fe 2p$_{1/2}$**	**Satellite**
Fe_2O_3	711	724.6	718.8
Fe_3O_4	710.6	724.1	-
FeO	709.5	723.2	715.5
Fe	706.8	719.8	-

Table 2.1: Binding energies in eV of the XPS Fe 2p peaks of Fe_2O_3, Fe_3O_4, FeO and Fe from Ref.[17, 18].

In general, photoelectrons will travel a few atomic layers before they lose all their energy. At this point, they will no longer contribute to the correspondent photoelectron peak or if they contribute, it will be to the structureless background. The number of electrons from a given element and kinetic energy (E_k) after traveling through a thickness z, is expressed by:

$$I_A = S_A \exp[-z/\lambda(E_k, Z)cos\theta] \tag{2.7}$$

where S_A is the atomic sensitivity factor, Z is the atomic number of the element A and θ is the angle of emission with respect to the surface normal. $\lambda(E_k,\ Z)$ is the inelastic mean free path (IMFP) that represents the depth at which photoelectrons have a probability of 1/e of escaping without energy loss. Despite the material dependency of the IMFP there is a "universal" trend of the IMFP with the energy for any material. As it can be seen from Figure 2.4 at the typical energies used for XPS measurements, the depth sensitivity is restricted to a few nm from the surface. For emission angles normal to the surface, Eq. 2.7 becomes:

$$I_A = S_A \exp[-z/\lambda(E_k, Z)] \tag{2.8}$$

Based on 2.8, the thickness of a thin film deposited on a substrate can be estimated by measuring the relative areas of characteristic peaks from the thin film and substrate according to [15]:

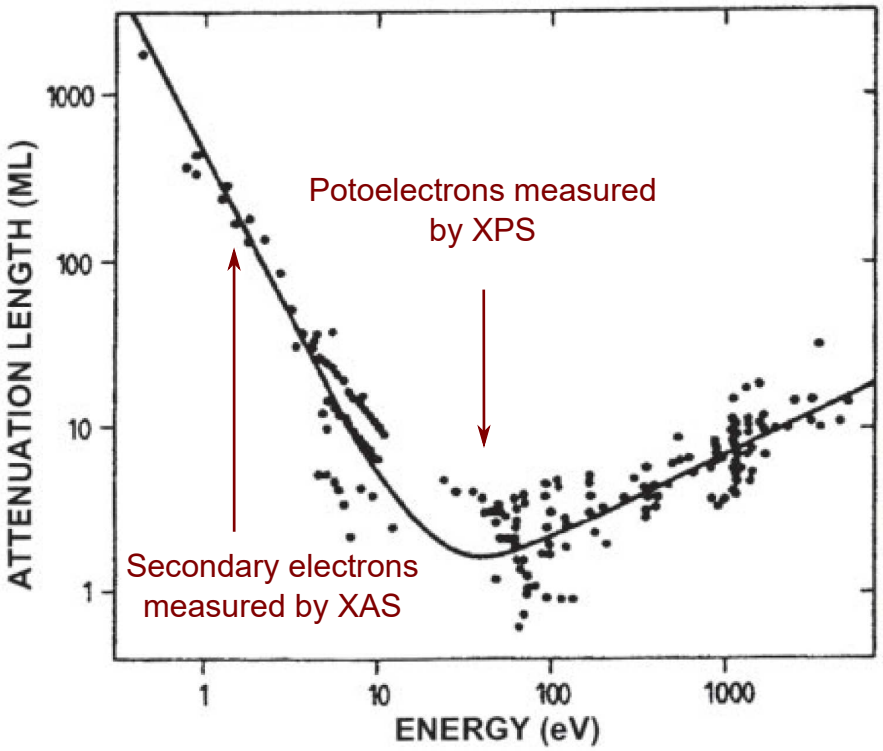

Figure 2.4: Electron attenuation length as a function of the energy. Reprinted from [19].

$$\frac{I_{film}}{I_{sub}} = \frac{S_{film}}{S_{sub}} \frac{[1-\exp(-z/\lambda_{film})]}{\exp(-z/\lambda_{sub})} \tag{2.9}$$

where I_{film} and I_{sub} stand for the areas of the correspondent core level peaks for the film and the substrate respectively, S_{film} and S_{sub} refer to their respective atomic sensitivity factors and z is the thickness of the deposited film. In our case, the values for λ_{film} and λ_{sub} were obtained from the NIST database [20] where instead of IMFP, the effective attenuation lengths (EALs) considering the elastic scattering of the electrons were used. In this work, the XPS data processing is performed using the CasaXPS program [21] where the atomic sensitivity factors are given by:

$$S_A = T(E_k) \cdot RSF(A) \cdot MFP(A) \tag{2.10}$$

where T is the transmission function evaluated for electrons at E_k (also called intensity/energy response function). The relative sensitivity factors (RSF) employed by CasaXPS are based on

the cross-sections of Scofield relative to C 1s [22]. They are used in combination with mean free paths (MFP) also relative to C 1s.

The atomic fraction of each element in the film is estimated from the ratio of the correspondent core level peak areas [15]:

$$C_A = \frac{I_A/S_A}{\sum_n (I_n/S_n)} \tag{2.11}$$

where C_A is the atomic concentration of the element A, I_n is the measured peak intensity of the element n, i.e. all the elements apart from the element A detected in the XPS spectrum and S_n is its relative sensitivity factor.

2.2.3 Ion Scattering Spectroscopy

Ion scattering spectroscopy (ISS) [16, 23] is a surface technique used to obtain information about the composition of the top-most surface layer. In an ISS experiment an ion beam of well-defined mass, energy (50 – 5000 eV) [24] and direction impinges on a surface sample. As a result of the collisions, there is a momentum transfer between the ions and the surface atoms. The scattered ions are collected and filtered as a function of their energy by the same energy analyzer used for XPS that can be used for ions by changing the appropriate voltages. Each element at the sample surface produces a peak at a different kinetic energy.

In an ISS experiment it is assumed that the atom in the collision with the ion behaves like a free atom which implies that the scattering process may be described as a classical two-body elastic collision following the laws of energy and momentum conservation [16]. If we consider an ion of mass M_1 and velocity v_0 the initial ion kinetic energy would be $E_0 = \frac{1}{2}M_1{v_0}^2$. After the collision, the total kinetic energy of the system is conserved and $\frac{1}{2}M_1{v_0}^2 = \frac{1}{2}M_1{v_1}^2 + \frac{1}{2}M_2{v_2}^2$ where M_2 is the atom mass and v_1 and v_2 are the velocity of the ion and the atom after collision respectively. From the momentum conservation, $M_1v_0 = M_1v_1\cos\theta_1 + M_2v_2\cos\theta_2$ where θ_1 and θ_2 are the deflection angles for the ion and the atom after the collision respectively. Combining these relations we obtain:

$$\frac{E_1}{E_0} = \frac{\cos\theta_1 \pm [(\frac{M_2}{M_1})^2 - \sin^2\theta_1]^2}{1 + (\frac{M_2}{M_1})} \tag{2.12}$$

As E_1, E_0, M_1 and θ_1 are known, it is possible to determine the atom present in the surface. The positive sign is applied for $M_2/M_1 > 1$.

Noble gases are usually used as primary ions in ISS as they are inert and prevent the contamination of the surface.

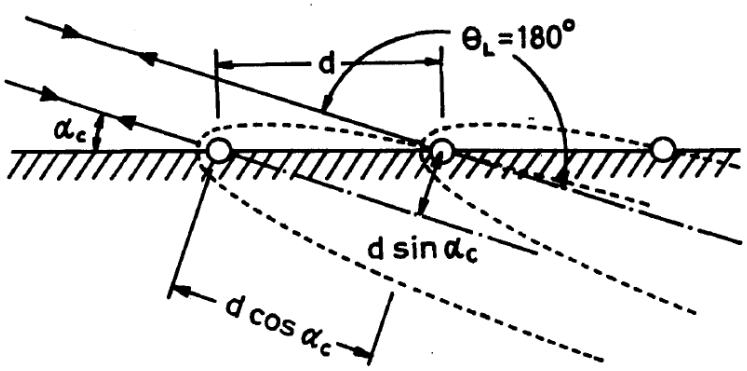

Figure 2.5: Schematic representation of the shadow cone generated at shallow incidences due to the Coulomb potential. Reprinted from [25].

When the ion beam approaches the surface atoms, a repulsive Coulomb potential creates a region behind the target into which no ion can penetrate. This region is called the shadow cone [26]. At small angles of incidence, all the atoms in the first layer are shadowed and no backscattered intensity is measured (see Figure 2.5). At a critical angle of incidence, the atoms emerge from the shadow cone and an increase in the backscattered atoms is observed. If we continue to increase the incident angle, a contribution from deeper layers can also be observed [25, 27]. Thus in ISS experiments changing the angle is very useful to obtain information on the surface composition.

2.2.4 Low-Energy Electron Microscopy

Low-Energy Electron Microscopy (LEEM) is a technique developed by E. Bauer [28] used to characterize surfaces in real space with nanometer resolution. It allows to monitor in real time physical processes like thin film deposition, chemical reactions or phase transitions. The typical LEEM has a resolution of ∼10 nm although aberration corrected systems approach a resolution of 1 nanometer.

The technique consists on an electron beam that illuminates a crystalline sample. The backscattered electrons are used to form a real space image of the sample surface. We will briefly introduce some notes about the experimental setup and the operation of the instruments.

Experimental setup

Figure 2.6 represents a simplified LEEM instrument. The main elements are the illumination column, a beam separator, the objective lens and the imaging column.

Illumination column. There are different possible sources to generate the electrons: thermionic, field emission or GaAs sources (see section 2.2.5). The thermionic-based LaB_6 source single crystal is a popular choice because it is cheap and has a long lifetime. Within the illumination column the electrons are accelerated up to 10–20 keV. This can be achieved either by accelerating the electron beam to high positive potential and maintaining the sample at a few eV or by maintaining the electron beam close to ground potential and the sample and cathode at -(10–20) keV. In addition, the sample is biased with respect to the electron source. This voltage is called the start voltage (Vs). A set of condenser lenses are placed at the illumination column to focus the electrons into a parallel beam. An illumination aperture limits the size of the electron beam on the surface, typically in the range 10–100 μm.

Beam separator. The beam separator separates the electrons that are going into the sample from the ones that are leaving the sample. This is accomplished by creating a magnetic field that bends the electron beam into the normal direction with respect the sample surface. The

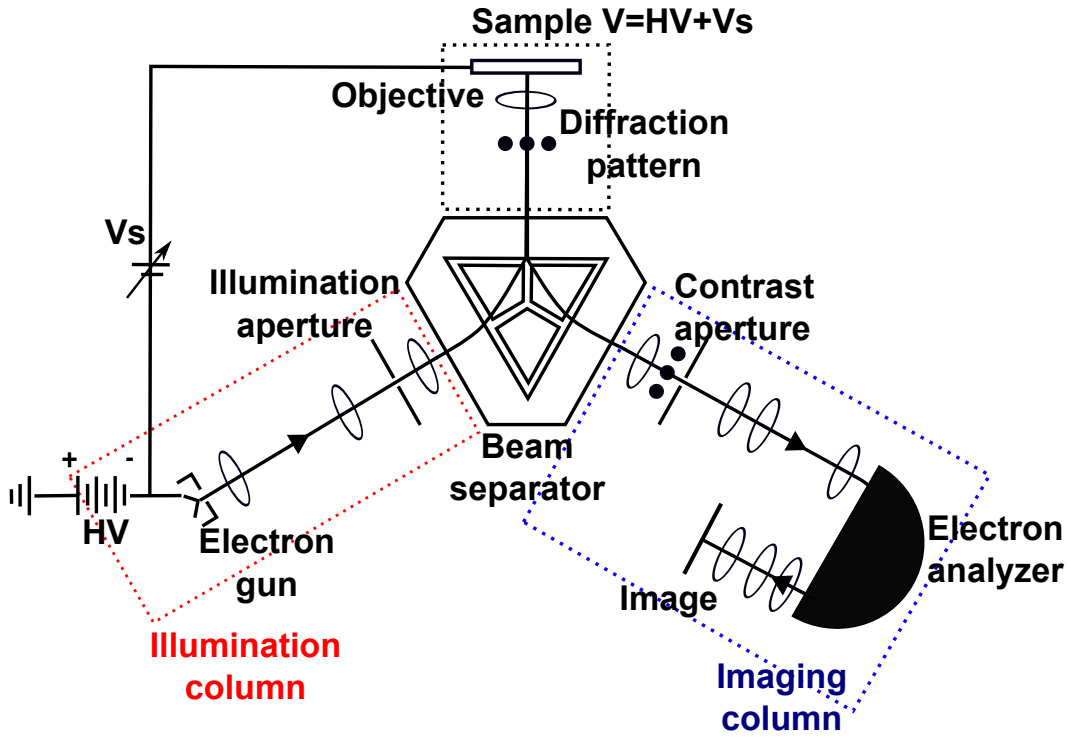

Figure 2.6: Schematic representation of the LEEM instrument of the type available at the ALBA synchrotron.

backscattered electrons are directed again towards the beam separator where they are deflected into the imaging column.

Objective lens. The objective lens is responsible for decelerating the electrons from the illumination column to energies of a few eV before reaching the surface. After interacting with the sample surface, the electrons are re-accelerated by the same objective lens. A diffraction pattern from the surface forms at the back-focal plane.

Imaging column. The imaging column contains a set of lenses that allow to adjust the field of view (FOV) to be imaged and to select between the observation of the magnified distribution of electrons or the diffraction pattern. Field of views between 1-100 μm can be selected. A contrast aperture is located at the back focal plane of the objective lens where the diffraction pattern is formed, and allows to select the diffracted beams that will contribute to the observed image. At the end of the imaging column, the electron beam is amplified by a microchannel plate and then impinges on a phosphor screen where the image is acquired with a CCD camera.

The instrument can additionally incorporate an electron energy analyzer within the imaging column. If a light source is available, like X-rays from a synchrotron, the instrument can also be used to perform other surface characterization techniques like XPS and PEEM.

Contrast and working modes

Contrast in LEEM images arises from different mechanisms that will be briefly discussed in the following. Figure 2.7 shows the LEEM image of a surface with visible atomic steps identified by dark sharp lines. That steps can be detected might be surprising as the lateral resolution of the microscope is typically of the order of $\sim$ 10 nm. The origin of this contrast, termed *phase contrast*, is the interference between electrons waves that are reflected at the upper and lower part of a step giving rise to a Fresnel diffraction pattern, which smoothed by the aberrations of the instrument gives rise to a single black line at the step position. The phase contrast is responsible for the subatomic vertical resolution of the LEEM. This contrast mechanism is also very useful to determine thin film thicknesses deposited on top of a substrate by measuring the electron reflectivity as a function of the energy. Due to the interference between electrons reflected from the film/substrate interface and from the film surface, the electron intensity will vary as a function of the energy and the film thickness.

Concerning the start voltage (Vs), if the sample is biased positively with respect to the electron source, the electrons scatter at the surface, and then are reflected back from the sample. On the other hand if the sample is biased slightly negative (Vs $\sim$ 1V) with respect to the electron source, the illuminating electrons are reflected above the surface, without hitting it. This imaging mode is known as mirror electron microscopy (MEM). *Composition* differences are another source of contrast variations. The reflected intensity depends on the band structure of the surface sample: if there are unoccupied electronic states available for the incoming electrons, they will enter the material and a drop in the reflected intensity will be observed and viceversa (see Fig. 2.7a).

The reciprocal space can be investigated by imaging the diffraction pattern from the surface (see Fig. 2.7b). As explained before, the diffraction pattern is formed at the back focal plane of

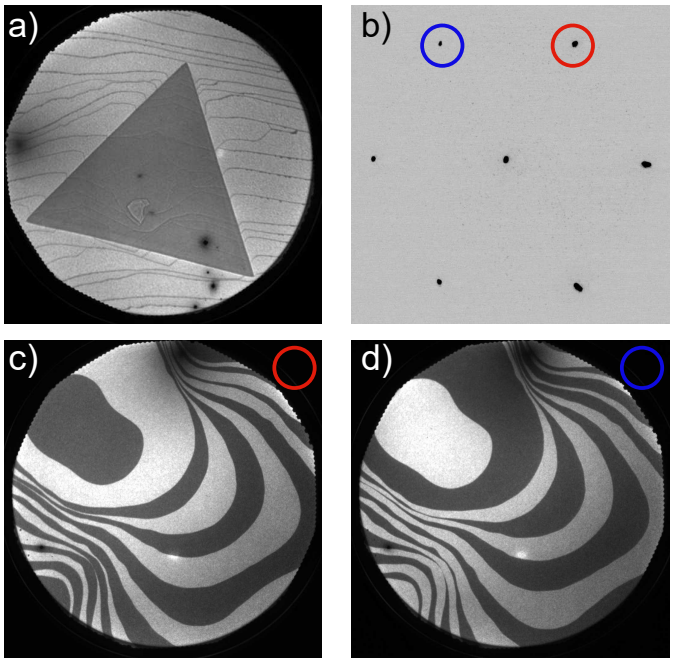

Figure 2.7: a) Bright field image showing the composition contrast between a cobalt ferrite island and the wetting layer below. The atomic steps are also visible as dark lines. The FOV is 10 μm and V_s = 32 V. b) LEED pattern of the Ru(0001) surface. The Vs is 35 eV. Two non-equivalent diffracted beams are marked with blue and red circles. Dark-field image using the c) blue and d) red circled diffracted beam showed in b). Adjacent terraces are imaged either black or white. The V_s = 32 eV and the FOV is 20 μm.

the objective lens and it can be imaged by adjusting the imaging column lenses. An illumination aperture can also be introduced in the beam path to obtain the LEED pattern from a particular region of the surface sample (μLEED).

To improve contrast, LEEM images are usually acquired by introducing the contrast aperture to limit all the diffracted beams that contribute to the image to the specular beam (0,0). This corresponds to the so-called *bright-field* imaging mode in TEM [29]. If we form an image by selecting a different diffracted beam it is called the *dark-field* mode. Every domain that gives rise to a different diffraction pattern can be imaged by selecting the correspondent diffracted beam with the contrast aperture. Thus, this mode is very useful as it provides information on the different domains of the surface. Fig. 2.7c and d show dark-field images of the hcp Ru(0001) surface. Each terrace has three fold symmetry. The atomic positions in consecutive terraces are rotated by 180° [30]. However the averaged LEED pattern displays six fold symmetry (see

Fig. 2.7b), as a consequence of the averaging over different atomic terraces. When selecting one of the three equivalent diffracted beams to form an image, i.e. the beam marked with a red circle, the terraces contributing to the selected diffracted beam appear bright whether those not contributing appear dark (see Fig. 2.7c). The opposite result is obtained when using the beam marked with a blue circle (see Fig. 2.7d).

2.2.5 Spin-Polarized Low-Energy Electron Microscopy

The main difference between a SPLEEM [31–33] and a LEEM system is that the electron source in a SPLEEM produces a (partially) spin-polarized beam. This technique complements the information obtained by LEEM with the capability of obtaining magnetic contrast images from ferromagnetic materials. When a spin-polarized electron beam with polarization **P** impinges onto a surface of a ferromagnetic sample with magnetization **M**, the number of backscattered electrons depends on the relative orientation of **P** and **M**. The difference of intensity of the backscattered beams normalized to the sum of intensities is called the exchange scattering asymmetry (A) and is proportional to **P**·**M**:

$$A = \frac{I_+ - I_-}{I_+ + I_-} \tag{2.13}$$

where I_+ and I_- are the measured intensities with opposite spin polarizations.

The magnetic contrast in SPLEEM arises from elastic and inelastic interactions between the spin-polarized incoming electrons and the electrons in the sample [31]. Regarding the elastic interactions, the spin-dependent reflectivity arises from the exchange-correlation potential, V_{ex}, originated by the interaction of the electrons in the sample. The incoming electrons experience this potential. If the spin of the incoming electrons is parallel to those of the surface electrons, the interaction potential (and then, the scattering) will be different than for the antiparallel spin case. This leads to the difference in the backscattered measured intensities, I_+ and I_-, for opposite spin polarized beams.

The other source of magnetic contrast arises from inelastic interactions. In a ferromagnet,

the number of unoccupied states above the Fermi level is larger for minority-spin electrons than for majority-spin electrons (see Figure 2.10). An incoming electron with spin parallel to the minority-spin electrons has a high probability of "falling" into an unoccupied minority state. Then, the energy losses associated to minority-spin incoming electrons are larger than for majority-spin electrons and consequently, reflectivity of majority electrons is larger than that of minority electrons.

An asymmetry image is the pixel by pixel representation of the reflected asymmetry. It is proportional to the projection of the surface magnetization vector along the direction defined by the spin polarization direction of the incoming beam. A typical SPLEEM image (see Figures 2.8b and c) will be composed of bright or dark features. The maximum contrast is obtained when $\mathbf{P} \parallel \pm\mathbf{M}$ and minimum when $\mathbf{P} \perp \mathbf{M}$.

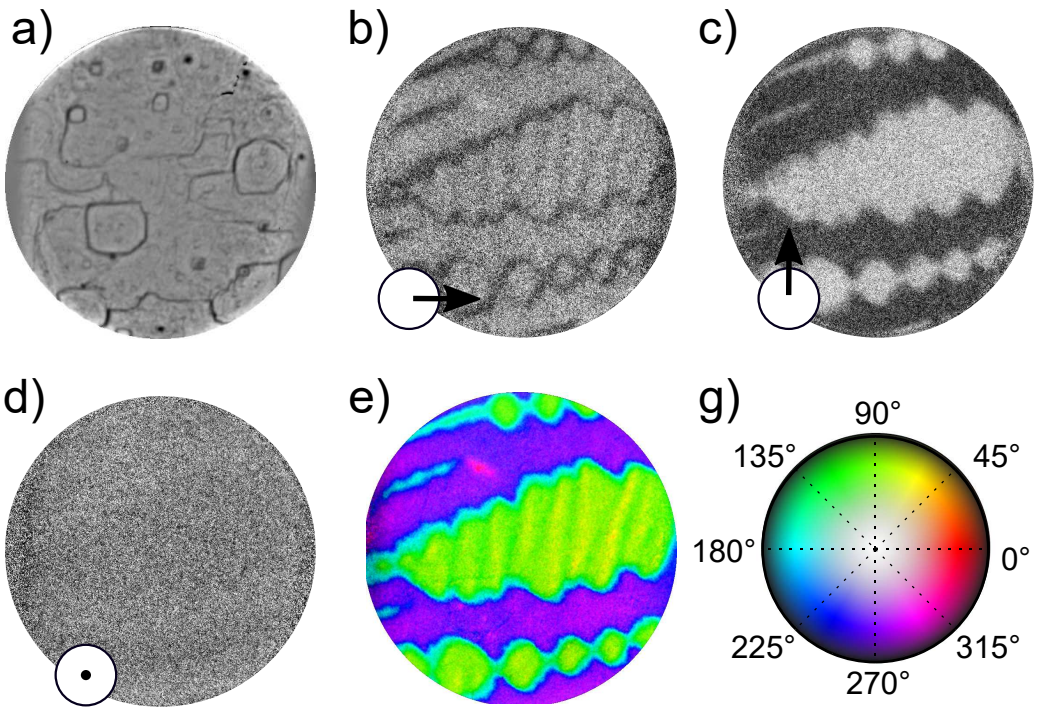

Figure 2.8: a) LEEM image of a $Fe_3O_4(100)$ surface showing the topography. SPLEEM asymmetry images of the same area showing the component of the magnetization along b) x, c) y and d) z axes of the images. The field of view is 12 μm and the start voltage is 8 V. e) Composite color image indicating the local magnetization vector using the color wheel indicated in (g).

If we measure the asymmetry images for three spin polarization directions we should be able to measure the magnetization vector field of the surface under investigation (see Fig. 2.8e). On the other hand, if the two images taken at opposite polarizations are added, we will obtain an image of pure structural contrast (see Fig. 2.8a). This two modes allow to correlate between magnetism and structure of the surface sample.

One of the advantages of the SPLEEM instrument compared to other techniques like magnetic force microscopy (MFM) or XPEEM is the short image acquisition time. In our case, the integration time per LEEM frame was typically 1 second, and to change the beam spin direction takes a fraction of a second. This allows to observe dynamic magnetic processes in real time.

As already mentioned, in a SPLEEM instrument the LEEM electron source is replaced by a spin polarized electron gun. The spin gun is composed of two elements: the spin polarized electron source that emits electrons with a known spin polarization and a spin manipulator that allows to control the spin polarization direction with respect to the surface sample. The spin-polarized source in the SPLEEM used in this thesis is a GaAs cathode which emits electrons when illuminated with circularly-polarized light. To emit electrons, the GaAs surface needs to present negative electron affinity [34]. This is accomplished by the deposition of Cs and oxygen. The surface of the GaAs cathode is prepared by first cleaning and then depositing the proper amount of Cs and oxygen. In order to obtain reasonable lifetimes, i.e. at least one day, the vacuum of the GaAs chamber must remain below 10^{-11} mbar.

2.2.6 X-Ray Photoemission Electron Microscopy

In X-ray photoemission microscopy (XPEEM) [35, 36] the sample is illuminated with X-rays instead of electrons. The methods described in this section requires a tunable X-ray source which makes the use of a synchrotron facility mandatory. In an XPEEM experiment, the incoming photons ionize the sample which emits photoelectrons. These are accelerated by the objective lens into the imaging column creating an image in the same way as in LEEM.

The XPEEM techniques used in this thesis are X-ray absorption spectroscopy (XAS), X-ray photoelectron spectroscopy (XPS), and X-ray magnetic circular dichroism (XMCD). XPS was introduced in section 2.2.2 and follows the same principles here. It is important to mention

that to use this technique requires the presence of an energy filter at the imaging column of the instrument. In the following we will introduce the main concepts of XAS and XMCD techniques.

- *X-ray absorption spectroscopy.*

In XAS experiments, the absorption of photons is recorded as a function of the photon energy. The process starts by illuminating the sample with X-rays. When the energy of an absorbed photon matches a core level energy, an electron is excited to an unoccupied valence state. The core hole is subsequently filled by an electron of a higher level followed by the emission of an Auger electron. In their way to the surface, the Auger electrons produce a secondary electron cascade that escapes from the sample [37]. Electronic transitions in L-edge XAS occur from the spin-orbit split 2p core shell to unoccupied electronic states in the 3d band (d holes) giving rise to an absorption spectrum characterized by two absorption peaks, named L_3 and L_2 edges, as shown in Figure 2.9. Accordingly, the measured intensity $I_{L_3} + I_{L_2}$ is proportional to the number of d holes.

A typical method to measure the X-ray absorption is the total electron yield mode. In this case, all the electrons escaping from the sample independent of their energy are counted. The signal is dominated by secondary electrons. However, PEEM suffers from chromatic aberrations and measuring all the electrons would lead to blurry images. Thus an energy filter is used to measure the secondary electrons and also to determine the probing depth of the measure.

During this thesis, the XAS spectra of Fe and Co were used to characterize the samples. Figure 2.9 shows the L-edge XAS for metallic Fe and Co and some of their oxides. The spectra for metallic Fe and Co are very similar although the L_3 and L_2 edges are located at different photon energies. Oxides, on the other hand, present a more complex structure (compare the L_3 edge for Co and CoO) due to multiplet splitting.

- *X-ray magnetic circular dichroism*

When a ferromagnetic material is illuminated with circular polarized X-rays, the XAS spec-

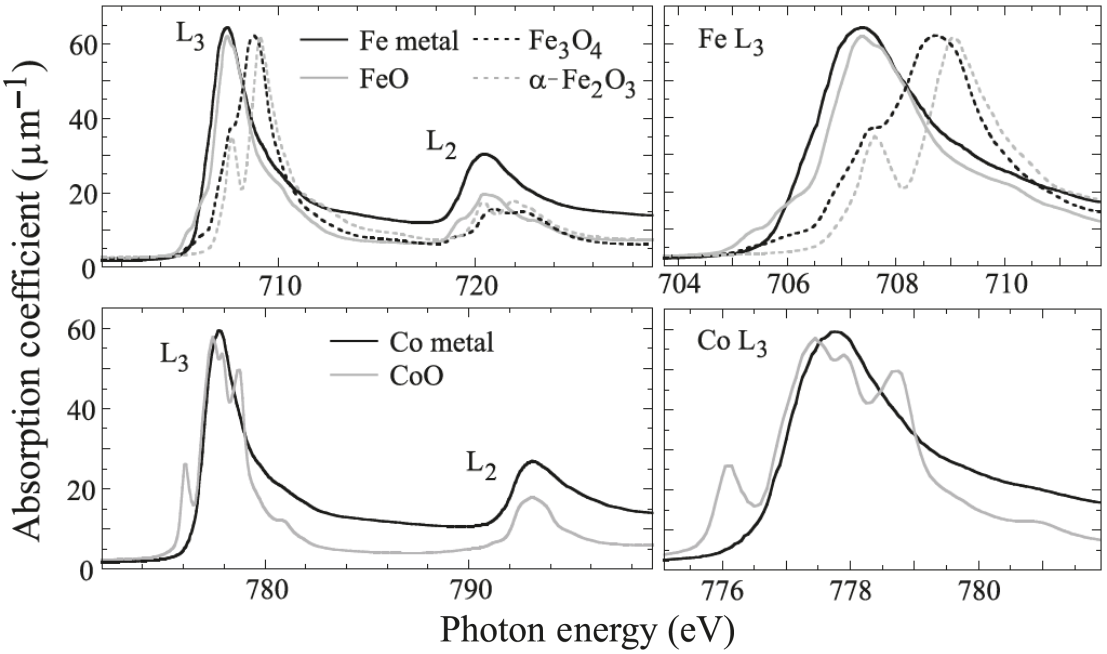

Figure 2.9: XAS for metallic Fe (top) and Co (bottom) and some of their oxides. In the right column the L_3 edge is showed in an expanded scale. Adapted from [38].

tra obtained for left and right helicities (P^+ and P^-) differ. XMCD is an element-specific technique and it allows to probe the valency, the site symmetry and the magnetic order of the elements. Every configuration is represented by a characteristic XMCD spectrum which is used as a fingerprint to determine the configuration of the sample under investigation.

In a ferromagnet, the spin magnetic moment is given by the difference in the number of spin-up and spin-down electrons (see Fig. 2.10). In the hole picture, this difference is also equivalent to the imbalance in the empty states (holes)[3][37]. As the L-edge XAS intensity is proportional to the 3d holes, by making the XAS process spin-dependent, it would be possible to measure the difference in the number of d holes with different spin and consequently, the spin magnetic moment. This is the base of the XMCD that can be explained in a two-step model [39]. In a first step, circularly polarized photons with right or left polarization transfer their angular momentum, $+h$ and $-h$ respectively, to the photoelectron. The angular momentum is transferred to the photoelectron spin via the spin orbit coupling. As the right and left circularly polarized photons carry opposite angular moments, photoelectrons with opposite spins are created depending on

[3]For a given shell, with angular momentum l, the occupation number is $2l+1$ for each spin. Thus, if the number of electrons are known, the number of holes is also determined.

the polarization of the light. In addition, at the L-edge, the L_3 and L_2 levels present opposite spin orbit coupling, (l+s) and (l-s) respectively, so, the photoelectrons carry opposite spins at the two edges. At the L_3 edge for example, right circularly X-rays excite more spin-up electrons than left circularly X-rays. The contrary occurs at the L_2 edge.

The electric dipole transitions do not allow for a spin flip during the XAS process, i.e., spin-up (spin-down) photoelectrons can only be excited to spin-up (spin-down) states [37]. Thus, in a second step, the valence shell acts like a spin detector for the spin polarized photoelectrons allowing to measure the number of holes in each band. During this process the secondary emission is proportional to the dot product between the sample magnetization direction ($\mathbf{M}$) and the photon helicity vector ($\mathbf{P}$). Thus, the XMCD will be maximum when $\mathbf{P} \parallel \pm \mathbf{M}$ and minimum when $\mathbf{P} \perp \pm \mathbf{M}$.

An XMCD spectrum is typically obtained in the following way: the sample is magnetically saturated by an applied magnetic field in the direction parallel to the X-ray propagation direction. The XAS absorption is then recorded in total electron yield mode for right, P^+, and left, P^-, circularly polarized X-rays, normalizing by the incoming X-ray beam intensity (I_0). The process is repeated after switching the magnetization direction to be opposite to the X-ray propagation direction. In total, four XAS curves are recorded: (M^+, P^+), (M^+, P^-), (M^-, P^+) and (M^-, P^-). Two XMCD curves are obtained by applying:

$$\begin{aligned} XMCD(M^+) &= I(M^+,P^+) - I(M^+,P^-) \\ XMCD(M^-) &= I(M^-,P^+) - I(M^-,P^-) \end{aligned} \tag{2.14}$$

The final XMCD spectrum is obtained by averaging both XMCD curves for M^+ and M^- in order to remove non-magnetic contributions [40].

The XMCD spectra of this thesis are obtained in a different way. As we are using PEEM, it is not possible to use a magnetic field to orient the sample's magnetization because it would modify the electron path emitted by the surface, so, the XMCD spectra are measured in remanence. As the XMCD effect depends on the alignment of the magnetization direction and the X-ray

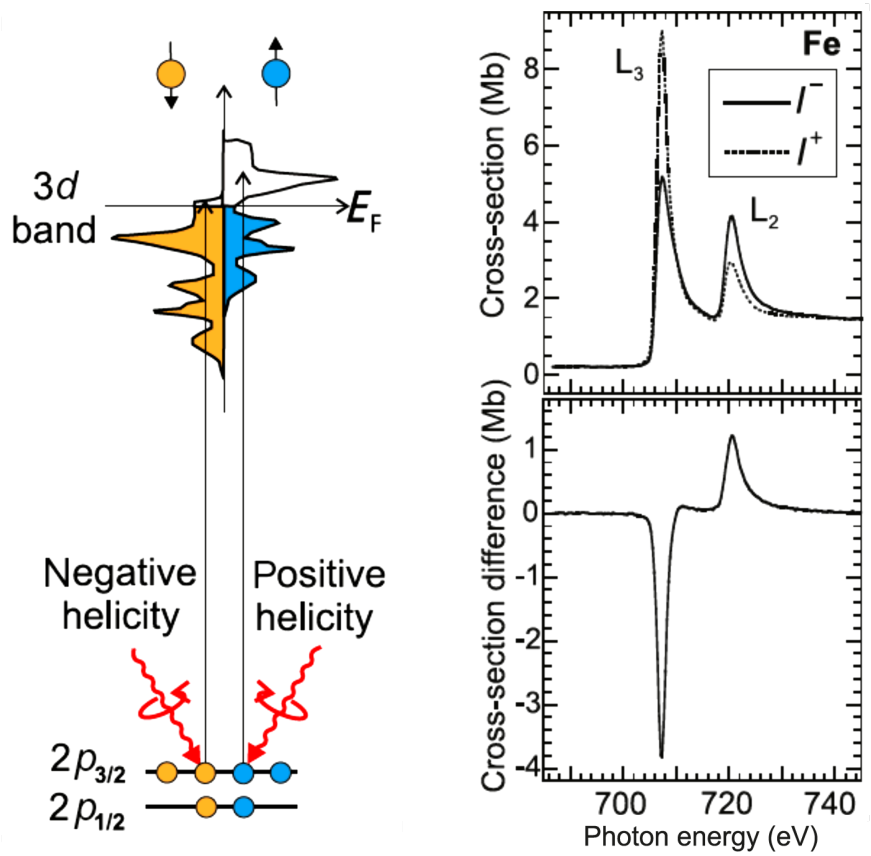

Figure 2.10: Left: XMCD effect for the L-edge absorption of Fe metal. Spin-up and spin-down states are depicted in blue and orange respectively. Right: (top) XAS spectra measured at the L-edge for Fe metal with left (I^-) and right (I^+) polarizations of the light. (bottom) XMCD spectrum given by I^- - I^+ for the data above. Figure adapted from [37].

propagation direction, the measurement in remanence requires first an accurate determination of the easy axes on the near surface region. The samples studied by XMCD during this thesis were a Fe_3O_4 single crystal and cobalt ferrite thin films. In the Fe_3O_4 case, the easy axes were first determined by SPLEEM and next identified by LEEM as explained in detail in Chapter 3. This simplifies the situation as we only need to orient the easy axes directions with respect the X-ray beam direction.

An alternative method was followed in the case of the cobalt ferrite thin films using XMCD images of the surface. The XMCD images are obtained by subtracting XAS images for opposite light polarizations at a photon energy that enhances the XMCD contrast (for example at the

energy of the negative peak of the XMCD spectrum in Fig. 2.10). Next, the sample is rotated with respect the X-ray beam direction and subsequent XMCD images are measured. By comparing the images it is possible to determine the easy axes. XMCD images of a cobalt ferrite island at three different angles of the sample with respect the X-ray beam direction are shown in Figure 2.11. The island presents domains oriented in different directions. As explained before, maximum contrast (black and white in the image) is observed for $\mathbf{P} \parallel \pm \mathbf{M}$ and minimum (gray in the image) when $\mathbf{P} \perp \pm \mathbf{M}$.

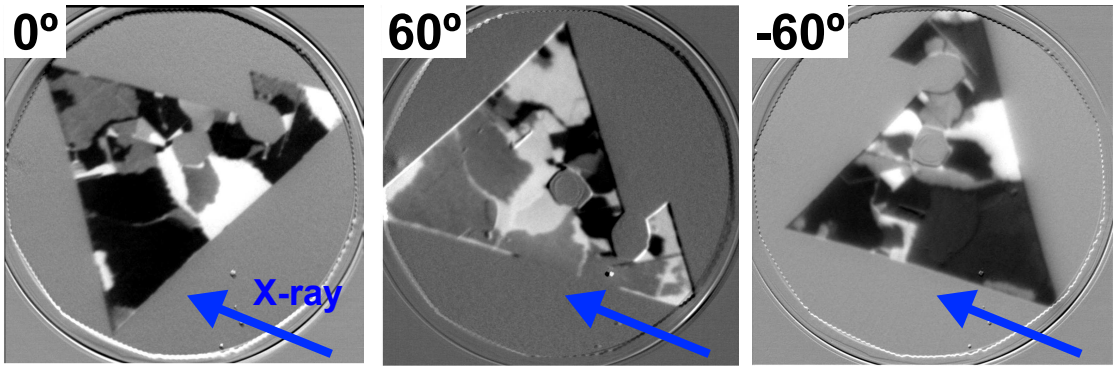

Figure 2.11: XMCD images from a cobalt ferrite island measured at the Fe L_3 edge rotated by 0°, 60° and -60° with respect the X-ray beam direction respectively. The X-ray direction is marked by a blue arrow.

Once the sample is oriented so at least two domains with opposite magnetizations are oriented along **P**, XAS images of the surface as a function of the photon energy are recorded with both right and left circularly polarized light. As in the regular case, four XAS curves are extracted: (M^+, P^+), (M^+, P^-), (M^-, P^+) and (M^-, P^-). The final XMCD spectrum is obtained following the process explained before.

The structure and magnetic properties of every compound studied in this thesis will be explained in detail in the correspondent chapter. Here we will just show the XMCD and the contributions to the spectrum of the ferrimagnetic iron and cobalt oxides used as a fingerprint to compare with our samples. The XMCD spectra measured at the Fe L-edge for $Co_{1-x}Fe_{2+x}O_4$ thin films (x = 0.01, 0.18, 0.39, 0.63 and 1) grown on MgO (001) substrates from Ref. [41] are presented in Figure 2.12. The XMCD structure arises from the contributions of the Fe cations

located at particular sites within the spinel structure and having different oxidation states. The specific contribution from each cation has been calculated using the CTM4XAS program [42] and shown in Figure 2.13. The weighted sum of these contributions gives rise to the Fe XMCD spectrum.

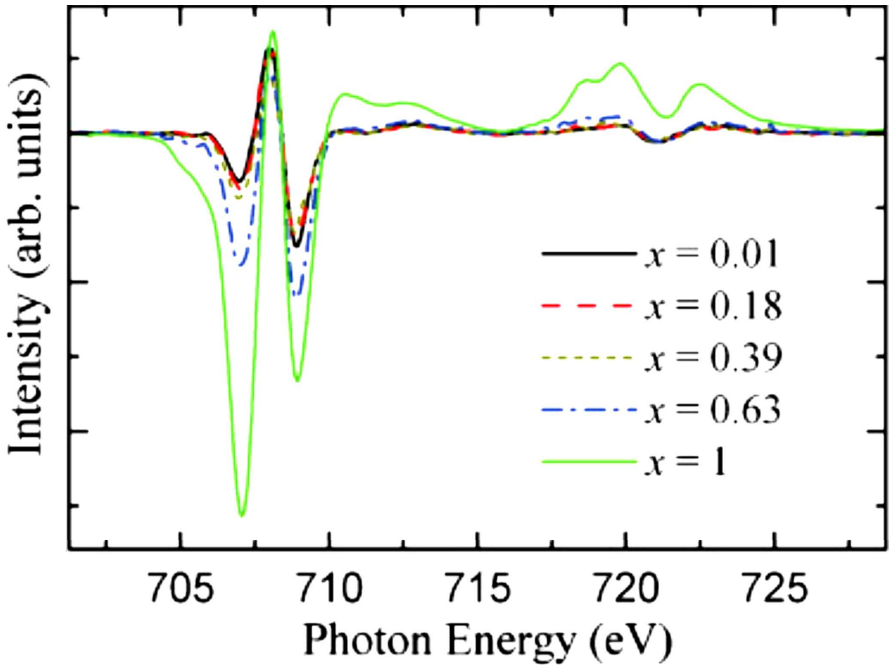

Figure 2.12: Fe L-edge XMCD spectra of $Co_{1-x}Fe_{2+x}O_4$ thin films with x = 0.01, 0.18, 0.39, 0.63, and 1. Adapted from [41].

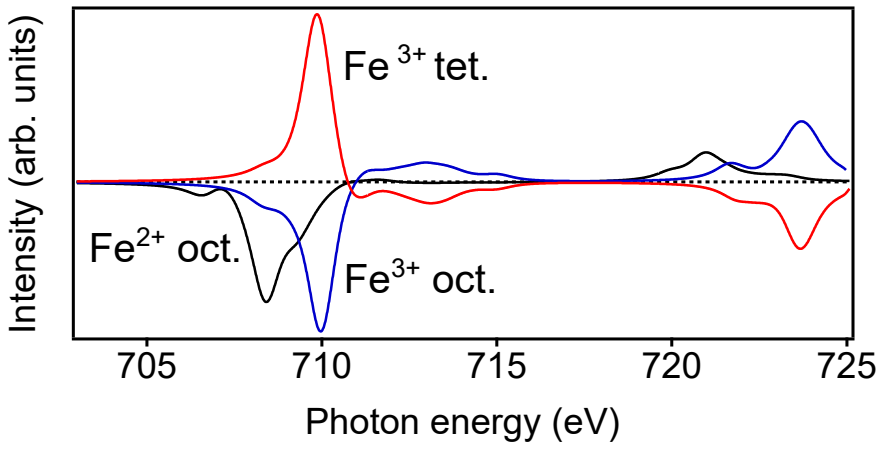

Figure 2.13: Calculated Fe^{2+} octahedral, Fe^{3+} octahedral and Fe^{3+} tetrahedral contributions to the XMCD spectrum of an spinel structure.

It can be seen that the positive peak arises from Fe^{3+} in tetrahedral positions and the second negative peak arises from Fe^{3+} in octahedral positions. The first negative peak is usually assigned to Fe^{2+} in octahedral positions only [43]. However, as it is shown, Fe^{3+} also contributes to this peak. This is the reason for the first small negative peak observed in the XMCD spectrum of $Co_{0.99}Fe_{2.01}O_4$ in Figure 2.12. The sense of the peaks indicates that $Fe^{2+}/^{3+}$ cations in octahedral positions are aligned ferromagnetically within the lattice and antiferromagnetically to Fe^{3+} in tetrahedral positions.

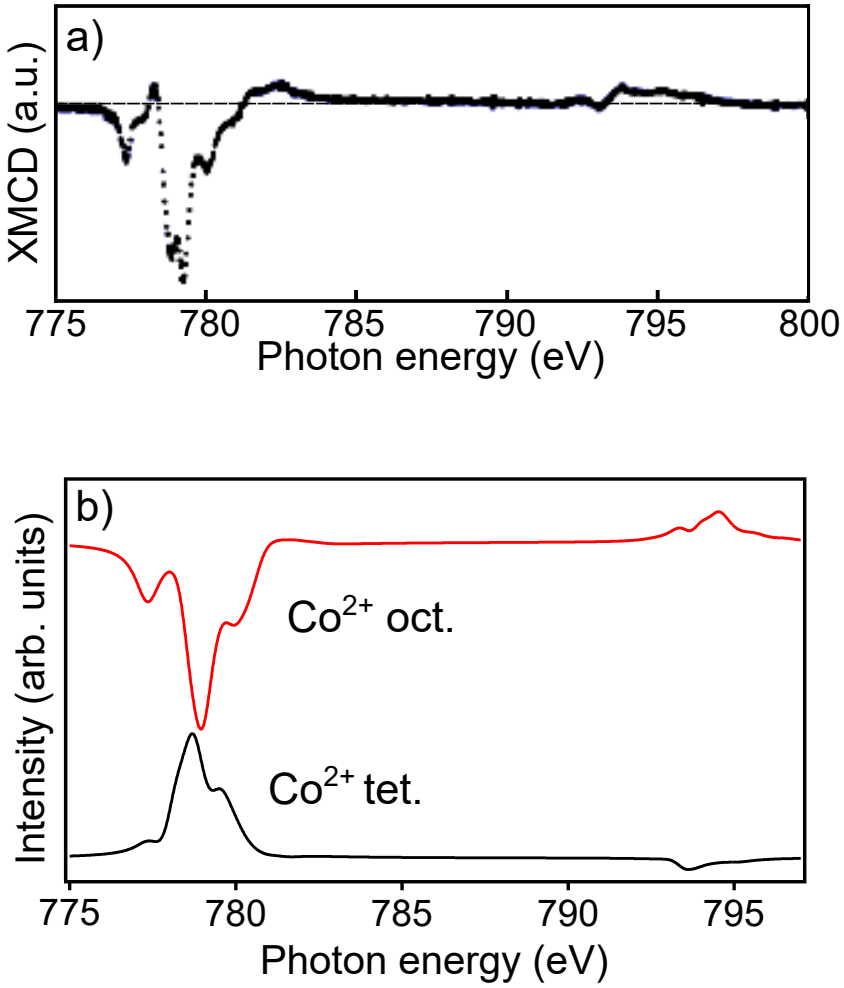

Figure 2.14: a) Co L-edge XMCD curves of a $CoFe_2O_4$ thin film grown on MgO. Adapted from [44]. b) Calculated Co^{2+} octahedral and Co^{2+} tetrahedral components of the XMCD spectrum of $CoFe_2O_4$.

The XMCD spectrum measured at the Co L-edge for a $CoFe_2O_4$ thin film grown on MgO from Ref. [44] is presented in Figure 2.14a. $CoFe_2O_4$ presents an spinel structure with Co^{2+} located mainly in octahedral positions although it may contain some Co^{2+} in tetrahedral positions. The spectrum is thus the result of the sum of both contributions as shown in Figure 2.14b. These curves were simulated using the CTM4XAS program as in the previous case.

Magnetic moments

We can estimate the spin and orbital magnetic moments for every magnetic element in the sample under investigation by applying the sum rules [45–47]:

$$m_{spin} = -\frac{6p-4q}{r}(10-n_d) + < T_z > \tag{2.15}$$

$$m_{orb} = -\frac{4q}{3r}(10-n_d) \tag{2.16}$$

$$p = \int_{L_3} XMCD\ dE \tag{2.17}$$

$$q = \int_{L_{3,2}} XMCD\ dE \tag{2.18}$$

$$r = \int_{L_{3,2}} XAS\ sum.\ dE \tag{2.19}$$

where m_{spin} and m_{orb} are the spin and orbital magnetic moments respectively, n_d represents the 3d electron occupation number per cation and $<\langle T_z \rangle>$ is the dipole operator. It is only non-zero for atoms in environments with symmetry less than cubic. p and q are the integrals of the XMCD spectrum over the L_3 edge and $L_{3,2}$ edge, respectively and r is the integral over the $L_{3,2}$ edge of the XAS summed spectrum which is calculated applying:

$$XAS\ sum. = \frac{1}{2}(I(M^+,P^+) + I(M^+,P^-) + I(M^-,P^+) + I(M^-,P^-)) \tag{2.20}$$

The XAS intensity is composed of 2p–3d transitions and a step-like background due to

additional transitions from 2p states into states above the 3d states which one need to remove [37, 48]. Thus, a background based on a two-step arctangent function is subtracted from the XAS summed spectrum before the integration. Figure 2.15 and 2.16 illustrates the procedure followed to obtain the m_{spin} and m_{orb} of Fe and Co in $CoFe_2O_4$ samples using the sum rules.

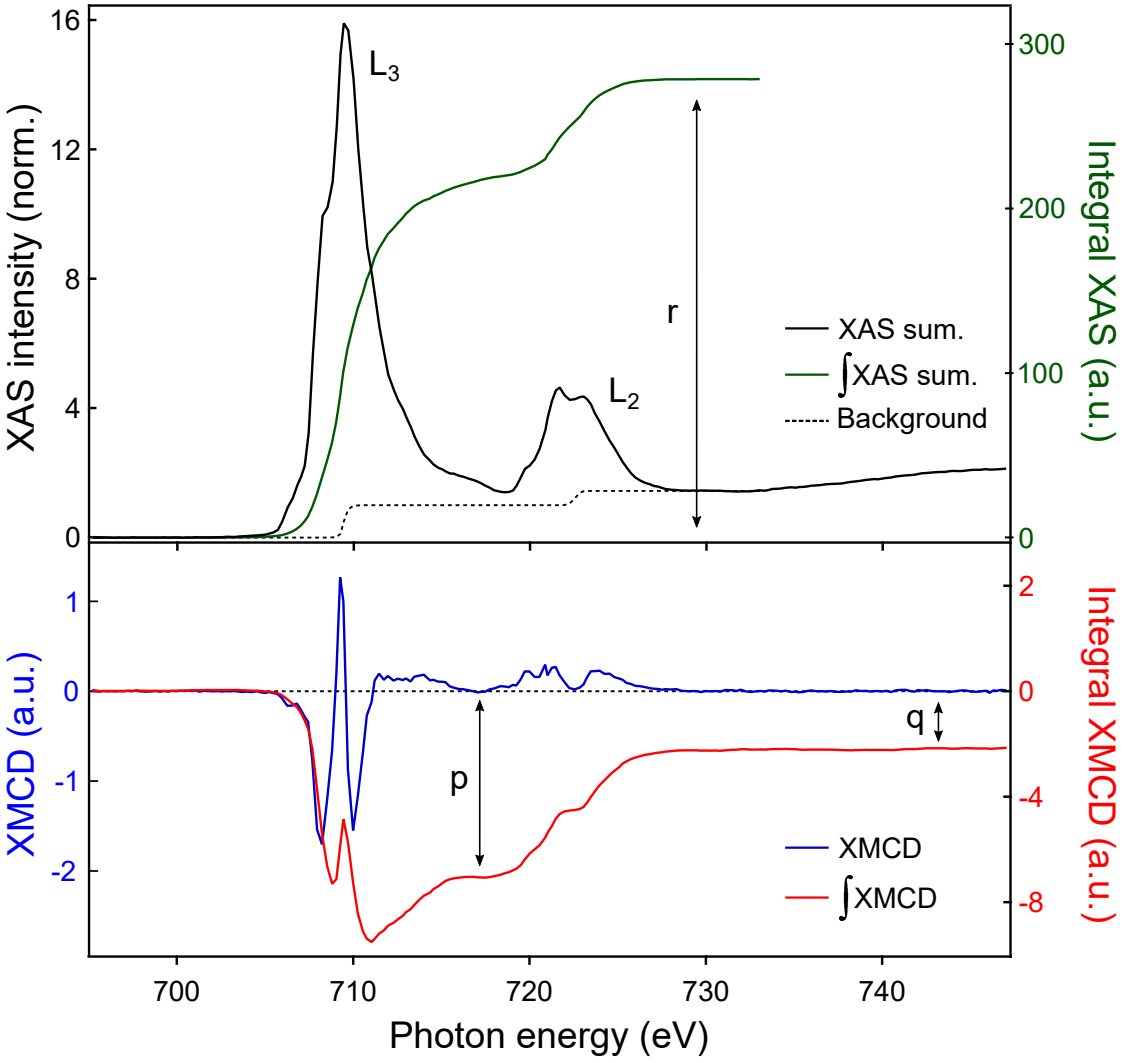

Figure 2.15: XAS summed (in black, top) and XMCD (in blue, bottom) spectra at the Fe $L_{3,2}$ absorption edge from a $CoFe_2O_4$ island. The red line corresponds to the integral of the XMCD curve. The dashed black line illustrates the two-step background based on an arctangent function. The green line corresponds to the integral of the XAS summed spectrum after background subtraction.

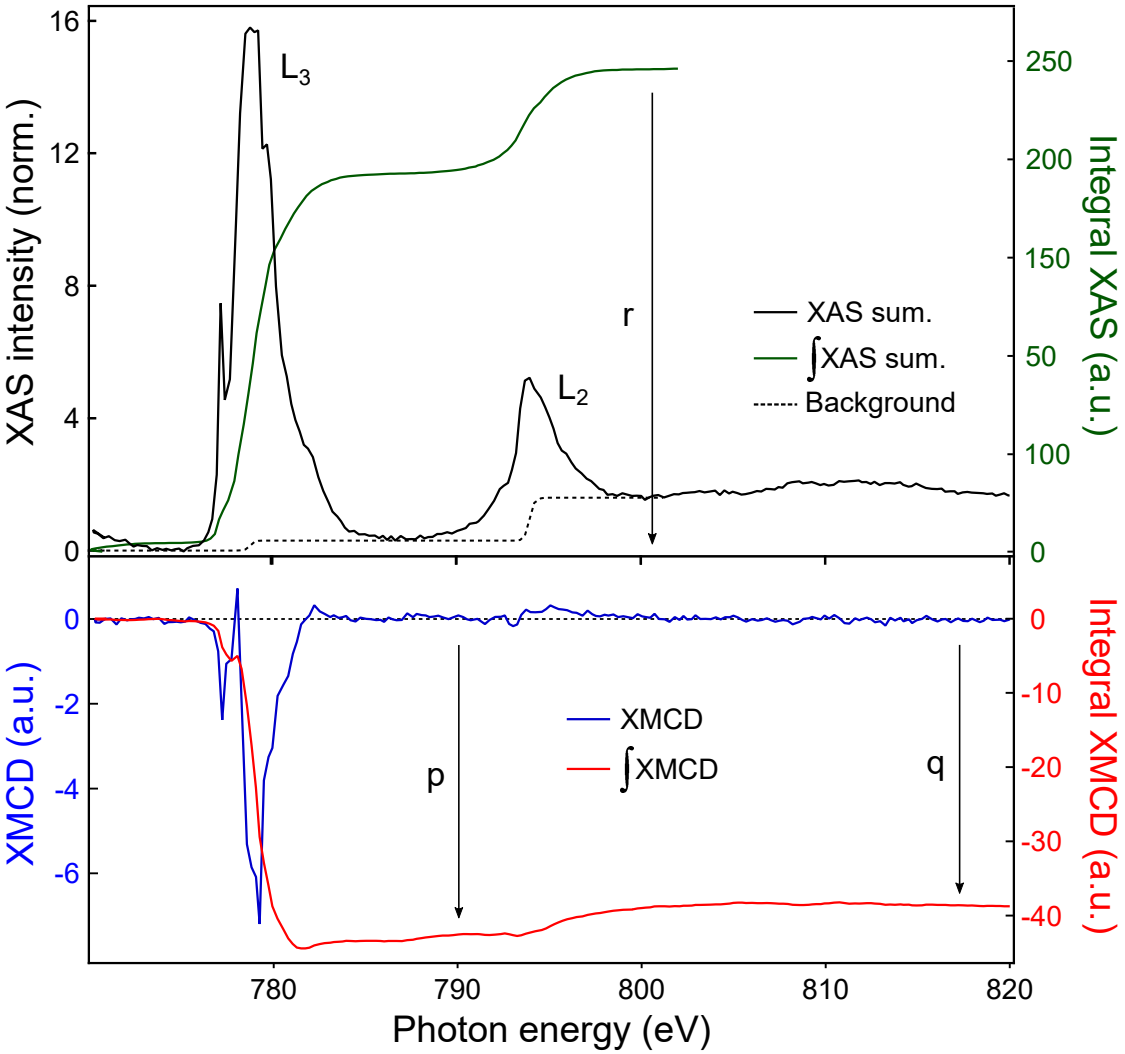

Figure 2.16: XAS summed (in black, top) and XMCD (in blue, bottom) spectra at the Co $L_{3,2}$ absorption edge from a $CoFe_2O_4$ island. The red line corresponds to the integral of the XMCD curve. The dashed black line illustrates the two-step background based on an arctangent function. The green line corresponds to the integral of the XAS summed spectrum after background subtraction.

Some aspects regarding the analysis procedure should be taken into account when obtaining spin and orbital magnetic moments through the sum rules.

Saturation effects for example occur when the electron escape depth, λ_e, becomes comparable to the X-ray absorption length, λ_x [37]. The measured absorption should in that case be corrected

by a factor [49]: f=1/(1+λ_e/λ_xcosθ) where θ is the X-ray incident angle with respect to the surface normal. At the secondary electron energies (∼1–2 eV), Figure 2.4 shows that the electrons that contribute to the absorption signal are originated within a few nm's depth. Particularly for Fe in Fe_3O_4, there is a work reporting λ_e = 5 nm [50]. Goering et al. [52] have argued that a much lower value is appropriate, in the range of 0.8 nm. Such number has been recently confirmed by experiments in ultrathin films where an estimate of 1.3 nm was measured [51]. The X-ray absorption length, λ_x, is a function of the photon energy and the smaller values are found close to the absorption edges. Particularly, λ_x at the L_3 edge is ∼ 17 nm for both Fe and Co [37] which is large compared to the estimate of λ_e ∼ 1 nm indicating that self-absorption effects should be small. However, saturation effects could be more important in our case as the X-ray angle of incidence is fixed to 16° with respect the sample surface. Considering λ_e = 5 nm, the correction factor f becomes 0.6 meaning that the measured absorption would be reduced by a 40% of the true value. However, for λ_e = 0.8 nm, the correction is smaller, f = 0.9, and the measured absorption would be reduced by a 10%. Moreover, Goering et al. studied in [52] the absorption at the Fe L-edge in a Fe_3O_4 single crystal as a function of the X-ray incident angle observing only very small peak height variations of ∼ 3 (5.4)% for the 90° (60°) incidence due to saturation effects.

Finally, Goering et al. have reported the importance of using an extended photon energy range to measure the XAS spectra [52]. The XAS intensity at the $L_{3,2}$ is affected by the presence of the magnetic extended fine-structure (MEXAFS) [53]. The MEXAFS from the L_3 is superimposed to the L_2 intensity leading to possible errors in the estimation of the magnetic moments. However, as we move away in energy from the L_2 edge, the intensity of the MEXAFS gets attenuated, the signal from the L_3 and L_2 edges have opposite signs and cancel each other. However, although we have used the extended photon energy range to measure the XAS spectra, the effect mentioned here was not observed and the dichroic signals for Fe and Co became zero after few eV above the L_2 edge. as illustrated in Figures 2.15 and 2.16.

2.3 The "Surfmoss" system

The "Surfmoss" system (see Figure 2.17) consists of a home-made multipurpose ultra-high vacuum (UHV) system divided in a preparation and a characterization chambers.

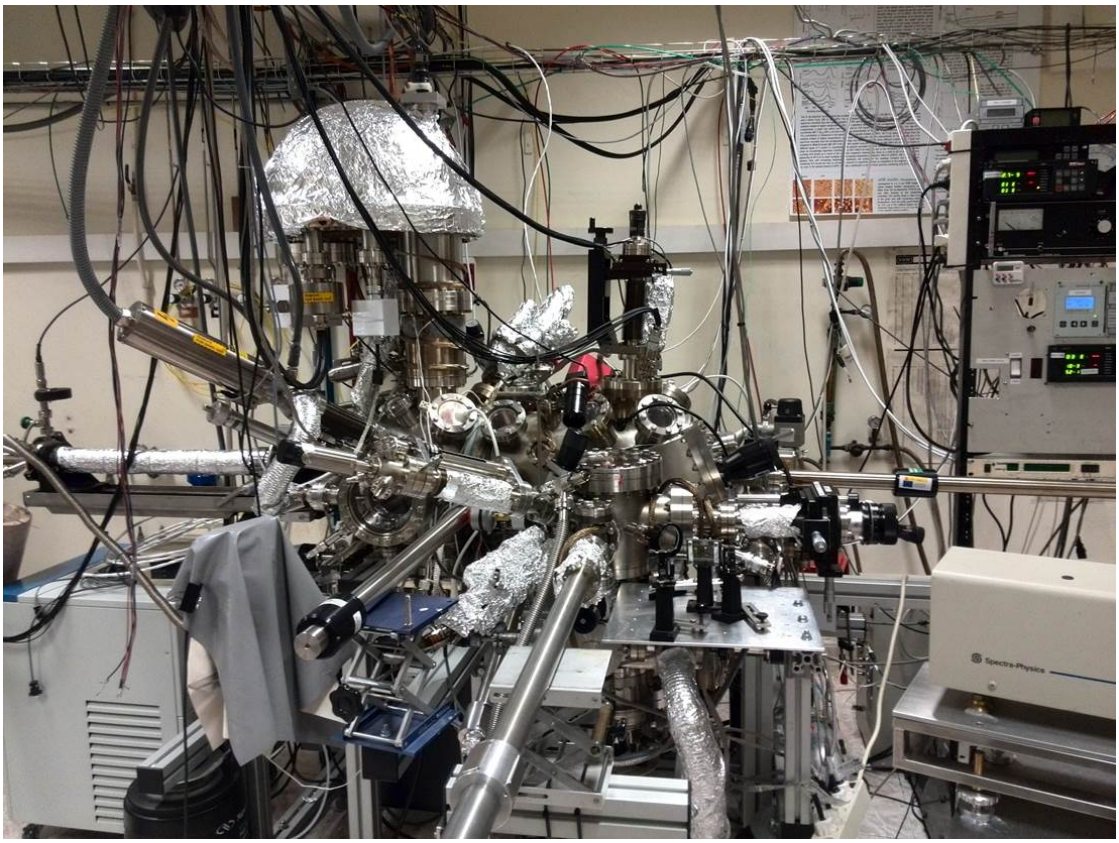

Figure 2.17: General view of the “Surfomss” system.

The preparation chamber was devised to perform molecular beam epitaxy (MBE) and pulsed laser deposition (PLD) thin film growth. At the beginning, it was equipped with several MBE sources and a sample holder with a heating filament. In addition, a pulsed laser deposition (PLD) system (see Figure 2.18) and a residual gas analyzer have been added during this thesis. The PLD system consists on a Q-switched Nd:YAG laser (Spectra Physics, Quanta Ray Indi-HG) operating at 1064 nm and a pulse duration of 5 ns and a repetition rate of 10 Hz. The laser beam was conducted by high reflective dichroic mirrors and focused on the surface of the target by a 25 cm focal length lens to achieve fluences of 4 J/cm^2. The laser beam impinged onto the target at 45° and the diameter of the irradiated region was determined by the print left on an unplasticized polyvinyl chloride sheet. A rotating sample holder was used in order to avoid target cratering during repetitive irradiation.

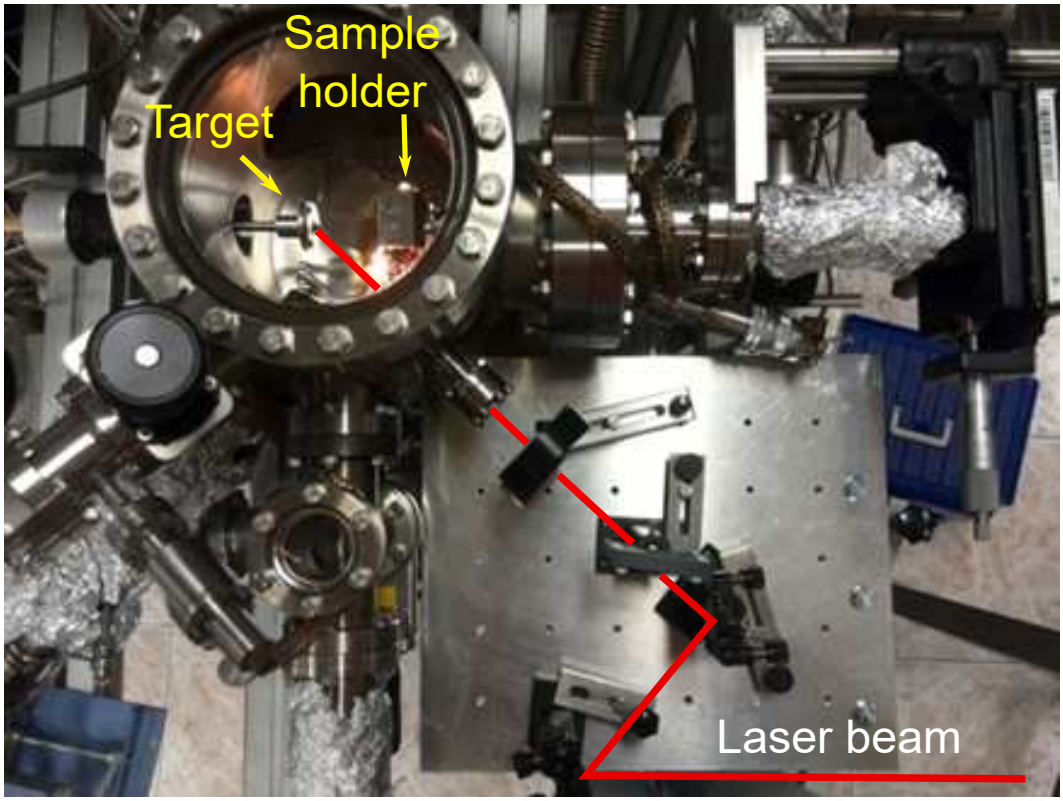

Figure 2.18: Top view of the PLD system showing the preparation chamber with the target and the sample holder inside. The laser beam path is showed in red.

The main chamber is equipped with different surface characterization techniques: a dual Mg/Al anode X-ray gun and an hemispherical Phoibos-150 analyzer employed for X-ray photoelectron, Auger and ion scattering spectroscopies and a low-energy electron diffractometer. In order to perform the cleaning procedures of the samples, the chamber is equipped with an ion gun for Ar^+ sputtering, a residual gas analyzer and a sample holder with a heating filament to perform the heating flashes to the sample. The ion gun is additionally employed for supplying He^+ ions to perform the ISS measurements.

The base pressure at the main chamber is $\simeq 2{\times}10^{-10}$ Torr while at the preparation chamber is $\simeq 7{\times}10^{-10}$ Torr. They both are equipped with independent pumping systems so the characterization chamber vacuum remains unaltered during the growth procedures.

2.4 National Center for Electron Microscopy

The SPLEEM system has been used at the National Center for Electron Microscopy at Lawrence Berkeley National Laboratory located in Berkeley (California, USA).

The microscope is equipped with a GaAs spin-polarized electron source. The system is divided into a main chamber housing the SPLEEM and several evaporator ports for MBE deposition, a preparation chamber equipped with surface preparation tools like an sputter gun and gas dosing valves and an additional chamber attached to the preparation chamber equipped with AES and LEED. The base pressure at the main chamber is $\sim 10^{-11}$ mbar. The sample is mounted in an Elmitec sample holder with a heating filament and a W/Re thermocouple to measure the temperature. It can be heated both in the preparation chamber and in the main chamber up to temperatures of 2000 K and cooled down to $\sim$ 100 K with liquid nitrogen.

2.5 ALBA synchrotron light facility

The ALBA synchrotron light facility is located in Barcelona (Spain). The experiments presented in this thesis were performed at the CIRCE beamline. The system consists in a LEEM-PEEM equipped with an electron energy analyzer [36] offering the possibility to characterize the structural, chemical and magnetic properties of surfaces within a single instrument. The system has been used in LEEM and LEED mode for imaging the sample surface and for diffraction measurements and in XPEEM mode to perform XAS, XPS and XMCD measurements.

The microscope chamber is attached to a preparation chamber equipped with different surface preparation tools like an sputter gun and gas dosing valves. The sample holder is the same as the one used in the SPLEEM system, thus, allowing for the heating and the measuring of the temperature of the sample. The main chamber houses the LEEM which is a commercial Elmitec LEEM III with a LaB_6 crystal as electron source. The lateral resolution achieved is $\sim$ 10 nm. The main chamber also allows for heating the sample up to 2000 K and for measuring the temperature and includes several evaporator ports for MBE deposition. The sample manipulator allows for rotating the sample around the surface normal. The typical pressure in the microscope chamber

is $\sim 10^{-10}$ mbar.

The beamline provides X-ray photons in the 100–2000 eV energy range with high intensity and resolution and any desired polarization. The X-ray incidence is 16° with respect the surface plane, i.e., near grazing incidence. This makes XMCD mostly sensitive to the in-plane magnetization of the sample. The lateral resolution achieved in PEEM is $\sim$ 20 nm.

2.6 Sample preparation

Different samples and substrates have been used during this thesis. First, Chapter 3 is based on the study of a magnetite single crystal with (001) orientation. The sample is a natural crystal from Mali. It has been cut to a hat shape and polished within 0.1° of a (001) orientation by a commercial supplier [54]. The hat shape is very convenient for use in LEEM and SPLEEM systems as it provides a uniform potential surface in front of the objective lens for use in variable temperature measurements. It bulk measured Verwey temperature (Tv) is 114 K.

The usual procedure to clean the surface from contaminants involves a brief sputtering with Ar^+ ions (HV = 1 kV, $p_{Ar^+} \backsimeq 1{\times}10^{-5}$ mbar, $\Delta t \backsimeq 10$ min) and subsequent annealing cycles at $\backsimeq$ 870 K, both in vacuum ($\Delta t \backsimeq 10$ min) to remove defects and in 10^{-6} mbar of O_2 ($\Delta t \backsimeq 10$ min) to restore the oxygen lost through preferential sputtering [55].

Chapter 4 and 5 are dedicated to the growth of Fe and Co oxides on Ru(0001) single crystals. Before experiments and also to recover a clean surface after each experiment, the substrates are subjected to heating flashes at 1500 K. If the surface presents contamination with carbon, the crystal is annealed in oxygen at 1100 K followed by heating flashes at 1500 K to remove the adsorbed oxygen. In adition, if the deposits are thick, it is necessary to apply cycles of Ar^+ sputtering (HV = 3.5 kV, $p_{Ar^+} \backsimeq 1{\times}10^{-4}$ mbar) before the heating cycles. The sputtering time depends on the thickness of the deposit. At the synchrotron, the state of the surface is checked by LEEM and LEED. If the surface is clean, the LEEM image does not show the presence of contaminants and the LEED pattern shows a 1×1 pattern. At the "Surfmoss" system, the state of the surface is checked by LEED and XPS.

Bibliography

[1] J. R. Arthur. Molecular beam epitaxy. *Surface Science*, 500(1-3):189–217, 2002.

[2] A. Y. Cho and J. R. Arthur. Molecular beam epitaxy. *Progress in Solid State Chemistry*, 10:157–191, 1975.

[3] S. A. Chambers. Epitaxial growth and properties of thin film oxides. *Surface Science Reports*, 39(5-6):105–180, 2000.

[4] M. Opel. Spintronic oxides grown by laser-MBE. *Journal of Physics D: Applied Physics*, 45(3):033001, 2012.

[5] P. R. Willmott. Deposition of complex multielemental thin films. *Progress in Surface Science*, 76(6-8):163–217, 2004.

[6] H. M. Christen and G. Eres. Recent advances in pulsed-laser deposition of complex oxides. *Journal of Physics: Condensed Matter*, 20(26):264005–264021, 2008.

[7] D. Yokoyama, K. Namiki, H. Fukasawa, J. Miyazaki, K. Nomura, and Y. Yamada. Mössbauer study of films produced by laser deposition of iron oxides. *Journal of Radioanalytical and Nuclear Chemistry*, 272(3):631–638, 2007.

[8] S. K. Hau, K. H. Wong, P. W. Chan, and C. L. Choy. Intrinsic resputtering in pulsed-laser deposition of lead-zirconate-titanate thin films. *Applied Physics Letters*, 66(2):245–247, 1995.

[9] H.-U. Krebs, M. Weisheit, J. Faupel, E. Süske, T. Scharf, C. Fuhse, M. Störmer, K. Sturm, M. Seibt, H. Kijewski, D. Nelke, E. Panchenko, and M. Buback. *Pulsed Laser Deposition (PLD) - A Versatile Thin Film Technique*, pages 505–518. Springer Berlin Heidelberg, 2003.

Bibliography

[10] M. Sanz, M. Oujja, E. Rebollar, J. F. Marco, J. de la Figuera, M. Monti, Bollero. A., Camarero. J., F. J. Pedrosa, M. García-Hernández, and M. Castillejo. Stoichiometric magnetite grown by infrared nanosecond pulsed laser deposition. *Applied Surface Science*, 282:642–651, 2013.

[11] T. Sun, J. Ma, Q. Y. Yan, Y. Z. Huang, J. L. Wang, and H. H. Hng. Influence of pulsed laser deposition rate on the microstructure and thermoelectric properties of $Ca_3Co_4O_9$ thin films. *Journal of Crystal Growth*, 311(16):4123 – 4128, 2009.

[12] K. Pussi and R. D. Diehl. *Low-Energy Electron Diffraction. Characterization of Materials.* John Wiley & Sons, 2002.

[13] J. B. Pendry. *Low-Energy Electron Diffraction*, pages 201–211. Springer US, 1990.

[14] F. Jona, J. A. Strozier Jr, and W. S. Yang. Low-energy electron diffraction for surface structure analysis. *Reports on Progress in Physics*, 45(5):527, 1982.

[15] D. Briggs and M. P. Seah. *Practical Surface Analysis, Auger and X-ray Photoelectron Spectroscopy.* Wiley, 1990.

[16] J. M. Walls. *Methods of Surface Analysis: Techniques and Applications.* Cambridge University Press, 1990.

[17] T. Yamashita and P. Hayes. Analysis of XPS spectra of Fe^{2+} and Fe^{3+} ions in oxide materials. *Applied Surface Science*, 254:2441–2449, 2008.

[18] P. C. J. Graat and M. A. J. Somers. Simultaneous determination of composition and thickness of thin iron-oxide films from XPS Fe 2p spectra. *Applied Surface Science*, 100:36–40, 1996.

[19] M. P. Seah and W. A. Dench. Quantitative electron spectroscopy of surfaces: A standard data base for electron inelastic mean free paths in solids. *Surface and Interface Analysis*, 1(1):2–11, 1979.

[20] C. J. Powel and A. Jablonski. *NIST Electron Effective-Attenuation-Length Database Version 1.3.* National Institute of Standards and Technology, Gaithersburg, 2011.

[21] Casa Software Ltd. www.casaxps.com.

Bibliography

[22] J. H. Scofield. Hartree-Slater subshell photoionization cross-sections at 1254 and 1487 eV. *Journal of Electron Spectroscopy and Related Phenomena*, 8(2):129–137, 1976.

[23] G. Bracco and B. Holst. *Surface Science Techniques*. Springer Series in Surface Sciences. Springer Berlin Heidelberg, 2013.

[24] E. N. Haeussler. Quantitative aspects of ion scattering spectroscopy. *Surface and Interface Analysis*, 2(4):134–139, 1980.

[25] M. Aono, C. Oshima, S. Zaima, S. Otani, and Y. Ishizawa. Quantitative surface atomic geometry and two-dimensional surface electron distribution analysis by a new technique in Low-Energy Ion Scattering. *Japanese Journal of Applied Physics*, 20(11):L829, 1981.

[26] H. Niehus, W. Heiland, and E. Taglauer. Low-energy ion scattering at surfaces. *Surface Science Reports*, 17(4-5):213 – 303, 1993.

[27] T. Fauster. Surface geometry determination by large-angle ion scattering. *Vacuum*, 38(2):129–142, 1988.

[28] E. Bauer. LEEM Basics. *Surface Review and Letters*, 5:1275–1286, 1998.

[29] D. B. Williams and C. B. Carter. *Transmission Electron Microscopy: A Textbook for Materials Science*. Springer, 1996.

[30] J. de la Figuera, J. M. Puerta, J. I. Cerda, F. El Gabaly, and K. F. McCarty. Determining the structure of Ru(0001) from low-energy electron diffraction of a single terrace. *Surface Science*, 600(9):L105–L109, 2006.

[31] E. Bauer. *Surface Microscopy with Low Energy Electrons*. Springer New York, 2014.

[32] N. Rougemaille and A. K. Schmid. Magnetic imaging with spin-polarized low-energy electron microscopy. *European Physical Journal Applied Physics*, 50(2):20101, 2010.

[33] K. Grzelakowski and E. Bauer. A flange-on type low energy electron microscope. *Review of Scientific Instruments*, 67(3):742–747, 1996.

[34] D. T. Pierce, F. Meier, and P. Zürcher. Negative electron affinity GaAs: A new source of spin-polarized electrons. *Applied Physics Letters*, 26(12):670–672, 1975.

Bibliography

[35] A. Locatelli, L. Aballe, T. O. Mentes, M. Kiskinova, and E. Bauer. Photoemission electron microscopy with chemical sensitivity: SPELEEM methods and applications. *Surface and Interface Analysis*, 38(12-13):1554–1557, 2006.

[36] L. Aballe, M. Foerster, E. Pellegrin, J. Nicolas, and S. Ferrer. The ALBA spectroscopic LEEM-PEEM experimental station: layout and performance. *Journal of Synchrotron Radiation*, 22(3):745–752, 2015.

[37] J. Stöhr and H. C. Siegmann. *Magnetism: From Fundamentals to Nanoscale Dynamics*. Springer, 2006.

[38] T. J. Regan, H. Ohldag, C. Stamm, F. Nolting, J. Lüning, J. Stöhr, and R. L. White. Chemical effects at metal/oxide interfaces studied by x-ray-absorption spectroscopy. *Physical Review B*, 64:214422, 2001.

[39] J. Stöhr and R. Nakajima. Magnetic properties of transition-metal multilayers studied with X-ray magnetic circular dichroism spectroscopy. *IBM Journal of Research and Development*, 42(1):73–88, 1998.

[40] W. Kuch and C. M. Schneider. Magnetic dichroism in valence band photoemission. *Reports on Progress in Physics*, 64:147–204, 2001.

[41] J. A. Moyer, C. A. F. Vaz, D. A. Arena, D. Kumah, E. Negusse, and V. E. Henrich. Magnetic structure of Fe-doped $CoFe_2O_4$ probed by x-ray magnetic spectroscopies. *Physical Review B*, 84(5):054447, 2011.

[42] E Stavitski and F. M. F. de Groot. The CTM4XAS program for EELS and XAS spectral shape analysis of transition metal L edges. *Micron*, 41(7):687 – 694, 2010.

[43] E. Pellegrin, M. Hagelstein, S. Doyle, H. O. Moser, J. Fuchs, D. Vollath, S. Schuppler, M. A. James, S. S. Saxena, L. Niesen, O. Rogojanu, G. A. Sawatzky, C. Ferrero, M. Borowski, O. Tjernberg, and N. B. Brookes. Characterization of nanocrystalline γ-Fe_2O_3 with synchrotron radiation techniques. *Physica Status Solidi (b)*, 215(1):797–801, 1999.

[44] S. Matzen, J.-B. Moussy, R. Mattana, F. Petroff, C. Gatel, B. Warot-Fonrose, J. C. Cezar, A. Barbier, M.-A. Arrio, and Ph. Sainctavit. Restoration of bulk magnetic properties by strain engineering in epitaxial $CoFe_2O_4$(001) ultrathin films. *Applied Physics Letters*, 99(5):052514, 2011.

[45] B. T. Thole, P. Carra, F. Sette, and G. van der Laan. X-ray circular dichroism as a probe of orbital magnetization. *Physical Review Letters*, 68:1943–1946, 1992.

[46] P. Carra, B. T. Thole, M. Altarelli, and X. Wang. X-ray circular dichroism and local magnetic fields. *Physical Review Letters*, 70:694–697, 1993.

[47] C. T. Chen, Y. U. Idzerda, H.-J. Lin, N. V. Smith, G. Meigs, E. Chaban, G. H. Ho, E. Pellegrin, and F. Sette. Experimental Confirmation of the X-ray Magnetic Circular Dichroism Sum Rules for Iron and Cobalt. *Physical Review Letters*, 75:152–155, 1995.

[48] F. M. F. de Groot. X-ray absorption and dichroism of transition metals and their compounds. *Journal of Electron Spectroscopy and Related Phenomena*, 67(4):529 – 622, 1994.

[49] R. Nakajima, J. Stöhr, and Y. U. Idzerda. Electron-yield saturation effects in L-edge x-ray magnetic circular dichroism spectra of Fe, Co, and Ni. *Physical Review B*, 59:6421–6429, 1999.

[50] S. Gota, M. Gautier-Soyer, and M. Sacchi. Fe 2p absorption in magnetic oxides: Quantifying angular-dependent saturation effects. *Physical Review B*, 62(7):4187–4190, 2000.

[51] G. F. M. Gomes, T. E. P. Bueno, D. E. Parreiras, G. J. P. Abreu, A. de Siervo, J. C. Cezar, H.-D. Pfannes, and R. Paniago. Magnetic moment of Fe_3O_4 films with thicknesses near the unit-cell size. *Physical Review B*, 90(13):134422, 2014.

[52] E. Goering, S. Gold, M. Lafkioti, and G. Schütz. Vanishing Fe 3d orbital moments in single-crystalline magnetite. *Europhysics Letters*, 73(1):97–103, 2006.

[53] L. Lemke, H. Wende, P. Srivastava, R. Chauvistré, N. Haack, K. Baberschke, J. Hunter-Dunn, D. Arvanitis, N. Mårtensson, A. Ankudinov, and J. J. Rehr. Magnetic extended x-ray absorption fine structure at the $L_{3,2}$ edges of 3d elements. *Journal of Physics: Condensed Matter*, 10(8):1917, 1998.

[54] Surface Preparation Laboratory. www.spl.eu.

[55] G. S. Parkinson, Z. Novotný, P. Jacobson, M. Schmid, and U. Diebold. A metastable Fe(A) termination at the $Fe_3O_4(001)(001)$ surface. *Surface Science*, 605:L42–L45, 2011.

CHAPTER 3

$Fe_3O_4(001)$

Part of the results presented in this chapter are published in:

- L. Martín-García, R. Gargallo-Caballero, M. Monti, M. Foerster, J. F. Marco, L. Aballe, and J. de la Figuera, *"Spin and orbital magnetic moment of reconstructed* $\sqrt{2} \times \sqrt{2}R45^{\circ}$ *magnetite(001)"*, Physical Review B **91**, 020408(R) (2015).

- L. Martín-García, A. Mascaraque, B. M. Pabón, R. Bliem, G. S. Parkinson, G. Chen, A. K. Schmid, and J. de la Figuera, *"Spin reorientation transition of magnetite (001)"*, Physical Review B **93**, 134419 (2016).

3.1 Introduction

Magnetite (Fe_3O_4) is the oldest magnetic material known [1]. People in ancient Greece and China took advantage of its ferrimagnetic nature already thousands of years ago to build compasses for navigating across the sea [1]. Since its discovery and through the history, magnetite has been useful in many different fields, for example, as source of iron or as a pigment [2]. As catalyst, it is known to promote the water gas shift reaction to produce hydrogen or the synthesis of ammonia [2]. In the form of nanoparticles they are used for protective coatings to prevent corrosion of metals [3, 4] or to remove heavy metals from contaminated water [5, 6]. In the field of biomedicine, Fe_3O_4 nanoparticles coated with drugs are used to release them in the desired location inside the body [7].

Nowadays, Fe_3O_4 is a very attractive candidate for spintronic applications. For example, Fe_3O_4 thin films have been proposed as electrodes in magnetic tunnel junctions (MTJs) [8–10] because of its high Curie temperature (Tc $\sim$ 850 K [2]) and its predicted half-metallicity at room temperature[1]. The electron current in bulk Fe_3O_4 is supposed to be fully spin-polarized [11], i.e., its minority spin-down band crosses the Fermi level while there is a gap for the majority spin-up band. However, the spin-polarization of magnetite measured using spin-resolved photoelectron spectroscopy has reported values that differ from the -100% predicted spin-polarization with either positive (+16%) [12] and negative values (-80% to -25%) [8, 13, 14]. Considering that this is a surface-sensitive technique, the variety of published results points towards the importance of controlling the surface and interfaces properties of magnetite. In addition, the measured tunneling magnetoresistance (TMR) of the Fe_3O_4-based MTJs is far below the expected and almost negligible at room temperature [8, 9, 15]. A variety of causes have been suggested to explain these disappointing results including the presence of a magnetically dead layer at the surface or at the interface region of magnetite [9, 16, 17] or to antiphase boundaries

[1]The tunneling magnetoresistance in MTJs depends on the difference of the density of states of spin-up and spin-down electrons at the Fermi level and is maximum for materials with only one spin orientation present at the Fermi level.

(APBs) [18]. These are defects occurring at the early stages of the growth process of thin films that can induce a magnetic disorder preventing the existence of a well-defined parallel and antiparallel magnetic state in the MTJ. The impact of the APBs on the properties of the material will be explained in detail in Chapter 5. The study of a surface of a magnetite single crystal free from defects, like the APBs, is important to understand the fundamental properties of the material as a previous step to fully exploit its potential for desired applications.

Finally, magnetite has attracted the interest of the scientific community in the search for multiferroic materials, as in addition to being ferrimagnetic, it has been shown to be ferroelectric at low temperatures [19]. In addition, the combination of magnetite with ferroelectric materials like $BaTiO_3$ to form multiferroic heterostructures has also been studied [20, 21].

Crystal structure

Fe_3O_4 crystallizes in the cubic inverse spinel structure (see Fig. 3.1) where one third of the iron cations in a Fe^{3+} oxidation state occupies tetrahedral (A) sites and the rest of the Fe^{3+} and Fe^{2+} cations are equally distributed in octahedral (B) sites [2]. The corresponding inverse spinel formula can be written as:

$$(Fe^{3+})_A[Fe^{3+}Fe^{2+}]_BO_4$$

The <001> direction in magnetite consists of planes containing two $Fe^{3+}{}_{tet}$ cations alternating with planes containing eight O^{2-} anions, two $Fe^{2+}{}_{oct}$ and two $Fe^{3+}{}_{oct}$. The octahedral sites run in rows along <110> directions. In the next layer the rows are rotated by 90° with respect to the one above. Every layer has a net charge of +/- 6 and

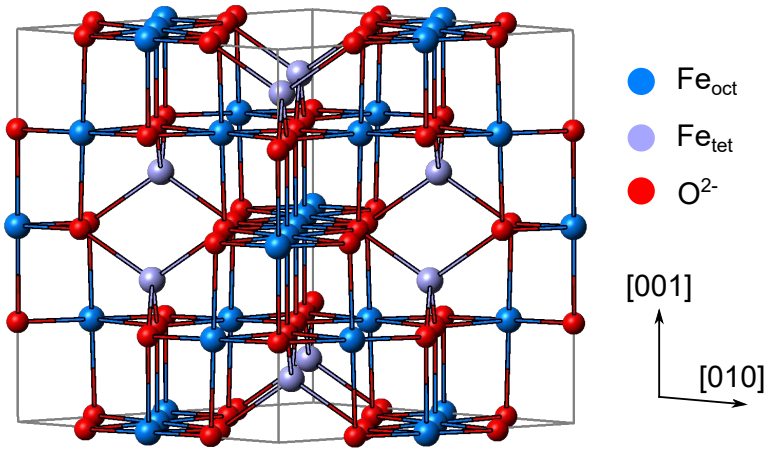

Figure 3.1: Schematic representation of the inverse spinel structure of Fe_3O_4.

thus, the surface region requires a compensation charge of +/- 3[2]. One way to achieve this is via surface reconstructions that consist on the rearrangement of the surface atoms [22]. This rearrangement results in a change in the periodicity of the surface structure, which can be easily detected by LEED.

Considering the (001) surface of Fe_3O_4, it was observed that after cleaning cycles of Ar^+ sputtering and annealing stages in vacuum and in an oxygen background, instead of the (1 × 1) bulk-like termination, the surface reconstructs into a $\sqrt{2} \times \sqrt{2}$R45° structure [23]. Different models were proposed to explain the reconstruction. The early ones were based on polarity compensation effects: a net charge of +/-3 can be obtained either with a surface layer containing only one $Fe^{3+}{}_{tet}$ or including oxygen vacancies [24, 25]. These models were not experimentally supported and Pentcheva and co-workers proposed next a "polar" bulk truncated surface where the $\sqrt{2} \times \sqrt{2}$R45° periodicity arises from a surface lattice distortion [23]. This model was supported by calculations and XRD measurements. However, the agreement between the experimental and theoretical LEED IV curves was poor.

[2] Alternating planes of $2\times Fe^{3+}{}_{tet}=6^+$ and $8\times O^{2-} + 2\times Fe^{2+}{}_{oct} + 2\times Fe^{3+}{}_{oct}=6^-$. The surface layer requires a compensation charge of +/- 3 due to the lack of an adjacent layer above.

The detailed atomic structure of the reconstruction was recently clarified by R. Bliem et al. [26] through the model named "Subsurface cation vacancy (SCV)". Under this model, the reconstruction is proposed to be a response of the material to the oxygen environment suggesting that the termination is a first stage in the oxidation of the surface to Fe_2O_3. The surface layer composed by octahedral Fe remains stoichiometric but there is a rearrangement in the subsurface layers with the replacement of two octahedral irons from the third layer by an extra tetrahedral cation in the second layer (see Fig. 3.2). This reorganisation introduces undulations at the surface that reproduces the $\sqrt{2} \times \sqrt{2}R45°$ periodicity. Moreover, this model implies that the four outermost layers consist on rows of Fe^{3+} cations as demonstrated by XPS [27].

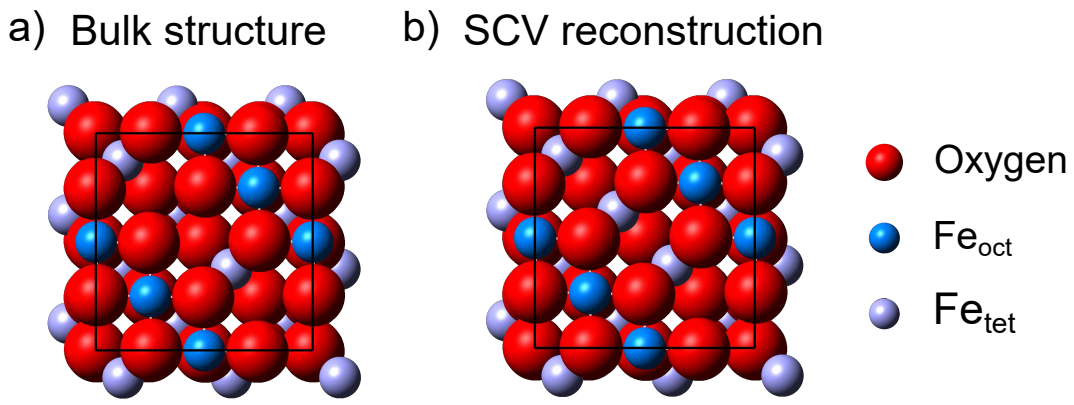

Figure 3.2: a) $Fe_3O_4(001)$ bulk surface representation. b) Subsurface cation vacancy structure representation.

In 1929 Verwey discovered that magnetite presents a metal-insulator transition (MIT) known as Verwey transition [28] where the conductivity decreases by two orders of magnitude when cooling below the Verwey temperature (T_v) $\approx$ 120K. This sharp drop in the electrical conductivity is accompanied by a structural distortion from cubic to monoclinic phase. The MIT phenomenon was explained by Verwey based on the conduction mechanism of magnetite. Above T_v, conductivity is due to the electron hopping between the Fe^{2+} and Fe^{3+} at B positions. Below the transition, the mobility of this extra

electron was supposed to be frozen inducing a long-range charge ordering of the Fe^{2+} and Fe^{3+} cations. During the last decades, an intense research has led to a substantial progress in the understanding of the Verwey transition. However some details, like the existence or not of charge ordering below T_v remain still under debate [29].

Magnetism

Magnetite is ferrimagnetic with a high Curie temperature of $\sim$ 850 K [2]. The magnetic ordering in magnetite arises from several exchange coupling mechanisms between the different cations [30] (see Figure 3.3). The predominant ones are:

- *Super-exchange (cation-oxygen-cation interaction)*: Fe ions couple via an overlap of their 3d orbitals with the 2p orbitals of an intermediate O^{2-}. The interaction is strongly antiferromagnetic (AF) when the overlap angle (α) is greater than 90°, whereas when α=90° the interaction is ferromagnetic (FM) although much weaker than the AF one. In Fe_3O_4 the most important super-exchange interaction is the one between the Fe ions at the A and B sites with an angle of α=127° and an energy J_{A-B} = -28 k_B where k_B is the Boltzmann constant. It aligns antiferromagnetically both lattices. There is also an AFM super-exchange interactions between the ions at A sites with J_{A-A} = -18 k_B and a weak FM super-exchange interaction between the ions at B sites with J_{B-B} = 3 k_B [2].

- *Double-exchange (cation-cation interaction)*: this interaction occurs when the extra electron in Fe^{2+} is transfered towards the empty d-level in $Fe^{3+}(3d^5)$. This interaction aligns ferromagnetically the Fe^{2+} and Fe^{3+} cations on the B sites. As the spin of the extra electron in Fe^{2+} is oppositely directed to those of the electrons in Fe^{3+}, the electron transfer is only possible if the spins of both ions are aligned ferromagnetically.

The spin magnetic moment (m_s) of Fe_3O_4 results from summing up the contributions from the different cations. Fe^{3+} cations have $m_s = 5\ \mu_B$ whereas Fe^{2+} cations have $m_s = 4\ \mu_B$. Considering the magnetic alignment between the cations, m_s (Fe_3O_4) = (-5 μ_B)$_A$ + [5 μ_B + 4 μ_B]$_B$= 4 μ_B. No orbital moment is expected from the Fe^{3+} cations. Since they are in a $3d^5$ configuration, i.e. half-filled shell, the orbital moment is predicted to be quenched following the Hund's rules.

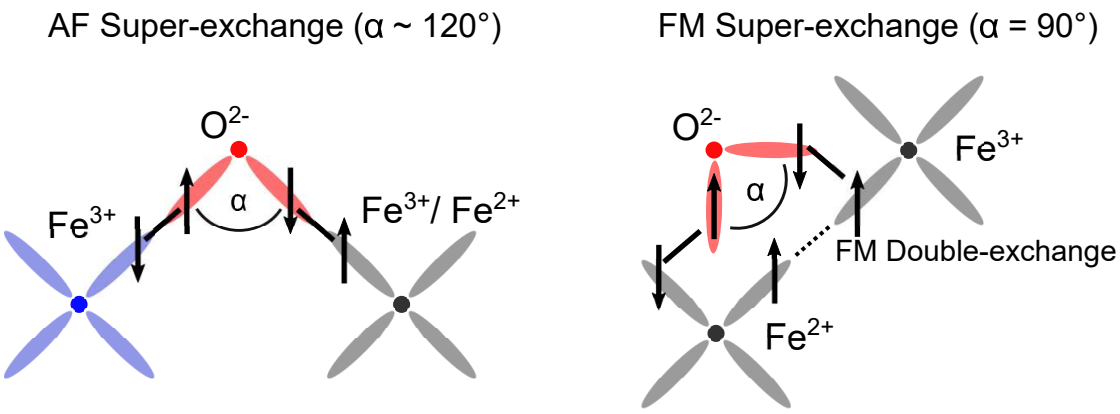

Figure 3.3: Magnetic exchange interactions in Fe_3O_4.

On the other hand, the Fe^{2+} cations are in a $3d^6$ configuration with an extra electron compared to the Fe^{3+} cations and then, an orbital moment can be expected. Theoretical results for bulk magnetite usually point to spin magnetic moments close to the expected value of 4 μ_B [31, 32] although no agreement is found respect to the orbital magnetic moment with vanishing [31] and non vanishing reported values [32]. Experimental studies have been performed either in single crystal [32–34] and thin films [20, 35, 36]. The obtained results expand from reduced m_{spin} compared to the expected bulk value of 4 μ_B [20, 32, 34, 35] with sizable [32, 35] and near zero [34] m_{orb} to m_{spin} values close to 4 μ_B and vanishing m_{orb} [33] and m_{spin} as higher as 7.7 μ_B [36]. In Ref. [33] the authors point out the importance of using high quality samples and a careful experimental procedure in order to obtain reliable results. In the case of thin films, the variety of results can be

Sample	$\mathbf{m}_{spin}$ (μ_B)	$\mathbf{m}_{orb}$ (μ_B)	**ratio** ($\frac{m_{orb}}{m_{spin}}$)	**Ref.**
Single crystal Fe_3O_4	3.68	0.65	0.18	[32]
Single crystal Fe_3O_4	3.90	-0.001	-0.0003	[33]
Single crystal Fe_3O_4	1.70	<0.03	<0.018	[34]
8 nm Fe_3O_4/MgO/GaAs(100)	2.84	0.47	0.17	[35]
2.5 nm Fe_3O_4/$BaTiO_3$(001)	1.2	-	-	[20]
5 nm Fe_3O_4/MgO(100)	7.7	-	-	[36]
Theory	4.0	0.43	0.108	[32]
Theory	3.7	0.02	0.005	[31]

Table 3.1: Spin and orbital magnetic moment of Fe_3O_4 reported in the Literature.

due to the presence of APBs [35]. Table 3.1 summarizes some of the values reported for the magnetic moment in Fe_3O_4.

Goering et al. [37] have tried to give an explanation to the differing experimental values obtained so far suggesting that there are large antiparallel orbital moments associated to the A and B lattices in Fe_3O_4. These moments cancel each other if the surface is perfectly stoichiometric giving rise to vanishing orbital moments. On the other hand, if there are changes in the surface stoichiometry, the orbital moments at each lattice would not cancel giving rise to the variety of results published. This work highlights the importance of a careful preparation of the surface as most of the experiments measure the orbital and spin components of magnetite using XMCD at total electron yield mode that probes the near surface region (see Section 2.2.6).

In addition, despite the number of experimental works reported so far, no attention has already been paid on how the $\sqrt{2}\times\sqrt{2}$R45° reconstruction could affect the magnetic moments of Fe_3O_4. As many technological applications rely on the properties exhibited by the surface it is important to determine the effect of the reconstructed magnetite surface on m_{orb} and m_{spin}.

In order to carry out a study of the magnetic domains in magnetite one needs to take into account the different energy contributions of a ferro- or a ferrimagnet. The most important are the exchange energy, the anisotropy energy, the magnetostrictive energy and the magnetostatic energy [38–40].

- *Exchange energy.* It is originated by the interaction between neighboring atoms and tends to orient the electron spins of the atoms in the same direction. It is given by:

$$E_x = -2J_{ex}\mathbf{S}_i\mathbf{S}_j \tag{3.1}$$

where J_{ex} is the exchange integral and S_i and S_j are the spin angular momentum of atoms i and j respectively. In a ferromagnet (antiferromagnet) it is a minimum when adjacent spins are oriented parallel (antiparallel).

- *Anisotropy energy.* It represents the energy stored in the crystal depending on the direction at which the magnetization points. In a cubic crystal, E_a is given by:

$$E_a = K_0 + K_1(\alpha_1^2\alpha_2^2 + \alpha_2^2\alpha_3^2 + \alpha_3^2\alpha_1^2) + K_2(\alpha_1^2\alpha_2^2\alpha_3^2) + ... \tag{3.2}$$

where α_i are the direction cosines of the magnetization direction with respect to the crystal axes. K_0, K_1 and K_2 are the anisotropy constants and they are specific of the material and of the temperature. K_0 and K_2 are usually neglected because K_0 is independent of the angle and K_2 is very small compared to K_1. In the case where the anisotropy energy dominates, the resulting easy axes will be those that minimize it. In the case of magnetite (see Figure 3.4), K_1 is negative from the Curie temperature down to ∼130 K and E_a will be minimum for the magnetization lying along ⟨111⟩ directions. At 130 K, magnetite presents a spin reorientation transition (T_{srt}) where K_1 changes its sign, from negative to positive, the ⟨111⟩ directions are no longer the

preferred ones and E_a becomes a minimum when the magnetization points along $\langle 100 \rangle$ directions [41]. It should be noted that the evolution of K_1 is non-monotonic [41, 42]: it first decreases with decreasing temperature from the Curie point to T $\simeq$ 250 K, then increases with decreasing temperature down to T_{srt}. The non-monotonic behavior of K_1 will be important to explain some of the results presented in this chapter.

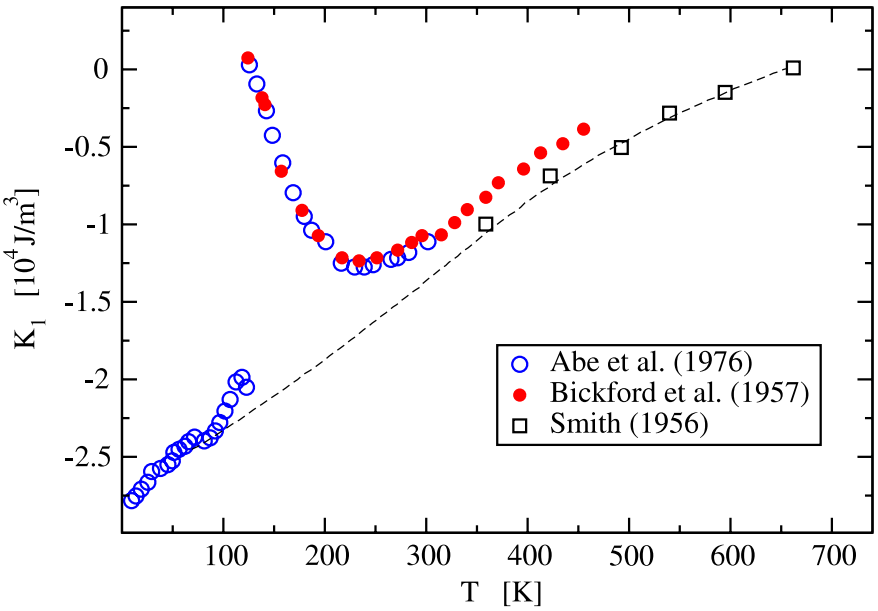

Figure 3.4: Temperature dependence of the magnetic anisotropy constant K_1 in bulk Fe_3O_4. Reprinted from [42].

- *Magnetostrictive energy.* It arises from the interaction between the magnetization and the strain of the lattice. The magnetostrictive energy for cubic crystals without external applied stress is given by:

$$E_{strict} = [\frac{9}{4}(c_{11} - c_{12})\lambda_{100}^2 - \frac{9}{2}c_{44}\lambda_{111}^2](\alpha_1^2\alpha_2^2 + \alpha_2^2\alpha_3^2 + \alpha_3^2\alpha_1^2) \tag{3.3}$$

where c_{11}, c_{12} and c_{44} are the elastic moduli and α_1, α_2 and α_3 are the direction cosines

as before. The constants λ_{100} and λ_{111} are the saturation magnetostrictions. They are material parameters that represent the fractional change in length ($\lambda = \frac{\Delta l}{l}$) of the sample when it is magnetized measured along the specific crystallographic direction. The saturation magnetostriction as a function of the increasing temperature was measured for polycrystalline bulk magnetite [43] as shown in Figure 3.5a. As the sample is polycrystalline, the saturation magnetostriction is characterized by a single constant λ_s. It can be seen that at room temperature $\lambda_s \simeq 40{\cdot}10^{-6}$ and the value smoothly decreases as the temperature increases. Figure 3.5b shows the saturation magnetostriction measured at low temperatures for a bulk magnetite single crystal for three crystallographic directions [44]. It can be seen that at low temperatures, the values of the magnetostriction do not show large variations.

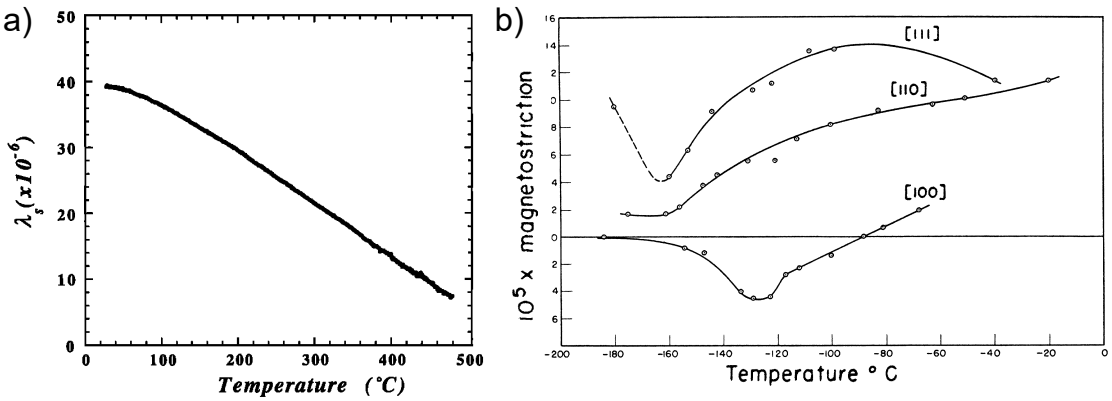

Figure 3.5: a) Saturation magnetostriction as a function of the increasing temperature measured in polycrystalline bulk Fe_3O_4. Adapted from [43]. b) Saturation magnetostriction measured at low temperatures in bulk magnetite single crystal. Adapted from [44].

- *Magnetostatic energy.* This term is related to the magnetic field generated by the magnetic sample itself, i.e., the demagnetizing field H_d. The expression for the magnetostatic energy is:

$$E_{ms} = \frac{\mu_0}{2} \int H_d^2 \, dV \tag{3.4}$$

where μ_0 is the permeability constant. The magnetostatic energy plays a primordial role in the formation of magnetic domains. If the sample is monodomain, north and south poles are formed at the ends of the sample generating a large H_d with also a large associated magnetostatic energy. However, this energy can be reduced if the sample splits in domains oriented antiparallel as they bring closer the north and south poles decreasing the spatial extent of H_d. The magnetostatic energy is also reduced when the magnetization lies in the surface of the sample as it reduces the surface poles.

H_d depends on the magnetization from which it originates: $H_d = N_d M$ where N_d is the demagnetizing tensor that depends on the shape of the sample. Therefore, shape can be the source of another type of magnetic anisotropy called shape anisotropy which is characterized by the shape anisotropy constant K_s given by:

$$K_s = \frac{\mu_0}{2} N_d M^2 \tag{3.5}$$

For the particular case of a thin film, $N_d = 1$.

Surface magnetic domains

The characterization of the magnetic domains at the magnetite surface has been mostly performed on the most compact surfaces: the (111), (100) and (110) orientations. The (110) surface comprises magnetic in-plane easy-axes, and thus, it presents closure domains that resemble bulk domains [45]. In contrast, both the (111) and the (100) lack easy-axes within the surface plane and the competition between anisotropies is expected to give rise to complex patterns [39]. In fact, both surfaces present a multiscale complex structure of magnetic domains first detected by Kerr microscopy on (111) surfaces [46] and by photoemission electron microscopy on the (100) surface [47].

There are few low temperature experiments observing the magnetic domains of magnetite in real space and most of them have been devoted to the Verwey transition [48, 49]. Experimental observations of the magnetic domains of magnetite at high temperatures are also rather scarce. The first ones were performed by the Bitter technique on magnetite grains. They point to a strong dependence of the domain structure with temperature [50]. However, this technique is only suitable for experiments where the sample temperature remains below 350°C because of the instability of the ferrofluid at higher temperatures. This limitation can be overcome by employing Kerr microscopy. A. Ambatiello et al. [46] studied the evolution of the magnetic domains on magnetite (110) at temperatures up to the Curie point, showing no significant changes in the shape and type of domains but a somehow reversible domain structure after heating and cooling cycles and a significant increase in the mean domain width for temperatures between 400°C and the Curie point. Thus, at high temperatures we lack from experimental reports that clarify whether there are or not changes of the surface magnetic domains when the temperature is modified. Given the importance of magnetite thin films for technological applications it is highly important to understand the evolution of the magnetic properties of the material with temperature.

In summary, in this chapter different questions will try to be addressed:

- Does the $\sqrt{2} \times \sqrt{2}$R45° reconstruction of the $Fe_3O_4(001)$ surface play a role on the magnetic moments?

- Has the increasing temperature any effect on the magnetic domain configuration of the $Fe_3O_4(001)$ surface? And if there are changes, how can we relate them with the existing interactions in the material?

- Concerning the spin reorientation transition occurring in magnetite, how does the magnetic domain configuration evolve through it? Does the easy axes reorientation occur smoothly or abruptly?

3.2 $Fe_3O_4(001)$ surface

Figure 3.6a shows the $Fe_3O_4(001)$ surface imaged by LEEM after a few cleaning cycles. It appears covered with square structure known as "mesas". These structures of typically 1–2 μm width, are aligned along the $\langle 110 \rangle$ in-plane directions which correspond to the compact orientations of surface steps. "Mesas" develop during the sputtering and annealing cycles due to the surface growth under oxygen exposure [51].

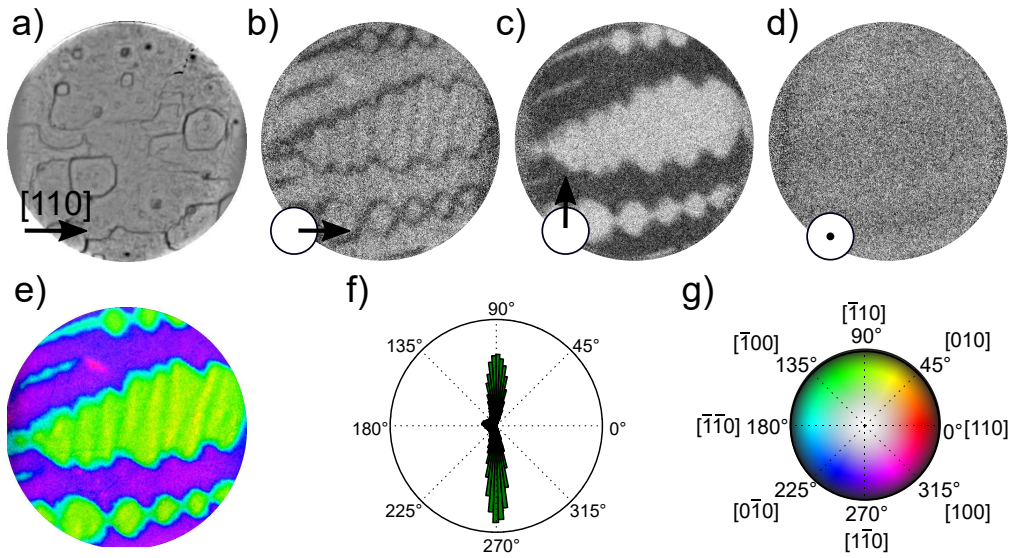

Figure 3.6: a) LEEM image of the surface of $Fe_3O_4(001)$ at room temperature (300 K). SPLEEM asymmetry images of the same area showing the component of the magnetization along b) x, c) y and d) z axes of the images. The field of view is 12 μm and the start voltage is 8 V. e) Composite color image indicating the local magnetization vector using the color wheel indicated in (g). f) Polar histogram of the magnetization from the image shown in (b). g) Color wheel indicating the correspondence between color and direction in image (e).

The magnetization configuration in 3 dimensions is determined easily by means of SPLEEM. It should be noted however that a fresh surface introduced from air without cleaning does not show magnetic contrast. As SPLEEM is mostly sensitive to the last few atomic layers, the absence of magnetic contrast can be attributed to the oxidation,

adventitious contamination and lack of good order on the surface. Only when the crystal surface has been cleaned by several cycles of sputtering and annealing, magnetic contrast is observed. Fig. 3.6b-d show the room temperature component of the magnetization along the x, y and z axes of the images, correspondingly. The images are taken with an exposure time of 1 sec. The asymmetry image along the perpendicular direction to the surface (see Figure 3.6d) exhibits a weak contrast, not significant compared with the in-plane contrast. The electron reflectivity asymmetry, i.e., the asymmetry in the electron reflectivity measured with the electron beam spin direction along the local magnetization orientation and antiparallel to it, is $\simeq 3\%$ for the images along x and y while for the image along z, the asymmetry is $\simeq 0.8\%$.

It was mentioned in the Introduction that the Fe_3O_4 easy axes at room temperature are the $\langle 111 \rangle$ ones. Near the surface, the shape anisotropy competes with the magnetocrystalline anisotropy, with the former pushing the magnetization into the surface plane in order to decrease the magnetostatic energy. If the shape anisotropy is larger than the magnetocrystalline one, the magnetization should be in the (001) plane. And within the (001) plane it should lie along the $\langle 110 \rangle$ directions, driven by the magnetocrystalline anisotropy as the shape anisotropy does not provide any in-plane preference [52].

By combining the asymmetry images we can determine the 3-dimensional magnetization vector. The image in Figure 3.6e shows the in-plane distribution of the magnetization on the same area observed in Figure 3.6a, employing a color palette of Figure 3.6g to indicate the vector direction. Magnetic domains are observed to be completely unrelated to the topographic features. Although SPLEEM is sensitive to the topmost layers, the magnetic domains arise from deeper, an thus, the observed domains should not be affected by the detailed atomic surface structure termination.

The magnetic domains in Figure 3.6e are oriented mostly along the $[\bar{1}10]$ axis: the green-yellow domains correspond to $[\bar{1}10]$ (90°), while the purple ones correspond to $[1\bar{1}0]$ (270°). The domain walls are wavy, and have a $[\bar{1}\bar{1}0]$ orientation of the magnetization

(180°). There is a band pattern in the greenish domains, with a micron-wide periodicity (observed in the image as green and yellow bands), while the oppositely oriented domains do not present this structure.

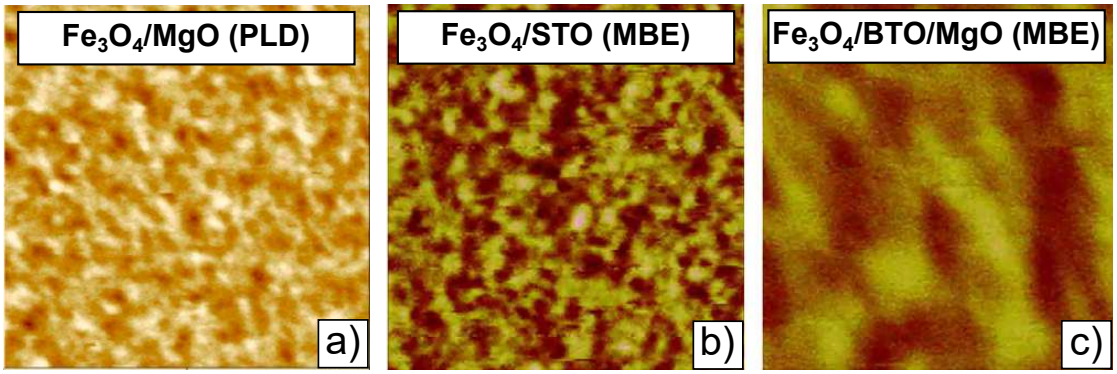

Figure 3.7: MFM images of a) Fe_3O_4 grown on MgO by PLD. The film thickness is 100 nm and the area shown is $2 \times 2\ \mu m^2$. Reprinted from [53]. Fe_3O_4 grown on $SrTiO_3$ (STO) (b) and on $BaTiO_3$(BTO)/MgO (c) by MBE. The film thickness is 20 nm and the area shown is $4 \times 4\ \mu m^2$. Reprinted from [54].

As a complementary way to visualize the magnetization orientation, we present in Figure 3.6f a polar histogram of the distribution of magnetization values from the image shown in Figure 3.6e. It clearly shows that in most of the surface the magnetization is oriented along the 90° and the 270° directions. The areas corresponding to the domain walls can also be observed in the histogram, along the 180° direction. This style of domains observed at the crystal surface are very different from domains experimentally observed in magnetite thin films with (001) orientation (see Figure 3.7). These films usually present irregular magnetic domains with domain widths smaller that the ones exhibited by the crystal surface. The difference in domain size and shape on thin films is likely due to the presence of antiphase domain boundaries (APBs) that strongly affect the local magnetization [18], but that are rare in bulk single crystals.

A disadvantage of the SPLEEM system is that the maximum field of view is around 12 μm due to the fixed apertures of the instrument [55]. To overcome this limitation and obtain a larger view of the magnetization configuration we show in Figure 3.8a a mosaic of LEEM images that covers an area of $\simeq 30\times30$ μm^2. The left-up corner image marked with a red circle corresponds to the same area of Fig. 3.6a. We can observe that Fig. 3.6a is representative of the general appearance of the surface with "mesas" covering the field of fiew although in the lower side there is a scratch crossing the area under observation. The magnetization vector distribution is shown in Figure 3.8b. The magnetization is again within the plane. The overall mosaic presents a complex magnetic domain distribution. A central area shows a mostly purple region (which corresponds to the magnetization being oriented along $[1\bar{1}0]$) with red ($[110]$) and cyan stripes ($[\bar{1}\bar{1}0]$).

Where the stripes become wider, they are seen to be sorrounding green ($[\bar{1}10]$) areas, sometimes with a square shape. Around this central region, extended green areas are present. The easy axes can be identified over the area under observation by plotting the histogram of the distribution of magnetization azimuthal angles, as shown in Figure 3.8c. It is clear that the magnetization is mostly along $[1\bar{1}0]$ and $[\bar{1}10]$ directions, which correspond to the purple and green areas in the color image, as expected. Besides the additional structure within each large purple or green domain, the magnetization map in figure 3.8b shows that the boundaries between the green and purple domains are composed of stripes which are either red or cyan, i.e., the 180° domain walls show an in-plane magnetization perpendicular to the adjacent domains.

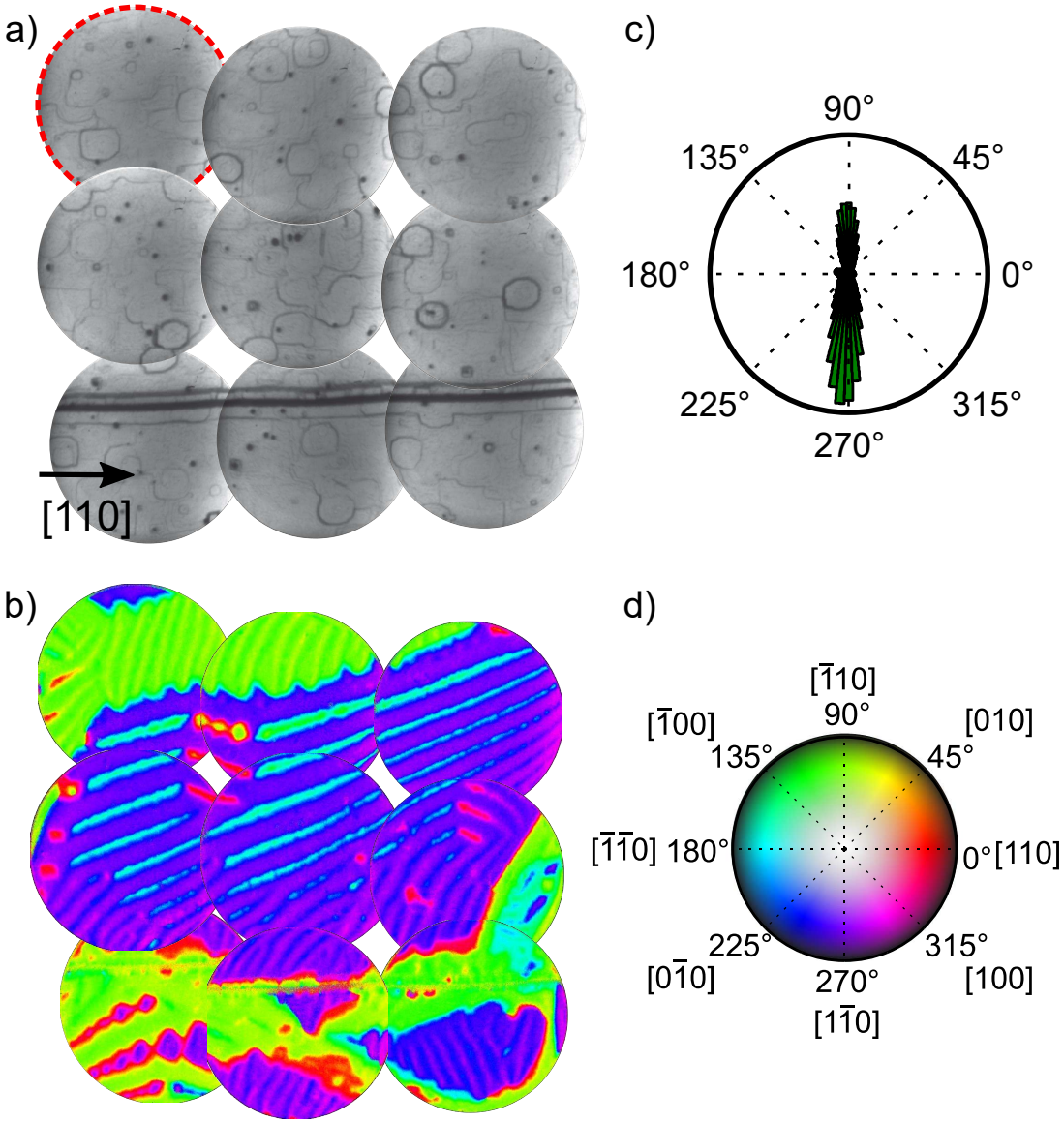

Figure 3.8: a) Mosaic of 9 LEEM images that cover an area of about 30×30 μm^2 (each individual image has a field of view of 12 μm). The left up corner image is the same area as shown in Fig. 3.6a. b) 3D magnetization map obtained at room temperature combining SPLEEM images acquired along three orthogonal axes in the same area shown in (a). c) Histogram of the in-plane component of the magnetization from (b). d) Colormap, with hue color wheel indicating the azimuthal angle and brightness indicating the polar angle.

Complementary, the magnetic domain configuration at the $Fe_3O_4(001)$ surface can be investigated by XPEEM. It should be mentioned that in contrast to SPLEEM, magnetic contrast is observed by PEEM without cleaning the surface. This is an indication of the different probing depth of both techniques. SPLEEM is sensitive mainly to the topmost layers while PEEM can probe depths of several nanometers. However, if the sample is going to be studied by LEEM and LEED, the cleaning cycles will still be necessary as these techniques are sensitive to the last atomic layers.

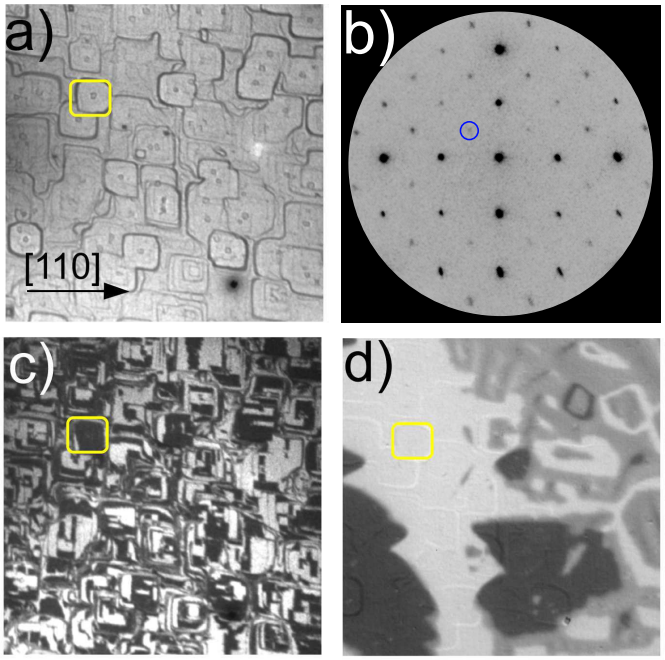

Figure 3.9: a) Low-energy electron microscopy image of the surface of the magnetite crystal, acquired at an electron energy of 5.5eV. b) LEED pattern of the $\sqrt{2}\times\sqrt{2}$R45° $Fe_3O_4(001)$ surface where one reconstruction spot is marked with a blue circle. The Vs is 32 eV. c) Dark-field image using one of the first order beams. d) XMCD-PEEM image showing magnetic domains. All the LEEM and PEEM images are acquired in the same area, and the same feature is highlighted with a yellow square in each one as a guide to the eye. The LEEM and PEEM images are 14 μm wide.

Figure 3.9a shows the LEEM image of the $Fe_3O_4(001)$ surface after several cleaning cycles with the characteristic "mesas" covering the field of view.

As mentioned in the Introduction, the surface of magnetite after the cleaning treatments does not exhibit the bulk structure, but an oxidized state with the replacement of two octahedral irons in the third layer by an extra tetrahedral cation in the second layer [26]. This is observed by LEED where instead of the (1x1) bulk-like termination, the surface exhibits a $\sqrt{2}\times\sqrt{2}$R45° reconstruction (see Figure 3.9b). In this way, the surface is terminated by octahedral Fe^{3+} rows running along the surface [110] directions [26]. When crossing an atomic step, the Fe rows switch by 90°. Given the symmetry of each terrace, images formed by one of the first order diffraction beams, i.e. dark-field images, show each consecutive atomic terrace as either white or black, as shown in Figure 3.9c. Also, from the dark-field image, it can be seen that most of the mesas comprise several atomic terraces.

The magnetic surface domains can be imaged by acquiring XMCD images as show in Figure 3.9d. The XMCD image was acquired at the photon energy corresponding to the first minimum of the XMCD spectrum as explained in 2.2.6 to maximize the magnetic contrast. The sample was aligned so that the X-ray incidence (x-axis of the figures) was along one of the in-plane [110] directions, i.e., one of the surface easy axes directions at room temperature. In consequence the XMCD image in Figure 3.9d shows only three different intensity levels: white, gray and dark. White and dark correspond, respectively, to domains oriented along and opposite to the in-plane direction of the X-ray beam, and the gray level corresponds to areas that give no XMCD signal and are thus composed of domains with the magnetization perpendicular to the X-ray beam direction.

3.3 Surface magnetism at high temperatures

We have studied the evolution of the $Fe_3O_4(001)$ surface magnetic domains at the SPLEEM system with increasing temperature. The sample was heated up to 900 K in steps of 100 K stopping for about one hour at each temperature to record the magnetic domain configuration. The area under investigation is the same as the studied in Fig. 3.8.

The evolution with temperature is shown in Figure 3.10, where the same area is presented at 500, 600 and 700 K respectively. The main difference in the first image (500 K) compared to room temperature (see Fig. 3.8b) is that the stripes within the purple domain and the wavy bands within the green ones are fainter. At 600 K, all the microstructure within the purple domain has disappeared, while some stripes are still observed in the lower left corner on the green domain. The domain walls are moving and becoming more straight. At 700 K each large magnetic domain presents a uniform orientation. From then on to the Curie temperature only a gradual decrease of the magnetic contrast is observed together with some motion of the 180° domain walls. The sample was heated up to 900 K where no contrast could be observed in the SPLEEM images.

After the experiments, the sample was cooled down to room temperature where the domain distribution was recorded again (see Fig. 3.11d). It is surprising the similitude between the overall domain distribution before and after annealing. The same purple domain covers most of the central area under observation, with green domains around it and the domain walls between the two regions have mostly the same sense. However, there are changes in the stripes within the purple domain, and within the wavy bands in the green upper domain. In the purple domain, the distribution of stripes has changed, with more red stripes along the central area. And the wall around a purple domain in the lower right corner (marked with an arrow), was initially split into two different ori-

entations, red and cyan, while after the annealing it has only one orientation, cyan. This suggests that the finer structure of the domain distribution is sensitive to temperature.

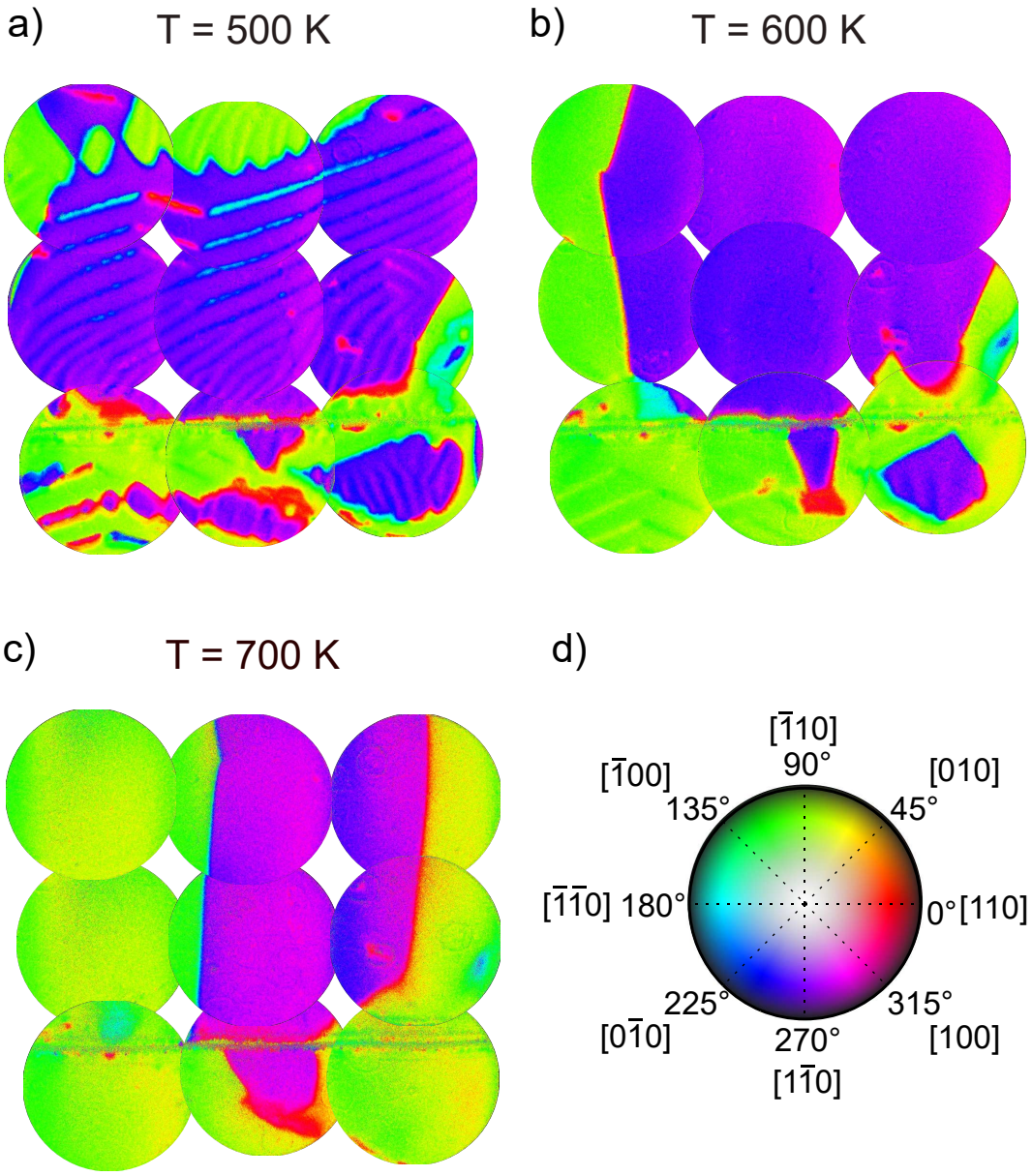

Figure 3.10: Evolution with temperature of the magnetic domains on magnetite measured by SPLEEM.The same mosaic of images is shown for 500 K (a), 600 K (b) and 700 K (c). d) Colormap indicating the correspondence between color and angle.

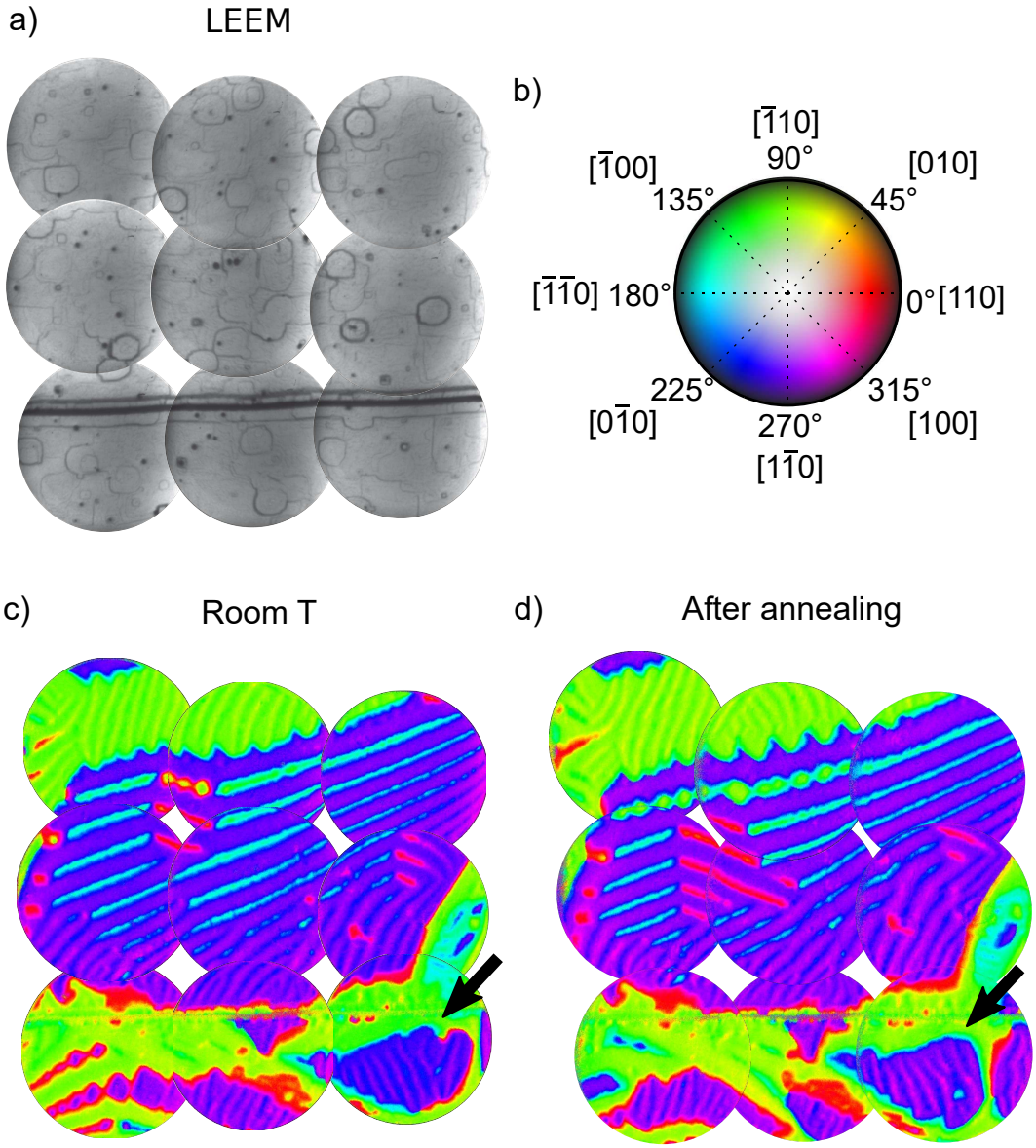

Figure 3.11: a) Mosaic of 9 LEEM images covering the same are of Fig. 3.8. The x-axis and y-axis directions correspond to [110] and [$\bar{1}$10] respectively. b) Colormap indicating the correspondence between color and angle. c) 3D magnetization map obtained at room temperature combining SPLEEM images acquired along three orthogonal axes in the same area shown in (a). d) 3D magnetization map of the same area acquired after annealing the crystal for several hours up to 900 K and cooling back to room temperature.

The reversibility of the process was studied in more detail as shown in Figure 3.12 by varying the temperature within a range close to room temperature. We acquired movie sequences at the area correspondent to Fig. 3.6 while the temperature was varied continuously, with the electron beam spin polarization fixed along the [110] direction. Thus, the images are white when there is a component of the magnetization along the [110] direction, black when the component of the magnetization is along $[\bar{1}\bar{1}0]$, and grey when the component along the x-axis is zero. It is clear that as the temperature is increased, there are different stages. First, the domain at the center which presents bands (marked with a white arrow) shrinks in size and breaks up into smaller rombohedral domains, between 293 K and 375 K. Then, those rombohedral domains decrease in size until they collapse into lines (401–433 K), and eventually the lines decrease in contrast and nearly disappear at 443 K. The reversibility of the process is shown by cooling from 443 K down to 364 K: the stripes first reappear, and although the square domains also reappear, they do it in a somewhat different distribution than during the heating ramp.

These changes in the magnetic domain configuration are quite unexpected as we are far away from the Curie point or any other transition temperature. To find out the origin of these changes, we consider the temperature dependence of the different interactions responsible for the appearance of magnetic domains. First, the shape anisotropy tracks the average magnetization decrease with temperature, so it does not change much in the 300–500 K range. The magnetostriction decreases quite slowly above room temperature (see Figure 3.5a). However the magnetocrystalline anisotropy decreases by a factor of 3 in that range (see Figure 3.4). To check the impact of the magnetocrystalline anisotropy in the magnetic domain configuration we have performed an additional test. If we take a look at the temperature dependence of K_1 (see Fig. 3.4), we can see that it decreases in magnitude not only when heating above room temperature, but also when cooling down below 210 K. If the magnetocrystalline anisotropy is responsible for the changes observed here, the same evolution of magnetic domains on the surface of magnetite (001) should be observed when cooling from 200 to 150 K (just before the spin reorientation

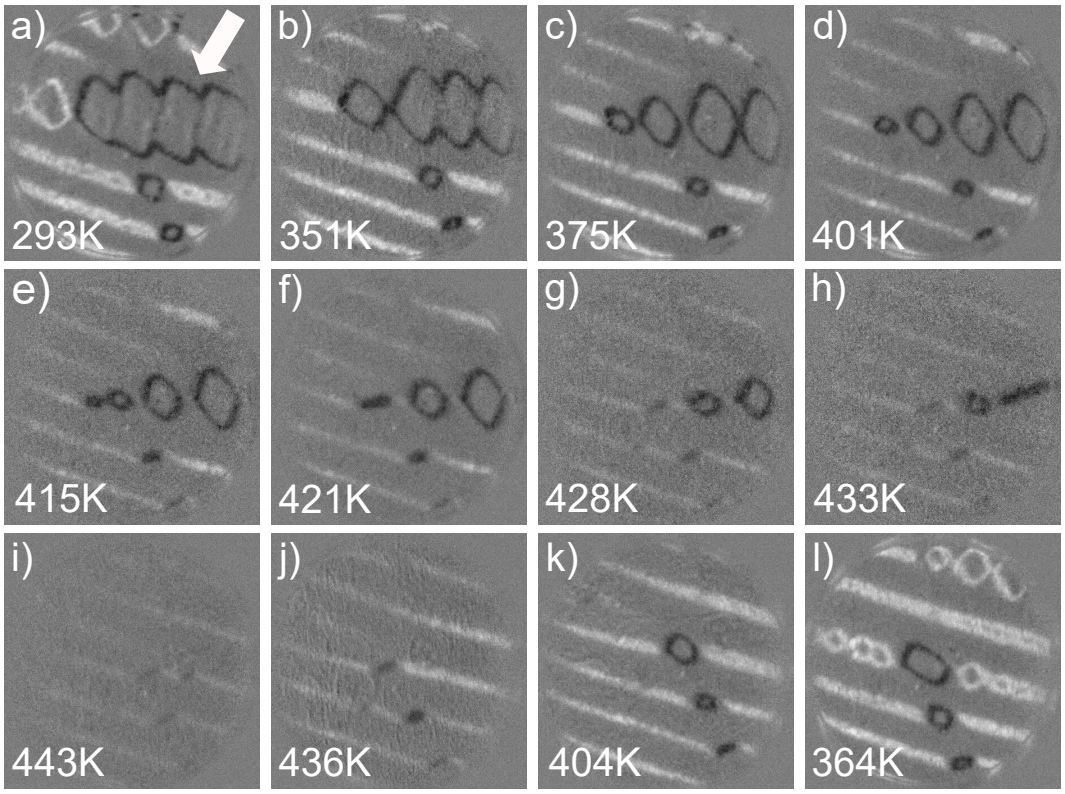

Figure 3.12: (a–l) SPLEEM asymmetry images showing the magnetization component along the x-axis, selected from a sequence of images saved during the annealing process. The crystal was heated from room temperature to 443 K (a–i), and cooled back to 364 K (i–l). The field of view is 12 μm.

transition). Thus, although this section refers to changes in the surface magnetic domain distribution of magnetite at high temperatures, we introduce here this additional test performed at low temperatures to explain the results presented above.

Figure 3.13 shows a sequence of images cooling down at the same area of the crystal that was followed above room temperature in Figure 3.12. The initial configuration is again composed of stripes and rombohedral domains. Upon cooling, the rombohedral domains collapse into lines. However, the second stage of changes upon heating where the striped domains disappear gradually is not observed when cooling below room temperature. We note again that, neither the saturation magnetization nor the magnetostriction constants (see Figure 3.5b) change appreciably below room temperature until the Ver-

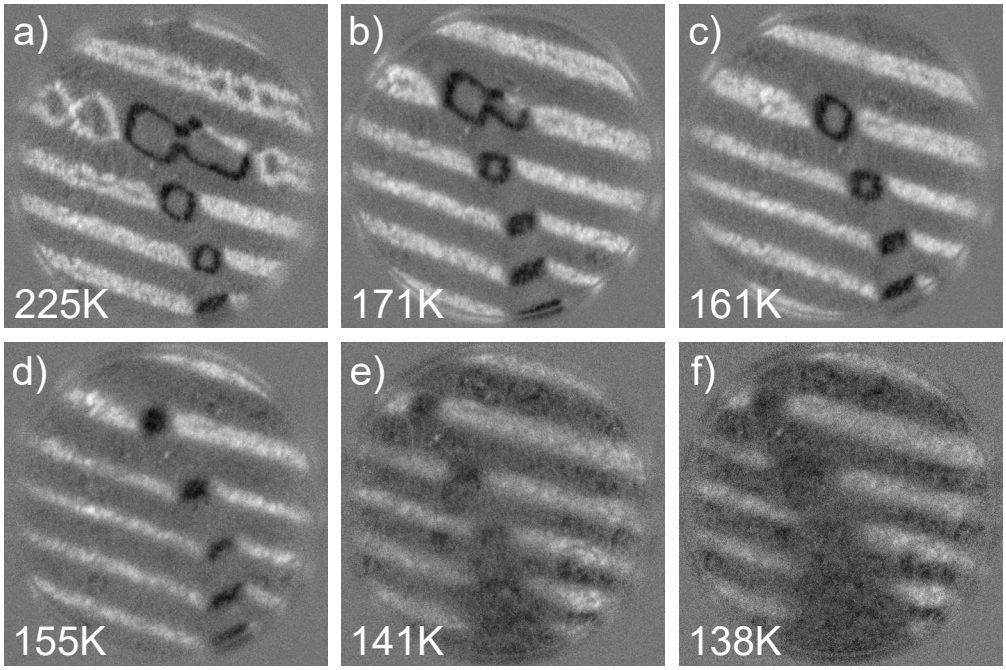

Figure 3.13: (a–f) SPLEEM asymmetry images showing the magnetization component along the x-axis, selected from a sequence of images saved while cooling from 225 to 138 K. The field of view is 12 μm.

wey transition. Thus, the observed changes at low temperature support the assumption that the magnetocrystalline anisotropy might be responsible for the magnetic domain changes as a function of the temperature.

3.4 Surface magnetism at low temperatures

Compared to the lack of experiments at high temperatures, the occurrence of the Verwey transition on magnetite has been responsible for an intense research at low temperatures to try to understand and characterize the transition [56]. But, in contrast, the spin reorientation transition has been poorly characterized: it is still not known if the transition occurs abruptly or continuously. In addition, there are no experiments in real space following the changes of the magnetic domain configuration through the spin reorientation transition.

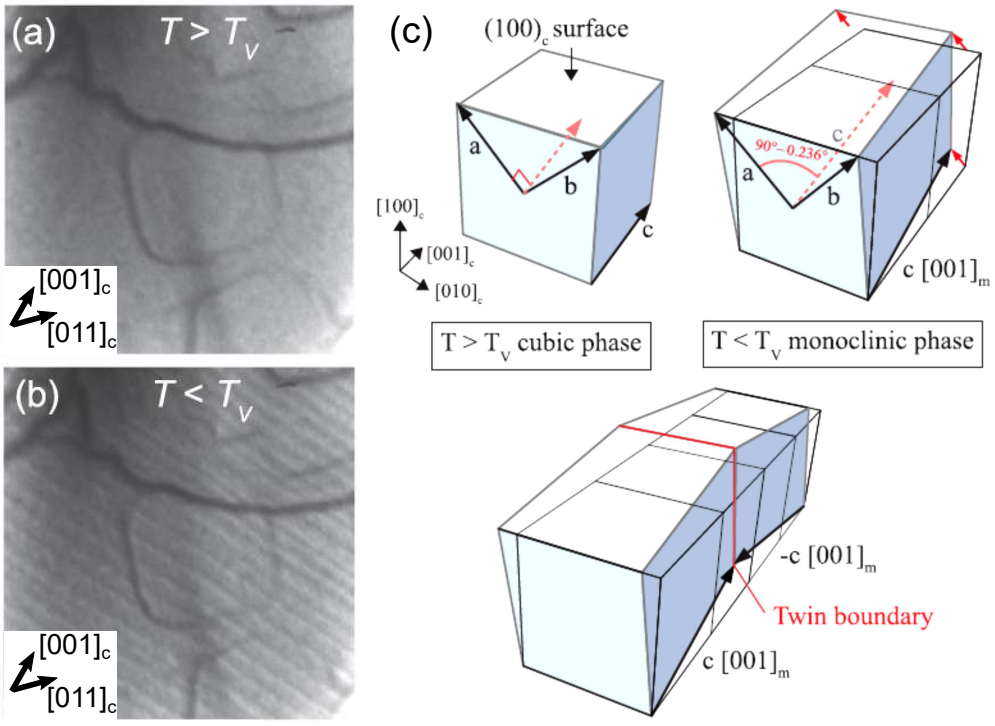

Figure 3.14: LEEM image of the $Fe_3O_4(100)$ surface acquired at a) room temperature and b) sub T_v. Light-dark stripes run perpendicular to the local $[001]_m$ direction of the monoclinic sub-T_v structure. c) Schematic illustrating the lattice distortions that occur in the Verwey transition in magnetite. Bottom: two mirrored monoclinic cells with opposite monoclinic c axis joined at a twin boundary (indicated by the red lines). Reprinted from [57].

Motivated by these reasons, we have followed the evolution of the magnetic domain configuration from room temperature across the spin reorientation transition up to above the T_v. The T_v can be determined by looking at the LEEM images while decreasing the temperature. When the transition is reached, the magnetite flat surface experiences a roof-like distortion observable as dark lines crossing the field of view (see Fig. 3.14a-b). These dark lines are twins that arise when the room temperature cubic unit cell of magnetite transforms into the monoclinic unit cell below T_v. The process is sketched in Fig. 3.14c. The twin boundary represented by red lines results from the join of two mirrored monoclinic cells. Then, within a given monoclinic direction, twins lie along the $[001]_m$ axis, observed in LEEM by parallel bands running perpendicular to this direction.

The $Fe_3O_4(001)$ surface below T_v is shown in Figure 3.15. The same area that was imaged at room temperature in Figure 3.6 was observed here below the Verwey transition. The observed T_v at the surface of the crystal was found at 108 K. At this point, the magnetite crystal structure has transformed into a monoclinic one. The parallel dark lines arising from the monoclinic phase twins can be observed in the LEEM image running along 45° in the upper part of the image, indicating that in such area the monoclinic c-axis is along the cubic $[\bar{1}00]$ direction (135°, perpendicular to the bands). A zoomed image of this area is shown in Figure 3.15g where the arrow indicates the direction of the bands for clarity. On the other hand, the dark lines are oriented along 135° on the right hand side of the image, indicating that in that region the monoclinic c axis is along 45°, [010] direction in the cubic phase. Thus two grains with different monoclinic c-axis are present in the field of view.

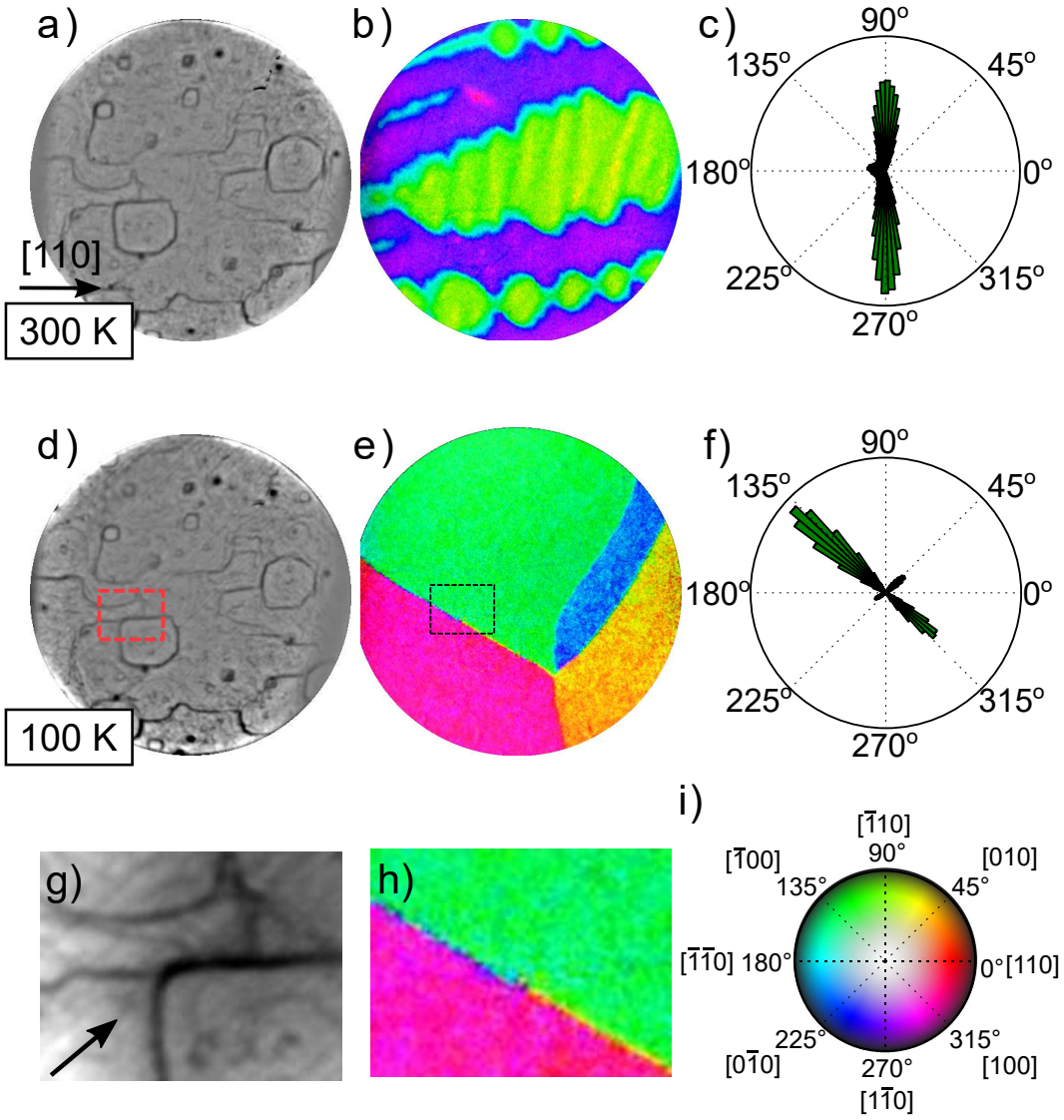

Figure 3.15: a) LEEM image of the surface of $Fe_3O_4(001)$ at room temperature (300 K). The field of view is 12 μm and the start voltage is 8 V. b) SPLEEM composite color image indicating the local magnetization vector using the color wheel indicated in i). c) Polar histogram of the magnetization from the image shown in b). d) LEEM image of the same area after cooling down to 100 K. e) SPLEEM composite color image of the magnetization. f) Polar histogram. g) Detail of the area marked in (d) with a dashed box, 2.9 μm wide. h) Magnetic contrast in the area shown in g). i) Color wheel indicating the correspondence between color and direction in images b) and e).

The SPLEEM data show that the magnetic domain distribution has changed completely from the room temperature one (compare Fig. 3.15b and e). Instead of the bands

within the green domains and the curved domain walls, straight domain walls separating large domains with uniform magnetization are observed. Four different domains can be distinguished. In the left part of the field of view, there are two domains with the magnetization pointing at 135° (green) and at 315° (pink) respectively. Recalling that in this area the monoclinic c axis is along 135°, it is clear that the surface magnetic easy axis is now along that axis. The other two domains, at the right side of the field of view, are oriented along 225° (blue) and along 45° (yellow). Thus, the surface magnetic easy axes have changed from the <110> at room temperature to the <100> below T_{srt}.

While in the high-temperature phase only 180° domain walls were present, in the low-temperature phase two different types can be distinguished, i.e. 90° and 180° domain walls. In Figure 3.15e (and the zoom shown in Figure 3.15h) the walls between the pink and green domains and between the blue and yellow ones separate domains with opposite magnetization, i.e. there are 180° domain walls. They are located in areas with the same overall c-axis. In contrast, the domain walls between the green and blue and between the pink and yellow domains are 90° magnetic domain walls and separate regions with different c-axis. Looking in more detail (see Fig. 3.15h) we observe that the spin rotation within the domain walls is resolved. In this particular case, the upper part of the wall is blue (225°) while the lower part is yellow (45°). Thus, within the 180° domain walls the magnetization is observed to be oriented perpendicular to the magnetization of the adjacent domains. Within the 90° walls, the observed magnetization points in the intermediate direction between the magnetization in the adjacent magnetic domains. For example, it is cyan (180°) for the wall between the green (135°) and blue (225°) domains. The different types of domain walls are consistent with micromagnetic simulations by Kasama and coworkers (compare Figure 3.15e with Fig. 3.16 reprinted from Ref. [48]). In Figure 3.16, the $[001]_m$ easy axis is parallel to x in the upper right domain and parallel to y in the lower left domain. A 90° domain wall is observed in the center of the figure separating two domains with different monoclinic c axes. The magnetization within the wall points at an intermediate direction of the adjacent domains. In the lower right part

of the figure a vertical 180° domain wall separates areas sharing the same monoclinic c axis (areas in yellow and blue). The domain wall magnetization points perpendicular to the magnetization direction of the adjacent domains (red and green following the color wheel in the inset).

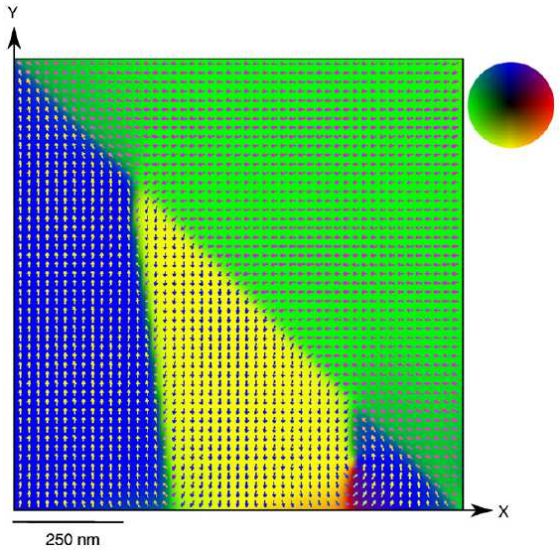

Figure 3.16: Micromagnetic simulation of the surface magnetic configuration in the sub T_v phase of Fe_3O_4. Reprinted from [48].

It is under discussion whether there is a difference in the magnetic moment from above to below the Verwey transition [34, 58]. By comparing the electron reflectivity asymmetries at room temperature and below the Verwey temperature one can determine if there are significant changes in the magnetic moment. The resulting electron reflectivity asymmetry is 2.7% at room temperature and 3% below T_v. The experimental asymmetry thus increases smoothly with decreasing the temperature below T_v. But the absence of large changes indicates that the magnetic moment in the near surface region does not vary significantly through the transition. However, there are still possible changes in the magnetic moment deeper in the crystal that are not sampled by SPLEEM.

Now that the Verwey transition has been characterized, the evolution of the domains

within the temperature range from room temperature to above T_v will be presented. The same area of Fig. 3.15 was imaged by SPLEEM while cooling from 157 K to 114 K, switching the electron beam spin-polarization direction every few frames. The information from images with magnetic contrast along orthogonal directions has been combined to provide the magnetization vector maps as shown in Figure 3.17.

Starting from room temperature, and cooling through 157 and 154 K, no new easy axis directions appear (Figure 3.17a and b) although we observe that the green central domain is breaking into smaller rombohedral domains. Similar changes were observed in the high temperature section and suggested to arise from the dependence of the first magnetocrystalline anisotropy with the temperature (compare with Fig. 3.13). The spread of magnetization angles is larger than at room temperature. Changes in the magnetization directions take place within a few degrees which in combination with thermal drift, introduce errors in the determination of the magnetization angles when averaging over few frames. When cooling down to 144 K (Figure 3.17c), a new domain structure appears in the upper left side of the field of view, with green and yellow colors corresponding to 45° and 135° magnetization directions. In the polar histogram the contribution of this new domain can be observed as small lobes along the 45° and 135° directions. These magnetization directions were not present before. They correspond to the in-plane ⟨100⟩ directions and thus indicate the start of the spin-reorientation transition. At 137 K, all the magnetization vectors are along the in-plane ⟨100⟩ directions, with three large domains (green, yellow, blue) oriented along 135°, 45° and 225° (Figure 3.17d). The 180° wall between the yellow and blue domains is straight, and shows a change in the spin rotation: it is green in the upper side while reddish in the lower one. The spin orientation at the 90° domain wall between the green and the yellow domains could not be resolved.

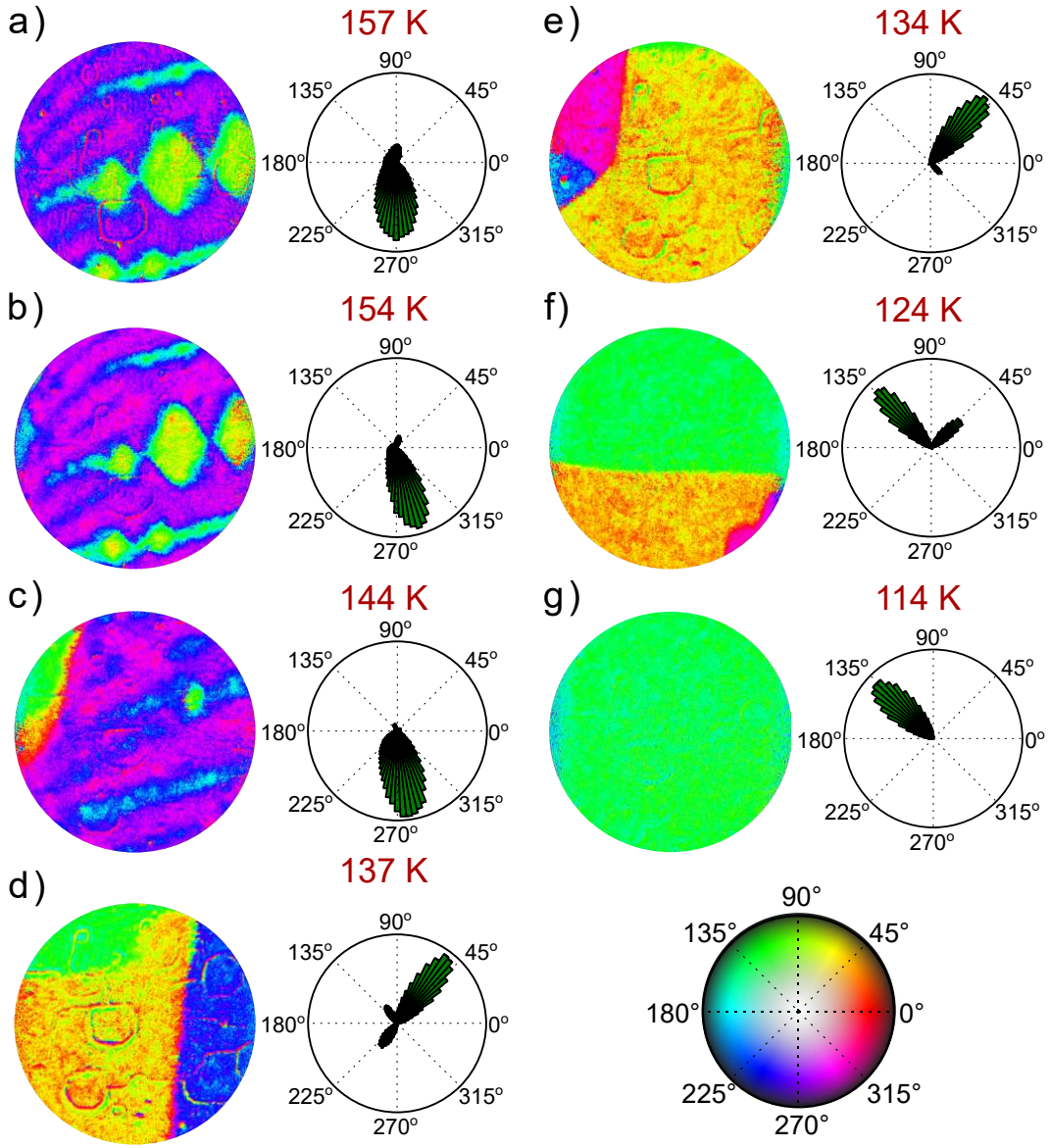

Figure 3.17: Evolution of magnetic domains upon cooling from room temperate down to just above the Verwey temperature, through the spin-reorientation transition measured by SPLEEM. For each temperature, both the real space image (left frame) and the polar histogram of the magnetization (right frame) is shown.

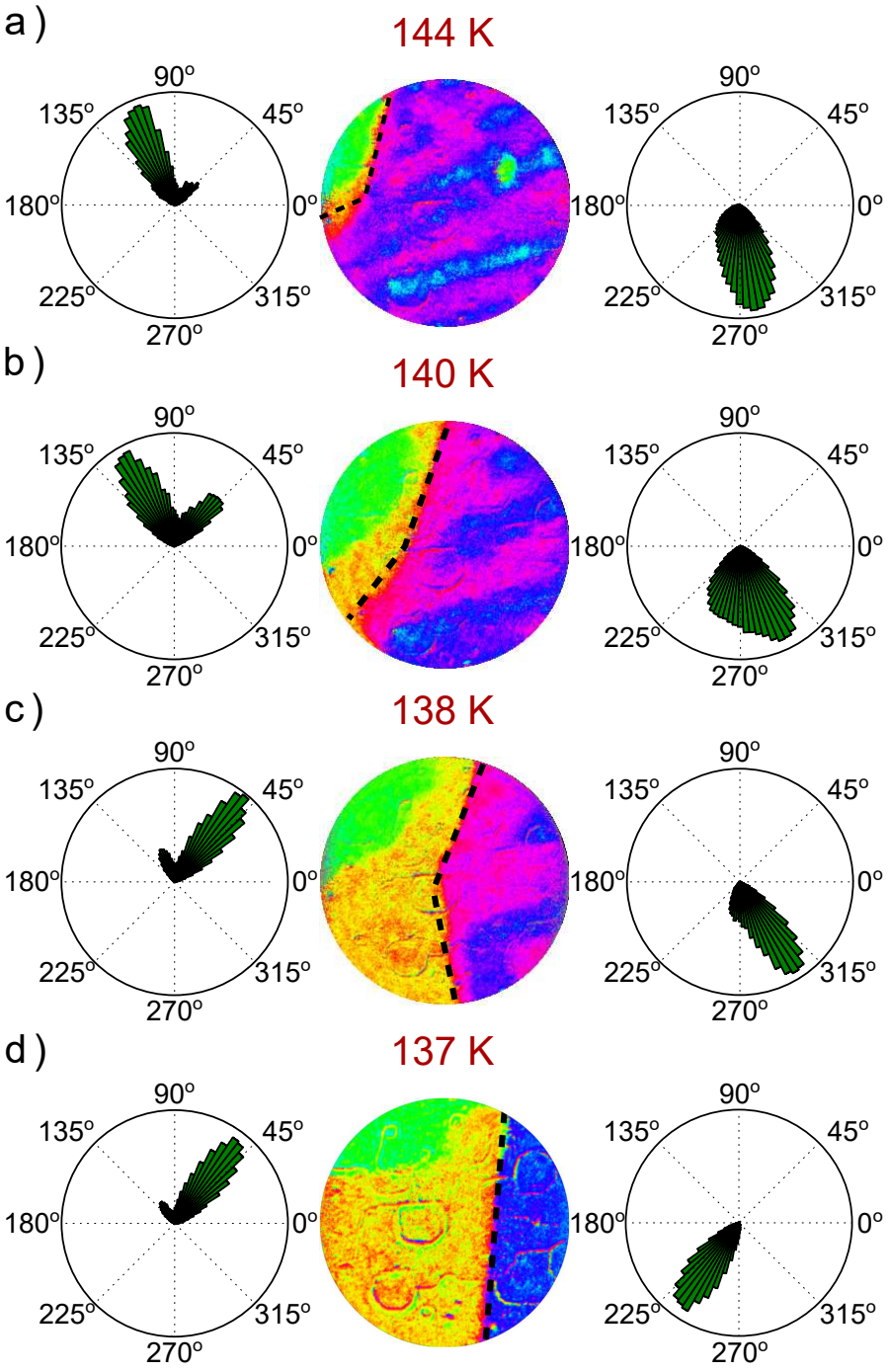

Figure 3.18: Detail of the evolution of the magnetic domains through the spin-reorientation transition measured by SPLEEM. a), b), c) and d) correspond respectively to 144, 140, 138 and 137 K. For each temperature, the color 2D magnetization image is shown in the center. The dashed lines indicate the boundary used to split the surface area into the regions used in the left and right hand side histograms.

The domains continue changing within the field of view while cooling down. At 124 K a single domain sweeps through the area and at 114 K, just above the Verwey transition for this crystal, the full field of view is a single domain (Figure 3.17g). No changes were observed in the topographic images for all the images in Figure 3.17.

Figure 3.18 shows a sequence of images taken close to the spin reorientation transition to study in more detail the changes in the magnetic easy axes. The first frame has also been shown in Figure 3.17c. The distribution of the magnetization is shown separately for the region on the upper-left corner (left histogram) and for the rest of the surface (right histogram). In this way, the magnetization of the new small domains can be resolved. Otherwise it would be masked by the contribution of the larger area.

At 144 K, in the right part of the image, the magnetic easy axes are the same as in the higher temperature frames: the magnetization points mostly along 270°, which corresponds to the $\langle 1\bar{1}0 \rangle$ orientation. In contrast, the green area at the left upper corner has new orientations, along 45° and between 90 and 135°. At 140 K, the green area has grown to occupy one third of the image, and it shows a wide yellow border, detected also in the corresponding histogram. The remaining area of the image has the magnetization mostly in the direction observed at higher temperatures, but the spread of magnetization angles is much wider although the thermal drift is comparable in both frames. At 138 K, the yellow domain has extended. But the remaining area on the right has now an average magnetization which is oriented closer to the [100] in-plane orientation (315°). Finally at 137 K, the yellow domain covers most of the field of view while in the right part of the image a blue domain is oriented along the $[0\bar{1}0]$ direction (225°). The data suggest that the spin-reorientation transition takes place in two stages: first the nucleation of domains with in-plane $\langle 100 \rangle$ orientation and their growth gives rise to a discontinuous change of magnetization. This is followed by a continuous rotation from the $\langle 110 \rangle$ to the $\langle 100 \rangle$ directions detected in the remaining area under observation.

We consider a possible explanation based on the magnetocrystalline anisotropy. In a single domain crystal with cubic magnetocrystalline anisotropy the evolution of the easy axes upon a change of K_1 depends on the sign of K_2. If K_1 goes from negative values to positive and K_2 remains positive, two consecutive transitions are expected: a discontinuous one between $\langle 111 \rangle$ and $\langle 110 \rangle$ easy axes, followed by a continuous one from $\langle 110 \rangle$ to $\langle 100 \rangle$ ones. Instead, if $K_2 < 0$, no intermediate transition to [110] easy axes is expected, and a single discontinuous transition from $\langle 111 \rangle$ to $\langle 100 \rangle$ should be observed [39, 59].

So far the sign of K_2 in magnetite through the spin-reorientation transition has not been unequivocally determined. Aragon et al. [60] indicated that it was negative (with a thermal dependence similar to K_1), but remarked that the uncertainties were at least an order of magnitude larger than for K_1. Instead Belov [61] cites a positive value attributed to Bickford. If the last case was taking place, two transitions could be expected, one discontinuous, and another continuous. Otherwise, only a single discontinuous transition should be observed. That we observe a two step transition is in line with a positive value of K_2 through the spin-reorientation transition. However we do not see the expected reorientatons for $K_2 > 0$. Instead we observed the initial nucleation of in-plane $\langle 100 \rangle$ surface domains, and then a smooth evolution from in-plane $\langle 110 \rangle$ to in-plane $\langle 100 \rangle$ ones. There may be different explanations. First, this is not a single domain situation and the surface of an approximately semi-infinite crystal is not comparable with the bulk. In the surface region, even at room temperature, the shape anisotropy dominates the magnetocrystalline one as shown by the observation of in-plane $\langle 110 \rangle$ easy axes instead of the bulk $\langle 111 \rangle$ expected ones. This influence of the shape anisotropy is more extreme closer to the spin-reorientation transition, where the magnetocrystalline anisotropy constant, K_1, is near zero. At this complicated scenario, further work will be needed to understand the observed two stage evolution of the magnetic domains in more detail.

3.5 Spin and orbital magnetic moments

The spin and orbital magnetic moments of Fe_3O_4 have not yet been unequivocally determined (see Table 3.1). The reported values span from zero to giant orbital magnetic moments and from integer to non integer spin magnetic moments. In addition, there are no detailed studies on the role played by the reconstruction in $Fe_3O_4(001)$ on the spin and orbital magnetic moments. In this section we try to address some information on this matter. We start from a clean surface that exhibits a $\sqrt{2} \times \sqrt{2}R45°$ reconstruction (see Fig. 3.9b). In this situation, the last four iron layers should be in a Fe^{3+} state. To confirm this point we perform XPS. The Fe $2p$ core level XPS spectrum shown in Figure 3.19 supports that the last iron layers are Fe^{3+} rich (compare with XPS spectrum of Figure 2.3a), as shown by the characteristic Fe^{3+} shake-up satellite at around 718 eV observed with an electron kinetic energy of $\simeq$ 100 eV. At this energy, the electron mean free path is expected to be in the sub-nanometer range (see Fig. 2.4) and thus, the measurement be representative of the topmost surface.

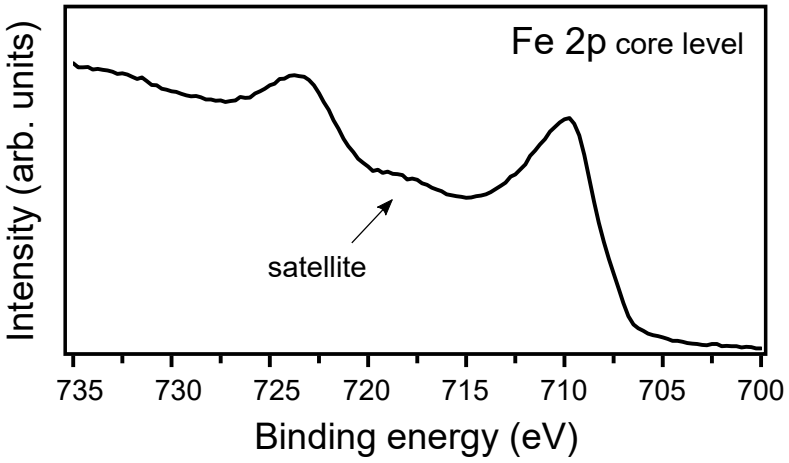

Figure 3.19: XPS spectra from the surface of the magnetite crystal acquired from a sequence of PEEM images.

We have determined by SPLEEM that the surface magnetic domains of magnetite

are in-plane. Thus, we measure the XMCD spectrum by means of PEEM following the process explained in 2.2.6. The kinetic energy of the detected secondary electrons determine the depth from which the information is sampled. In order to vary the probing depth we use first a low kinetic energy (about 2 eV, equivalent to the total electron yield measurements) and 50 eV. In the latter case, the electron mean free path should be quite small, as it is near the minimum of the universal mean free path curve (see Fig. 2.4). As mentioned in 2.2.6, although there is a reported work with a measured electron mean free path of 5 nm [62], Goering et al. have argued that a much lower value is appropriate, in the range of 0.8 nm, a value that has been confirmed by experiments in ultrathin films with an estimate of 1.3 nm [63]. In such case, both spectra would not be expected to differ much for the two kinetic energies, and thus be expected to provide a high sensitivity to the near surface structure of the crystal.

The results are shown in Figure 3.20. We calculate the orbital and spin magnetic moments by applying the sum rules and following the process explained in 2.2.6. The number of holes (= 13.5) has been taken from the literature [32]. The magnetic spin and orbital moment obtained are, respectively 2.61 and 0.30 μ_B (i.e. a total moment of 2.91 μ_B and a ratio of 0.11) when measured with an electron kinetic energy of 2 eV and 3.03 and 0.45 μ_B for the spin and orbital par when measured using electrons with a kinetic energy of 50 eV, i.e. (i.e. a total moment of 3.48 μ_B and a ratio of 0.13). In all cases we obtain a significantly reduced spin moment when compared with the expected value for bulk magnetite, 4.07 μ_B and significant orbital magnetic moments (0.3–0.4 μ_B).

We may consider self-absorption effects to be the reason for the reduced spin moments. But in our case, the electron sampling depth is below 1 nm, and the estimated effective X-ray absorption length are 7 nm and 18 nm at the L_3 and the L_2 absorption edges respectively [32]. Thus, if they have an effect in our measurements it should be small.

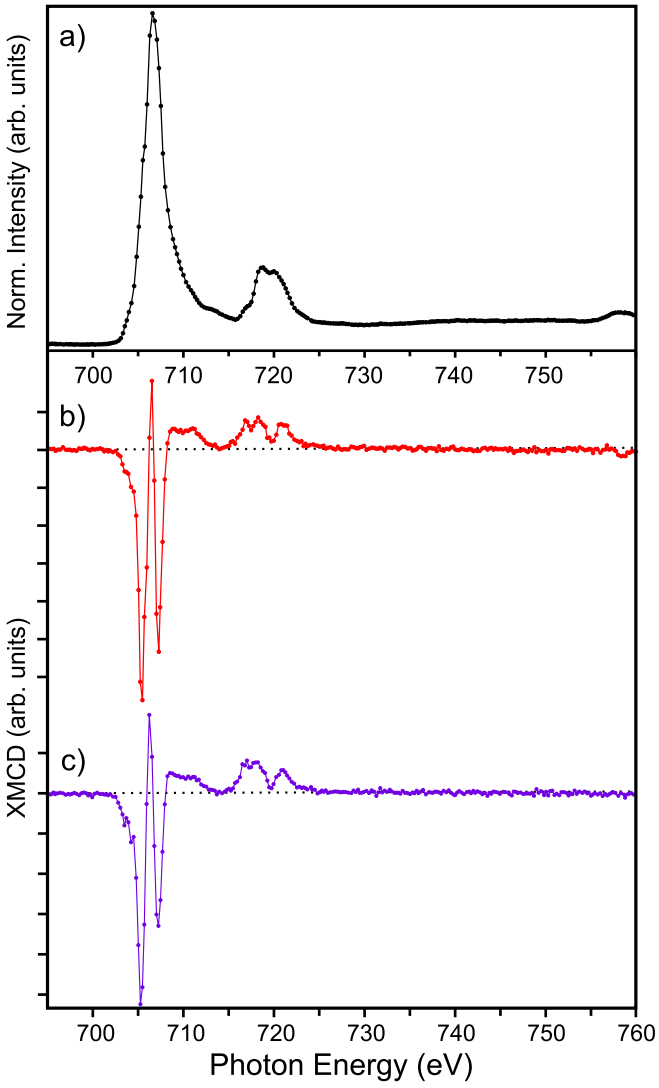

Figure 3.20: a) Averaged XAS spectra, from individual spectra measured with positive and negative helicity. XMCD spectra acquired from sequences of images detecting electrons with two different kinetic energies, b) with low kinetic energy (∼2 eV) and c) 50 eV.

Another possible explanation resides in the reconstruction itself. The reconstructed surface of $Fe_3O_4(001)$ can be considered as an intermediate state between magnetite and maghemite. Maghemite exhibits the same spinel structure of magnetite but while magnetite contains $Fe^{2+/3+}$, maghemite is composed only by Fe^{3+}. The charge balance is obtained by the inclusion of vacancies at octahedral sites. The formula unit could be written with the spinel formula: $(Fe^{3+})_A[Fe^{3+}_{\frac{5}{3}}\square_{\frac{1}{3}}]_BO_4$ where $\square$ represents the atomic vacancies. The antiferromagnetic coupling between the two iron sublattices results in a net magnetic moment of: $[5/3 \cdot 5\ \mu_B] + (-5\ \mu_B) = 3.33\ \mu_B$ per $\gamma-Fe_2O_3$ formula unit.

So it is clear that the reconstructed termination should reduce the magnetic moment of the magnetite surface. Since the XMCD experiment probes mostly the near surface layers affected by the reconstruction it is proposed that the origin of the reduced magnetic moment measured in a carefully characterized reconstructed surface of magnetite lies in the reconstruction itself. This argument follows the conclusions of Goering et al. [37] where it was suggested that the particular stoichiometry could have a large effect on the

Regarding the orbital component, we obtain between 0.3 and 0.4 μ_B. The counting scheme used to suggest the role of the surface in the spin magnetic moment does not give any information about the origin of the orbital moment, specially as the reconstruction is composed of Fe^{3+}-like cations which should, in principle, present no orbital moment. Calculations reported in Ref. [37] by Goering et al. points to sizable orbital magnetic moments at both octahedral and tetrahedral lattices that compensate due to the antiferromagnetic alignment of both lattices but only if the sample is perfectly stoichiometric. Such compensation should not occur in the reconstructed surface with a different ratio of cations in the two sublattices leading to significant orbital magnetic moments.

3.6 Conclusions

The surface of $Fe_3O_4(001)$ has been observed by a combination of LEEM, LEED, SPLEEM and XMCD. The asymmetry images taken by SPLEEM at room temperature reveal magnetic domains with easy axes along <110> directions that correspond to the projection of the <111> bulk easy axes onto the (001) surface. No out of plane magnetization was detected which indicates that in the near surface region the shape anisotropy should be larger than the magnetocrystalline anisotropy.

The evolution of the surface magnetic domains with increasing temperature has been followed. Starting from the initial magnetic domain configuration at room temperature, increasing the temperature from 300 to 700 K results in losing all the detailed microstruc-

tures within the domains giving rise to large domains with uniform magnetization. The domain walls also transform from curved to straight domain walls. From 700 K to the Curie temperature only a gradual decrease of the magnetic contrast is observed with some motion of the domain walls. Surprisingly, the behavior turned to be reversible. After cooling down, the room temperature domain pattern configuration was in great part recovered. The dependence of the first order magnetocrystalline anisotropy constant with the temperature is suggested to be responsible for the observed changes. We performed an additional test taking advantage of the temperature dependence of K_1 that exhibits a similar trend between 300–700K than for 300–T_{srt}. The observed magnetic domain changes turned to be equivalent for both temperature ranges supporting the assumption that the magnetocrystalline anisotropy might be behind the magnetic domain changes as a function of the temperature.

At T_{srt} the easy axis directions switch from the in-plane $\langle 110 \rangle$ directions at room temperature to the in-plane $\langle 100 \rangle$ directions below the spin-reorientation transition and then to the local monoclinic c-axis in the below-Verwey phase. No significant change in the spin-dependent electron reflectivity was detected trough either transition, indicating that there is no change in the surface magnetization. Through the spin-reorientation transition, we observe a multistage process. While initially the growth of new domains oriented along the $\langle 100 \rangle$ directions is observed, at a later stage the remaining areas appear to change orientation. The continuity or discontinuity of the spin reorientation transition depends on the sign of the second order magnetocrystalline anisotropy, K_2, upon the change of K_1. However the sign of K_2 has not been fully determined yet and although the two stage process would point to a positive sign of K_2 further work will be needed to understand the two stage reorientation of the magnetic domains.

To complete the magnetic characterization of the $Fe_3O_4(001)$ surface, the spin and orbital magnetic moments have been determined by means of XMCD. A reduced spin magnetic moment of 2.61–3.03 μ_B compared with the bulk value and an orbital magnetic moment of 0.3–0.45 μ_B were measured. Since the XMCD probes mostly the near

surface layers it is suggested that the reduced spin magnetic moments arise from the reconstructed surface. In addition, the sizable orbital magnetic moments is explained based on the unbalance of Fe cations at octahedral and tetrahedral lattices that can give rise to an uncompensated orbital moment.

Bibliography

[1] M. Blackman. The lodestone: A survey of the history and the physics. *Contemporary Physics*, 24(4):319–331, 1983.

[2] R. M. Cornell and U. Schwertmann. *The Iron Oxides: Structure, Properties, Reactions, Occurrences and Uses*. VCH, Weinheim, 1997.

[3] A. M. Atta, G. A. El-Mahdy, H. A. Al-Lohedan, and S. A. Al-Hussain. Synthesis of Environmentally Friendly Highly Dispersed Magnetite Nanoparticles Based on Rosin Cationic Surfactants as Thin Film Coatings of Steel. *International Journal of Molecular Sciences*, 15:6974–6989, 2014.

[4] P. Benda and A. Kalendová. Anticorrosion Properties of Pigments based on Ferrite Coated Zinc Particles. *Physics Procedia*, 44:185 – 194, 2013.

[5] A. R. Mahdavian and M. A.-S. Mirrahimi. Efficient separation of heavy metal cations by anchoring polyacrylic acid on superparamagnetic magnetite nanoparticles through surface modification. *Chemical Engineering Journal*, 159(1-3):264–271, 2010.

[6] C. Basualto, J. Gaete, L. Molina, F. Valenzuela, C. Yañez, and J. F. Marco. Lanthanide sorbent based on magnetite nanoparticles functionalized with organophosphorus extractants. *Science and Technology of Advanced Materials*, 16:035010, 2015.

[7] F. Dilnawaz, A. Singh, C. Mohanty, and S. K. Sahoo. Dual drug loaded super-

paramagnetic iron oxide nanoparticles for targeted cancer therapy. *Biomaterials*, 31(13):3694–3706, 2010.

[8] G. Hu and Y. Suzuki. Negative Spin Polarization of Fe_3O_4 in Magnetite/Manganite-Based Junctions. *Physical Review Letters*, 89:276601, 2002.

[9] X. W. Li, A. Gupta, G. Xiao, W. Qian, and V. P. Dravid. Fabrication and properties of heteroepitaxial magnetite (Fe_3O_4) tunnel junctions. *Applied Physics Letters*, 73(22):3282–3284, 1998.

[10] A. M. Bataille, J.-B. Moussy, F. Paumier, S. Gota, M.-J. Guittet, M. Gautier-Soyer, P. Warin, P. Bayle-Guillemaud, P. Seneor, K. Bouzehouane, and F. Petroff. Crystalline γ-Al_2O_3 barrier for magnetite-based magnetic tunnel junctions. *Applied Physics Letters*, 86(1):012509, 2005.

[11] Z. Zhang and S. Satpathy. Electron states, magnetism, and the Verwey transition in magnetite. *Physical Review B*, 44:13319–13331, 1991.

[12] H.-J. Kim, J.-H. Park, and E. Vescovo. Fe_3O_4(111)/Fe(110) magnetic bilayer: Electronic and magnetic properties at the surface and interface. *Physical Review B*, 61:15288–15293, 2000.

[13] Y. S. Dedkov, U. Rüdiger, and G. Güntherodt. Evidence for the half-metallic ferromagnetic state of Fe_3O_4 by spin-resolved photoelectron spectroscopy. *Physical Review B*, 65:064417, 2002.

[14] D. J. Huang, C. F. Chang, J. Chen, L. H. Tjeng, A. D. Rata, W. P. Wu, S. C. Chung, H. J. Lin, T. Hibma, and C. T. Chen. Spin-resolved photoemission studies of epitaxial Fe_3O_4(100) thin films. *Journal of Magnetism and Magnetic Materials*, 239(1-3):261–265, 2002.

[15] P. J. van der Zaag, P. J. H. Bloemen, J. M. Gaines, R. M. Wolf, P. A. A. van der Heijden, R. J. M. van de Veerdonk, and W. J. M. de Jonge. On the construction of

an Fe_3O_4-based all-oxide spin valve. *Journal of Magnetism and Magnetic Materials*, 211(1-3):301–308, 2000.

[16] P. J. H. Bloemen, P. A. A. van der heijden, R. M. Wolf, J. A. de Stegge, J. T. Kohlhepp, A. Reinders, R. M. Jungblut, P. J. van der Zaag, and W. J. M. de Jonge. Magnetic and Structural Properties of MBE-grown Oxidic Multilayers. *MRS Proceedings*, 401, 1995.

[17] S. S. P. Parkin, R. Sigsbee, R. Felici, and G. P. Felcher. Observation of magnetic dead layers at the surface of iron oxide films. *Applied Physics Letters*, 48(9):604–606, 1986.

[18] W. Eerenstein. *Spin-dependent transport across anti-phase boundaries in magnetite films*. PhD thesis, Laboratory of Physical Chemistry/University of Groningen, Netherlands, 2003.

[19] M. Alexe, M. Ziese, D. Hesse, P. Esquinazi, K. Yamauchi, T. Fukushima, S. Picozzi, and U. Gösele. Ferroelectric Switching in Multiferroic Magnetite (Fe_3O_4) Thin Films. *Advanced Materials*, 21(44):4452–4455, 2009.

[20] V. H. Babu, R. K. Govind, K.-M. Schindler, M. Welke, and R. Denecke. Epitaxial growth and magnetic properties of ultrathin iron oxide films on $BaTiO_3(001)$. *Journal of Applied Physics*, 114(11):113901, 2013.

[21] C. A. F. Vaz, J. Hoffman, A.-B. Posadas, and C. H. Ahn. Magnetic anisotropy modulation of magnetite in $Fe_3O_4/BaTiO_3(100)$ epitaxial structures. *Applied Physics Letters*, 94(2):022504, 2009.

[22] J. B. Hudson. *Surface Science*. Architectural Press, 1992.

[23] R. Pentcheva, F. Wendler, H. L. Meyerheim, W. Moritz, N. Jedrecy, and M. Scheffler. Jahn-Teller Stabilization of a "Polar" Metal Oxide Surface: $Fe_3O_4(001)$. *Physical Review Letters*, 94:126101, 2005.

[24] R. Wiesendanger, I. V Shvets, D. Bürgler, G. Tarrach, H. J Güntherodt, J. M. D Coey, and S. Gräser. Topographic and Magnetic-Sensitive Scanning Tunneling Microscope Study of Magnetite. *Science*, 255(5044):583–586, 1992.

[25] B. Stanka, W. Hebenstreit, U. Diebold, and S. A. Chambers. Surface reconstruction of Fe_3O_4(001). *Surface Science*, 448(1):49 – 63, 2000.

[26] R. Bliem, E. McDermott, P. Ferstl, M. Setvin, O. Gamba, J. Pavelec, M. A. Schneider, M. Schmid, U. Diebold, P. Blaha, L. Hammer, and G. S. Parkinson. Subsurface cation vacancy stabilization of the magnetite (001) surface. *Science*, 346(6214):1215–1218, 2014.

[27] S. A. Chambers and S. A. Joyce. Surface termination, composition and reconstruction of Fe_3O_4(001) and γ-Fe_2O_3(001). *Surface Science*, 420(2-3):111–122, 1999.

[28] E. J. W. Verwey. Electronic conduction of magnetite Fe_3O_4 and its transition point at low temperatures. *Nature*, 144:327–328, 1939.

[29] F. Walz. The Verwey transition - a topical review. *Journal of Physics: Condensed Matter*, 14(12):R285–R340, 2002.

[30] J. Stöhr and H. C. Siegmann. *Magnetism: From Fundamentals to Nanoscale Dynamics*. Springer, 2006.

[31] V. N. Antonov, B. N. Harmon, and A. N. Yaresko. Electronic structure and x-ray magnetic circular dichroism in Fe_3O_4 and Mn-, Co-, or Ni-substituted Fe_3O_4. *Physical Review B*, 67:024417, 2003.

[32] D. J. Huang, C. F. Chang, H. T. Jeng, G. Y. Guo, H. J. Lin, W. B. Wu, H. C. Ku, A. Fujimori, Y. Takahashi, and C. T. Chen. Spin and orbital magnetic moments of Fe_3O_4. *Physical Review Letters*, 93:077204, 2004.

[33] E. Goering, S. Gold, M. Lafkioti, and G. Schütz. Vanishing Fe 3d orbital moments in single-crystalline magnetite. *Europhysics Letters*, 73(1):97–103, 2006.

Bibliography

[34] E. Goering, M. Lafkioti, S. Gold, and G. Schuetz. Absorption spectroscopy and XMCD at the Verwey transition of Fe_3O_4. *Journal of Magnetism and Magnetic Materials*, 310(2):e249–e251, 2007.

[35] W. Q. Liu, Y. B. Xu, P. K. J. Wong, N. J. Maltby, S. P. Li, X. F. Wang, J. Du, B. You, J. Wu, P. Bencok, and R. Zhang. Spin and orbital moments of nanoscale Fe_3O_4 epitaxial thin film on MgO/GaAs(100). *Applied Physics Letters*, 104(14):142407, 2014.

[36] S. K. Arora, H. C. Wu, R. J. Choudhary, I. V. Shvets, O. N. Mryasov, H. Yao, and W. Y. Ching. Giant magnetic moment in epitaxial Fe_3O_4 thin films on MgO(100). *Physical Review B*, 77:134443, 2008.

[37] E. Goering. Large hidden orbital moments in magnetite. *Physica Status Solidi (b)*, 248(10):2345–2351, 2011.

[38] B. D. Cullity and C. D. Graham. *Introduction to Magnetic Materials*. John Wiley Sons, Inc., 2008.

[39] A. Hubert and R. Schäfer. *Magnetic domains: the analysis of magnetic microstructures*. Springer, 1998.

[40] C. Kittel. Physical Theory of Ferromagnetic Domains. *Reviews of Modern Physics*, 21:541–583, 1949.

[41] A. R. Muxworthy and E. McClelland. Review of the low-temperature magnetic properties of magnetite from a rock magnetic perspective. *Geophysical Journal International*, 140(1):101–114, 2000.

[42] R Řezníček, V Chlan, H Štěpánková, P Novák, and M Maryško. Magnetocrystalline anisotropy of magnetite. *Journal of Physics: Condensed Matter*, 24(5):055501, 2012.

[43] B. M. Moskowitz. High-temperature magnetostriction of magnetite and titanomagnetites. *Journal of Geophysical Research: Solid Earth*, 98(B1):359–371, 1993.

[44] C. A. Domenicali. Magnetic and Electric Properties of Natural and Synthetic Single Crystals of Magnetite. *Physical Review*, 78:458–467, 1950.

[45] Ö. Özdemir, S. Xu, and D. J. Dunlop. Closure domains in magnetite. *Journal of Geophysical Research*, 100(B2):2193, 1995.

[46] A. Ambatiello, K. Fabian, and V. Hoffmann. Magnetic domain structure of multidomain magnetite as a function of temperature: observation by Kerr microscopy. *Physics of the Earth and Planetary Interiors*, 112(1-2):55–80, 1999.

[47] P. K. Ingo. *Magnetic Proximity Effects in Highly-ordered Transition Metal Oxide Heterosystems studied by Soft X-Ray Photoemission Electron Microscopy.* PhD thesis, Duisburg-Essen, 2008.

[48] T. Kasama, N. S. Church, J. M. Feinberg, R. E. Dunin-Borkowski, and R. J. Harrison. Direct observation of ferrimagnetic/ferroelastic domain interactions in magnetite below the Verwey transition. *Earth and Planetary Science Letters*, 297(1-2):10–17, 2010.

[49] T. Kasama, R. J. Harrison, N. S. Church, M. Nagao, J. M. Feinberg, and R. E. Dunin-Borkowski. Ferrimagnetic/ferroelastic domain interactions in magnetite below the Verwey transition. Part I: electron holography and lorentz microscopy. *Phase Transitions*, 86(1):67–87, 2013.

[50] F. Heider, S. L. Halgedahl, and D. J. Dunlop. Temperature dependence of magnetic domains in magnetite crystals. *Geophys. Res. Lett.*, 15(5):499–502, 1988.

[51] S. Nie, E. Starodub, M. Monti, D. A. Siegel, L. Vergara, F. El Gabaly, N. C. Bartelt, J. de la Figuera, and K. F. McCarty. Insight into Magnetite's Redox Catalysis from Observing Surface Morphology during Oxidation. *Journal of the American Chemical Society*, 135(27):10091–10098, 2013.

[52] J. de la Figuera, L. Vergara, A. T. N'Diaye, A. Quesada, and A. K. Schmid. Mi-

cromagnetism in (001) magnetite by spin-polarized low-energy electron microscopy. *Ultramicroscopy*, 130:77–81, 2013.

[53] Y. Z. Chen, J. R. Sun, Y. N. Han, X. Y. Xie, J. Shen, C. B. Rong, S. L. He, and B. G. Shen. Microstructure and magnetic properties of strained Fe_3O_4 films. *Journal of Applied Physics*, 103:07D703, 2008.

[54] J. Cheng, G. E. Sterbinsky, and B. W. Wessels. Magnetic and magneto-optical properties of heteroepitaxial magnetite thin films. *Journal of Crystal Growth*, 310(16):3730 – 3734, 2008.

[55] K. Grzelakowski and E. Bauer. A flange-on type low energy electron microscope. *Review of Scientific Instruments*, 67(3):742–747, 1996.

[56] J. García and G. Subías. The Verwey transition-a new perspective. *Journal of Physics: Condensed Matter*, 16(7):R145–R178, 2004.

[57] J. de la Figuera, Z. Novotny, M. Setvin, T. Liu, Z. Mao, G. Chen, A. T. N'Diaye, M. Schmid, U. Diebold, A. K. Schmid, and G. S. Parkinson. Real-space imaging of the Verwey transition at the (100) surface of magnetite. *Physical Review B*, 88(16):161410, 2013.

[58] M. B. Yazdi, M. Major, A. Wildes, F. Wilhelm, A. Rogalev, W. Donner, and L. Alff. Possible evidence for a spin-state crossover in the Verwey state in Fe_3O_4 thin films. *Physical Review B*, 93(1):014439, 2016.

[59] K. P. Belov, A. K. Zvezdin, A. M. Kadomtseva, and R. Z. Levitin. Spin-reorientation transitions in rare-earth magnets. *Soviet Physics Uspekhi*, 19(7):574–596, 1976.

[60] R. Aragón. Cubic magnetic anisotropy of nonstoichiometric magnetite. *Physical Review B*, 46(9):5334–5338, 1992.

[61] K. P. Belov. Electronic processes in magnetite (or, "Enigmas of magnetite"). *Physics-Uspekhi*, 36(5):380–391, 1993.

[62] S. Gota, M. Gautier-Soyer, and M. Sacchi. Fe 2p absorption in magnetic oxides: Quantifying angular-dependent saturation effects. *Physical Review B*, 62(7):4187–4190, 2000.

[63] G. F. M. Gomes, T. E. P. Bueno, D. E. Parreiras, G. J. P. Abreu, A. de Siervo, J. C. Cezar, H.-D. Pfannes, and R. Paniago. Magnetic moment of Fe_3O_4 films with thicknesses near the unit-cell size. *Physical Review B*, 90(13):134422, 2014.

CHAPTER 4

Mixed Fe-Co monoxides on Ru(0001)

The results presented in this chapter have been published in:

- L. Martín-García, I. Bernal-Villamil, M. Oujja, E. Carrasco, R. Gargallo-Caballero, M. Castillejo, J. F. Marco, S. Gallego, and J. de la Figuera, *"Unconventional properties of nanometric FeO(111) films on Ru(0001): stoichiometry and surface structure"*, Journal of Materials Chemistry C **4**, 1850-1859 (2016).

- L. Martín-García, A. Quesada, L. Pérez, M. Foerster, L. Aballe, and J. de la Figuera, *"Initial stages of the growth of mixed iron-cobalt oxides on Ru(0001)"*, Physics Procedia **85**, 12-19 (2016).

4.1 Introduction

The oxides of divalent Co and Fe, have many similarities. They both present the rocksalt structure (see Figure 4.1) with very similar lattice spacings $\sim$ 4.3 Å [1, 2] although this value depends on the vacancies content. The rock salt structure can be explained on the basis of the spinel structure considering the fcc oxygen lattice where the tetrahedral sites are now empty and the divalent cations occupy all the available octahedral sites. Along the [111] direction layers of Fe^{2+}/Co^{2+} cations and O^{2-} anions alternate. At the (111) plane they present an hexagonal unit cell with an in-plane lattice spacing of $\sim$ 3.04 Å. They are both insulators and below the Néel temperatures of 290 and 200 K for CoO and FeO, respectively, they are antiferromagnetic with adjacent ferromagnetic (111) cation planes coupled antiferromagnetically.

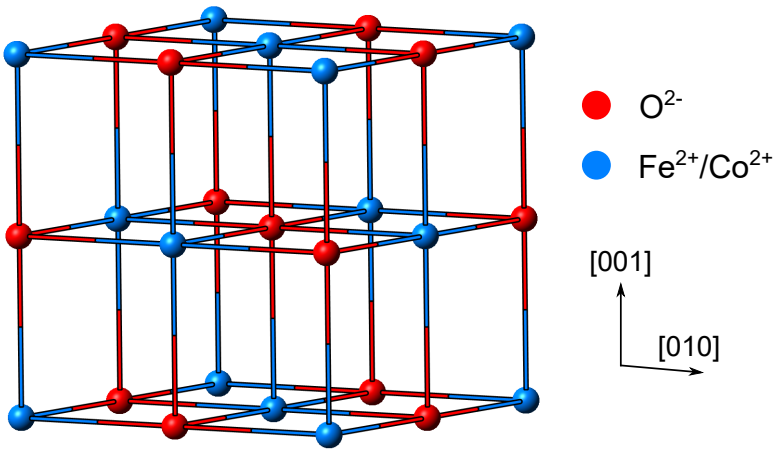

Figure 4.1: Schematic representation of the rock salt structure of FeO and CoO.

In addition, they can present a deviation from the ideal stoichiometry. FeO usually presents a large number of iron vacancies, in the range of 5-15% [3] while the deviation in CoO is smaller, up to 1% [4]. In the case of FeO, the structural and physical properties as for example, lattice expansions, resistivity and magnetic properties, depend on the

Fe vacancies [1]. Actually, these defects are found to be ordered in clusters containing Fe^{3+} that might be related to the evolution of FeO to magnetite [1].

4.1.1 FeO thin films

FeO films of subnanometric thickness have received large attention in recent years due to their catalytic activity. Monolayer thick FeO(111) films grown on Pt(111) have been shown to promote low temperature CO oxidation into CO_2 [5] and water splitting reactions [6]. The antiferromagnetic order of FeO is also exploited for exchange-bias in core/shell FeO/Fe_3O_4 nanoparticles [7]. In this case, the presence of Fe vacancies and the related appearance of Fe^{3+} cations is a disadvantage as it may alter the AFM state of the FeO and deteriorate the exchange bias coupling between FeO and Fe_3O_4.

FeO ultrathin films are usually grown by MBE where first a layer of Fe is deposited at the surface followed by its oxidation at $\sim$ 900 K in an oxygen atmosphere. This process can be repeated until the desired film thickness is achieved [8]. Ultrathin FeO films can also be grown by continuous iron metal deposition under an oxygen background, i.e. O-MBE [9]. Films one and two monolayers thick can be grown even in thermodynamic conditions where other iron oxides, usually magnetite, should appear, for example, up to 2 atomic layers on Pt(111) [10], or up to 4 layers on Ru(0001) [11]. Even the growth of the stable iron oxide forms on different substrates takes place through the initial formation of FeO(111) layers (followed by Fe_3O_4/γ-Fe_2O_3) [12]. The iron oxide growth proceeds by a Stranski-Krastanov mode: a wetting layer with monoxide composition covering the surface is followed by the growth of three dimensional islands of a more stable iron oxide. A common experimental feature for such films is the expansion of the in-plane lattice parameter with respect to the bulk value, typically 0.320 nm versus 0.304 nm [11, 13]. This has been related to a minimization of the surface energy to avoid the divergence of the surface potential. The (111) surface termination exposes either only oxygen or iron atoms, which means that it presents a polar surface termination. The dependence

of the surface potential of a polar film with thickness z is of the form: V(z) $\propto \sigma z$ where σ is the charge density. Thus, an in-plane lattice expansion reduces the perpendicular distance and consequently the surface potential of the film [11, 14].

Previous efforts to synthesize thicker FeO films have resulted in samples with poor crystalline quality [15] or Fe^{3+} sites that evidence the presence of defects [16]. Typically, a (2×2) surface symmetry is obtained, indicative of structural or magnetic disorder, or a initial stage in the evolution to magnetite [17, 18]. Even in ultra high vacuum with a careful control of the preparation conditions, such as the oxygen partial pressure or the iron deposition rate, it is very difficult to produce it without the coexistence of Fe_3O_4 [8]. Even so, Spiridis et al. in Ref.[12] achieved to grow FeO films up to 4 nm thick by a careful optimization of the oxidation conditions. However, thicker films oxidize to magnetite when using such growth method.

Although the growth of thick FeO films seems to be not possible using MBE, alternative methods such as the use of PLD have not been tested yet. This technique is widely used for growing films of a variety of materials with different properties that can be tuned by varying the laser and growth parameters. In PLD, the growth conditions are out of equilibrium, with a large energy per atom deposited on the surface [19] that can lead to different results than those obtained by MBE. Although in our case we employ an infrared (IR) wavelength, the use of an ultraviolet (UV) wavelength is a common choice for PLD of oxides. The reported benefits include surface uniformity and the avoidance of target particulate ejection. However, the use of an IR wavelength of 1064 nm to grow magnetite thin film layers on several substrates [20, 21] led to an improved film crystalline quality over the results obtained with an UV wavelength. It was observed that while the use of an UV wavelength resulted in more uniform films than when using an IR wavelength, the shape of the grains in the former case were less defined than in the last case, where the grains were larger and with well developed facets, resulting in a better crystallinity [20].

4.1.2 CoO thin films

As in the case of FeO, CoO has also found applications in different fields. For example, the catalytic activity of CoO_x has been intensively studied in the water splitting reaction. In a water splitting system, the oxygen and hydrogen are generated in the anode and cathode respectively. The efficiency of this reaction is limited by the large overpotential of the oxygen evolution reaction (OER) at the anode and intensive effort has been devoted to find efficient OER catalysts [22]. In this sense, CoO_x thin films have been proposed as an alternative to the widely used RuO_2 and IrO_2 [23, 24]. CoOx has also been proposed as cathode for Li-air batteries as an alternative to the carbon-based cathodes that can suffer from decomposition [25, 26]. In the field of electronics, the resistance switching behaviour of CoO_x thin films has been studied for application in resistive random access memories (RRAM) [1] [27, 28]. In low dimensional exchange bias systems, the antiferromagnetism of CoO is used to avoid the appearance of the superparamagnetism in small Co clusters. [29, 30]. In addition, CoO has been used in spin valve systems as exchange bias layer [31, 32] showing an enhancement of the giant magnetoresistance effect in comparison with spin valves with FeMn exchange bias layers [31].

The CoO thin film growth has been less studied as compared to the FeO case and no reported works have been found of CoO on Ru(0001). The methods employed for CoO films growth are also based on the sequential deposition of cobalt metal and its subsequent oxidation [30, 33, 34] or on the reactive deposition of Co under an oxygen background [2, 35]. A reported work of CoO(111) multilayer growth on Pt(111) [33] shows an unexpected result: the films exhibit an anomalous wurtzite-tipe surface termination. It has been suggested that the Co and O atoms in the last layers are not in octahedral but in tetrahedral environment. This change in the stacking near the surface contributes to the energy compensation of the (111) polar surface [33]. The same

[1] A RRAM is composed of two electrodes separated by a switching layer that shows two different resistive states (high and low) depending on the applied voltage.

result was obtained for CoO(111) films grown on Ir(100) [35] where the wurtzite-like termination appears to induce also a metallic character to the surface.

A more comprehensive work using Ir(100) [2, 34–38] and Co/Ir(100) [2] as substrates shows that, depending on the experimental conditions, different cobalt oxides can be obtained: from Co_3O_4 under oxygen rich and low temperature conditions, to CoO at high temperatures. Also the orientation of the CoO films can be tuned from CoO(111) to CoO(100) depending on the substrate [2]. While in the case of FeO(111), films with thicknesses beyond two monolayers turn into a more stable iron oxide phase like Fe_3O_4, CoO(111) films appear to be stable regardless the thickness and reaching 13 nm in Ref.[36].

4.1.3 Mixed Fe-Co oxides

Oxides with mixed compositions of Fe and Co were also investigated in this chapter. Some of the catalytic applications explained above for the FeO and CoO case have been also investigated for mixed oxides containing Fe and Co. For example, ultrathin Fe-Co oxide nanosheets showed excellent catalytic activity for the oxygen evolution reaction (OER) in comparison with catalysts of single metal oxides [39]. Oxide films containing specific concentrations of Fe and Co and also Ni were used to study how metal composition affects the OER [40]. It was observed that Fe plays an important role in the stabilization of high oxidation levels of the film which translated into improved catalytic activities and the incorporation of Co and Ni lowered the overpotential at which the reaction started. The low temperature oxidation of CO over iron-cobalt mixed oxide nanocatalysts was also explored [41] where the catalytic results were drastically different depending on the Fe/Co ratio. In the cases above, amorphous mixed Fe-Co oxides with Fe and Co in high oxidation states [40] or with poor crystalline quality [39, 41] were reported. In this sense, the synthesis of mixed Fe-Co monoxides and their possible application on catalysis and other fields remain unexplored.

In principle, the similar lattice spacing, structure and chemical characteristics of CoO and FeO suggest that they could form mixtures. The Fe-Co-O phase diagram [42] confirms the existence of $Fe_xCo_{1-x}O$ in a wide range of experimental conditions, although for most of the composition range it coexists with the spinel phase. Wether it is possible to obtain a mixed Fe-Co monoxide phase or not is an issue that will be the subject of the present study.

In this chapter we will try to address the following questions:

- Is it possible to grow FeO thin films on Ru(0001) using IR-PLD? Do the obtained films exhibit different properties than those observed when using MBE? Is there a limit in the FeO film thickness achievable using PLD?

- The growth of ultrathin FeO films by MBE on metallic substrates is well known and characterized. As CoO and FeO present similarities, can the FeO/Ru(0001r) growth mode be extended to the case of CoO?

- Departing from the particular experimental conditions that lead to FeO and CoO phases, can a mixed Fe and Co monoxide phase be obtained if Fe and Co are dosed simultaneously? Does the growth proceed in the same way as the independent FeO and CoO growth?

4.2 Growth of FeO by PLD

A hematite (α-Fe_2O_3) pellet was used as target in the PLD process. Although α-Fe_2O_3 corresponds to the most thermodynamically stable iron oxide phase, volatile elements like oxygen are frequently lost during the ablation process [43, 44]. In our particular case, PLD in UHV environment does not allow to grow neither hematite thin films nor magnetite ones, unless 10^{-6} Torr oxygen is dosed during growth. Since the goal

was to fabricate FeO films, no oxygen was dosed into the preparation chamber during deposition. The target was ablated using a Q-switched Nd:YAG laser with a pulse duration of 5 ns and a repetition rate of 10 Hz with a 1064 nm excitation wavelength. The laser energy per unit area was fixed to 4.4 J/cm^{-2}. The target-substrate distance (d_{ts}), the deposition time and the temperature of the substrate were varied during the experiments in order to study the dependence of the film properties on these parameters.

Figure 4.2 shows the XPS spectrum of a FeO film grown on Ru(0001) at 873 K, with a deposition time of 5 min and a distance (d_{ts}) of 4 cm from the target. The XPS spectrum here and in the rest of this chapter were acquired using Al Kα radiation (hν = 1486.6 eV). They were recorded at an electron take-off angle of 90° (unless in the cases explicitly mentioned) with a constant analyzer pass energy of 20 eV. The spectra were fitted with pseudo Voigt line profiles and a Shirley background using the CasaXPS software [45]. The Lorentzian/Gaussian mixing ratio and FWHM of the different components were fixed along the series of spectra. The binding energies were referred to the Ru 3d$_{\frac{5}{2}}$ signal, which was set to 280.0 eV. The XPS spectrum of Figure 4.2 was fitted considering a photoemission spin-orbit doublet at 709.7 (Fe 2p$_{\frac{3}{2}}$) and 722.7 eV (Fe 2p$_{\frac{1}{2}}$) with a full width at half maximum (FWHM) of 3.7 eV. We added two additional components at binding energies of 712.7 eV and 725.4 eV to account for the broadening due to multiplet splitting [46, 47]. The XPS spectrum also presents prominent shake-up satellite structure, which was fitted with two peaks at 716.4 eV and 729.8 eV. The presence of these satellite peaks and the binding energy difference of nearly 6 eV with respect to the main photoemission lines are clear evidence of Fe^{2+} (compare the spectrum with that of FeO in Figure 2.3c).

The thickness and the stoichiometry of the film were estimated following the processes described in 2.2.2. Doing so, the film thickness resulted in $\sim$ 4.7 nm. Surprisingly, and in spite of the large thickness well beyond the bilayer limit, the composition of the film was estimated to be Fe_xO ($x = 0.99 \pm 0.03$) which corresponds to an iron deficiency of $\sim$1%. This means that the stoichiometry of the film is closer to the ideal value than

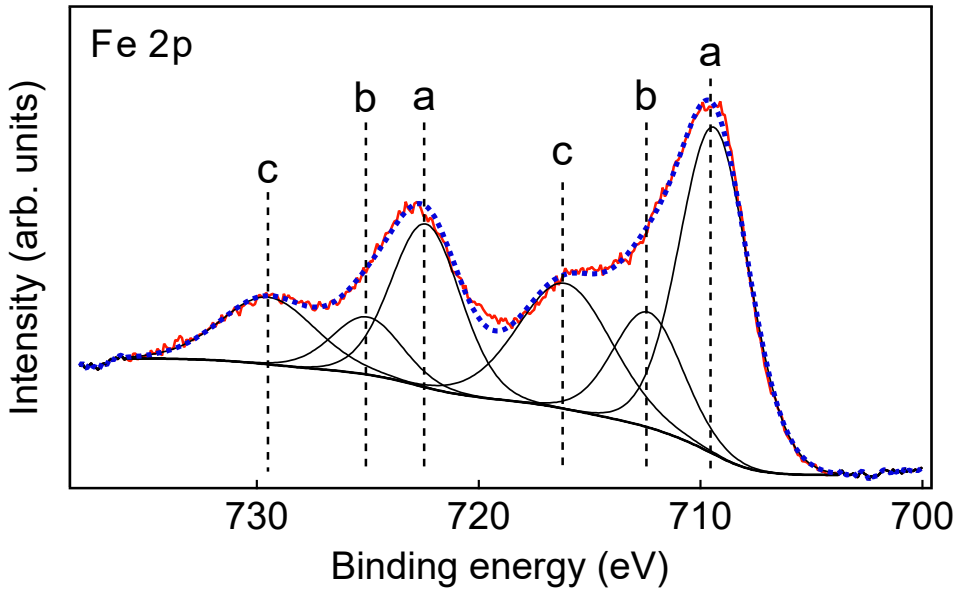

Figure 4.2: XPS Fe 2p core level spectrum of a 4.7 nm thick FeO film grown on Ru(0001) by IR-PLD at 873 K for 5 min at a d_{ts} of 4 cm. The experimental curve is represented by a red line while the fit is shown with a blue dashed line. The labeled peaks correspond to a: main photoemission peaks, b: peaks to account for multiplet splitting and c: shake-up satellites.

most bulk samples, which present iron deficiencies of 5-15%.

Low energy electron diffraction (LEED) patterns were acquired to provide information about the surface structure of the film. A typical LEED pattern, shown in Figure 4.3a, reveals a 1×1 hexagonal pattern. In addition, comparing the spacing of the first-order diffracted spots with those of the Ru substrate, they are found to correspond to a distance of 0.307 nm, i.e., slightly larger than the in-plane lattice spacing of perfectly stoichiometric bulk FeO (0.304 nm) [1].

To determine the surface termination of the grown films, ISS measurements were performed. The spectra were acquired using He^+ ions with energies of 525 eV. The angle of incidence[2] was varied by rotation of the sample manipulator and the collecting angle was normal to the surface. Figure 4.3b shows the ISS spectra of a film deposited

[2]The angle of incidence is defined by the angle of the ion beam with respect to the sample plane.

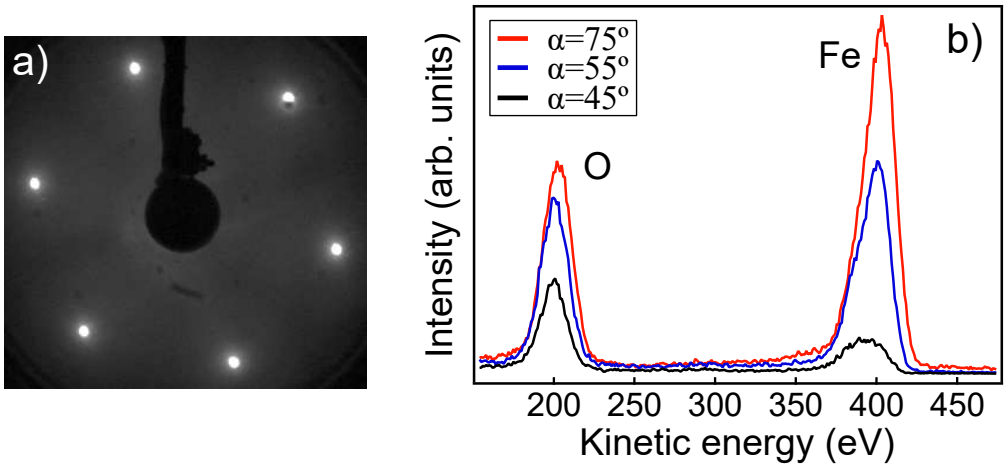

Figure 4.3: a) LEED of a 4.7 nm thick FeO film grown on Ru(0001) by IR-PLD at 873 K for 5 min at a d_{ts} of 4 cm. The electron energy is 50 eV. b) ISS spectra acquired at three different beam incidence angles: 75°, 55° and 45° from a FeO film deposited at 873 K, d_{ts} of 4 cm and 14 nm estimated thickness. A lower angular value is related to a higher grazing He^+ incidence and a higher surface sensitivity. The peak at 201.6 eV corresponds to oxygen and the peak at 403.6 eV to iron. The relative intensity of O to Fe increases at lower scattering angles, indicating an O-terminated surface.

at 873 K, d_{ts} of 4 cm and 14 nm estimated thickness. This value was extrapolated from the deposition time as at this thickness the Ru 3d core level peaks are not observable. Spectra were measured at different beam incidence angles. Two peaks are observed at 201.6 and 403.6 eV, where the former corresponds to O and the latter to Fe. Reducing the incidence angle, i.e. approaching more grazing incidence of the He^+ ions, the Fe contribution almost disappears whereas that of the O remains. This result strongly suggests that the FeO films are oxygen terminated.

Ex-situ AFM measurements were performed in order to obtain surface morphological information. The AFM image of a 4.7 nm thick FeO is shown in Figure 4.4. It displays a quite homogeneous film surface with a mean roughness of 0.6 ± 0.3 nm. LEED and XPS were performed after sample reintroduction into the UHV chamber to detect possible surface modifications. No LEED pattern was observed, and the Fe $2p_{\frac{3}{2}}$ and $2p_{\frac{1}{2}}$ photoemission peaks in the XPS spectrum shifted to higher binding energies, 710.7 and 723.8 eV, respectively (see Figure 4.5). This shift, together with the appearance of a new

satellite at 719.7 eV indicated the presence of Fe^{3+} (compare spectrum with the one from Figure 2.3b). The oxidation of the films under exposure to air evidences the requirement of an UHV environment in order to obtain reliable data on unaltered surfaces of FeO films.

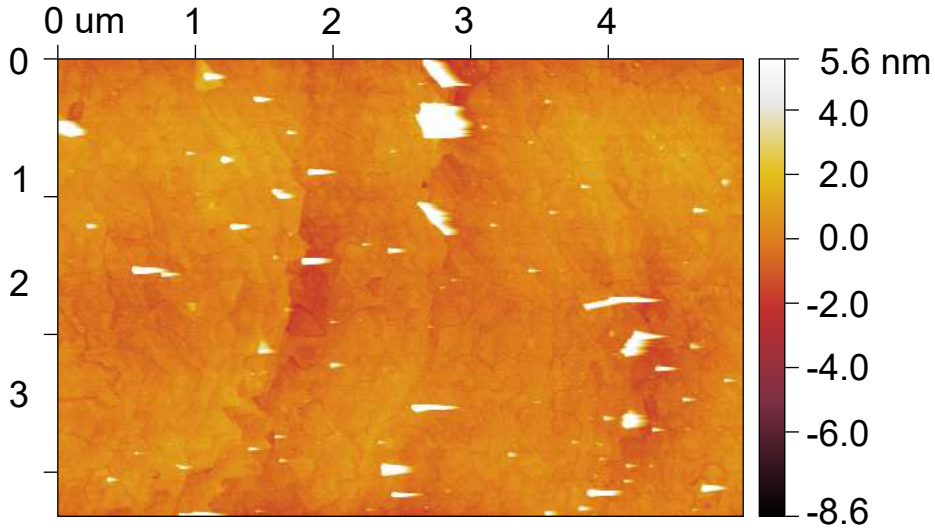

Figure 4.4: AFM image of a 4.7 nm thick FeO film grown on Ru(0001).

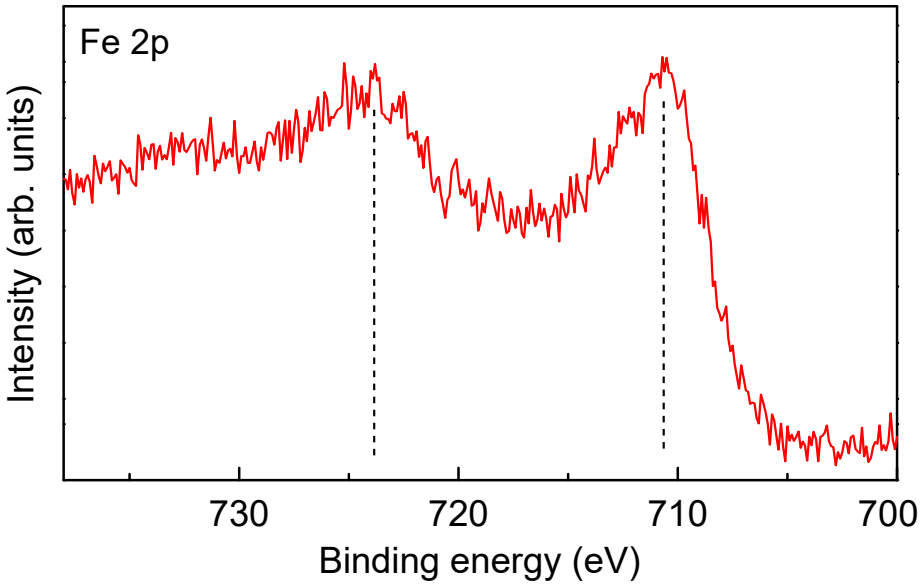

Figure 4.5: XPS Fe 2p core level spectrum of a 4.7 nm thick FeO film grown on Ru(0001) after exposure to air.

Influence of film thickness

The influence of the substrate-target distance on the growth of FeO films was next investigated. Figure 4.6 shows the Fe 2p core level XPS spectra recorded from films deposited at different target-substrate distances, while maintaining the rest of the growth parameters fixed. The films grown at the shortest distance, 2 cm, present the typical Fe 2p spectra of FeO as shown in Figure 4.2. At larger d_{ts} values a second spin-orbit doublet appears at lower binding energies, 706.7 eV (Fe $2p_{\frac{3}{2}}$) and 719.7 eV (Fe $2p_{\frac{1}{2}}$), respectively, which is consistent with the presence of metallic iron.

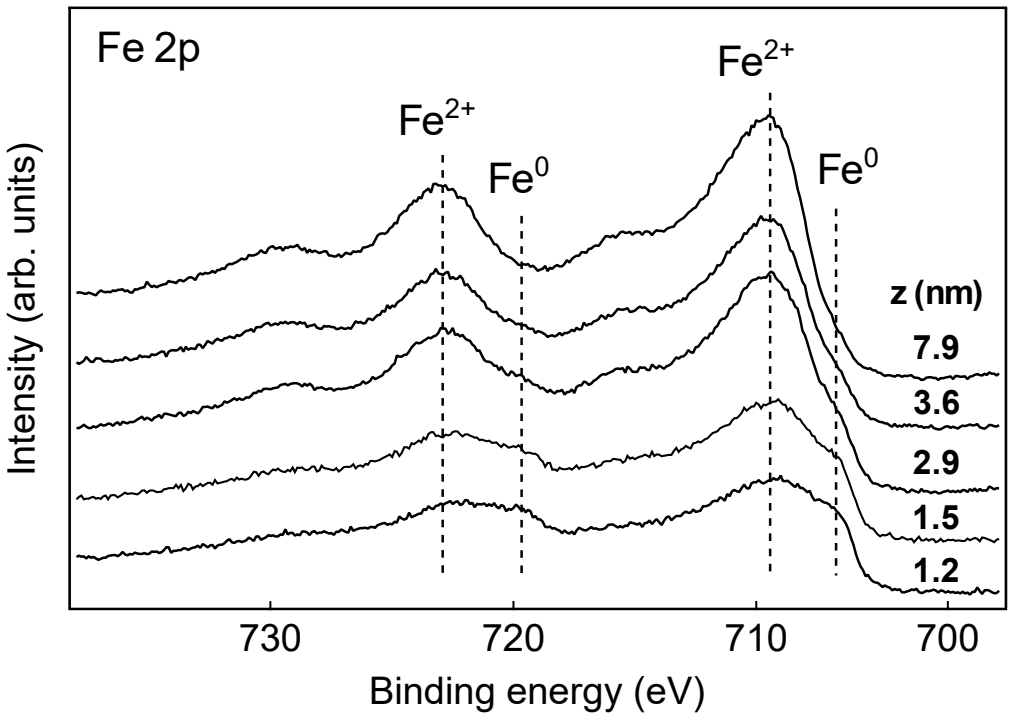

Figure 4.6: XPS Fe 2p core level spectra of different iron oxide films grown by IR-PLD at 873 K, with a deposition time of 6 min and film thicknesses (z) of: 7.9, 3.6, 2.9, 1.5 and 1.2 nm (from top to bottom). The corresponding d_{ts} are: 2, 3, 4, 5 and 6 cm, respectively.

Figure 4.7a shows the fitting of the XPS spectrum of a 1.2 nm thick film to a combination of FeO and metallic Fe. This analysis gives a ratio of 86% FeO to 14% Fe.

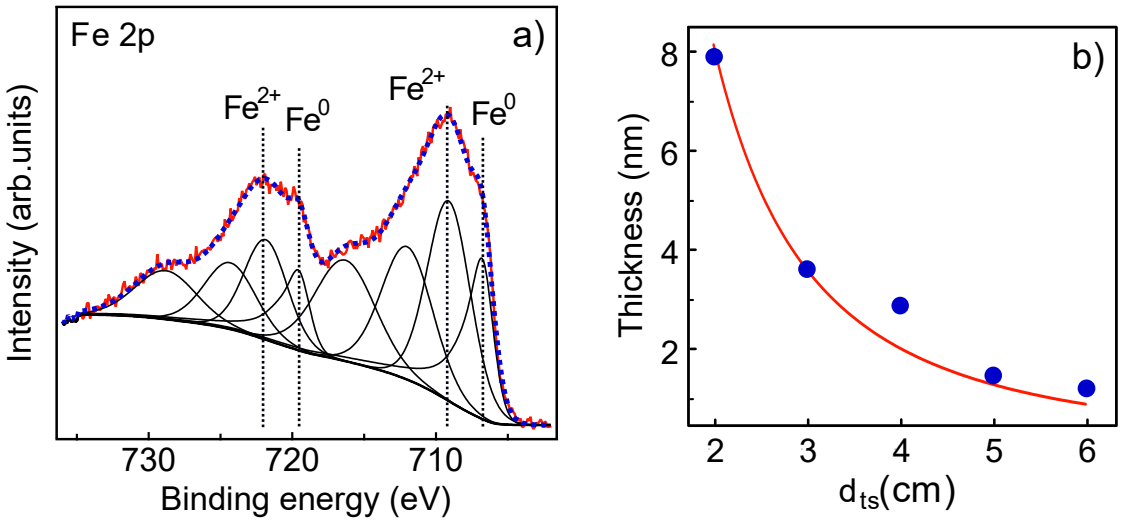

Figure 4.7: a) Fit of the Fe 2p core level spectrum of the 1.2 nm thick film ($d_{ts} = 6$ cm) displaying FeO and metallic Fe contributions. b) Variation of the thickness of the FeO films with d_{ts}. The experimental results are shown by circles while the fit to an inverse-square law is shown by a continuous line.

It can be observed in Figure 4.7b that the thickness of the films is strongly reduced if the substrate-target distance is increased at a fixed deposition time. The evolution of the thickness with d_{ts} is well described by an inverse-square law characteristic of a free plume expansion [48].

Figures 4.8a-e show the corresponding LEED patterns of the FeO films whose XPS spectra are displayed in Figure 4.6 from top to bottom. Figure 4.8f displays the LEED pattern of a 0.3 nm thick film prepared at 873K with a deposition time of 1 min and d_{ts} = 5cm. The LEED pattern of the thickest film (7.9 nm) (Figure 4.8a) displays a 1×1 hexagonal pattern like the pattern shown in Figure 4.3a. By decreasing the film thickness, additional spots start to appear around the first order spots (see Figures 4.8b-e). These LEED patterns are similar to those exhibited in ultrathin films grown by reactive-MBE [9] or sequential deposition and oxidation of iron [11]. In addition, these films present larger lattice parameters when the thickness is progressively diminished: from 0.307 nm for 4.7 nm thick films to 0.320 nm for subnanometric thicknesses. In fact, one and two atomic layers thick FeO films on Ru(0001) have a lattice spacing of

0.320 nm [9, 11]. These results can be interpreted as the same moiré pattern arising from the coincidence of six FeO units on seven Ru atoms. Thus, the LEED patterns show an evolution from those of FeO for the thickest film (shortest d_{ts}) to the moiré pattern of FeO/Ru for the thinner thicknesses. The LEED results are thus fully consistent with the evolution of FeO to mixed FeO/Fe detected by XPS.

This evolution in the composition of the films may be related either to the difference in distance from the substrate to the target or to the thickness of the film. To clarify this point, deposits have been grown at a fixed d_{ts} and different deposition times. The corresponding XPS spectra are shown in Figure 4.9, where two different d_{ts} values have been explored, changing the deposition times to obtain films with the same thickness. The inspection of the spectra reveals that the metallic iron component is related to the film thickness and not to d_{ts}. Equivalent XPS spectra are obtained at both d_{ts} while changes of the film thickness result in different film compositions. These results indicate that the Ru substrate at the given temperature induces the growth of metallic iron at the early stages of deposition. In a later stage, the growth of FeO takes place upon continuing deposition.

It also suggests that even thick films with a FeO surface composition might contain some metallic Fe at the film/substrate interface. However, this can not be determined as the probing depth of the XPS is below the thickness of the film and the interface Ru/FeO is not accessible. The previous experiments have been performed on a Ru substrate heated at 873 K. A relatively high substrate temperature can produce the evaporation of oxygen from the surface in PLD [49]. Given that Ru is considered an essentially inert substrate in high vacuum conditions and Fe wetting on Ru is favoured by substrate heating, we speculate that oxygen evaporation takes place with higher probability at the interface with the Ru substrate than later on, when the FeO film is growing.

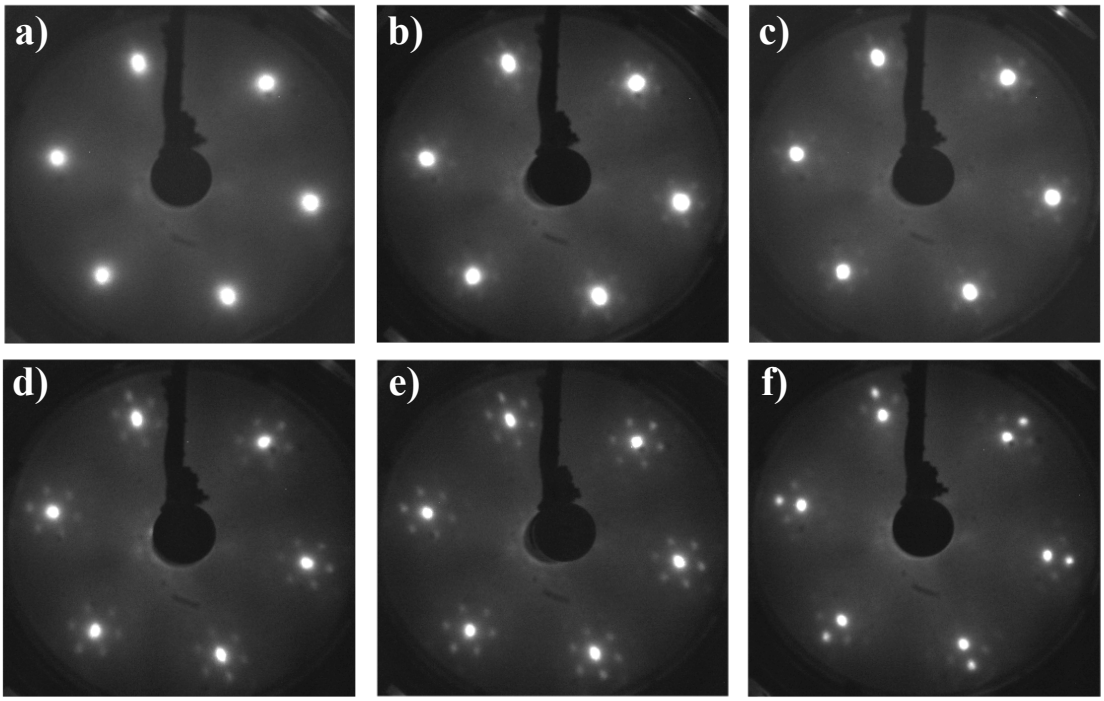

Figure 4.8: LEED patterns from films grown at 873 K, with a deposition time of 6 min and thicknesses of: 7.9, 3.6, 2.9, 1.5 and 1.2 nm from a) to e). The last pattern labelled as f) corresponds to a 0.3 nm thick film prepared at 873 K, with a deposition time of 1 min and $d_{ts} = 5$ cm.

Effect of substrate temperature

From the previous section it was clear that the temperature was playing a role in the film composition. Therefore, films grown at different substrate temperatures were next synthesized to study in more detail the effect of the temperature in the obtained films. Figure 4.10 shows the Fe 2p XPS core level spectra recorded from films grown at three different substrate temperatures. It is clear that the XPS spectrum of the films prepared at 300 K is different from the rest. Comparing it to the spectrum of FeO depicted in Figure 4.2, the main photoemission lines appear at slightly higher binding energies and the intensity of the characteristic Fe^{2+} shake-up satellites is also smaller. Together with an Fe/O ratio of 48/52 (i.e. a higher oxygen content), the results suggest that the deposited film can contain some Fe^{3+}.

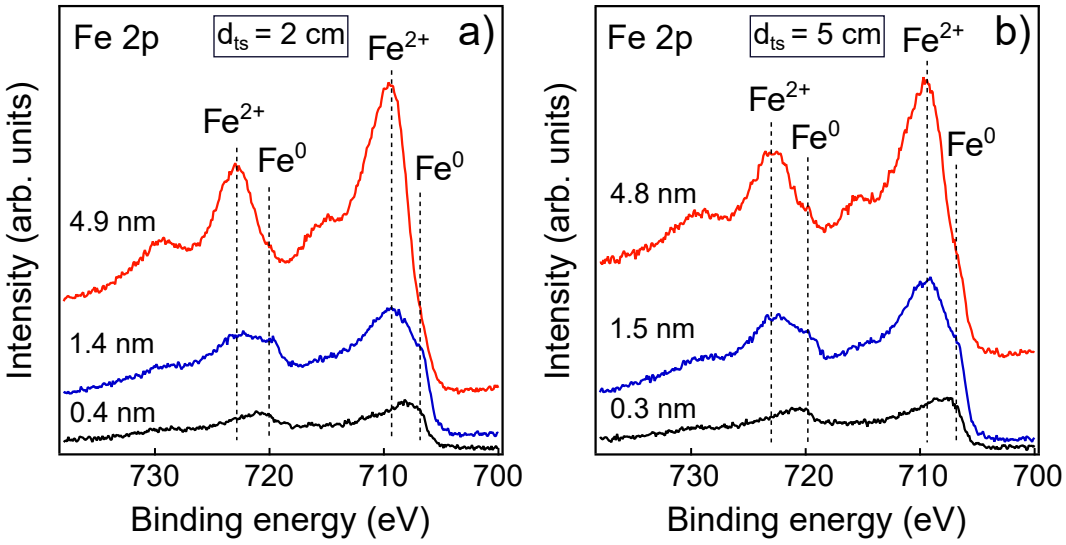

Figure 4.9: XPS Fe 2p core level spectra of different iron oxide films grown by IR-PLD at 873 K. a) $d_{ts} = 2$ cm. The deposition times from top to bottom are: 3 min, 1 min and 10 s. The corresponding film thicknesses are: 4.9, 1.4 and 0.4 nm, respectively. b) $d_{ts} = 5$ cm. The deposition times from top to bottom are: 30, 6 and 1 min. The related film thicknesses are: 4.8, 1.5 and 0.3 nm, respectively.

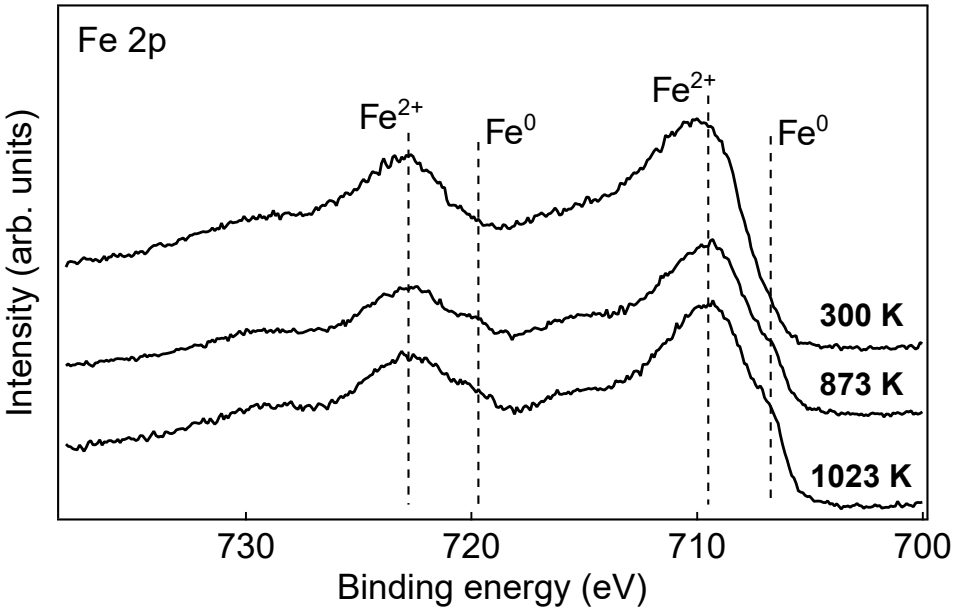

Figure 4.10: XPS Fe 2p core level spectra of different iron oxide films grown at the substrate temperatures of 300 K, 873 K and 1023 K. The corresponding film thicknesses are 3.1, 2.7 and 2.1 nm, respectively. In all cases, d_{ts} was fixed at 4 cm and the deposition lasted for 3 min.

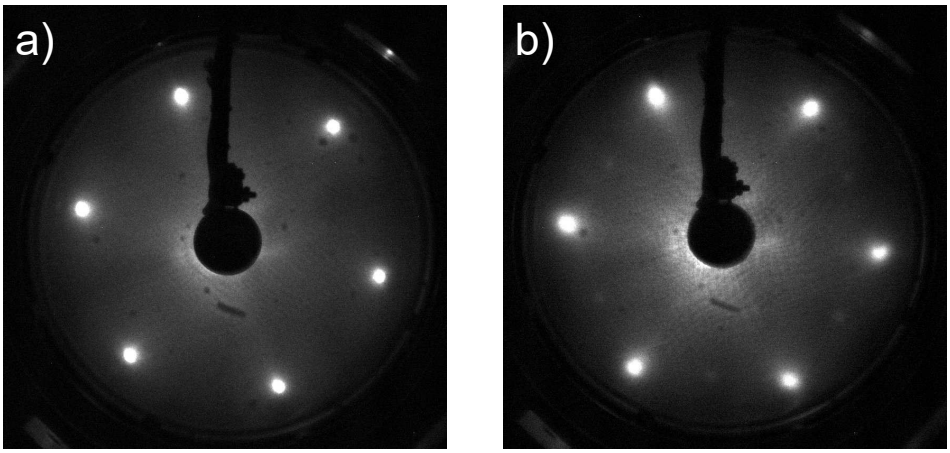

Figure 4.11: a) LEED of a 4.7 nm thick FeO film grown on Ru(0001) at 873 K for 5 min at a d_{ts} of 4 cm. The electron energy is 42 eV. b) LEED of a 4.7 nm thick FeO film grown on Ru(0001) at 300 K for 3 min at a d_{ts} of 4 cm after annealing in vacuum. The electron energy is 42 eV.

The as-grown film does not show a LEED pattern, evidencing a disordered surface. After subsequent annealing to 873 K in vacuum, the surface reflects a 2×2 LEED pattern with a reduced oxygen-oxygen lattice parameter of 0.302 nm, both suggesting a magnetite termination (see Figure 4.11b where the 1x1 LEED pattern from the 4.7 nm thick FeO film grown at 873 K is shown for comparison).

The films grown at 873 K and 1023 K both present XPS spectra characteristic of FeO plus an additional contribution at lower binding energies due to metallic iron, which increases from 3% at 873 K to 6% at 1023 K. They are both crystalline with a LEED displaying an hexagonal 1×1 pattern. In addition, these films are thinner than the one prepared at 300 K. This could be attributed in part to the formation of a more compact and ordered film as the temperature is increased.

Thus, by varying the temperature of the substrate, the surface composition of the sample (from a mixed Fe^{2+}/Fe^{3+} to only Fe^{2+}), the crystallinity (from a disordered surface to a monocrystalline one) and the surface structure of the films (from 2×2 to 1×1 surface termination) can be controlled. It can be concluded then that the properties

of films grown by PLD are highly dependent on the substrate temperature which governs the aggregation of ejected plume species on the heated surface.

Theoretical results

The results above showed that to grow FeO films with thicknesses beyond the bilayer limit is possible when using IR-PLD. The obtained films show some unexpected features like the lack of Fe^{3+} sites and a slightly expanded lattice parameter compared to bulk FeO. To clarify these points, first principle calculations based on the density functional theory calculations were performed by I. Bernal-Villamil and S. Gallego from the Instituto de Ciencia de Materiales de Madrid (CSIC).

The conditions of the calculations have been chosen departing from the optimized values determined for bulk FeO [50]. Octahedral coordination sites at the FeO thin films were first considered as these are the ones that exist in the rocksalt (RS) lattice of stoichiometric bulk FeO. However, the (1×1) symmetry admits the existence of stacking faults, similar to those observed at the O-ended CoO(111) surface apparently in connection to polarity compensation effects [35]. Then, the simulations also allowed for the existence of a tetrahedral coordination. In order to have an adequate bulk reference for the tetrahedral symmetry, bulk FeO has been modeled with the wurtzite (WZ) structure. The electronic properties obtained for the WZ FeO are similar to those of RS FeO: a wide gap insulator that orders antiferromagnetically with opposite spin orientations for Fe atoms at adjacent (0001) planes [51]. However, the RS structure results to be more stable than the WZ one by 104.5 meV/atom.

The FeO(111) films have been modelled by slabs of different thicknesses that contain from 4 to 9 Fe planes, supported on a Ru(0001) layer and including a vacuum region of at least 17 Å. In the case of a WZ-ended structure, the simulations allowed for a WZ-like coordination involving the three outermost planes, as shown in the right panel of figure

4.12 for an O-ended surface.

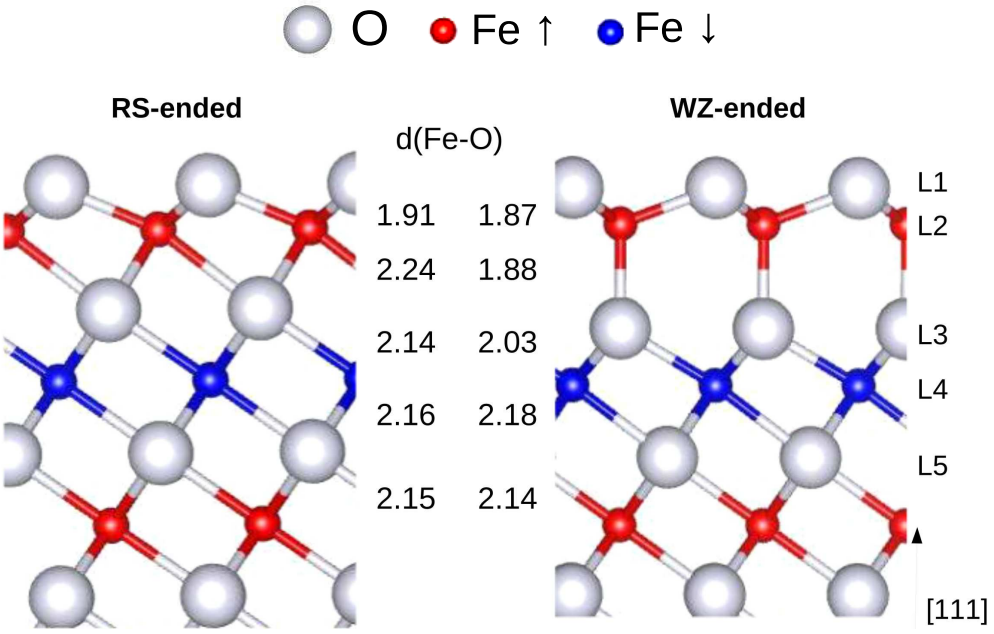

Figure 4.12: Atomic structure of the O-ended FeO(111) surfaces under RS- and WZ-terminations. The interatomic Fe-O distances are provided in Å.

The relative energies of Fe- and O-terminations under all possible surface stackings were compared. The results indicated that exposing an O layer is the favored situation, in agreement with the ISS results, and also with previous calculations [52]. Thus, in the following only O-terminations were considered.

The results also indicated that below the fourth layer, bulk-like properties were essentially recovered, putting a limit in the extension of the surface region in the films. The surface features were common to all slab thicknesses considered. The WZ-ended surface, as well as the RS-termination preserved the layered antiferromagnetic order. In the case of RS stacking the loss of neighbors of the surface O atoms increases the demand of charge to the remaining Fe neighbors, giving rise to Fe^{3+} sites. Similar results are obtained in the case of $Fe_{1-x}O$ and Fe_3O_4 [50, 53]. Thus the presence of these Fe atoms should manifest in additional peaks in the XPS spectra, contrarily to the

experimental evidence. Regarding the WZ-like termination, the tetrahedral environment of the Fe subsurface atoms improves the charge compensation to the surface O atoms and a surface region with only Fe^{2+} sites is then favoured [50, 53]. Thus, the existence of a WZ-like termination can explain the experimental evidence of a (1×1) O-ended surface with only Fe^{2+}. This result then extends the existence of a stacking-fault reconstruction beyond the case of CoO(111).

The interatomic Fe-O distances shown in figure 4.12 show that there are significant restructurations of the interlayer spacings. The structural changes are deeper for the WZ-stacking, that tends to reduce considerably the bonds at the surface region to improve the charge compensation. In both structures, the bulk-like interatomic distances are essentially recovered below the fourth layer.

By comparing the total energies of both surfaces it turned out that the WZ-stacking was favored over the uniform RS model by 30 meV in the 9 Fe layers thick slab. This energy difference is not negligible, but normalizing to the number of atoms in both slabs it reduces to only 1 meV/atom, too low to explain the stability of the WZ-termination. However, different factors within the calculations that were disregard could explain this. First, both slabs only differ in the surface region, comprised by no more than 5 layers, so the energy difference should be ascribed to only a few atoms in the structure. In addition, a common in-plane lattice parameter was used for all atomic planes, which in this case corresponds to the equilibrium RS bulk structure, $a(RS) = 3.04$ Å, lower than the experimental estimation for the thin films. Furthermore, a WZ symmetry would also favor a larger volume as $a(WZ) = 3.26$ Å. Thus, the O-ended slabs were modeled again for all surface stackings and thicknesses but using the equilibrium WZ lattice parameter.

The surface features described above like the contraction of the outermost interatomic spacings, the emergence of Fe^{3+} (Fe^{2+}) features under RS (WZ) terminations, the continuity of the antiferromagnetic coupling, and the recovery of the bulk-like properties below the fourth layer remained essentially unaltered. But interesting differences

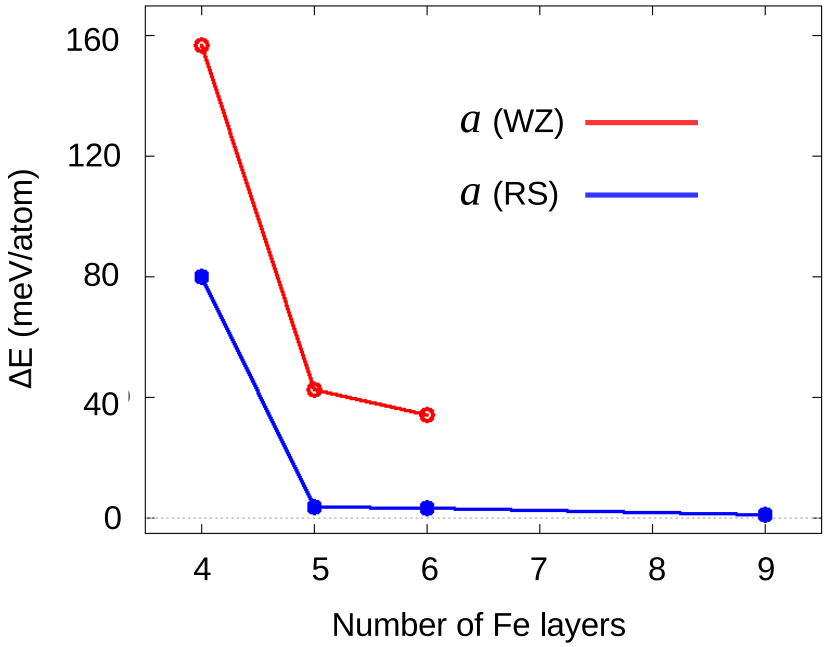

Figure 4.13: Relative energy difference between the WZ- and RS-terminations, normalized to the number of FeO atoms in the slab, as a function of the slab thickness (measured by the number of Fe planes) for the two lattice parameters considered. Positive values correspond to stability of the WZ termination.

emerged from the relative stability of the WZ-termination over the RS-ended surface at fixed lattice parameter. This is shown in figure 4.13 as a function of the slab thickness. It can be observed that an expanded lattice significantly favors the WZ termination. In addition, the energy differences, normalized to the number of atoms in the slabs, are higher the thinner the films, where the dominant energy terms come from the surface region. In summary, the unusual properties of the stoichiometric FeO(111) films, lack of Fe^{3+} cations, 1×1 symmetry and expanded lattice in-plane parameter, are explained by first-principle calculations as arising from the existence of a WZ-like environment at the surface.

4.3 Growth of FeO by O-MBE

As explained before, FeO ultrathin films are usually grown by means of O-MBE. In this case, it is observed that the growth depends on the temperature and the pressure employed during growth. When the growth is performed in an oxygen pressure of 10^{-6} mbar, the islands are of bilayer thickness (Fe-O-Fe-O). In contrast, under a pressure of 10^{-8} mbar, the islands are a single FeO layer thick (Fe-O). On the other hand, increasing the substrate temperature in the range 800-900 K, modifies the number of nucleation sites on the substrate leading to fewer but larger islands at high temperatures [9].

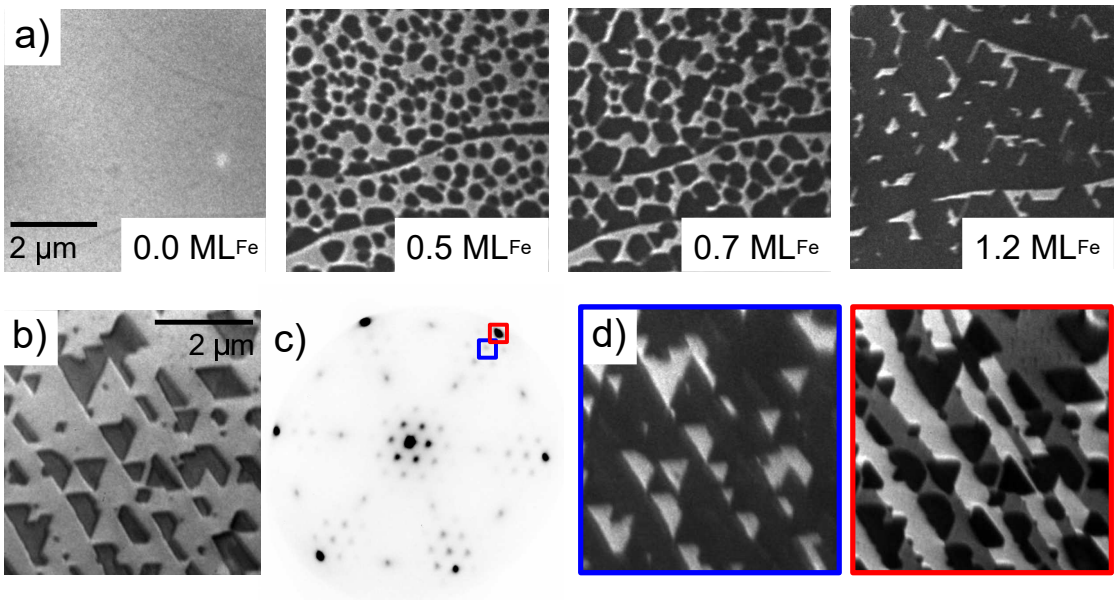

Figure 4.14: a) Frames selected from a sequence of LEEM images acquired (at a start voltage of 19 V) during the growth of FeO on Ru(0001). The frames correspond to 0, 0.5, 0.7 and 1.2 ML of Fe respectively. b) Incomplete film showing triangular islands. c) LEED of the surface imaged in (b), acquired with a start voltage of 36 V. The red circle marks one of the first order Ru diffracted beams, while the blue square marks one of the first order FeO ones. d) Dark-field image using the marked beams in (c) with either a blue square (left image) or a red circle (right image), using the same start voltage of 36 V.

The FeO thin film growth on Ru(0001) has been followed in real time and space

using LEEM. The Fe doser was first calibrated by Fe growth on Ru(0001) in UHV. Then, 1 ML_{Fe} refers to a complete layer of Fe covering the Ru surface. It should be noticed that given the difference in lattice spacing between metallic Fe and FeO(111), 1 ML_{Fe} corresponds to $\sim$ 1.38 ML_{FeO} [9]. The Fe deposition was performed on Ru(0001) under an oxygen pressure of 10^{-6} mbar, which should give rise to bilayer islands. The substrate temperature was fixed at 1150 K. The growth process is shown in the frames of Figure 4.14a. After the initial nucleation stage, the islands grow in size until they coalesce forming a continuous bilayer. The bilayer growth is indicated by the coverage of 1.2 ML_{Fe} (which corresponds to $\sim$1.7 ML_{FeO}) that does not cover completely the substrate. If the growth is interrupted before completing the layer, the islands tend to have a triangular shape with two opposite orientations on each terrace (Figure 4.14b). The two orientations correspond to twin stacking sequences relative to the substrate, and have already been detected in monolayer islands by scanning tunneling microscopy [54].

The LEED pattern from the FeO islands (see Fig. 4.14c) are equivalent to those shown for the thinnest FeO films grown by PLD (compare with Fig. 4.8). The ultrathin FeO layers present a 1×1 hexagonal pattern with additional spots around the first order ones (marked with a blue square). The resulting in-plane lattice spacing is 0.32 nm in agreement with the value reported for FeO ultrathin films on Ru(0001) [9]. The FeO LEED pattern is aligned with the Ru one (outer darker spots, one of them marked with a red square). In addition, in the midway between the Ru first order diffracted beams there are additional 2×2 spots. These arise from the oxygen adsorbed on the uncovered Ru surface [55, 56].

Acquiring images with one of the FeO diffracted beams, i.e. dark-field imaging, shows the same image with some of the FeO islands appearing bright (left frame of Figure 4.14d), the ones sharing the same orientation. By selecting a different FeO diffracted beam, a non-equivalent one, the opposite oriented FeO islands would appear bright. If one of the Ru diffracted beams is used instead, it is the one of the two hcp

Ru substrate terminations that is imaged bright (right frame of Figure 4.14d). Thus, in summary, at a pressure of 10^{-6} mbar, FeO growth proceeds by the nucleation of bidimensional islands as expected. The islands wet the oxygen-covered Ru substrate and grow until they complete the bilayer.

4.4 Growth of CoO by O-MBE

Cobalt oxide is next tried to be grown in the same way than FeO on Ru(0001). Previous to the experiments and as in the case of Fe, the Co doser was calibrated by growth on Ru(0001) in UHV. Then, 1 ML_{Co} refers to a complete layer of Co covering the Ru surface. A sequence of LEEM images acquired during growth is presented in Figure 4.15a. In contrast with the case of FeO, deposition of one ML of Co leads to small islands which nucleate around the substrate steps, even if the substrate temperature, pressure and deposition rate are similar to those of the FeO case. Lowering the temperature does not change the growth mode: in Figure 4.15b we show the surface after growing 4 ML_{Co} at 950 K. However, in this case we obtain triangular islands with two opposite orientations. Additionally, rectangular shape islands are found, although in much smaller contribution.

The diffraction pattern of such a surface is shown in Figure 4.15c. The brightest spots, marked with red circles, correspond to the first order Ru diffracted beams. Oxygen on the bare Ru substrate gives rise to additional diffracted beams with a 2×2 periodicity. In addition there are two new patterns: a 30° rotated pattern (marked with blue triangles), and a square pattern (marked with green boxes). There is no moiré pattern as observed in FeO growth. The blue hexagon spots are attributed to the triangular islands, although some intensity can also be due to diffraction from the oxygen covered Ru, and the square pattern is suggested to arise from the rectangular islands. The lattice spacing of the triangular islands is 0.31 nm, slightly larger than the Ru(0001) lattice spacing of 0.27 nm. The simple hexagonal pattern strongly suggests a (111)-oriented rock-salt structure for

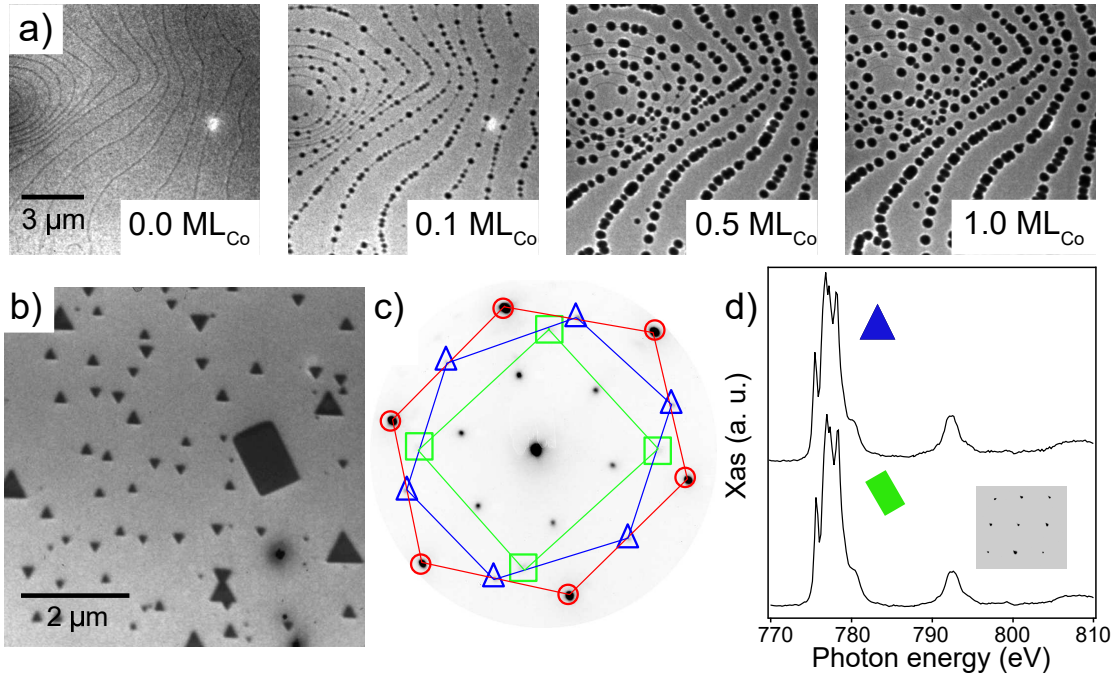

Figure 4.15: (a) Sequence of LEEM images acquired during the growth of CoO on Ru(0001) at 1200 K in a background oxygen pressure of $2 \cdot 10^{-6}$ mbar. The images correspond to a cobalt dose of 0, 0.07, 0.5 and 1.0 ML respectively. The start voltage is 5 V. (b) LEEM image of a film after the growth of 4 ML of Co at 950 K in $1.5 \cdot 10^{-6}$ mbar, with clearly defined triangular and rectangular islands. (c) LEED pattern on the same area, acquired at a start voltage of 47 V. (d) Selected-area X-ray absorption spectroscopy data acquired respectively on one of the triangular islands, and on the rectangular one. In the latter, the inset shows the LEED diffraction pattern, acquired also at 47 V.

the triangular islands: an unreconstructed spinel phase would appear as a structure with a 2×2 periodicity due to the twice-as-large unit cell within a (111) plane [57]. Likewise, a corundum structure would show additional spots at $\sqrt{3} \times \sqrt{3}$R30° positions [10]. The square pattern, in contrast, corresponds to a lattice spacing of 0.20 nm.

To gain insight into the chemical nature of the two types of islands we have measured the x-ray absorption near the L_3 and L_2 Co absorption edges, from a triangular and a rectangular island respectively as shown in Figure 4.15d. The two spectra are the same, and have the typical structure shown by Co^{2+} in CoO [58]. Thus both types of islands, triangular and rectangular, are composed of CoO. The triangular islands correspond to (111) oriented islands with the LEED pattern in reasonable agreement with the expected

hexagonal arrangement having a lattice spacing in real space of 0.31 nm. The rectangular island, instead, has a square diffraction pattern (inset in bottom of Figure 4.15d) suggesting a (001) orientation. These two orientations have already been reported for CoO on Ir(001) depending on the preparation procedure [59]. Apart from the coexistence of two different orientations, of which one of them comprises the majority of the islands, the 3D growth was unexpected given the known propensity of FeO to grow in the form of extremely flat layers in a wide temperature range [9]. So while iron oxide grows as FeO wetting the Ru substrate in either monolayer or bilayer flat islands with (111) orientation and aligned with the substrate, cobalt grows as CoO in three dimensional mode and in two different orientations.

4.5 Growth of mixed Fe and Co compositions by O-MBE

Mixed iron and cobalt compositions were investigated by simultaneously depositing Fe and Co on the surface of Ru(0001) in an oxygen background pressure of 10^{-6} mbar and at a substrate temperature of 1000K.

The sequence of the growth is shown in Figure 4.16a. There seems to be two types of islands with different reflectivity (i.e. gray level in the images), most clearly seen in the second frame (0.2 ML_{Fe+Co}). A similar film is shown in Figure 4.16b, where the LEEM image was acquired at a start voltage of 40 V where the contrast between islands is more evident. In this case all the islands have a clear triangular shape in contrast with the CoO growth where rectangular islands were also present. Furthermore, all the islands with a given reflectivity have two possible orientations, each of one being a mirror image of the other, as was previously noted for FeO islands (compare with Fig. 4.14). But when comparing islands with different reflectivity, there is a 30° rotation between the two families, as marked in Figure 4.16b.

The low-energy electron diffraction pattern from the surface is shown in Figure 4.16c.

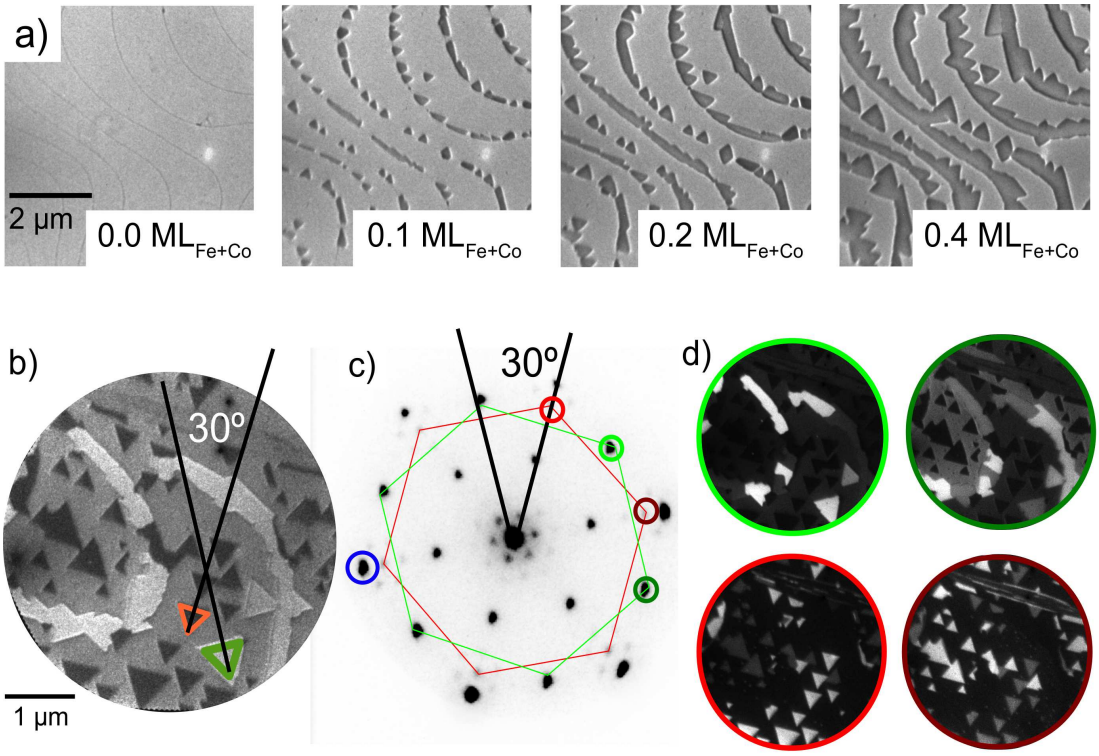

Figure 4.16: (a) Frames of a sequence of LEEM images acquired during the codeposition of Co and Fe on Ru(0001) in a $2 \cdot 10^{-6}$ mbar of oxygen. The substrate temperature is 1000 K, and the Co:Fe ratio is 0.8:1. The start voltage is 19 V. (b) LEEM image showing in detail the two types of islands. The start voltage is 40 V. The field of view is 5 μm. (c) LEED pattern of the same surface, acquired at a start voltage of 35 V. (d) Dark-field images acquired with the beams marked by the same symbols shown in the LEED pattern (c).

The LEED pattern shows the Ru diffracted beams, one of which is marked by a blue circle. Then there is a 2×2 lattice pattern, already seen before and arising from exposed areas of Ru covered with oxygen. Then there are the spots marked by green circles. Those beams are at positions that can be attributed to a structure rotated by 30° with a lattice spacing of 0.31 nm. Finally, and close to the Ru beams, there is the same pattern of beams (marked with red circles) and satellites that have been previously observed for FeO (Figure 4.14c). They can be attributed in the same way to a moiré pattern of an hexagonal structure with a lattice spacing close to 0.31 nm, and aligned with the underlying Ru substrate. Thus, it could be suggested that the "white" islands,

whose shape is rotated by 30°, have the rotated diffraction pattern, while the "dark" islands correspond to the unrotated (moiré) pattern. This point was checked by taking dark field images as shown in Figure 4.16d. When one of the moiré diffracted beams is employed one family of islands appear bright where the two opposite orientations can be imaged selecting two different first order moiré beams (see bottom images marked with bright and dark red circles correspondingly). If now one of the rotated diffracted beams is selected, then the rotated 30° islands are imaged where again the two possible orientations are imaged by using two different rotated diffracted beams (see top images marked with a bright and dark green circles). So there is a clear link between orientation and crystal structure on each type of island.

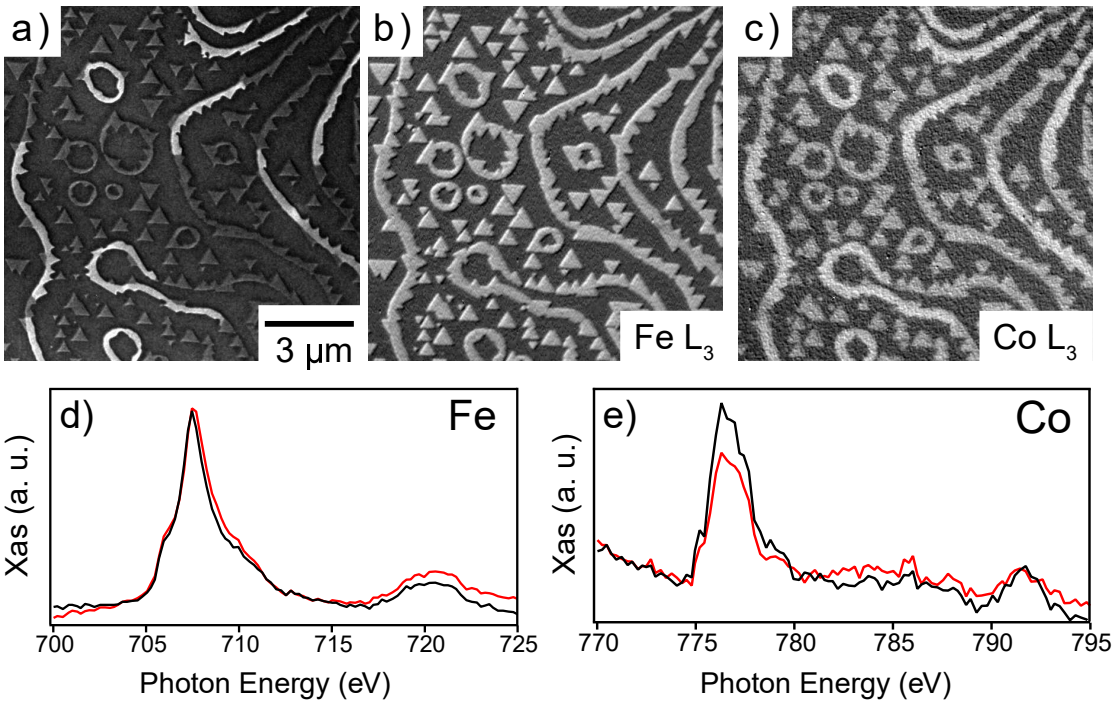

Figure 4.17: a) LEEM image of codeposition of 0.5 ML of Fe and Co (Co:Fe 0.8:1) at a substrate temperature of 990 K and an oxygen pressure of $0.9 \cdot 10^{-6}$mbar, acquired at a start voltage of 2.7 V. b) Difference image between images acquired at photon energies corresponding to the L_3 peak and 5 eV below for b) Fe and c) Co. Each image corresponds to a start voltage of 1 V. Selected-area spectra acquired from dark-gray islands of image (a) in red, and of bright ribbons decorating the substrate steps in black at the d) Fe and e) Co L-edge.

Thus, codeposition of Fe and Co in oxygen at the particular pressure and temperatures used in the experiment gives rise to flat islands with the same orientation and crystal structure of pure FeO on Ru(0001), and to islands with a rotated structure. In addition, they both present a simple hexagonal unit cell with a 0.31 nm lattice spacing. That structure and lattice spacing are compatible with a rocksalt structure of either FeO or CoO with a (111) orientation, considering a similar lattice spacing to the experimentally observed for ultrathin FeO. Given that no rotated structure has ever been observed on pure FeO on Ru(0001)[11, 13], it is clear that the rotated structure is due to the addition of Co. In fact, for CoO-only growth, the triangular islands exhibited the same rotated orientation. So in principle it could be assumed that the different orientation is related to the islands composition.

To confirm this point we recorded XAS images and spectra from both type of islands. For comparison, a LEEM image of the same area is shown in Figure 4.17a. The XAS images were acquired at the L_3 absorption edge of either Co or Fe. In order to increase the chemical contrast, two images at different photon energies, at the Fe/Co L_3 peak and 5 eV below respectively, have been subtracted. By doing so, possible absorption differences between islands are enhanced. The result is shown in Fig. 4.17b-c for Fe and Co respectively. In the LEEM image the two different types of islands are observed. The rotated ones appear brighter than the ones aligned with the substrate. Most of the bright islands are decorating the step edges, something that was already apparent in Figure 4.16b. The Fe XAS image does not indicate any difference between the two regions. The full spectra acquired at the two type of areas is also similar (Figure 4.17d) where the dark (red) line corresponds to the rotated (nonrotated) islands correspondingly. However, in the Co XAS image the rotated islands appear brighter (see Fig. 4.17c). The same is observed in the selected area spectra of Figure 4.17e. This result clearly indicates that the rotated islands are enriched in cobalt, confirming the hypothesis that related their composition with their orientation. Both types of islands, however, are not either iron or cobalt monoxide, but rather correspond to mixed compositions.

4.6 Conclusions

FeO(111) thin films have been growth on Ru(0001) by both IR-PLD and O-MBE. The films obtained by PLD are single crystal and in contrast with the bilayer limit observed using MBE, PLD allow to synthesize FeO(111) films with thicknesses of several nm with an improved stoichiometry over the bulk form. The films present a (1×1) symmetry without Fe^{3+} at the topmost layers. These features are explained by first-principles calculations based on the existence of a WZ-like surface stacking that has already been reported for O-ended CoO(111). The WZ-surface environment is related to polarity compensations effects and it seems to play a primordial role in the stabilization of the stoichiometric FeO films beyond the bilayer limit. These results extend the thickness range to stabilize stoichiometric FeO at ambient conditions, avoiding its transformation to the more thermodynamically stable Fe oxide forms, magnetite and hematite. It was also found that the exposure of the films to air induces chemical surface transformations.

The effect of the substrate-target distance and the substrate temperature on the properties of the FeO films was also investigated. It was found that the film thickness is inverse-square related to the substrate-target distance and that films with thicknesses below 5 nm are of a mixed composition of FeO and metallic iron. The deposition of metallic iron is suggested to take place at the initial stages of the growth at the Ru surface followed by the growth of FeO. On the other hand, variation of the substrate temperature in the [300-1000 K] range, leads to a surface composition variation from mixed Fe^{2+}/Fe^{3+} to only Fe^{2+} respectively. In addition, there is a change of crystallinity, from disordered (at 300 K) to a monocrystalline surface by increasing the temperature.

The FeO ultrathin films growth on Ru(0001) by O-MBE has been followed by LEEM. Growing at a pressure of 10^{-6} mbar gives rise to islands of bilayer height that grow until they cover all the surface. If the growth is stopped before completing the layer, triangular shaped islands are observed in two opposite orientations. The obtained diffraction

pattern presents a moiré aligned with the Ru one evidence of a (111) orientation.

The CoO growth turned out to be completely different from the FeO case. Instead of the 2D growth we obtain a strong 3D growth with small rounded islands nucleating around the Ru(0001) steps. Decreasing the substrate temperature (from 1200 to 950 K) the CoO islands grow with a triangular shape with two opposite orientations. In addition, fewer rectangular islands are observed. The triangular islands present an hexagonal LEED pattern indicating a (111) orientation. However in this case the pattern is rotated with respect the Ru one by 30°. The rectangular islands present a square diffraction pattern suggesting a (100) orientation.

Mixed depositions of Fe and Co grow again wetting the substrate. The result of the growth are two families of islands rotated by 30° between them with a correspondent LEED pattern that shows two hexagonal patterns rotated by the same amount. One of the patterns is aligned with the Ru one while the other is rotated by 30°. XAS indicates that both families of islands are composed of Fe and Co although the islands whose LEED pattern is rotated by 30° relative to the Ru substrate are enriched in Co. Thus, simultaneous deposition of Fe and Co at the particular temperature and pressure employed at the experiment leads to islands of mixed FeO and CoO compositions with (111) orientation and with different Co content while the Fe content remains constant among the different islands.

Bibliography

[1] R. M. Hazen and R. Jeanloz. Wüstite ($Fe_{1-x}O$): a review of its defect structure and physical properties. *Reviews of Geophysics and Space Physics*, 22:37, 1984.

[2] K. Heinz and L. Hammer. Epitaxial cobalt oxide films on Ir(100)-the importance of crystallographic analyses. *Journal of Physics: Condensed Matter*, 25(17):173001, 2013.

[3] R. M. Cornell and U. Schwertmann. *The Iron Oxides*. John Wiley & Sons Ltd, Weinheim, 1997.

[4] M. Chen, B. Hallstedt, and L. J. Gauckler. Thermodynamic assessment of the Co-O system. *Journal of Phase Equilibria*, 24(3):212–227, 2003.

[5] Y.-N. Sun, Z.-H. Qin, M. Lewandowski, E. Carrasco, M. Sterrer, S. Shaikhutdinov, and H.-J. Freund. Monolayer iron oxide film on platinum promotes low temperature CO oxidation. *Journal of Catalysis*, 266:359–368, 2009.

[6] Q. Fu, W.-X. Li, Y. Yao, H. Liu, H.-Y. Su, D. Ma, X.-K. Gu, L. Chen, Z. Wang, H. Zhang, B. Wang, and X. Bao. Interface-Confined Ferrous Centers for Catalytic Oxidation. *Science*, 328:1141–1144, 2010.

[7] X. Sun, H. N. Frey, A. Sigdel, and S. Sun. Tuning Exchange Bias in Core/Shell FeO/Fe_3O_4 Nanoparticles. *Nano Letters*, 12(1):246–251, 2012.

Bibliography

[8] G. D. Waddill and O. Ozturk. Epitaxial growth of iron oxide films on Ag(111). *Surface Science*, 575:35–50, 2005.

[9] I. Palacio, M. Monti, J. F. Marco, K. F. McCarty, and J. de la Figuera. Initial stages of FeO growth on Ru(0001). *Journal of Physics: Condensed Matter*, 25(48):484001, 2013.

[10] W. Weiss and W. Ranke. Surface chemistry and catalysis on well-defined epitaxial iron-oxide layers. *Progress in Surface Science*, 70:1–151, 2002.

[11] G. Ketteler and W. Ranke. Heteroepitaxial growth and nucleation of iron oxide films on Ru(0001). *The Journal of Physical Chemistry B*, 107(18):4320–4333, 2003.

[12] N. Spiridis, D. Wilgocka-Ślęzak, K. Freindl, B. Figarska, T. Giela, E. Młyńczak, B. Strzelczyk, M. Zając, and J. Korecki. Growth and electronic and magnetic structure of iron oxide films on Pt(111). *Physical Review B*, 85(7):075436, 2012.

[13] B. Santos, E. Loginova, A. Mascaraque, A. K. Schmid, K. F. McCarty, and J. de la Figuera. Structure and magnetism in ultrathin iron oxides characterized by low energy electron microscopy. *Journal of Physics: Condensed Matter*, 21:314011, 2009.

[14] C. Noguera. Polar oxide surfaces. *Journal of Physics: Condensed Matter*, 12(31):R367–R410, 2000.

[15] S. Couet, K. Schlage, K. Saksl, and R. Röhlsberger. How Metallic Fe Controls the Composition of its Native Oxide. *Physical Review Letters*, 101:056101, 2008.

[16] J. Gurgul, E. Mlynczak, N. Spiridis, and J. Korecki. Layer-by-layer epitaxial growth of polar FeO(111) thin films on MgO(111). *Surface Science*, 606:711, 2012.

[17] H. C. Galloway, J. J. Benítez, and M. Salmeron. Growth of FeO_x on Pt(111) studied by scanning tunneling microscopy. *Journal of Vacuum Science & Technology A*, 12:2302, 1994.

[18] K. Mori, M. Yamazaki, T. Hiraki, H. Matsuyama, and K. Koike. Magnetism of a FeO(111)/Fe(110) surface. *Physical Review B*, 72:014418, 2005.

[19] P. R. Willmott. Deposition of complex multielemental thin films. *Progress in Surface Science*, 76(6-8):163–217, 2004.

[20] M. Sanz, M. Oujja, E. Rebollar, J. F. Marco, J. de la Figuera, M. Monti, A. Bollero, J. Camarero, F. J. Pedrosa, M. García-Hernández, and M. Castillejo. Stoichiometric magnetite grown by infrared nanosecond pulsed laser deposition. *Applied Surface Science*, 282:642–651, 2013.

[21] M. Monti, M. Sanz, M. Oujja, E. Rebollar, M. Castillejo, F. J. Pedrosa, A. Bollero, J. Camarero, J.-L. F. Cuñado, N. M. Nemes, F. J. Mompean, M. Garcia-Hernández, S. Nie, K. F. McCarty, A. T. N'Diaye, G. Chen, A. K. Schmid, J. F. Marco, and J. de la Figuera. Room temperature in-plane $\langle 100 \rangle$ magnetic easy axis for $Fe_3O_4/SrTiO_3(001)$:Nb grown by infrared pulsed laser deposition. *Journal of Applied Physics*, 114(22):223902, 2013.

[22] R. L. Doyle and M. E. G. Lyons. *Photoelectrochemical Solar Fuel Production: From Basic Principles to Advanced Devices*. Springer, 2016.

[23] N. Weidler, S. Paulus, J. Schuch, J. Klett, S. Hoch, P. Stenner, A. Maljusch, J. Brotz, C. Wittich, B. Kaiser, and W. Jaegermann. CoO_x thin film deposited by CVD as efficient water oxidation catalyst: change of oxidation state in XPS and its correlation to electrochemical activity. *Physical Chemistry Chemical Physics*, 18:10708–10718, 2016.

[24] J. Yang, J. K. Cooper, F. M. Toma, K. A. Walczak, M. Favaro, J. W. Beeman, L. H. Hess, C. Wang, C. Zhu, S. Gul, J. Yano, C. Kisielowski, A. Schwartzberg, and I. D. Sharp. A multifunctional biphasic water splitting catalyst tailored for integration with high-performance semiconductor photoanodes. *Nature Materials*, 16:335–341, 2017.

Bibliography

[25] C. Shang, S. Dong, P. Hu, J. Guan, D. Xiao, X. Chen, L. Zhang, L. Gu, G. Cui, and L. Chen. Compatible interface design of CoO-based Li-O_2 battery cathodes with long-cycling stability. *Scientific Reports*, 5:8335, 2015.

[26] P. Poizot, S Laruelle, S. Grugeon, L. Dupont, and J-M. Tarascon. Nano-sized transition-metal oxides as negative-electrode materials for lithium-ion batteries. *Nature*, 407:496–499, 2000.

[27] H. Shima, F. Takano, H. Akinaga, Y. Tamai, I. H. Inoue, and H. Takagi. Resistance switching in the metal deficient-type oxides: NiO and CoO. *Applied Physics Letters*, 91(1):012901, 2007.

[28] J. S. Kwak, Y. H. Do, Y. C. Bae, H. Im, and J. P. Hong. Reproducible unipolar resistive switching behaviors in the metal-deficient CoO_x thin film. *Thin Solid Films*, 518(22):6437 – 6440, 2010.

[29] V. Skumryev, S. Stoyanov, Y. Zhang, G. Hadjipanayis, D. Givord, and J. Nogués. Beating the superparamagnetic limit with exchange bias. *Nature*, 423:850, 2003.

[30] M. Gruyters and D. Riegel. Strong exchange bias by a single layer of independent antiferromagnetic grains: The CoO/Co model system. *Physical Review B*, 63:052401, 2000.

[31] F. Voges, H. de Gronckel, C. Osthöver, R. Schreiber, and P. Grünberg. Spin valves with CoO as an exchange bias layer. *Journal of Magnetism and Magnetic Materials*, 190(3):183 – 186, 1998.

[32] J. I. Fujikata, K. Ishihara, K. Hayashi, H. Yamamoto, and K. Yamada. Magnetoresistance effects in spin-valve structures with CoO/NiO superlattices. *IEEE Transactions on Magnetics*, 31(6):3936–3938, 1995.

[33] M. De Santis, A. Buchsbaum, P. Varga, and M. Schmid. Growth of ultrathin cobalt oxide films on Pt(111). *Physical Review B*, 84(12):125430, 2011.

[34] M. Gubo, C. Ebensperger, W. Meyer, L. Hammer, and K. Heinz. Substoichiometric cobalt oxide monolayer on Ir(100)-(1x1). *Journal of Physics: Condensed Matter*, 21(47):474211, 2009.

[35] W. Meyer, D. Hock, K. Biedermann, M. Gubo, S. Mueller, L. Hammer, and K. Heinz. Coexistence of rocksalt and wurtzite structure in nanosized CoO films. *Physical Review Letters*, 101(1):016103, 2008.

[36] K. Biedermann, M. Gubo, L. Hammer, and K. Heinz. Phases and phase transitions of hexagonal cobalt oxide films on Ir(100)-(1x1). *Journal of Physics: Condensed Matter*, 21(18):185003, 2009.

[37] C. Ebensperger, M. Gubo, W. Meyer, L. Hammer, and K. Heinz. Substrate-induced structural modulation of a CoO(111) bilayer on Ir(100). *Physical Review B*, 81(23):235405, 2010.

[38] M. Gubo, C. Ebensperger, W. Meyer, L. Hammer, and K. Heinz. Structural elements in the oxidation process of a single cobalt layer on Ir(100)-(1x1). *Physical Review B*, 83(7):075435, 2011.

[39] L. Zhuang, L. Ge, Y. Yang, M. Li, Y. Jia, X. Yao, and Z. Zhu. Ultrathin Iron-Cobalt Oxide Nanosheets with Abundant Oxygen Vacancies for the Oxygen Evolution Reaction. *Advanced Materials*, 29(17):1606793, 2017.

[40] R. D. L. Smith, M. S. Prévot, R. D. Fagan, S. Trudel, and C. P. Berlinguette. Water Oxidation Catalysis: Electrocatalytic Response to Metal Stoichiometry in Amorphous Metal Oxide Films Containing Iron, Cobalt, and Nickel. *Journal of the American Chemical Society*, 135(31):11580–11586, 2013.

[41] B.-R. Abolfazl and R. Mehran. Low temperature CO oxidation over Fe-Co mixed oxide nanocatalysts. *Chemical Engineering Journal*, 184:141 – 146, 2012.

[42] W.-W. Zhang and M. Chen. Thermodynamic modeling of the Co-Fe-O system. *Calphad*, 41:76–88, 2013.

Bibliography

[43] H. M. Christen and G. Eres. Recent advances in pulsed-laser deposition of complex oxides. *Journal of Physics: Condensed Matter*, 20(26):264005–264021, 2008.

[44] D. Yokoyama, K. Namiki, H. Fukasawa, J. Miyazaki, K. Nomura, and Y. Yamada. Mössbauer study of films produced by laser deposition of iron oxides. *Journal of Radioanalytical and Nuclear Chemistry*, 272(3):631–638, 2007.

[45] Casa Software Ltd. www.casaxps.com.

[46] N. S. McIntyre and D. G. Zetaruk. X-ray photoelectron spectroscopic studies of iron oxides. *Analytical Chemistry*, 49(11):1521–1529, 1977.

[47] A. P. Grosvenor, B. A. Kobe, M. C. Biesinger, and N. S. McIntyre. Investigation of multiplet splitting of Fe 2p XPS spectra and bonding in iron compounds. *Surface and Interface Analysis*, 36(12):1564–1574, 2004.

[48] S. I. Anisimov, D. Bäuerle, and B. S. Lukyanchuk. Gas dynamics and film profiles in pulsed-laser deposition of materials. *Physical Review B*, 48(16):12076–12081, 1993.

[49] R. Kumar, G. Kumar, and A. Uhmar. Pulse laser deposited nanostructured ZnO thin films: A review. *Journal of Nanoscience and Nanotechnology*, 14(3):1911–1930, 2014.

[50] I. Bernal-Villamil and S. Gallego. Electronic structure and polaronic charge distributions of fe vacancy clusters in $Fe_{(1-x)}O$. *Physical Review B*, 90(19):192126, 2014.

[51] I. Bernal Villamil. *Low dimensional Fe_3O_4 and $Fe_{1-x}O$: an ab initio approach.* PhD thesis, Instituto de Ciencia de Materiales de Madrid/UAM, Madrid, 2015.

[52] Y.L. Li, K.L. Yao, Z.L. Liu, and G.Y. Gao. First-principles study of the composition, structure and stability of the FeO(111) surface. *Physical Review B*, 72:155446, 2005.

[53] I. Bernal-Villamil and S. Gallego. Phase transitions at magnetite $Fe_3O_4(001)$: surface and Verwey charge orders. *Journal of Physics: Condensed Matter*, 27(19):012001, 2015.

[54] H. Zeuthen, W. Kudernatsch, L. R. Merte, L. K. Ono, L. Lammich, F. Besenbacher, and S. Wendt. Unraveling the Edge Structures of Platinum(111)-Supported Ultrathin FeO Islands: The Influence of Oxidation State. *ACS Nano*, 9(1):573–583, 2015.

[55] S. L. Parrott, G. Praline, B. E. Koel, J. M. White, and T. N. Taylor. Oxygen chemisorption on a stepped Ru ($\sim$ 001) crystal. *The Journal of Chemical Physics*, 71(8):3352–3354, 1979.

[56] M. Lindroos, H. Pfnür, G. Held, and D. Menzel. Adsorbate induced reconstruction by strong chemisorption: Ru(001)p(2x2)-O. *Surface Science*, 222(2):451 – 463, 1989.

[57] M. Monti, B. Santos, A. Mascaraque, O. Rodríguez de la Fuente, M. A. Niño, T. O. Mentes, A. Locatelli, K. F. McCarty, J. F. Marco, and J. de la Figuera. Magnetism in nanometer-thick magnetite. *Physical Review B*, 85(2):020404, 2012.

[58] T. J. Regan, H. Ohldag, C. Stamm, F. Nolting, J. Lüning, J. Stöhr, and R. L. White. Chemical effects at metal/oxide interfaces studied by x-ray-absorption spectroscopy. *Physical Review B*, 64:214422, 2001.

[59] M. Gubo, C. Ebensperger, W. Meyer, L. Hammer, K. Heinz, F. Mittendorfer, and J. Redinger. Tuning the Growth Orientation of Epitaxial Films by Interface Chemistry. *Physical Review Letters*, 108(6):066101, 2012.

CHAPTER 5

Cobalt ferrite islands on Ru(0001)

Part of the results presented in this chapter have been published in:

- L. Martín-García, A. Quesada, C. Munuera, J. F. Fernández, M. García-Hernández, M. Foerster, L. Aballe, and J. de la Figuera, *"Atomically Flat Ultrathin Cobalt Ferrite Islands"*, Advanced Materials **27**, 39 (2015).

5.1 Introduction

$CoFe_2O_4$ (CFO) is a promising candidate in the search of new materials for multifunctional devices because of its unique properties among others ferrites. It presents a strong magnetocrystalline anisotropy that can be exploited in fields like magnetic recording and spintronics [1]. It also exhibits a large magnetostriction constant that can be useful for strain-driven multiferroic nanostructures, i.e, in combination with ferroelectric or piezoelectric materials the magnetization of cobalt ferrite can be controlled by an electric field [2, 3]. As a hard ferrimagnet, it can also be combined with soft materials to exploit exchange-coupling effects [4]. As $CoFe_2O_4$ is a magnetic insulator, it presents spin-filter

capabilities that can result in the creation of theoretically 100% spin-polarized currents [1]. However, the observed efficiencies in tunnel junctions are far below the expected value [5, 6].

The structure of $CoFe_2O_4$ (see Figure 5.1) is, like in Fe_3O_4, a cubic inverse spinel where the octahedral Fe^{2+} cations in Fe_3O_4 have been replaced by Co^{2+} cations. The corresponding inverse spinel formula can be written as:

$$(Fe^{3+})_A[Fe^{3+}Co^{2+}]_BO_4$$

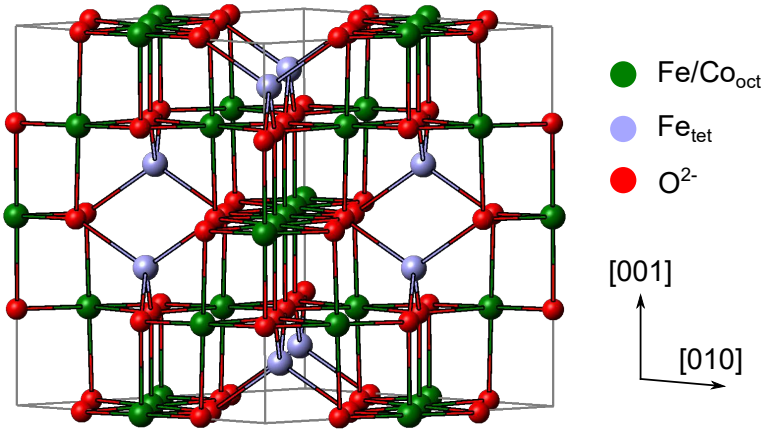

Figure 5.1: Schematic representation of the inverse spinel structure of $CoFe_2O_4$.

Usually, $CoFe_2O_4$ presents a non completely inverse structure with a small fraction of Co^{2+} cations (2-24%) located at tetrahedral sites [7, 8]. The distribution of Co^{2+} cations depends on the thermal history of the sample and the preparation method [9–11].

$CoFe_2O_4$ is ferrimagnetic with a Curie temperature $T_c \simeq 793K$ [12]. The first anisotropy constant, K_1, is positive leading to <100> magnetic easy axes directions

[1] The conduction band in a magnetic insulator is spin splitted and the electrons tunneling through the material experience different barrier heights as a function of their spin leading to a difference in the probability of tunneling transition.

[13]. The predominant magnetic exchange interaction is the AF super-exchange interaction between $Fe^{3+}{}_A$ and $Fe^{3+}{}_B/Co^{2+}{}_B$ with an energy J_{A-B}=-25k_B . This causes the AF alignment between A and B lattices. Additionally, there is an intrasublattice AF super-exchange interaction involving only Fe^{3+} at A sites with an energy J_{A-A}=-19k_B. Finally, the FM alignment of the Fe^{3+} and Co^{2+} at B sites is due to the FM super-exchange interaction with an energy of J_{B-B}=4k_B and the weak FM double-exchange interactions [14].

As in the case of Fe_3O_4, the contribution from the $Fe^{3+}{}_{A,B}$ cations to the spin magnetic moment cancel out and the ideal spin magnetic moment is due to the contribution of the octahedral Co^{2+} cations resulting in m_s=3 μ_B per formula unit. Also, the angular momentum of the Fe^{3+} is quenched as the corresponding levels are half occupied. However, each Co^{2+} ($3d^7$ configuration) in octahedral sites contains one unpaired electron whose spin would be strongly coupled to the lattice by the spin-orbit interaction resulting in an expected orbital magnetic moment of m_{orb}=1 μ_B. This is responsible for the strong magneto-crystalline anisotropy and also the magnetostriction observed in $CoFe_2O_4$.

Table 5.1 summarizes some of the magnetic moments of CFO reported in the literature. These values have been either predicted by theory [15, 16] or experimentally measured for CFO in bulk [17], in thin film [18, 19], in powder [20] and in nanoparticle form [21]. In the case of Co^{2+}, calculations predict m_{orb} [16] to be close to the expected value while m_{spin} being slightly lower [15, 16]. For Fe^{3+}, values close to 0 μ_B are predicted for m_{orb} [16] and m_{spin} [15, 16] as expected. On the other hand, the measured experimental values show no agreement. In the case of Co^{2+}, m_{spin} values from 0.15 μ_B [21] to 2.55 μ_B [20] have been found. The measured values for m_{orb} are lower than the expected one varying from 0.1 μ_B [21] to 0.6 μ_B [20]. For the Fe case, m_{spin} values from 0.1 μ_B [19] to 0.69 μ_B [20] were found with m_{orb} close to 0 μ_B as expected [19, 21]. The total magnetic moment (M_T) predicted by theory [15] is in agreement with the expected value of 3 μ_B although again we find a variety of reported experimental values ranging

Sample	m_{spin} (Co)	m_{orb} (Co)	m_{spin} (Fe)	m_{orb} (Fe)	M_T	Ref.
Bulk CFO	-	-	-	-	3.65	[17]
5 nm CFO/MgO	-	-	-	-	0.9	[18]
5 nm CFO/$MgAl_2O_4$	-	-	-	-	3.4	[18]
20 nm CFO/MgO	0.75	0.42	∼0.1	0.03	1.43	[19]
CFO powder	2.55	0.6	0.69	-	3.58	[20]
CFO nanoparticles	0.15	0.101	0.67	0.044	1.64	[21]
Theory	2.58	-	0	-	3	[15]
Theory	2.54	1.07	0.15	∼ 0	-	[16]

Table 5.1: Spin and orbital magnetic moment in units of μ_B of $CoFe_2O_4$ reported in the literature.

from 0.9 μ_B [18] to 3.65 μ_B [17]. The low M_T values measured in 5 nm [18] and 20 nm [19] thick CFO thin films grown on MgO [21] contrast with the large M_T value of 3.4 μ_B measured in 5 nm thick CFO thin films grown on $MgAl_2O_4$ [18]. These results were attributed to the increased presence of antiphase boundaries (APBs) in films grown on MgO compared to films grown on an spinel substrate like $MgAl_2O_4$ [18] where the antiphase boundaries are expected in smaller proportion due to the shared structure and symmetry between film and substrate [22].

As introduced before, $CoFe_2O_4$ presents very attractive properties to be exploited in nanotechnology. To do that, we must be able to synthesize the material in the nanoscale while maintaining the original bulk properties. However, the attempts to use the potential of cobalt ferrite in thin films have led to disappointing results [5, 12, 23]. At the thin film limit, the role of the surface becomes more relevant and thus, careful attention must be paid to the effect of the structural defects or surface roughness as it might dominate over the intrinsic properties of the material. The successful integration of cobalt ferrite and other materials into devices comes from the control of the growth process. Only by the synthesis of structurally perfect thin films, substantial progress in nanotechnological applications of CFO will be achieved.

One of the most common defects in ferrite thin films are antiphase boundaries [12, 24, 25]. These defects become more relevant as the thickness is reduced and they can have a critical influence in the exhibited properties of the material. The formation of APBs occurs at the early stages of the growth process of thin films. They result from the coalescence of growth nuclei whose atomic structures are shifted with respect to each other by noninteger unit cell distances. In these cases, the anion lattice remains continuous but there is a translation of the cationic lattice at the interface. The magnetic interaction across the boundary depends on the type of shift between both lattices [22]. In some cases a strong AF-coupling across the interface can be generated with a significant impact on the magnetic and transport properties of the material [12, 22, 26]: difficulties experienced to achieve saturation while the bulk form is quickly fully magnetized, presence of superparamagnetism at the ultrathin limit, decrease of remanence and magnetization at high fields. The transport properties are also affected since the resistivity of thin films with APBs is always higher than in bulk form and usually they present magnetoresistance [2] that is non-existent in single crystal form.

Since APBs have a dramatic influence on the magnetic and magneto-transport response it will be crucial to reduce their density in order to, first, reveal the properties of the novel material free from APBs and second, to improve their functionalities for applications. We propose to increase the control on the cobalt ferrite growth process by following it *in-situ* and in real time using surface electron microscopy. Using this approach we can study the magnetic and structural properties of islands that originated from a single nucleus. As APBs can only form when two islands collide, the nanostructures fabricated in this way are not expected to suffer from them.

[2] Change of the resistance as a function of the applied magnetic field.

5.2 Cobalt ferrite growth

The CFO growth was performed at the CIRCE beamline of the ALBA Synchrotron Light Facility. The use of LEEM helped to explore the effect of the different growth parameters, as the deposition rates or the substrate temperature, on the obtained structures. The best result was obtained by co-depositing Fe and Co onto a Ru(0001) substrate kept at T = 1130 K in 1×10^{-6} mbar O_2. The growth mode was observed to follow the Stranski-Krastanov growth mode: a wetting bilayer covered the surface uniformly on top of which the 3-dimensional growth of the islands took place.

The result of the growth is shown in Figure 5.2a. The islands have a triangular shape and present very straight edges. As each individual island grows from a single crystallographic nucleus, APB can only form when two islands collide (as in the case highlighted by a red square in Fig.5.2a), and an extremely low APB density is thus expected.

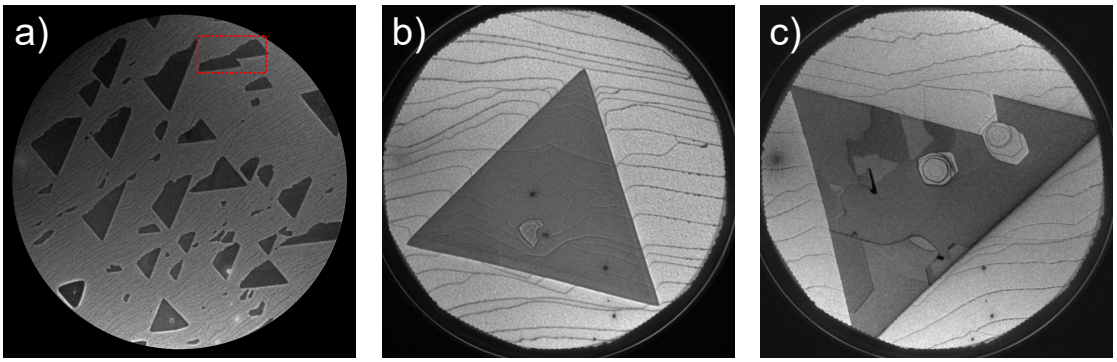

Figure 5.2: a) LEEM image of an ensemble of triangular CFO islands. The field of view is 50 μm and Vs is 3.4 V. b) and c) LEEM image of triangular islands. The field of view is 10 μm. Vs is 32 V and 5.1 V respectively.

Some islands present an homogeneous and flat surface like the one shown in Figure 5.2b while others present different contrast levels on the LEEM image like the one presented in Figure 5.2c. This can be attributed either to thickness differences or to

twin boundaries, which are regions with different stacking sequences. These defects have been previously reported in spinel ferrite thin films [27–29]. The discrimination between both is not possible based only on the LEEM image.

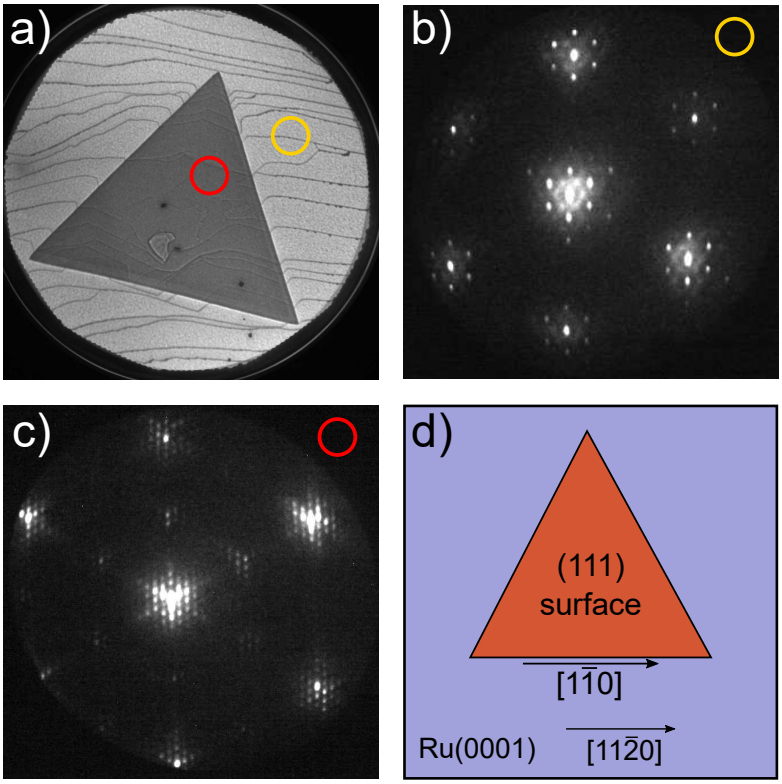

Figure 5.3: a) LEEM image of an island with a yellow and a red circles representing the places where the LEED pattern of the substrate (b) and the island (c) have been taken. The V_s is 40 eV. d) Schematic representation of the epitaxial relationship between the islands and the Ru(0001) substrate.

Micro-spot low-energy electron diffraction (μ-LEED) was performed both on the islands and on the wetting layer. The results are shown in Figures 5.3b and c. The wetting layer (Figure 5.3 b) presents a 1×1 pattern with extra satellite spots arising from the in-plane difference between the wetting layer and the substrate. A similar pattern was obtained in Chapter 4 after the growth of iron monoxide on a Ru(0001) substrate (see Figure 4.8e). The islands on the other hand, show additional spots at 2×2 positions

(Figure 5.3c), in agreement with the unit cell of an spinel structure along the [111] direction. The triangle sides are aligned with the compact directions of the underlying substrate as [1-10]//[11-20] giving rise to (111) surfaces, the ones with the lowest energy (see Fig. 5.3d). The closely spaced satellite spots might arise from the so-called bi-phase spinel surface reconstruction [30]. Similar LEED patterns have been reported for $Fe_3O_4(111)$ [31–33] and α-$Fe_2O_3(0001)$ [34]. In both cases, the reconstruction is related to the coexistence at the surface of $Fe_{1-x}O(111)$ and $Fe_3O_4(111)$ or $Fe_{1-x}O(111)$ and α-$Fe_2O_3(0001)$ phases respectively. There is an oxygen lattice mismatch between the $Fe_{1-x}O(111)$ overlayer forming on the $Fe_3O_4(111)/\alpha$-$Fe_2O_3(0001)$ phases. The O-O distance in $Fe_{1-x}O(111)$ is 3.04 Å while for $Fe_3O_4(111)$ and α-$Fe_2O_3(0001)$ is 2.97Å and 2.9Å. This mismatch gives rise to a long-range order observable at the LEED pattern by the extra spot around the first order diffracted ones. In the case presented here, this would mean that the surface of the islands can present slightly reduced areas.

5.3 Magnetic properties

The magnetic properties of the sample were investigated by XMCD at the Fe and Co L-edges at both the islands and the wetting layer.

- *Wetting layer*

As it can be seen from Figures 5.4 and 5.5, the wetting layer is composed of both iron and cobalt. The spectra are similar to those of the Fe^{2+} and Co^{2+} absorption curves of FeO and CoO reported in the literature [35–37] and also shown in Figure 2.9 suggesting an iron-cobalt monoxide composition. However, the main peak of the Fe XAS spectrum exhibits a shoulder (marked with an arrow) and the Co XAS spectrum is missing a pre-peak characteristic of Co^{2+} at $\sim$ 777.5 eV and the fine structure at the L_3 peak

indicating that the oxide wetting layer can be slightly reduced [37–39]. In addition, it presents a small dichroic signal, more clear in the Fe case (see Fig. 5.4 (bottom)) in agreement with the presence of some metallic Fe/Co.

The Fe:Co ratio can be roughly estimated from the edge jump of the XAS spectra[3] which is proportional to the number of absorbing atoms in the sample and the linear absorption coefficient (μ_x) [38]. However, in the present case, both XAS spectra are sitting on a background signal that complicates the estimation of the edge jump.

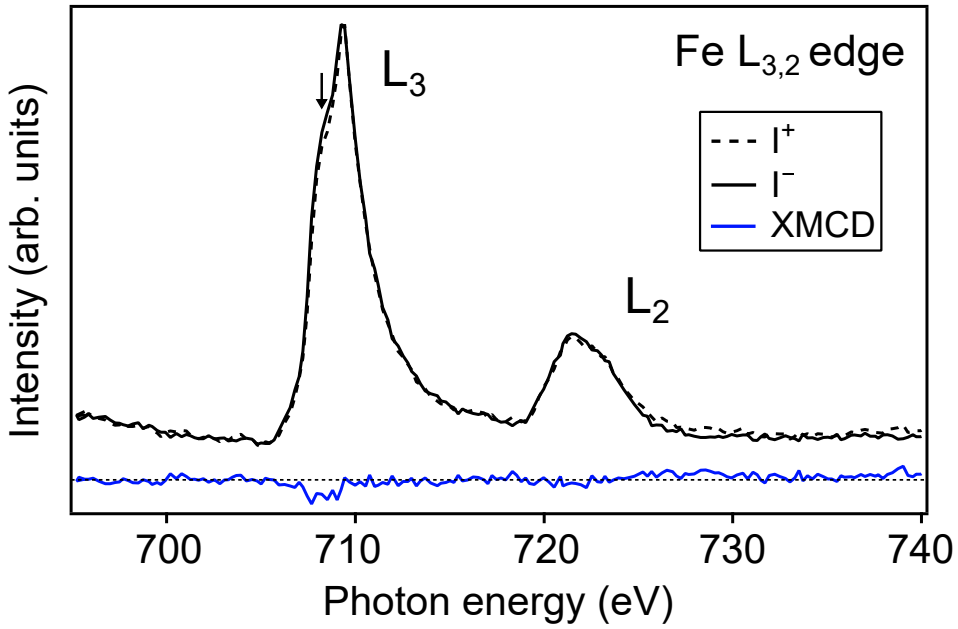

Figure 5.4: XAS (top) and XMCD spectra (bottom) at the Fe L-edge measured at the wetting layer.

Nevertheless, given that the linear absorption coefficient at the L_3 peak is similar for both elements[4], the comparison of the absorption intensities at both L_3 peaks results in a suggested Fe:Co ratio close to 2:1.

[3] The edge jump is defined as the difference of the intensities above and below an absorption edge
[4] μ_x at L_3 peak for Fe and Co are 6.0×10^{-2} nm^{-1} and 5.8×10^{-2} nm^{-1} respectively [38].

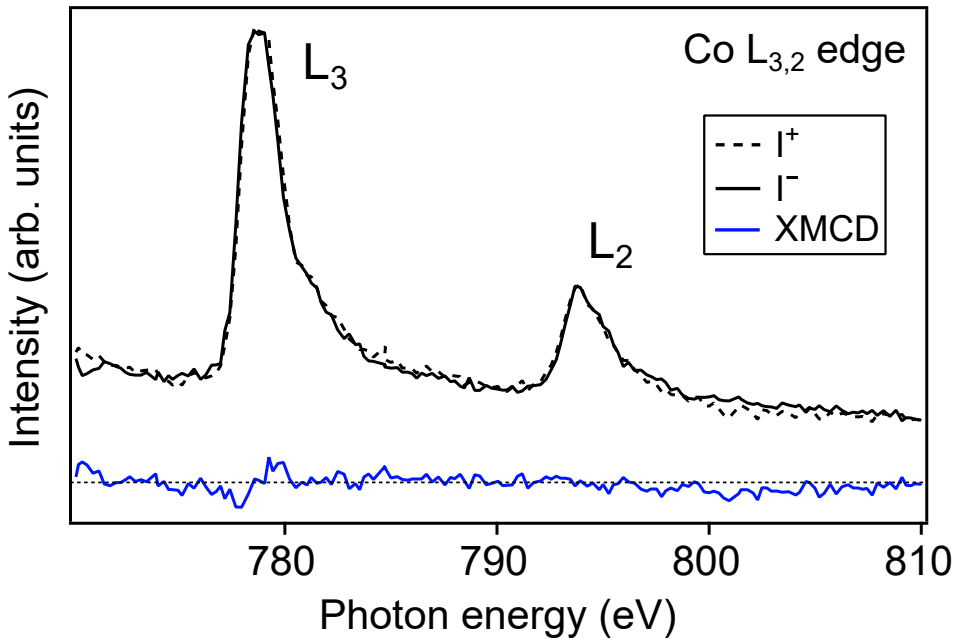

Figure 5.5: XAS (top) and XMCD spectra (bottom) at the Co L-edge measured at the wetting layer.

- *Islands*

The magnetic domain structure of the island shown in Figure 5.2c was imaged by XMCD-PEEM at room-temperature as shown in Figures 5.6b and c. The energies at which the XMCD images were taken correspond to the main peak for the Co XMCD spectrum and the first minimum of the Fe XMCD spectrum (see Figure 5.8 and 5.9). The domain structures associated with Fe and Co match perfectly. The same contrast at both images is a visual indication of the ferromagnetic alignment of the Fe and Co cations in octahedral positions. The magnetic domains are remarkably large, reaching over 4 μm^2 in some regions, in contrast with the typical image of cobalt ferrite film domains with domain sizes in the nanometer range [26] and indicative of the exceptional high crystalline quality of the structures obtained.

Comparing the LEEM and XMCD images we observe that some of the magnetic domain walls coincide with contrast changes in the LEEM image and must then be related to morphological features but others do not seem to be pinned to structural features and are expected to be determined by the balance of magnetic anisotropies.

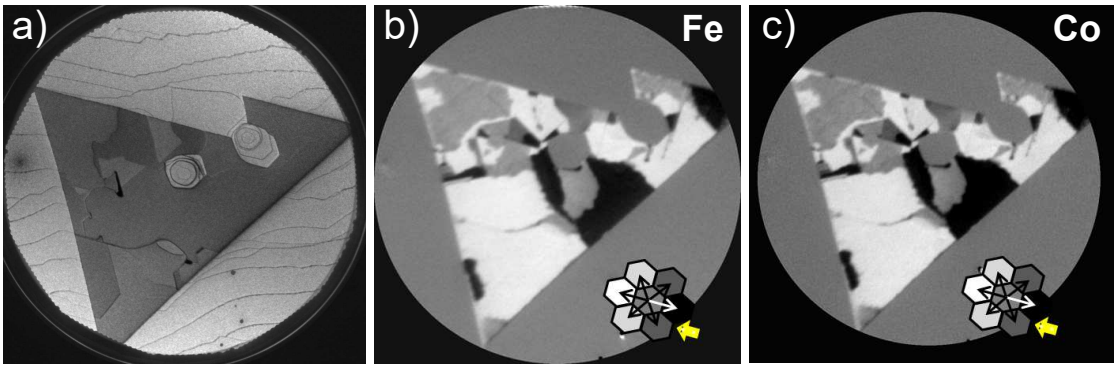

Figure 5.6: a) LEEM image and XMCD-PEEM images obtained at the b) Fe and c) Co L_3-edge showing the magnetic domain configuration. Grayscale magnetic contrast according to the depicted arrow symbol, with beam direction indicated by yellow arrow.

In order to determine the surface magnetization vector we followed a similar process as the one explained in 2.2.5 for SPLEEM images. The asymmetry images in the SPLEEM system are measured by changing the spin polarization direction with respect to the surface sample. However, at the synchrotron the photon beam direction is fixed and to obtain the asymmetry images at different angles, the sample must be rotated with respect to the photon beam. This complicates the process. Even if the lens system of the microscope is carefully aligned, minor distortions in the images will result in small differences between the measured images after each rotation. These non equivalent images can not be directly combined to study the surface magnetism of the sample. To solve this, the shape of the islands were deformed using the plugin Landmark Correspondences available in the Fiji program [40] to make them match each other. Using this process, the images obtained at the synchrotron can be combined to obtain the

dichroic asymmetry vector, which is expected to be proportional to the magnetization vector [38].

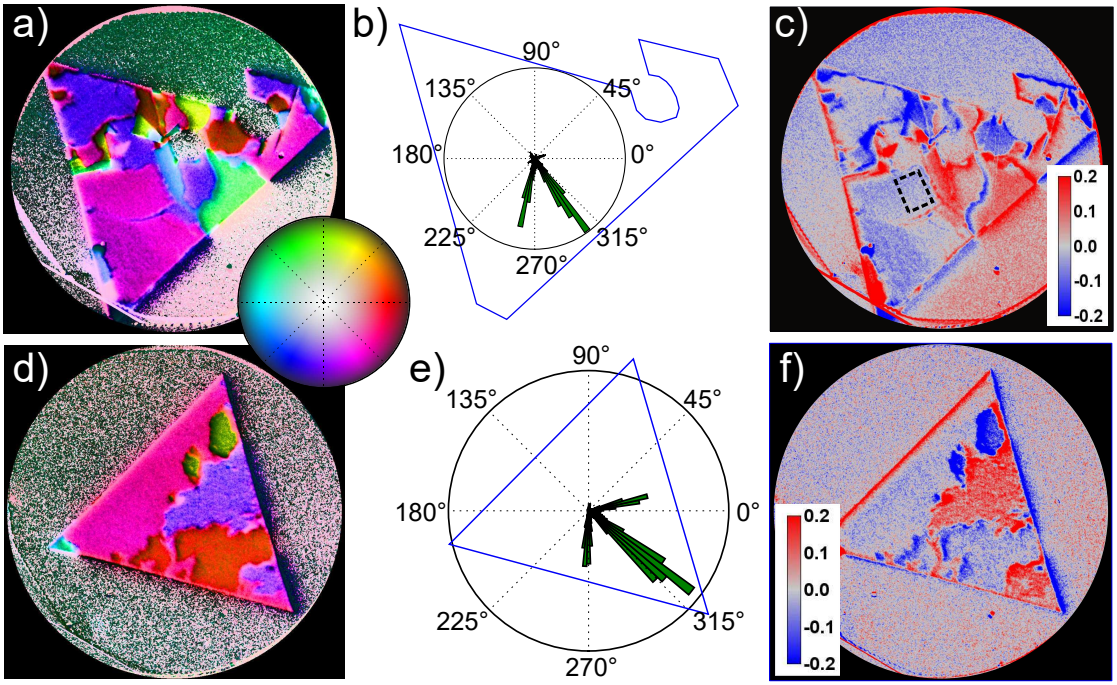

Figure 5.7: a) Composite color image of the island of Fig. 2.13 indicating the local magnetization with color wheel in the inset indicating the correspondence between color and brightness and direction of magnetization. b) Histogram of the magnetization from the data shown in a). c) Magnetization component along the z axis from the same island. The square indicates the area where the XMCD and XAS curves were extracted. d-f) Same as in a-c but for island shown in Fig. 5.2b.

Following this procedure, Figure 5.7a shows the distribution of the magnetization of the island shown in Figure 5.6 where the vector direction is indicated by the color palette of the inset where the color indicates the azimuthal direction of the magnetization and the brightness represents the polar direction of the magnetization. Figure 5.7b shows the histogram of the distribution of the in-plane magnetization values together with the sketch of the island shape as a guide to the eye. The magnetic domains are mostly oriented perpendicular to the island sides, i.e. along the bisectors of the triangle. The in-

plane directions, taking into account Figure 5.3d, correspond to in-plane [112] which are the projections of the bulk easy axis, i.e. [100], onto the (111) plane. Figure 5.7c shows the dichroic asymmetry component along the z direction. Positive z values (red color) indicate that it is pointing outwards the island surface while negative values (blue color) indicate that the magnetization is pointing inwards the island surface. The zero value (gray color) corresponds to a full in-plane component of the magnetization. We observe that some of the magnetic domains are in-plane while others exhibit a significant out of plane component. Similarly, Figure 5.7d shows the distribution of the magnetization of the island in Figure 5.2b. As in the previous case, the magnetization direction is mostly oriented along [112] directions (see Fig. 5.7e). In Figure 5.7f the magnetization component along the z axis reveals in-plane and out of plane magnetic domains where in the latter case, the magnetization points either outwards and inwards the island surface.

In section 2.2.6 we described the process to calculate the magnetic moments using the sum rules. The XMCD and XAS curves used to obtain the magnetic moments result from the average of two XMCD and XAS curves obtained from two magnetic domains magnetized in opposite in-plane directions, i.e. nearly coplanar to the X-ray propagation direction[5]. Figure 5.7 shows that the islands present either in plane and out of plane domains and particularly, the islands studied by XAS did not present opposite magnetized domains with the same orientation relative to the X-ray beam. Thus, the XMCD and XAS curves were extracted from only one in-plane domain, the one marked with a black square in Figure 5.7c.

[5]The X-ray incidence is 16° relative to the surface plane of the sample.

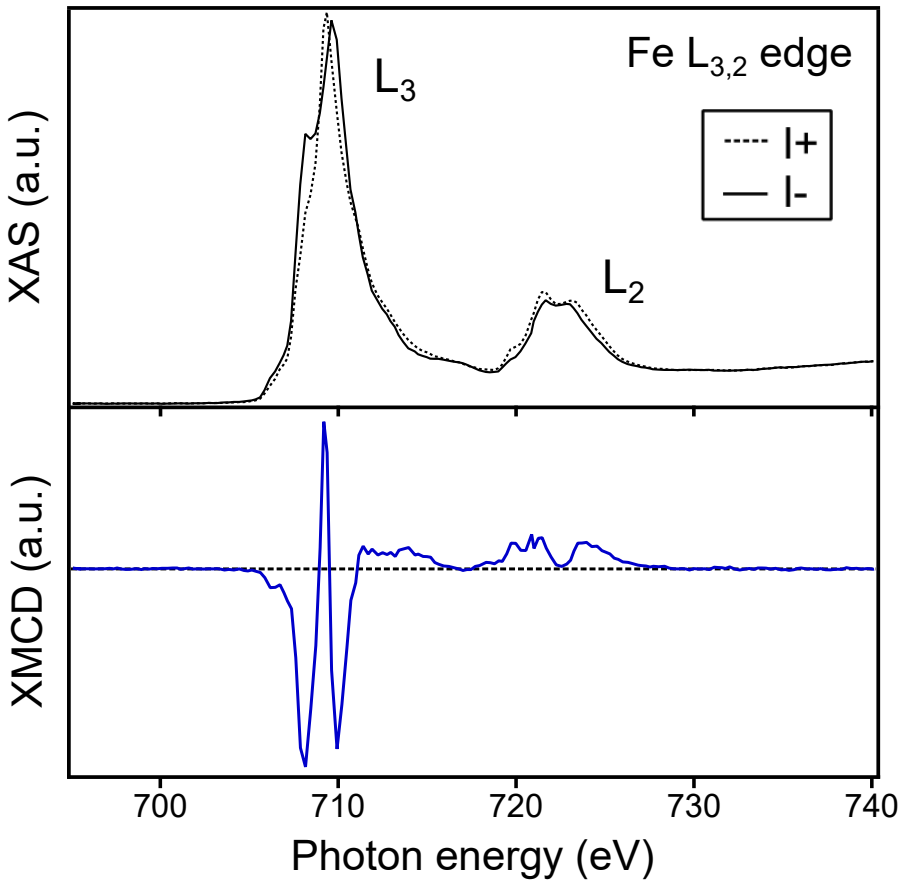

Figure 5.8: XAS (top) and XMCD spectra (bottom) at the Fe L-edge from the island shown in Figure 5.7c.

Figures 5.8 and 5.9 show the Fe and Co XAS and XMCD spectra from the island in Figure 5.7c. The Fe L-edge XMCD spectrum has many similarities with the one exhibited by Fe_3O_4 (compare with spectra of Figure 2.12). It presents at the L_3 region two negative peaks surrounding a positive one. The intensity of the first downward peak compared to that of stoichiometric $CoFe_2O_4$ indicates that the islands contains Fe^{2+} in octahedral positions. The Fe^{3+} cations are distributed between tetrahedral and octahedral sites. The orientation of the peaks indicates that the Fe_{tet} cations are aligned antiferromagnetically to the Fe_{oct} cations while the Fe^{2+} and Fe^{3+} in octahedral positions are ferromagnetically aligned.

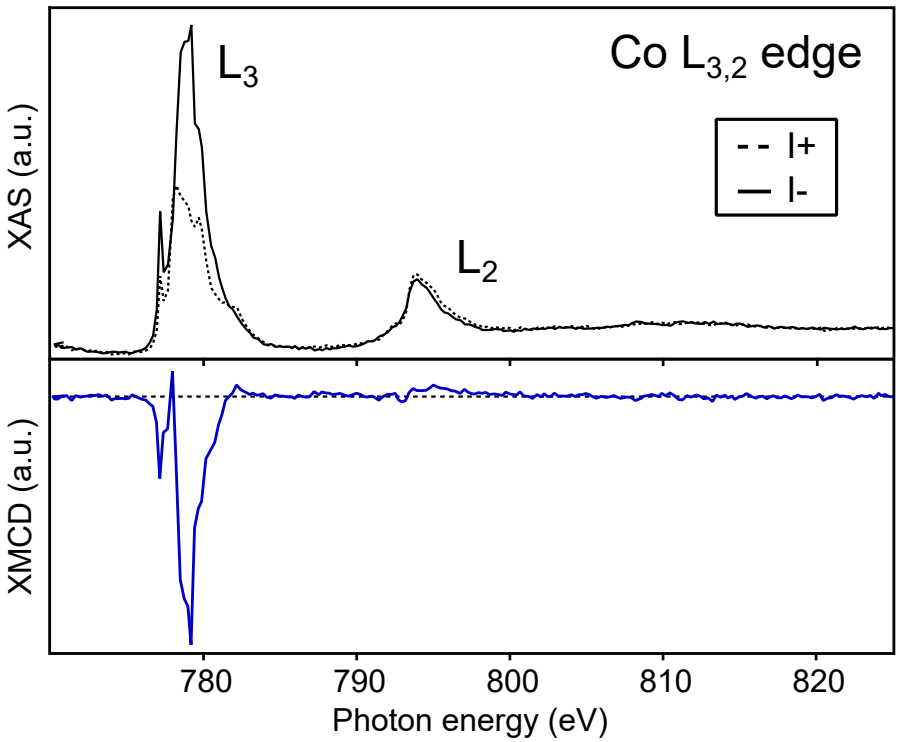

Figure 5.9: XAS (top) and XMCD spectra (bottom) at the Co L-edge from the island shown in Figure 5.7c.

The Co L-edge XMCD spectrum presents a main negative peak in agreement with that of octahedral Co^{2+} measured at $Co_{1-x}Fe_{2+x}O_4$ thin films (compare with Figure 2.14). However, the presence of some Co^{2+} in tetrahedral positions can not be excluded since the main dichroic peak of tetrahedral Co^{2+} is located at the same photon energy as for octahedral Co^{2+} as shown in 2.14. The orientation of the peaks at both Fe and Co XMCD spectra indicates that Co_{oct} is ferromagnetically aligned with Fe_{oct} and antiferromagnetically aligned with Fe_{tet} as shown in Figure 5.6b and c. The general shape, the magnetic alignment of the Fe and Co cations and the presence of Fe^{2+} are indicatives of the formation of a non-stoichiometric Fe-Co spinel.

Following the same argument as for the wetting layer, it is possible to give an estimate of the Fe:Co ratio by comparing the X-ray absorption at the L_3 peak for both elements.

The Fe:Co ratio was found to be 5:1 suggesting a $Co_{0.5}Fe_{2.5}O_4$ island composition.

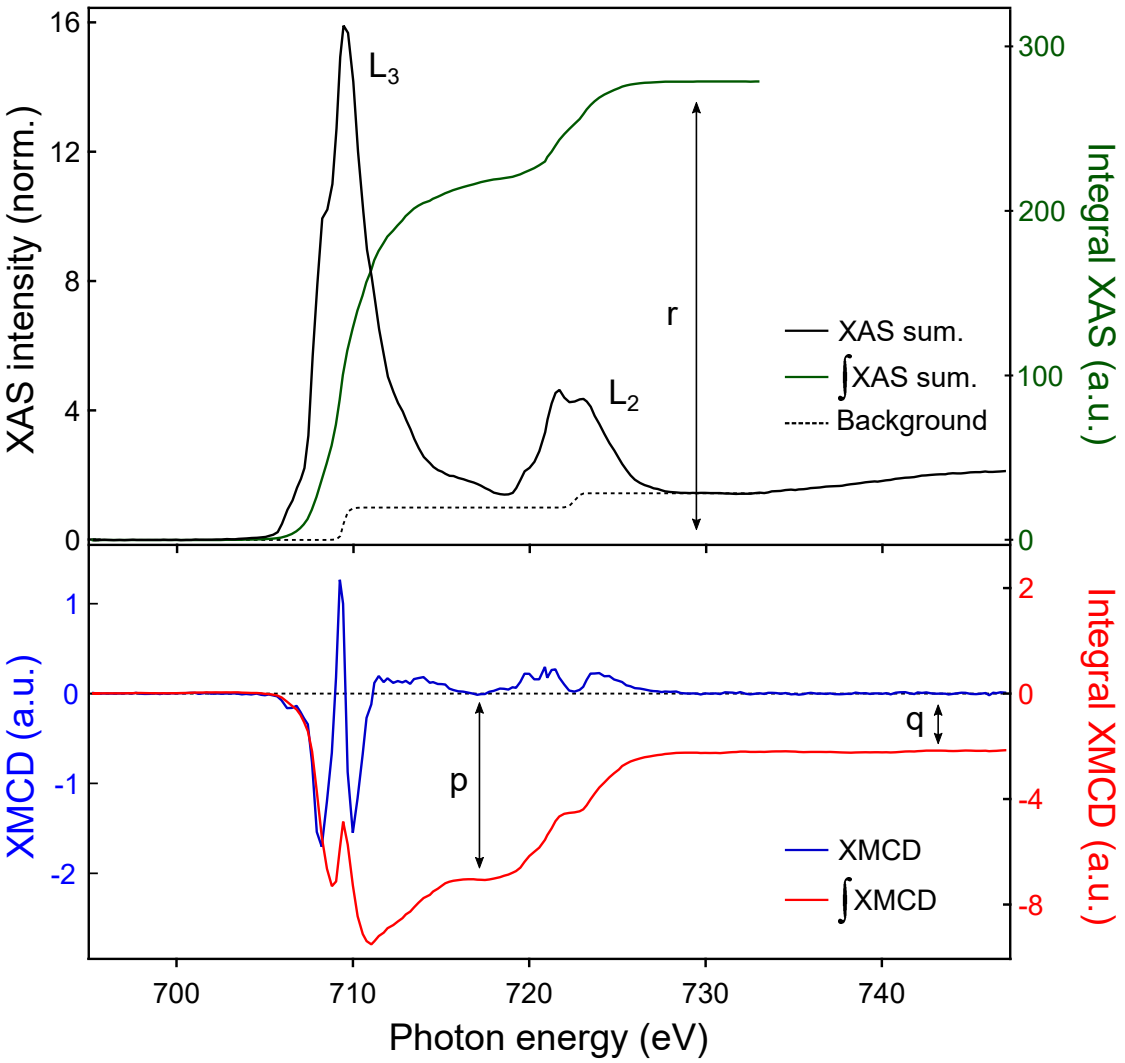

Figure 5.10: XAS summed (in black, top) and XMCD (in blue, bottom) spectra at the Fe $L_{3,2}$ absorption edge. The red line corresponds to the integral of the XMCD curve. The green line corresponds to the integral of the XAS summed spectrum after background subtraction.

The spin and orbital magnetic moments were calculated applying the sum rules. For that, we need to know the electron occupation number per cation, n_d. For simplicity a constant oxidation state for each cation was assumed: Fe was assumed to be in the

Fe^{3+} state with $n_d = 5.3$ [19, 41] and Co to be in the Co^{2+} state with $n_d = 7.21$ [19, 42]. The result of integrating the XMCD and XAS curves for Fe is shown in Figure 5.10. We obtain $m_{spin} = 0.6\ \mu_B$/cation and $m_{orb} = 0.1\ \mu_B$/cation with $\frac{m_{orb}}{m_{spin}} = 0.2$. The high m_{spin} obtained compared with the expected value for stoichiometric CFO is in agreement with the presence of Fe^{2+} in octahedral positions.

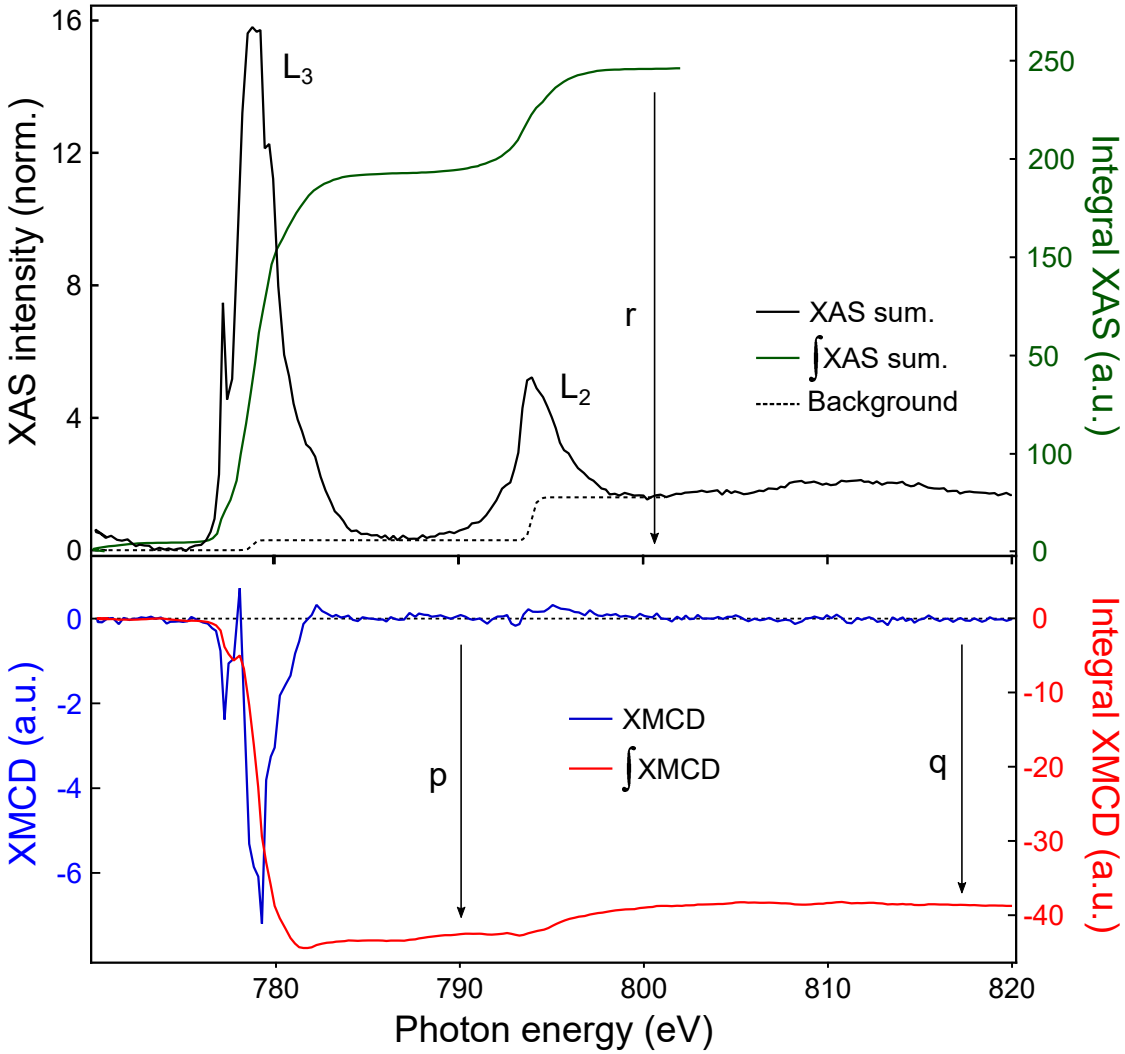

Figure 5.11: XAS summed (in black, top) and XMCD (in blue, bottom) spectra at the Co $L_{3,2}$ absorption edge. The red line corresponds to the integral of the XMCD curve. The green line corresponds to the integral of the XAS summed spectrum after background subtraction.

A similar result was previously reported [21] where the high m_{spin} obtained for Fe was also suggested to arise from the replacement of Co^{2+} by Fe^{2+} in octahedral sites.

Figure 5.11 shows the result of integrating the XMCD and XAS curves for Co. We obtain m_{orb} = 0.6 μ_B/cation and m_{spin} = 1.2 μ_B/cation resulting in $\frac{m_{orb}}{m_{spin}}$= 0.5. The orbital magnetic moment is larger than the one obtained per Fe cation as expected from the unpaired electron of Co^{2+} in octahedral environment. However, both values are below the expectation values of m_{orb} = 1 μ_B/cation and m_{spin} = 3 μ_B/cation.

Considering that the expected m_{spin}/Co cation = 3 μ_B, taking into account the Fe:Co ratio of 5:1 and considering the possibility of having some Co^{2+} in tetrahedral positions, the corresponding composition for the CFO islands is $(Co^{2+}{}_{0.05}Fe^{3+}{}_{0.95})_A[Fe^{3+}Fe^{2+}_{0.55}Co^{2+}_{0.45}]_BO_4$ where A stands for tetrahedral and B for octahedral sites. However that would imply a much higher m_{spin}/Fe cation that the one obtained, 2.35 μ_B/cation vs the obtained 0.6 μ_B/cation. Different explanations can be argued. First, saturation effects were not considered. However, the results obtained in Chapter 3 indicate that saturation effects alone can not be responsible for such a decreased of the m_{spin} value. An alternative explanation for the reduced magnetic moments measured in mixed $Co_{1-x}Fe_{2+x}O_4$ spinels was given by Moyer et al. in Ref. [19]. A $Co_{1-x}Fe_{2+x}O_4$ scenario results in a Fe^{3+} octahedral/tetrahedral ratio > 1. In this situation, it is possible that two Fe^{3+} cations being next-nearest neighbors in the octahedral sublattice had a Co^{2+} cation instead of a Fe^{3+} cation as their next-nearest neighbor in the tetrahedral sublattice. This scenario, with a change of the next nearest neighbors would modify the superexchange interactions that keep the octahedral/tetrahedral cations aligned antiferromagnetically and the octahedral cations aligned ferromagnetically and would result in changes of the magnetic moments. Although our Co^{2+} tetrahedral site occupancy is suggested to be small, it is clear that changes of the superexchange interactions between cations would modify the exhibited magnetic moments for Fe and Co. A different explanation is suggested based on the LEED pattern measured at the islands (see Figure 5.3c). The observed reconstruction may indicate areas with slightly

reduced composition at the surface. If that is the case, and given that XAS is a surface sensitive technique, small variations of the surface composition would also lead to changes in the magnetic moments.

From the values of the projection of the magnetization along the x, y and z coordinates, it is possible to calculate the magnetization polar angle of the domains that exhibit an out of plane component by applying:

$$\theta = \arctan \frac{m_z}{\sqrt{m_x^2 + m_y^2}}$$

Figure 5.12a shows a line crossing two domains with opposite out of plane magnetization directions along which the polar angle has been determined (see Figure 5.12b). The obtained value is 30±10° which is close to the angle between the [100] directions with the (111) plane, i.e. 35° (see Fig. 5.12c). This result suggests that the magnetic orientation of these areas is given by the magnetocrystalline anisotropy overcoming the shape anisotropy.

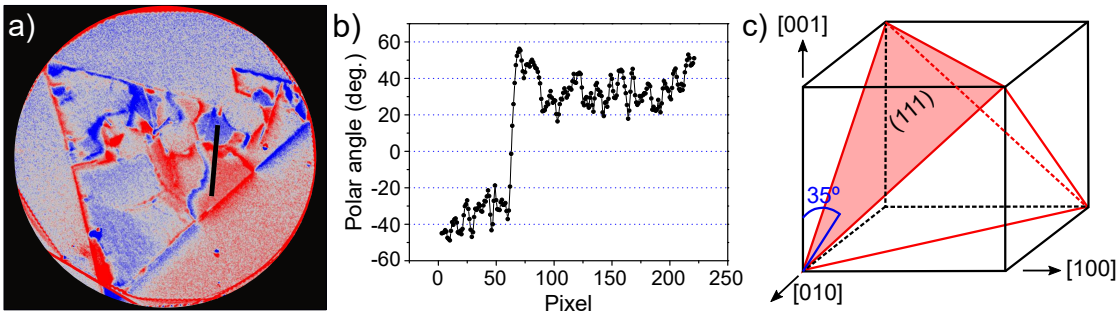

Figure 5.12: a) Magnetization component along the z axis from the island shown in Fig. 5.6 with a line crossing two domains with opposite out of plane magnetization direction. b) Calculated polar angle along the line shown in a). c) Schematic figure indicating the angle between the magnetocrystalline easy axes with the (111) plane of the islands.

The magnetocrystalline anisotropy constant for stoichiometric $CoFe_2O_4$ is found to be $2{\cdot}10^5$ Jm^{-3} [13] although for a cobalt deficient cobalt ferrite it is expected to be smaller as the source of magnetocrystalline anisotropy comes mostly from the Co cations. The shape anisotropy constant for an ultrathin-film is calculated by applying:
$K_s = \frac{1}{2}\mu_0 N {M_s}^2$, where μ_0 is the permeability constant, N is the shape-dependent demagnetization tensor (which is equal to 1 for a thin film) and M_s is the saturation magnetization. By taking M_s for stoichiometric $CoFe_2O_4$ from the literature [43], the value for K_s is $\simeq 1{\cdot}10^5$ Jm^{-3}. This value is close to the magnetocrystalline anisotropy constant and suggests that we are in a situation where both, shape and magnetocrystalline anisotropies compete with similar strength giving rise to a complex pattern where out of plane and in-plane domains coexist.

Annealing in oxygen and exposure to air

XMCD images were measured while increasing the temperature under an oxygen background of $1{\times}10^{-6}$ mbar in order to avoid the creation of vacancies. Magnetic contrast was detected up to a Curie temperature of Tc $\simeq$ 735 K, close to the Curie temperature for bulk $CoFe_2O_4$ (793 K) and Fe_3O_4 (858 K) [12]. This is indicative of the robust magnetic order of these ultrathin islands in contrast to thin films affected by APBs where even a superparamagnetic behaviour has been observed for films below 5 nm thickness [22]. The annealing time was 1 hour. After annealing to T_c and cooling down, we observed that the magnetic domain distribution had changed (see Fig. 5.13b) confirming that most of the domain walls are not pinned to particular defects and the domain configuration should be determined by the competition of different interactions present in the material like the magnetocrystalline anisotropy or the the shape anisotropy. Thus, annealing the sample above Tc changes the magnetic domain configuration of the islands.

The sample was next taken out from the system and was exposed to air for 30 minutes. After that, the sample was reintroduced to the system and XAS spectra were recorded at the islands and the wetting layer in order to identify possible changes. However, they were recorded at a different island, as it was not possible to find the same area of islands explored before. Thus, the conclusions derived from comparing the results obtained before and after the annealing and the exposure to air should be taken with caution.

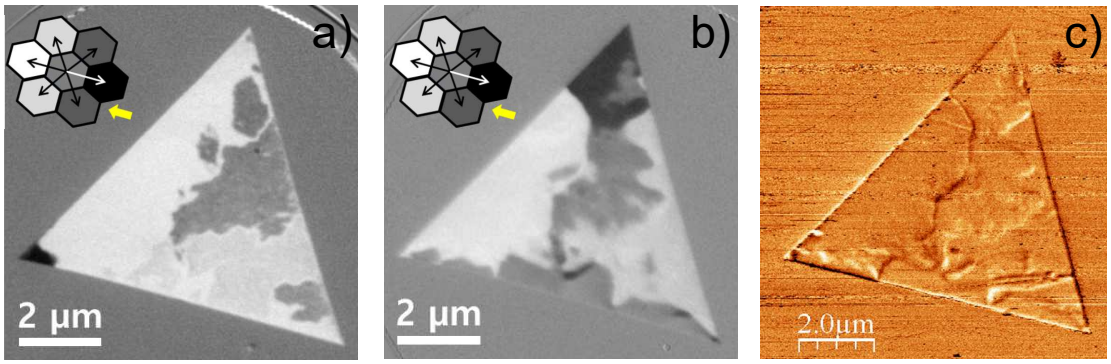

Figure 5.13: XMCD-PEEM images obtained at room temperature a) before and b) after annealing above 735 K. Grayscale magnetic contrast according to the depicted arrow symbol, with beam direction indicated by yellow arrow. c) MFM image of the same island after annealing above 735 K and exposing to air.

- *Wetting layer*

Fig. 5.14 and 5.15 show the XAS (top) and XMCD (bottom) spectra measured at the Fe and Co L-edge at the wetting layer respectively. The Fe XAS spectra are similar to those obtained for the as grown wetting layer and thus, in agreement with Fe^{2+}. However, the left shoulder that was attributed to metallic iron has decreased and moreover there is no signal of dichroism.

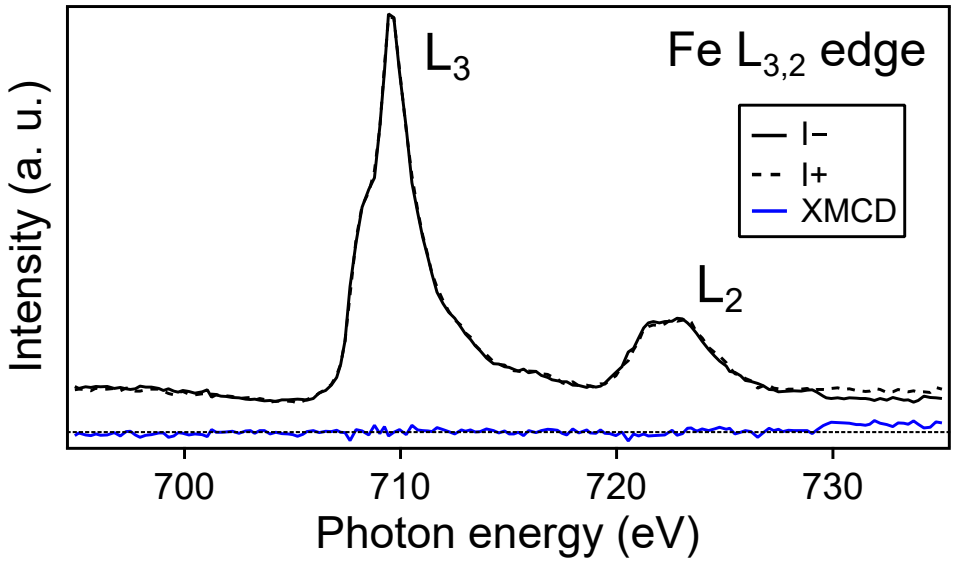

Figure 5.14: XAS (top) and XMCD spectra (bottom) at the Fe L-edge measured at room temperature at the wetting layer after annealing and exposing to air.

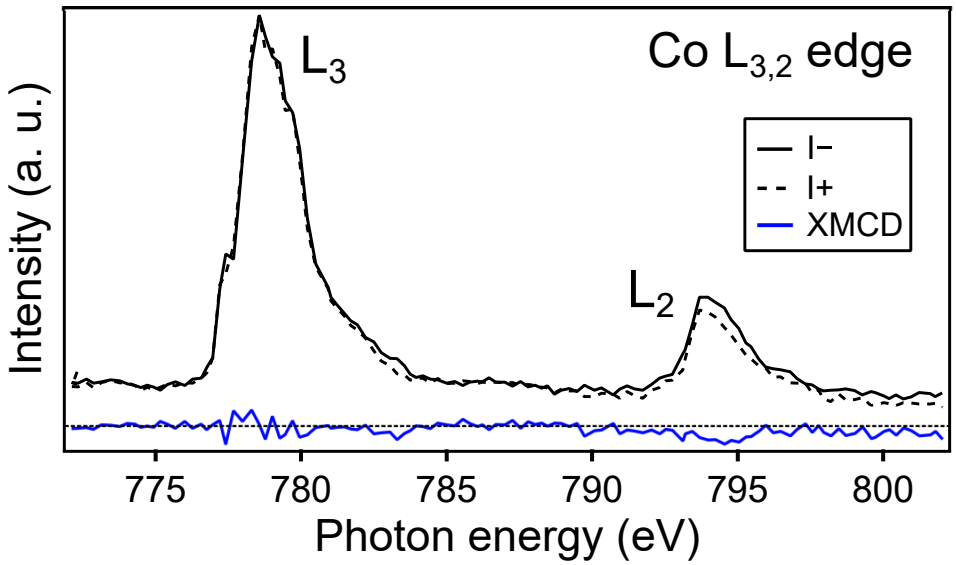

Figure 5.15: XAS (top) and XMCD spectra (bottom) at the Co L-edge measured at room temperature at the wetting layer after annealing and exposing to air.

The Co XAS and XMCD spectra show similar results. The XAS spectra show the typical signatures of a Co^{2+} oxidation state: a clear pre-peak before the L_3 peak and the fine structure at the L_3 peak that were not present for the as grown wetting layer. In addition, no dichroism is observed. Then, after the annealing and exposure to air the wetting layer does no longer show indications of metallic Fe/Co but only the signatures of Fe^{2+}/Co^{2+} oxidations states.

- *Islands*

Figure 5.16 shows the XAS (top) and XMCD (bottom) spectra measured at the Fe-L edge at one of the islands. The general shape of the spectra is similar to the ones obtained for the as grown islands. The XMCD spectrum shows the three peak structure at the L_3 peak in agreement with an spinel structure.

The individual m_{orb} and m_{spin} were not calculated because the surface magnetization vector was not measured and the out of plane orientation of the magnetic domains with respect to the X-ray beam direction remained unknown. However, the ratio $\frac{m_{orb}}{m_{spin}}$ does not depend on the orientation between the magnetization and the X-ray direction. Thus, from the integration of the XMCD curve we obtain $\frac{m_{orb}}{m_{spin}} = 0.2$, the same result as for the as grown islands.

The Co XAS spectrum shown in Fig. 5.17 (top) is also very similar to the one obtained for the as grown islands indicating that the Co cations remain in a Co^{2+} oxidation state where the XMCD spectrum is in agreement with Co^{2+} mainly in octahedral positions. The ratio $\frac{m_{orb}}{m_{spin}} = 0.5$ is also the same as for the as grown islands.

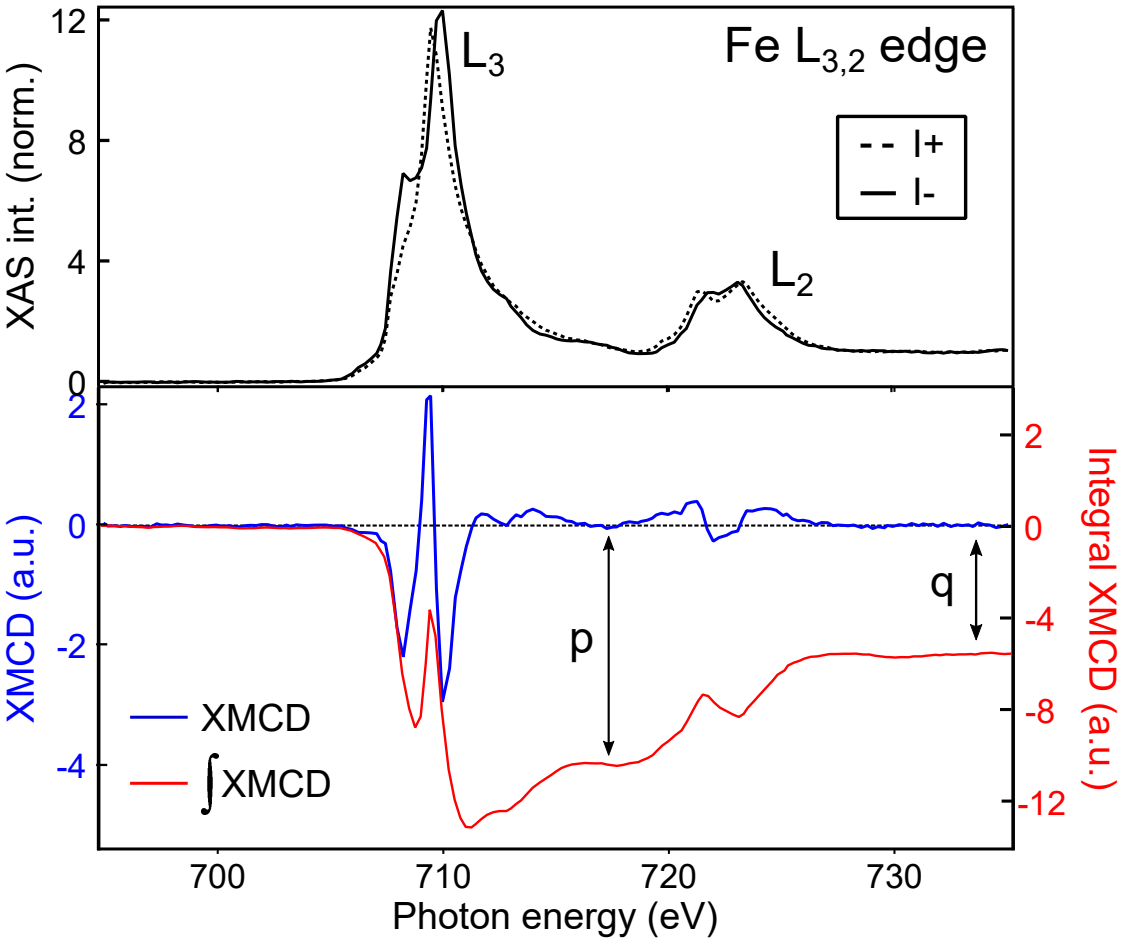

Figure 5.16: XAS (top) and XMCD spectra (bottom) at the Fe L-edge measured at the island.

Interestingly, there are significant changes observed when comparing the XMCD curves measured as growth and after the annealing and exposure to air (see Fig. 5.18 and Fig. 5.19). The XMCD measured at the island as grown are shown with a blue line while the XMCD measured after the annealing and exposure to air are shown by a green line. Comparison of both XMCD spectra at the Co-L edge in Fig. 5.18 reveals an increase in the dichroism after the annealing and exposure to air implying that the contribution from the Co^{2+} in octahedral positions has increased. It has been reported that the cation distribution in CFO depends on

the heat treatment [8, 9]. In our case, the annealing may have led to a migration of the original Co^{2+} located in tetrahedral positions at the as grown islands into Co^{2+} in octahedral positions.

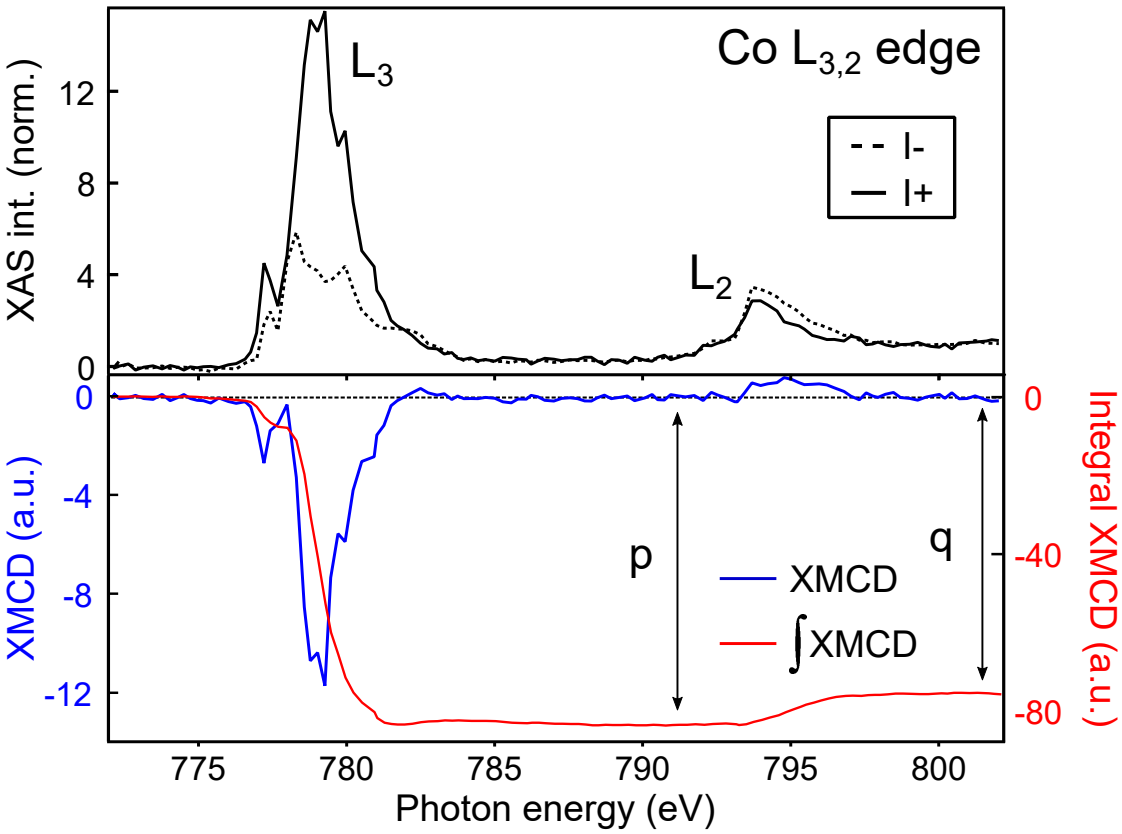

Figure 5.17: XAS (top) and XMCD spectra (bottom) at the Co L-edge measured at the island.

The comparison of the Fe XMCD spectra is shown in Fig. 5.19. The first downward peak which is mainly attributed to Fe^{2+} in octahedral positions has decreased after the annealing and exposure to air leading to an XMCD curve closer to the spectrum reported for an stoichiometric $CoFe_2O_4$.

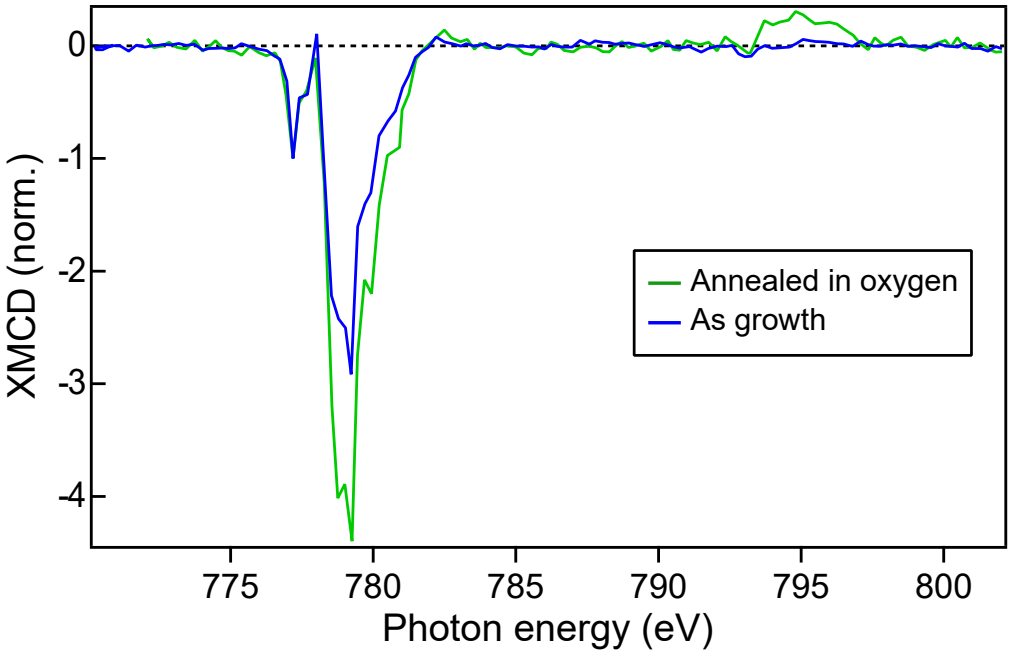

Figure 5.18: Co XMCD spectra measured at the islands a) as growth and b) after annealing in oxygen and normalized to the intensity at 777.2 eV.

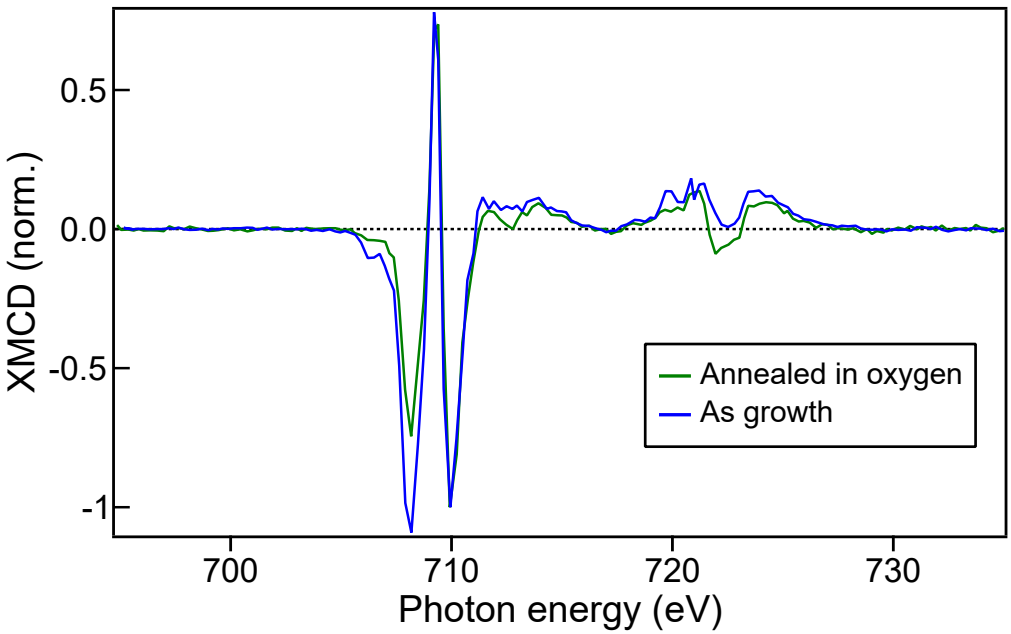

Figure 5.19: Fe XMCD spectra measured at the islands a) as growth and b) after annealing in oxygen and normalized to the intensity at 710 eV.

In conclusion, by annealing and exposing the sample to air, the cationic distribution at the islands changed giving rise to an spinel structure with an increased degree of inversion. Most of the Co^{2+} is in octahedral positions while the Fe^{2+} contribution has decreased. This is an important observation in agreement with previous results that report that annealing treatments induce a change in the cationic distribution of CFO.

5.4 *Ex-situ* AFM/MFM characterization

The surface topography of the islands and the magnetism was studied *ex-situ* by AFM and MFM techniques. The measurements were performed by C. Munuera at the Instituto de Ciencia de Materiales de Madrid (ICMM, CSIC). To correlate the data obtained by PEEM with the A(M)FM information it was necessary first to identify the same previously studied islands with an optical microscope. This was possible due to the large size of the islands which could be detected with such an instrument.

Figure 5.20a contains an AFM image of the same island shown in Fig. 5.3a. The profile shown in Fig. 5.20b shows that the thickness of the island varies between 5 nm and 10 nm. This height difference at both sides is explained by the underlying substrate slope shown in the 3D lateral view of Fig. 5.20c. It should be noted that the surface of the island was found to be almost perfectly flat. By measuring a series of islands it was found that in most cases the surface roughness was below 0.38 nm (rms), which, given the fact that chemical species are adsorbed when exposed to air, is equivalent to atomic flatness.

Fig. 5.20e shows an AFM image of an island with a region thinner than 1 nm, with the associated XMCD magnetic domain structure shown in Fig. 5.20f. The

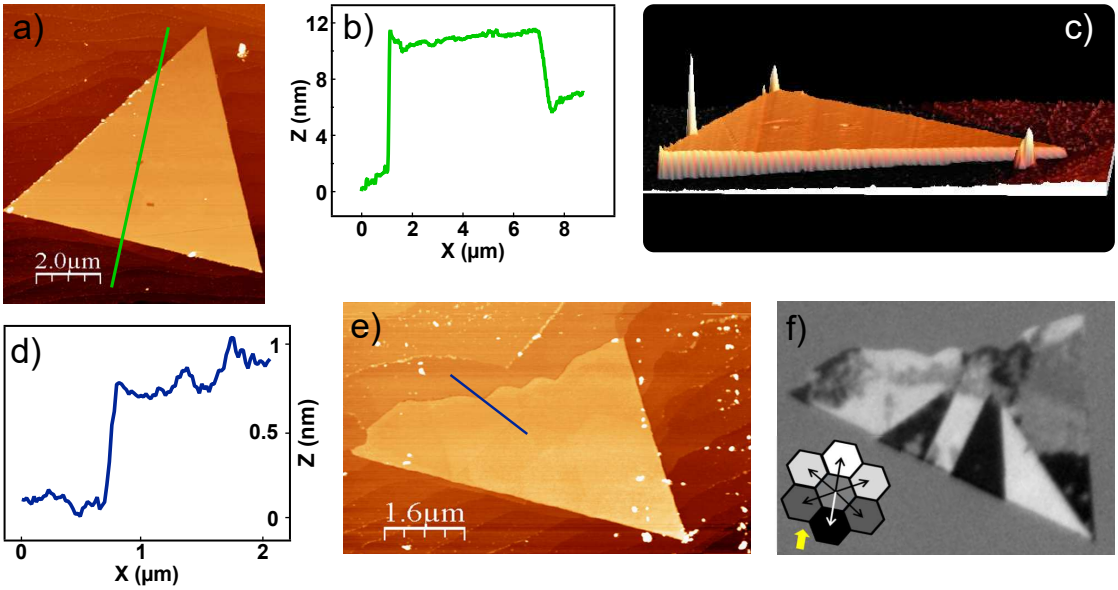

Figure 5.20: a) AFM image of the same island in 5.3a. The green profile line is shown in (b). c) 3D lateral view of the same island highlighting the increase in thickness along the substrate downhill direction. d) Blue line profile of the island shown in (e). f) XMCD-PEEM image portraying the magnetic domain structure of the island shown in (e). Grayscale magnetic contrast according to the depicted arrow symbol, with the beam direction indicated by a yellow arrow.

thickness profile is depicted in Fig. 5.20d. Again, due to the substrate slope below, only one of its edges is below 1 nm, with the rest of the structure being thicker. Remarkably, the magnetic order persists at these ultrathin regions with slightly less XMCD contrast due to the lesser amount of material.

The thickness range of the islands were found to be between 1 and 100 nm while widths ranged from 0.7 to 11 μm, with an inverse correlation between island size and thickness.

The combination of LEEM and AFM techniques allows us to correlate some of the observed physical properties with morphological features of the islands, like the pinning sites for domain walls. For example, the domain wall indicated by a black arrow in Fig. 5.21a is pinned to a step as shown in the profile of Fig. 5.21c.

The measured step height was 0.5±0.2 nm height, in reasonable agreement with the CFO unit cell height along the <111> direction of 0.48 nm. On the other hand, the domain wall marked with a red arrow is not associated with a thickness change, and might be attributed to a twin boundary.

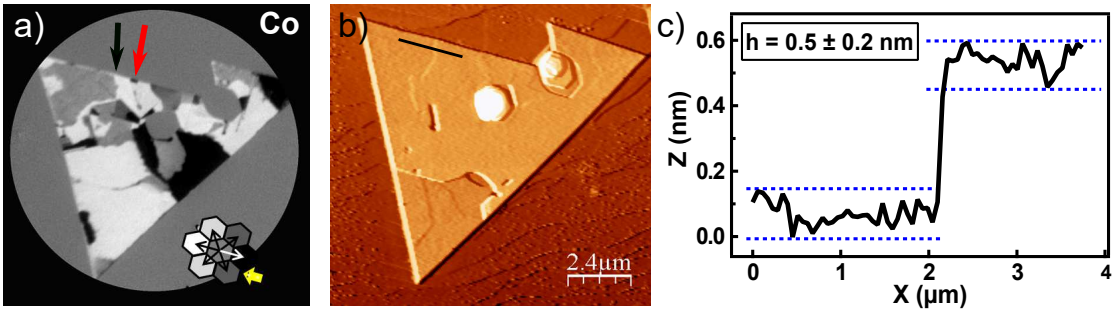

Figure 5.21: a) XMCD-PEEM image measured at the Co-L_3 edge of the island shown in 5.6a. b) AFM image of the same island whose black profile line is shown in (c). The domain wall marked with a black line in (a) is pinned to a step with a measured height of 0.5 nm.

The stability of the surface magnetic domain configuration after several weeks of air exposure is confirmed by comparing Fig. 5.13b and c. We note that due to the geometry of the incident photon beam, the XMCD-PEEM is more sensitive to the in-plane component of the magnetization. In this sense, MFM measurements provide a complementary information as the tips used to acquire the images are magnetized perpendicular to the sample plane and the contrast observed arises then from the variation of the tip-sample interaction along the direction perpendicular to the sample. Thus, the in-plane magnetic domains do not present significant MFM contrast while domain walls are clearly revealed. The magnetic domain distribution from Fig. 5.13b and c matches what means that the magnetic domain configuration has not changed after a few weeks of air exposure.

5.5 Conclusions

High-quality single crystals of iron-cobalt spinel oxide were synthesized by O-MBE on Ru(0001) by following the growth in real time and real space by LEEM. The islands are atomically flat and each one arises from a presumably single nucleus avoiding the formation of antiphase boundaries. The composition and magnetic properties of the islands and the wetting layer have been investigated by XAS and XMCD. The wetting layer is composed of a Fe-Co monoxide although there were signatures of the presence of a small amount of metallic Fe and Co. The islands present an spinel structure where the Co^{2+} cations are mainly located at octahedral positions and the Fe^{3+} is at both tetrahedral and octahedral positions. Additional Fe^{2+} is also present at octahedral positions. The composition was estimated by XAS to be $Co_{0.5}Fe_{2.5}O_4$. The magnetic moments were calculated applying the sum rules obtaining m_{spin} = 0.6 μ_B and m_{orb} = 0.1 μ_B per Fe cation and m_{spin} = 1.2 μ_B and m_{orb} = 0.6 μ_B per Co cation. The high (low) m_{spin} obtained for Fe and Co respectively is in agreement with the presence of Fe^{2+} substituting Co^{2+} in octahedral positions. In addition, we measure a larger m_{orb} for Co than for Fe as expected from the unpaired electron of Co^{2+} in octahedral environment.

The thinnest islands studied by PEEM present a magnetic pattern which was suggested to arise from the competition between the shape and the magnetocrystalline anisotropy. The Co^{2+} and $Fe^{3+/2+}$ at octahedral positions are aligned ferromagnetically exhibiting the same in plane configuration. The high crystalline quality leads to a magnetic domain configuration that is robust up to 735 K, down to the nanometer level, with stable large magnetic domains several orders of magnitude larger than reported previously in the literature. After the annealing and exposure to air the Fe and Co at the wetting layer are only in a Fe^{2+}/Co^{2+} oxidation state. The measured island show an increase of the dichroic intensity at the

Co-L edge compatible with the migration of Co^{2+} originally located in tetrahedral positions to octahedral positions. This result is in agreement with the XMCD spectrum of Fe measured after the annealing and exposure to air that shows a decrease of the Fe^{2+} signal. The magnetic domain configuration remained unaltered after few weeks of exposure in air as revealed by the comparison of MFM with XMCD images. In addition, the combination of *in-situ* experiments and *ex-situ* characterization allowed us to correlate the structure ans physical properties like the pinning sites of the domain walls at the islands.

Bibliography

[1] S. N. Piramanayagam. Perpendicular recording media for hard disk drives. *Journal of Applied Physics*, 102(1):011301, 2007.

[2] H. Zheng, F. Straub, Q. Zhan, P.-L. Yang, W.-K. Hsieh, F. Zavaliche, Y.-H. Chu, U. Dahmen, and R. Ramesh. Self-Assembled Growth of $BiFeO_3$-$CoFe_2O_4$ Nanostructures. *Advanced Materials*, 18(20):2747–2752, 2006.

[3] S. M. Stratulat, X. Lu, A. Morelli, D. Hesse, W. Erfurth, and M. Alexe. Nucleation-Induced Self-Assembly of Multiferroic $BiFeO_3$-$CoFe_2O_4$ Nanocomposites. *Nano Letters*, 13(8):3884–3889, 2013.

[4] Y. Suzuki, R. B. van Dover, E. M. Gyorgy, J. M. Phillips, and R. J. Felder. Exchange coupling in single-crystalline spinel-structure (Mn,Zn)Fe_2O_4/$CoFe_2O_4$ bilayers. *Physical Review B*, 53:14016–14019, 1996.

[5] A. V. Ramos, M.-J. Guittet, J.-B. Moussy, R. Mattana, C. Deranlot, F. Petroff, and C. Gatel. Room temperature spin filtering in epitaxial cobalt-ferrite tunnel barriers. *Applied Physics Letters*, 91(12):122107, 2007.

[6] A. V. Ramos, T. S. Santos, G. X. Miao, M.-J. Guittet, J.-B. Moussy, and J. S. Moodera. Influence of oxidation on the spin-filtering properties of $CoFe_2O_4$ and the resultant spin polarization. *Physical Review B*, 78:180402, 2008.

[7] Y. H. Hou, Y. J. Zhao, Z. W. Liu, H. Y. Yu, X. C. A. Zhong, W. Q. Qiu,

D. C. Zeng, and L. S. Wen. Structural, electronic and magnetic properties of partially inverse spinel $CoFe_2O_4$: a first-principle study. *Journal of Physics D: Applied Physics*, 43:445003, 2010.

[8] G. A. Sawatzky, F. Van Der Woude, and A. H. Morrish. Mössbauer Study of Several Ferrimagnetic Spinels. *Physical Review*, 187:747–757, 1969.

[9] G. Hu, J. H. Choi, C. B. Eom, V. G. Harris, and Y. Suzuki. Structural tuning of the magnetic behavior in spinel-structure ferrite thin films. *Physical Review B*, 62:R779–R782, 2000.

[10] D. Carta, G. Mountjoy, G. Navarra, M. F. Casula, D. Loche, S. Marras, and A. Corrias. X-ray Absorption Investigation of the Formation of Cobalt Ferrite Nanoparticles in an Aerogel Silica Matrix. *Journal of Physical Chemistry C*, 111(17):6308–6317, 2007.

[11] T. A. S. Ferreira, J. C. Waerenborgh, M. H. R. M. Mendonça, M. R. Nunes, and F. M. Costa. Structural and morphological characterization of $FeCo_2O_4$ and $CoFe_2O_4$ spinels prepared by a coprecipitation method. *Solid State Sciences*, 5(2):383 – 392, 2003.

[12] J.-B. Moussy. From epitaxial growth of ferrite thin films to spin-polarized tunnelling. *Journal of Physics D: Applied Physics*, 46(14):143001, 2013.

[13] B. D. Cullity and C. D. Graham. *Introduction to Magnetic Materials*. John Wiley Sons, Inc., 2008.

[14] S. J. Kim, S. W. Lee, and C. S. Kim. Mössbauer Studies on Exchange Interactions in $CoFe_2O_4$. *Japanese Journal of Applied Physics*, 40(8R):4897, 2001.

[15] Z. Szotek, W. M. Temmerman, D. Ködderitzsch, A. Svane, L. Petit, and

H. Winter. Electronic structures of normal and inverse spinel ferrites from first principles. *Physical Review B*, 74:174431, 2006.

[16] Y. K. Wakabayashi, Y. Nonaka, Y. Takeda, S. Sakamoto, K. Ikeda, Z. Chi, G. Shibata, A. Tanaka, Y. Saitoh, H. Yamagami, M. Tanaka, A. Fujimori, and R. Nakane. Electronic structure and magnetic properties of magnetically dead layers in epitaxial $CoFe_2O_4/Al_2O_3/Si(111)$ films studied by X-ray magnetic circular dichroism. *Pre-print*. arXiv:1704.01712.

[17] W. H. Wang and X. Ren. Flux growth of high-quality $CoFe_2O_4$ single crystals and their characterization. *Journal of Crystal Growth*, 289(2):605 – 608, 2006.

[18] S. Matzen, J.-B. Moussy, R. Mattana, F. Petroff, C. Gatel, B. Warot-Fonrose, J. C. Cezar, A. Barbier, M.-A. Arrio, and Ph. Sainctavit. Restoration of bulk magnetic properties by strain engineering in epitaxial $CoFe_2O_4(001)$ ultrathin films. *Applied Physics Letters*, 99(5):052514, 2011.

[19] J. A. Moyer, C. A. F. Vaz, D. A. Arena, D. Kumah, E. Negusse, and V. E. Henrich. Magnetic structure of Fe-doped $CoFe_2O_4$ probed by x-ray magnetic spectroscopies. *Physical Review B*, 84(5):054447, 2011.

[20] H. S. Mund, S. Tiwari, J. Sahariya, M. Itou, Y. Sakurai, and B. L. Ahuja. Investigation of orbital magnetization in inverse spinel cobalt ferrite using magnetic Compton scattering. *Journal of Applied Physics*, 110(7):073914, 2011.

[21] S. Nappini, E. Magnano, F. Bondino, I. Píš, A. Barla, E. Fantechi, F. Pineider, C. Sangregorio, L. Vaccari, L. Venturelli, and P. Baglioni. Surface Charge and Coating of $CoFe_2O_4$ Nanoparticles: Evidence of Preserved Magnetic and Electronic Properties. *Journal of Physical Chemistry C*, 119(45):25529–25541, 2015.

Bibliography

[22] W. Eerenstein. *Spin-dependent transport across anti-phase boundaries in magnetite films.* PhD thesis, Laboratory of Physical Chemistry/University of Groningen, Netherlands, 2003.

[23] M. Coll, Josep M. Montero M., J. Gazquez, K. Nielsch, X. Obradors, and T. Puig. Low Temperature Stabilization of Nanoscale Epitaxial Spinel Ferrite Thin Films by Atomic Layer Deposition. *Advanced Functional Materials*, 24(34):5368–5374, 2014.

[24] W. Eerenstein, T. T. M. Palstra, S. S. Saxena, and T. Hibma. Spin-Polarized Transport across Sharp Antiferromagnetic Boundaries. *Physical Review Letters*, 88:247204, 2002.

[25] M. Luysberg, R. G. S. Sofin, S. K. Arora, and I. V. Shvets. Strain relaxation in $Fe_3O_4/MgAl_2O_4$ heterostructures: Mechanism for formation of antiphase boundaries in an epitaxial system with identical symmetries of film and substrate. *Physical Review B*, 80:024111, 2009.

[26] S. A. Chambers, R. F. C. Farrow, S. Maat, M. F. Toney, L. Folks, J. G. Catalano, T. P. Trainor, and G. E. Brown Jr. Molecular beam epitaxial growth and properties of $CoFe_2O_4$ on MgO(001). *Journal of Magnetism and Magnetic Materials*, 246(1-2):124–139, 2002.

[27] D. Gilks, Z. Nedelkoski, L. Lari, B. Kuerbanjiang, K. Matsuzaki, T. Susaki, D. Kepaptsoglou, Q. Ramasse, R. Evans, K. McKenna, and V. K. Lazarov. Atomic and electronic structure of twin growth defects in magnetite. *Scientific Reports*, 6(20943), 2016.

[28] M. T. Johnson, P. G. Kotula, and C. B. Carter. Growth of nickel ferrite thin films using pulsed-laser deposition. *Journal of Crystal Growth*, 206(4):299 – 307, 1999.

[29] B. Santos, E. Loginova, A. Mascaraque, A. K. Schmid, K. F. McCarty, and J. de la Figuera. Structure and magnetism in ultrathin iron oxides characterized by low energy electron microscopy. *Journal of Physics: Condensed Matter*, 21(31):314011, 2009.

[30] G. S. Parkinson. Iron oxide surfaces. *Surface Science Reports*, 71(1):272 – 365, 2016.

[31] N. G. Condon, F. M. Leibsle, T. Parker, A. R. Lennie, D. J. Vaughan, and G. Thornton. Biphase ordering on $Fe_3O_4(111)$. *Physical Review B*, 55:15885–15894, 1997.

[32] M. Monti. *Ultrathin Iron Oxide Films on Ru(0001)*. PhD thesis, Universidad Autónoma de Madrid, Spain, 2014.

[33] M. Paul, M. Sing, R. Claessen, D. Schrupp, and V. A. M. Brabers. Thermodynamic stability and atomic and electronic structure of reduced $Fe_3O_4(111)$ single-crystal surfaces. *Physical Review B*, 76:075412, 2007.

[34] N. G. Condon, F. M. Leibsle, A. R. Lennie, P. W. Murray, D. J. Vaughan, and G. Thornton. Biphase Ordering of Iron Oxide Surfaces. *Physical Review Letters*, 75:1961–1964, 1995.

[35] P. S. Miedema and F. M. F. de Groot. The iron L edges: Fe 2p X-ray absorption and electron energy loss spectroscopy. *Journal of Electron Spectroscopy and Related Phenomena*, 187:32 – 48, 2013.

[36] H. J. Lee, G. Kim, D. H. Kim, J.-S. Kang, C. L. Zhang, S.-W. Cheong, J. H. Shim, S. Lee, H. Lee, J.-Y. Kim, B. H. Kim, and B. I. Min. Valence states and occupation sites in $(Fe,Mn)_3O_4$ spinel oxides investigated by soft x-ray absorption spectroscopy and magnetic circular dichroism. *Journal of Physics: Condensed Matter*, 20(29):295203, 2008.

[37] T. J. Regan, H. Ohldag, C. Stamm, F. Nolting, J. Lüning, J. Stöhr, and R. L. White. Chemical effects at metal/oxide interfaces studied by x-ray-absorption spectroscopy. *Physical Review B*, 64:214422, 2001.

[38] J. Stöhr and H. C. Siegmann. *Magnetism: From Fundamentals to Nanoscale Dynamics*. Springer, 2006.

[39] G. Radaelli, D. Petti, E. Plekhanov, I. Fina, P. Torelli, B. R. Salles, M. Cantoni, C. Rinaldi, D. Gutiérrez, G. Panaccione, M. Varela, S. Picozzi, J. Fontcuberta, and R. Bertacco. Electric control of magnetism at the Fe/BaTiO 3 $interface. Nature Communications, 5 : 3404, 2014.$

[40] J. Schindelin, I. Arganda-Carreras, E. Frise, V. Kaynig, M. Longair, T. Pietzsch, S. Preibisch, C. Rueden, S. Saalfeld, B. Schmid, J.-Y. Tinevez, D. J. White, V. Hartenstein, K. Eliceiri, P. Tomancak, and A. Cardona. Fiji: an open-source platform for biological-image analysis. *Nature Methods*, 9:676–682, 2012.

[41] T. Saitoh, A. E. Bocquet, T. Mizokawa, and A. Fujimori. Systematic variation of the electronic structure of 3d transition-metal compounds. *Physical Review B*, 52:7934–7938, 1995.

[42] G. van der Laan, E. Arenholz, R. V. Chopdekar, and Y. Suzuki. Influence of crystal field on anisotropic x-ray magnetic linear dichroism at the Co^{2+} $L_{2,3}$ edges. *Physical Review B*, 77:064407, 2008.

[43] A. F. Júnior, V. Zapf, and P. Egan. Magnetic properties of nanoparticles of $Co_xFe_{(3-x)}O_4$ (0.05≤x≤1.6) prepared by combustion reaction. *Journal of Applied Physics*, 101(9):09M506, 2007.

CHAPTER 6

Conclusions

1. $Fe_3O_4(001)$

- The (001) surface of a Fe_3O_4 single crystal was studied by a combination of LEEM, LEED, SPLEEM and XMCD. The surface magnetic domain configuration was investigated by combining SPLEEM asymmetry images acquired with the spin-polarized beam along orthogonal directions. This approach allowed us to obtain the surface magnetization vector and helped us to investigate in detail the evolution of the surface magnetization with temperature and through the Verwey and spin reorientation transitions.

- The magnetic domain configuration was sensitive to changes of the sample temperature. When annealing the sample in the 300–700 K range or cooling in the 300–T_{srt} K range the magnetic domains lost all the fine microstructure transforming into large domains with uniform magnetization and separated by straight domain walls. These results were explained based on the changes of the magnetocrystalline anisotropy with the temperature. In addition, the crystal surface exhibited a "memory effect", i.e., the

magnetic domain configuration exhibited before the annealing/cooling was in great part recovered when returning back to room temperature.

- The spin reorientation transition of the crystal was found at T∼144 K. At T_{srt} the magnetic easy axis directions switched from the in-plane ⟨110⟩ directions to the in-plane ⟨100⟩ directions. The spin reorientation transition took place in two steps: first, there was the nucleation of new domains oriented along the ⟨100⟩ directions followed by a smooth orientation of the remaining domains to the low temperature easy axes. To our knowledge this was the first time that the evolution of the magnetic domains through the spin reorientation transition has been followed. However, further work is needed to understand the origin of the two step process.

- The spin and orbital magnetic moments of the reconstructed $Fe_3O_4(001)$ surface were determined by XMCD. We obtained a reduced spin magnetic moment of 2.61–3.03 μ_B and an orbital magnetic moment of 0.30–0.45 μ_B. As the near surface region of the reconstructed $Fe_3O_4(001)$ contains only Fe^{3+} the reduced spin magnetic moment was suggested to be related to the reconstruction. In addition, the sizable orbital magnetic moment was explained based on the non-stoichiometry of the reconstructed surface that can give rise to uncompensated orbital moments.

2. Mixed Fe-Co oxides on Ru(0001)

- FeO(111) thin films were grown on Ru(0001) by IR-PLD. Films with thicknesses up to several nanometers were synthesized using IR-PLD in contrast to the thickness limit of four monolayers achievable by MBE on Ru(0001). The films exhibited unexpected properties as a (1×1) termination and the lack of Fe^{3+} usually observed in thin films grown by MBE and that is related to the evolution of FeO to Fe_3O_4. These features were explained by first-principles calculations based on the existence of a wurtzite-like

surface stacking in contrast with the rocksalt structure of bulk FeO. The variation of the substrate-target distance was investigated revealing that the PLD growth took place by the initial deposition of metallic iron followed by the growth of FeO. It was also observed that the substrate temperature played an important role on the structure of the films. Films deposited at room temperature were disordered and contained Fe^{3+} while films deposited at substrate temperatures above 873 K were crystalline and contained only Fe^{2+}.

- The growth of ultrathin FeO films on Ru(0001) by O-MBE was investigated by LEEM. The growth performed at a pressure of 10^{-6} mbar of O_2 led to islands of bilayer height that covered all the surface. Stopping the growth before completing the layer led to triangular shaped islands with opposite orientations. The obtained diffraction pattern presented a moiré aligned with the Ru one in agreement with a (111) orientation. CoO growth was different compared to the FeO case. The deposition at different temperatures proceeded by the growth of three dimensional islands nucleating around the Ru(0001) steps. The growth at 950 K gave rise to CoO islands with a triangular shape with two opposite orientations. In addition, fewer rectangular islands were obtained. The triangular islands presented an hexagonal LEED pattern indicating a (111) orientation. However in this case the pattern was rotated with respect the Ru one by 30°. The rectangular islands presented a square diffraction pattern suggesting a (100) orientation.

- Mixed Fe-Co oxides were grown on Ru(0001) by O-MBE. The growth proceeded in a similar way to the FeO case with islands growing until covering the surface of the substrate. Two families of islands rotated by 30° between them were obtained with hexagonal LEED patterns rotated by the same amount. XAS confirmed that both families of islands were of a mixed composition of Fe and Co monoxides although they exhibited a different amount of Co. The Fe content remained constant between the two families of islands.

3. Cobalt ferrite islands on Ru(0001)

- High-quality single crystals of cobalt ferrite were synthesized by O-MBE on Ru(0001) by following the growth in real time and real space by LEEM. The obtained islands were atomically flat and each one arose presumably from a single nucleus, avoiding the formation of antiphase boundaries. The thickness of the islands investigated by AFM was found to be between 1 and 100 nm while widths ranged from 0.7 to 11 μm, with an inverse correlation between island size and thickness.

- The composition and magnetic properties of the islands and the wetting layer were investigated by XAS and XMCD. The wetting layer was composed of a Fe-Co monoxide although there were signatures of the presence of a small amount of metallic Fe and Co. The islands presented an spinel structure with Co^{2+} cations mainly located at octahedral positions. The Fe^{3+} cations were at both tetrahedral and octahedral positions and additional Fe^{2+} was also found at octahedral positions. The composition of the islands was suggested to be $Co_{0.5}Fe_{2.5}O_4$. The magnetic moments were calculated by applying the sum rules in XMCD and resulted in m_{spin} = 0.6 μ_B/Fe cation and m_{orb} = 0.1 μ_B/Fe cation and m_{spin} = 1.2 μ_B/Co cation and m_{orb} = 0.6 μ_B/Co cation. The high m_{spin} obtained for Fe was in agreement with the presence of Fe^{2+} in octahedral positions.

- The islands studied by PEEM presented a magnetic domain pattern which was suggested to arise from the competition between the shape and the magnetocrystalline anisotropy. The magnetic domain structure imaged by XMCD-PEEM for Fe and Co matched perfectly. The high crystalline quality of the islands led to a magnetic domain configuration that was robust up to 735 K, down to the nanometer thickness and with large magnetic domains of up to 4 μm^2.

- The effect of annealing and exposing the sample in air was also investigated. The subsequent characterization of the wetting layer revealed only the signatures of Fe^{2+}/Co^{2+} oxidation states. On the other hand, the islands exhibited a change in the cation distribution with a decrease of the Fe^{2+} signal at the Fe XMCD spectrum and an increase of the Co XMCD signal suggesting a migration of Co^{2+} originally located at tetrahedral positions to octahedral positions. However, these results are taken with caution as different islands were compared before and after the annealing and the exposing in air. Further work is thus needed to investigate in more detail the effect of post-annealings and exposures in air on the cation distribution of the CFO islands. In addition, the magnetic domain configuration remained unaltered after few weeks of exposure in air as revealed by the comparison of MFM with XMCD images.

Appendix A

List of acronyms and abbreviations

SPLEEM Spin Polarized Low-Energy Electron Microscopy

UHV Ultra-high vacuum

MBE Molecular Beam Epitaxy

PLD Pulsed Laser Deposition

XPS X-ray Photoelectron Spectroscopy

AES Auger Electron Spectroscopy

ISS Ion Scattering Spectroscopy

LEED Low-Energy Electron Diffraction

μ-LEED Micro-spot Low-Energy Electron Diffraction

HV High Voltage

$\mathbf{I}_{Fil}$ Filament current

$\mathbf{I}_{emiss}$ Emission current

ML Monolayer

$\mathbf{E}_k$ Kinetic energy

$\mathbf{E}_b$ Binding energy

S Atomic sensitivity factor

Appendix A. List of acronyms and abbreviations

Z Atomic number

IMFP Inelastic Mean Free Path

EAL Effective Attenuation Length

RSF Relative Sensitivity Factor

C Atomic concentration

LEEM Low-Energy Electron Microscopy

Vs Start voltage

FOV Field Of View

PEEM Photoemission Electron Microscopy

MEM Mirror Electron Microscopy

hcp hexagonal close-packed

P Polarization

M Magnetization

A Asymmetry

MFM Magnetic Force Microscopy

XPEEM X-ray Photoelectron Emission Microscopy

XAS X-ray Absorption Spectroscopy

XMCD X-ray Magnetic Circular Dichroism

$\mathbf{m}_{spin}$ Spin magnetic moment

$\mathbf{m}_{orb}$ Orbital magnetic moment

$\mathbf{N}_h$ Number of 3d holes per formula unit

$\mathbf{n}_d$ Number of 3d electrons per cation

$\mathbf{T}_z$ Dipole operator

σ XAS absorption

λ_e Electron scape depth

λ_x X-ray absorption length

$\mathbf{T}_v$ Verwey temperature

p Pressure

MTJ Magnetic tunnel junction

TMR Tunneling magnetoresistance

Oct Octahedral

Tet Tetrahedral

IV Intensity-Voltage

SCV Subsurface Cation Vacancy

MIT Metal-Insulator Transition

AF Antiferromagnetic

FM Ferromagnetic

μ_B Bohr magneton

APB Antiphase Boundary

$\mathbf{k}_B$ Boltzmann constant

$\mathbf{E}_a$ Anisotropy energy

K Magnetocrystalline anisotropy constant

$\mathbf{E}_{strict}$ Magnetostrictive energy

λ_s Saturation magnetostriction

$\mathbf{E}_{ms}$ Magnetostatic energy

μ_0 Permeability constant

$\mathbf{H}_d$ Demagnetizing field

$\mathbf{N}_d$ Demagnetizing tensor

$\mathbf{T}_{srt}$ Spin reorientation transition temperature

$\mathbf{M}_s$ Saturation magnetization

$\mathbf{A}_{ex}$ Exchange stiffness

IR Infrared

UV Ultraviolet

OER Oxygen evolution reaction

RRAM Resistive random access memory

$\mathbf{d}_{ts}$ Target-substrate distance

FWHM Full Width at Half Maximum

AFM Atomic Force Microscopy

Appendix A. List of acronyms and abbreviations

WZ Wurtzite

RS Rocksalt

a Lattice parameter

O-MBE Oxygen assisted Molecular Beam Epitaxy

T_c Curie temperature

CFO Cobalt ferrite

Å Amstrong

K_s Shape anisotropy constant

Appendix B

List of publications

• L. Martín-García, R. Gargallo-Caballero, M. Monti, M. Foerster, J. F. Marco, L. Aballe, and J. de la Figuera. *Spin and orbital magnetic moment of reconstructed* $\sqrt{2} \times \sqrt{2}R45°$ *magnetite(001).* Physical Review B **91**, 020408(R) (2015).

• L. Martín-García, A. Quesada, C. Munuera, J. F. Fernández, M. García-Hernández, M. Foerster, L. Aballe, and J. de la Figuera. *Atomically Flat Ultrathin Cobalt Ferrite Islands.* Advanced Materials **27**, 39 (2015).

• L. Martín-García, S. Ruiz-Gómez, M. Abuín, Y. Montaña, N. Carmona, and L. Pérez. *Multifunctional core-shell Co-*SiO_2 *nanowires via electrodeposition and sol-gel techniques.* RSC Advances **5**, 97503-97507 (2015).

• J. de la Figuera, A. Quesada, L. Martín-García, M. Sanz, M. Oujja, E. Rebollar, M. Castillejo, P. Prieto, Á. Muñoz-Martín, L. Aballe, and J. F. Marco. *Self-organized single crystal mixed magnetite/cobalt ferrite films grown by infrared pulsed-laser deposition.* Applied Surface Science **359**, 480-485 (2015).

• J. de la Figuera, A. Quesada, L. Martín-García, M. Sanz, M. Oujja, M. Castillejo,

Appendix B. List of publications

A. Mascaraque, A. T. N'Diaye, M. Foerster, L. Aballe, and J. F. Marco. *Mössbauer and Magnetic Properties of Coherently Mixed Magnetite-Cobalt Ferrite Grown by Infrared Pulsed-Laser Deposition.* Croatica Chemica Acta **88** (4), 453-460 (2016).

- L. Martín-García, I. Bernal-Villamil, M. Oujja, E. Carrasco, R. Gargallo-Caballero, M. Castillejo, J. F. Marco, S. Gallego, and J. de la Figuera. *Unconventional properties of nanometric FeO(111) films on Ru(0001): stoichiometry and surface structure.* Journal of Materials Chemistry C **4**, 1850-1859 (2016).

- L. Martín-García, A. Mascaraque, B. M. Pabón, R. Bliem, G. S. Parkinson, G. Chen, A. K. Schmid, and J. de la Figuera. *Spin reorientation transition of magnetite (001).* Physical Review B **93**, 134419 (2016).

- R. Gargallo-Caballero, L. Martín-García, A. Quesada, C. Granados-Miralles, M. Foerster, L. Aballe, R. Bliem, G. S. Parkinson, P. Blaha, J. F. Marco, and J. de la Figuera. *Co on Fe_3O_4(001): Towards precise control of surface properties.* The Journal of Chemical Physics **144**, 094704 (2016).

- L. Martín-García, A. Quesada, L. Pérez, M. Foerster, L. Aballe, and J. de la Figuera. *Initial stages of the growth of mixed iron-cobalt oxides on Ru(0001).* Physics Procedia **85**, 12-19 (2016).

- P. Prieto, J. de la Figuera, L. Martín-García, J. E. Prieto, and J. F. Marco. *Fourfold in-plane magnetic anisotropy of magnetite thin films grown on TiN buffered Si(001) by ion-assisted sputtering.* Journal of Materials Chemistry C **4**, 7632-7639 (2016).